THE UNIVERSITY *of* EDINBURGH

This thesis has been submitted in fulfilment of the requirements for a postgraduate degree (e.g. PhD, MPhil, DClinPsychol) at the University of Edinburgh. Please note the following terms and conditions of use:

This work is protected by copyright and other intellectual property rights, which are retained by the thesis author, unless otherwise stated.
A copy can be downloaded for personal non-commercial research or study, without prior permission or charge.
This thesis cannot be reproduced or quoted extensively from without first obtaining permission in writing from the author.
The content must not be changed in any way or sold commercially in any format or medium without the formal permission of the author.
When referring to this work, full bibliographic details including the author, title, awarding institution and date of the thesis must be given.

The development of quantitative scanning electrochemical microscopy (SECM) imaging of single and array micro and nanoband edge platinum electrodes

THE UNIVERSITY *of* EDINBURGH

Ugne Mitrikeviciute

Degree of Doctor of Philosophy

The University of Edinburgh

2019

DECLARATION

I hereby declare that the work presented in this thesis has been written by me and is my own unless otherwise credited. The work has not been submitted for any other degree or professional qualification.

Ugne Mitrikeviciute

August, 2019

ACKNOWLEDGEMENTS

Firstly, I would like to thank my supervisor Prof Andrew R. Mount and my industrial supervisor Dr Andrew J. Wain who gave me the opportunity to work with them and have been supportive all the way through this four-year journey, especially during the last few months. Thanks also to my supervisors Prof. Ian Underwood and Prof Anthony J. Walton in the School of Engineering for challenging engineering discussions during our interdisciplinary meetings and welcoming me to the SMC. Thanks to Dr Fernando A. Castro, as the topic of my PhD was his idea. Thanks to Prof Anita C. Jones who initially encouraged me to apply for a PhD position and was my external examiner during the first year viva. I am a very lucky student to have such an army of not only academically brilliant but also understanding and genuinely nice supervisors.

Many thanks to those who were so kind and spared their time and knowledge to help me or were there to share the typical ups and downs of the PhD rollercoaster.

To be more specific, thanks to:

- Dr Andrew Piper for helping with my initial electrochemistry work, all the advice regarding electrode cleaning, data analysis and theory explanations;
- Dr Ilka Schmueser for teaching me the electrode fabrication in the clean room, introduction to COMSOL and such a generous overall support and patience during all these teaching interactions;
- Dr Justin Elliott, Dr Simon Reeves, Dr Hannah Levene who patiently read my poster and Roche Continents application drafts to improve my writing and English, for sharing their electrochemistry knowledge and being a great company during lunch breaks as well as sharing the highs and the lows within the group;
- Dr Camelia Dunare, Dr Ewen Blair, Dr Andreas Tsiamis who helped me with the electrode fabrication processes;
- Prof Alan F. Murray for the help in the clean room and some theory teaching (SMC);
- Prof Philip J. Camp for suggesting using modified Bessel function for fitting diffusion from point sources on a ring. It contributed to a majority of the data analysis in this thesis;
- to everyone in NPL, who made me feel welcome during my visits there, and people who helped me with my work, especially M. A. O'Connell, an expert of SECM-SICM;
- Katie Ember for being the best desk neighbour in the office;
- My new colleagues at work, Anja Stevens, Elena Sunchugasheva and Christian Boermel, who have been supportive, optimistic and understanding during these last

months of my thesis write up. It has been great having these lovely people outside the university to laugh with and at me regarding this write up experience.

Thanks to all these people mentioned above, as well as Ahmet Ucar and the whole Mount group for everything that is possible to thank for during the PhD experience. And especially thanks for being not only colleagues but also friends.

Last but definitely not least, thanks to my family, Aiste, Janina and Algirdas, for always believing in me and encouraging me to never give up. I made it.

LAY SUMMARY

Scanning electrochemical microscopy (SECM) is an established imaging technique, where a probe electrode moves parallel to a surface of interest, typically at a set and constant height, and records a local current or voltage signal in an electrolyte (salt) solution. SECM obtains useful electrochemical information about spatial differences in activity of the sample, which is usually made up of a combination of insulating (inactive) and conducting electrode (active) regions. SECM has been used to study a range of processes at surfaces including, for example, localised electrochemical reactions, uptake/release of chemical species by biological cells, metal corrosion or adsorption. When using this technique, it is common to validate the measured response using a well-characterised reference sample consisting of micro or nanoscale structures of known dimensions and electrochemical behaviour.

In this thesis, robust, high-precision test samples consisting of micro and nanoscale electrodes with well-defined disc and square geometries and well characterised electrochemical behaviour have been fabricated and used as substrates for the SECM. The generated images clearly show the conducting electrode regions surrounded by areas of insulator and it has been demonstrated that these samples are suitable as potential benchmark systems for SECM imaging by developing and applying both qualitative and quantitative analysis.

Prior to quantitative analysis, the separation between the tip and the substrate, *d*, had to be identified. This was achieved by performing probe approach curve (PAC) experiments, where the tip slowly approaches the insulator surface and stops when the measured current reaches a specified value. Values of *d* were then extracted by comparison of this experimental data with data predicted by theoretical calculations and mathematical models.

Next, SECM was employed to record images of the substrates, during which a range of parameters were varied, such as the probe working distance (*d*), the scanning speed and the voltage applied to the probe and sample. SECM images of such well-defined substrates are easily predictable. Therefore, any discrepancies in the SECM images regarding the expected electrode shape and size or the electrochemical response of the insulating or conducting surface can point to two possible issues: (i) mechanical or electrical problems with the performance of the SECM imaging system or probe; (ii) imaging artefacts in which the signal recorded gives a false impression of the sample. The most significant imaging artefact that was observed was enhanced current signals resulting from solution stirring by the movement of the probe, and these effects have been identified and evaluated qualitatively and quantitatively by analysing horizontal and vertical line profiles extracted from the recorded SECM images.

Finally, the SECM images generated also provided interesting information about the electrodes, such as uniformity and fidelity of the surfaces as well as visualization of the diffusion of the electroactive species arising from these electrodes (due to oxidation and reduction processes on the electrode surface) which has the potential to provide new practical and/or fundamental insights.

ABSTRACT

Imaging by scanning electrochemical microscopy (SECM) is an established technique that mixes electrochemistry with microscopy. To name a few examples of its broad applicability, it is used for imaging nanoparticles, enzymes, monitoring corrosion processes and redox processes in living cells. However, the information gathered from such images is mostly qualitative, rather than quantitative. Gold band arrays have been used as a standard substrate of nominally defined dimensions for conventional SECM imaging, but they are known to be non-uniform across the electrode surface and suffer ageing, producing significantly time-variant currents among other uncertainties. This thesis addresses this by imaging robust single and array micro and nanoband edge electrodes of controlled design, shape, size dimension and spacing and assists the quantitative analysis of the response.

Both qualitative and quantitative analysis was performed on these SECM images. First, data from experimental probe approach curve (PAC) experiments obtained before imaging were compared to the established analytical model reported by *Lefrou et al.*, confirming its applicability. This was then used to fit COMSOL simulated data to extract real tip working distances in µm above the insulator surface specific for these experiments. Then, qualitative analysis of SECM images of micro array, single micro and nanoband edge platinum (Pt) electrodes allowed the evaluation of the impact of effects such as convection, sample orientation and changes in the response of the SECM tip with time in feedback (FB) and substrate generator-tip collector (SG-TC) mode. From single electrode analysis, differences between the imaging modes regarding image resolution and imaging artefacts, also disc and square geometry impact, and differences between imaging micro and nanoband edge electrodes are discussed. Two types of arrays, hexagonal and square, were used as SECM substrates, also allowing to evaluate hemispherical diffusion field overlap evolution from differently arranged arrays. This allowed to visually evaluate the quality of the in-house fabricated electrodes which has not been reported before, together with visual evaluation and direct evidence that hemispherical diffusion field evolves from both disc and square geometry micro and nanoband edge electrodes.

Extraction of line profiles from various parts of the images was then used to further compare SG-TC and FB modes. This lead to the quantitative analysis of the tip response of selected scan lines (both vertical and horizontal) in these 2D images collected at fixed tip working distances. The responses of square nanoband edge electrodes were shown to fit to Gaussian distributions and to be consistent with a combination of diffusional broadening and convolution of the sample and tip response. Further, the tip currents were shown to follow the expected concentration profiles of diffusion from the ring nanoband generated analytically using modified Bessel function.

Finally, imaging settings and substrate and tip size were varied to evaluate their effect on image spatial resolution, on artefact occurrence and the effectiveness of the above quantitation. Images of a smaller disc nanoband edge electrode of 50 µm diameter instead of the previously used 100 µm were collected using SECM FB and SG-TC modes and were comparable to the 100 µm diameter electrodes. A Pt tip of 1 µm diameter, which is 10 times smaller than the original Pt tip, was used to probe the effect of the tip size. Finally, the effectiveness of quantitative approaches using Gaussian and modified Bessel functions on disc nanoband substrate of 50 µm diameter was evaluated and compared to 100 µm fitting results. Together this data analysis has enabled the evaluation of such electrodes as a benchmark system for SECM probe response validation, method development, optimisation and quantitation.

LIST OF ABBREVIATIONS

AFM – atomic force microscopy

Ar – Argon

CA – chronoamperometry

C_{dl} – capacitance of the electrical double layer

CE – counter electrode

CV – cyclic voltammetry

d – tip-substrate separation during SECM experiments

FB – feedback

FcMeOH – ferrocenemethanol

FWHM – full width at half maximum

G-C – generator-collector

H – horizontal

i_T^{bulk} – bulk current measured at the tip

LHS – left hand side

MNEE – microsquare/microdisc nanoband edge electrode

N_2 – nitrogen

NPs – nanoparticles

NPL – National Physical Laboratory

PAC – probe approach curve

PC – personal computer

Pd – palladium metal

Pt – platinum metal

PTFE – polytetrafluoroethylene

PVD – physical vapor deposition

RE – reference electrode

RHS – right hand side

SCE – saturated calomel electrode

SECM – scanning electrochemistry microscopy

SICM – scanning ion conductance microscopy

SG-TC – substrate generator-tip collector

SMC – Scottish Microelectronics Centre

SRN – silicon rich nitride

Ti – titanium

TG-SC – tip generator-substrate collector

UME – ultramicroelectrode

UoE – University of Edinburgh

V – vertical

WE – working electrode

TABLE OF CONTENTS

1 INTRODUCTION

1.1 SCANNING ELECTROCHEMICAL MICROSCOPY (SECM)

Scanning electrochemical microscopy (SECM) is a probe microscopy imaging technique, powerful when studying topography and/or electrochemical processes/reactivity across a specific area of the substrate. This is achieved by physically scanning above the area (the x-y plane) using a micro-/nano-electrode (known as a tip or a probe) placed close (z value small and often fixed) to the substrate (insulator or conductor) surface, as shown in Figure 1-1.[1,2] Both the probe and the substrate must be immersed in an electrolyte solution, in which electroactive species are also referred to as the redox mediator.[3] The tip current is recorded as a function of the tip location/position (x, y), and the resulting image is a two-dimensional current map of the surface. Image resolution and collection time is dependent on the step size and the step time (time spent by the tip at each point) as well as the tip radius[4] and the tip-substrate separation, also known as the tip working distance, *d*. For example, a decrease in resolution with increasing *d* resulting in image blurring has been shown to be related to the electrode's diffusion profile.[5]

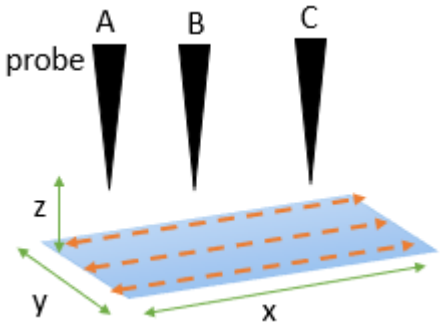

Figure 1-1. Graphical presentation of the SECM functioning, when the probe moves left to right on x-axis. The probe is shown to be above three locations (A-C) in a single line profile (dashed orange line), which can be either horizontal or vertical (depending on the direction of scanning: left to right or front to back, respectively). Each dash represents a step size.

Engstrom et al in 1986[6] first reported experiments similar to the scanning electrochemical microscopy (SECM) imaging technique, where direct observation of concentration profiles within the diffusion layer at an electrode-solution interface was recorded. Two electrodes, one macroscale (Pt wire) and the other microscale (carbon fibre, diameter = 10 µm), were placed close to each other in potassium ferrocyanide and potassium chloride solution, and the microelectrode was moved both parallel and orthogonal to the macro electrode. The macroelectrode had a step in potential applied to it between -0.2 V and +0.6 V, while the microelectrode was set at a constant -0.2 V potential. Such set up enabled monitoring of the

product species of ferricyanide generated at the macro electrode using the micro electrode. Upon stepping to the macroelectrode potential value at which ferrocyanide was oxidized to ferricyanide, the current at the microelectrode increased (positive feedback), representing that the product species generated at the macroelectrode diffused to the microelectrode and got reduced. When mass-transfer limited reaction at the macroelectrode was reached, the microelectrode current reached a plateau. Also, with increasing distance between the two electrodes, the current at the smaller one decreased, representing a smaller concentration of the product species available at the microelectrode. A time delay in the current response was also representative of the time needed for the product species to reach the microelectrode.[6]

Soon after this, SECM was introduced to the scientific community and now it has become a significantly more sophisticated system for sensing and imaging surfaces and their electrochemical behaviour. Conventional SECM was developed and introduced by Bard in 1989 and it mixes electrochemistry with microscopy.[7,8] The microelectrode tip never contacts the substrate surface, which is one of the main differences between SECM and other traditional scanning probe techniques.[9] The first commercial instrument was delivered by CH Instruments in 1999, resulting in a dramatic increase of SECM usage in many research groups.[10]

1.1.1 Applications of SECM

Since SECM development in the 1980s, this unique electrochemistry imaging technique has been modified to increase imaging resolution and to adjust to different substrates of interest, allowing the use of SECM in a variety of applications.[11] In general, SECM is a great tool for analysing localized electrochemical reactions, the uptake/release of chemical species at the surface, including processes in biological cells,[12,13] and micrometer and submicrometer- size structures and processes. Electron, ion or molecule transfers can be examined at many interfaces: solid-liquid[6,14], liquid-liquid and liquid-air, allowing the visualization and investigation of a variety of processes, such as metal corrosion, where corrosion products and diverse reactive species can be detected,[15,16] metabolism and the other redox processes in living cells, and adsorption processes to name a few.[10,13]

Original studies by Mirkin and Amemiya have shown that not only micro, but also nano-resolution with SECM is possible.[17,18] As such, SECM is emerging as a powerful tool in obtaining nanoscale electrochemical imaging and investigation of electron-transfer processes when using nanometer-sized electrodes as imaging probes.[19,20] Nanoscale SECM has been used to investigate: the topography of electrochemically active nano-objects[21], electrocatalytic reactions at single nanoparticles (NPs),[22] the detection of short-lived reaction intermediates[23] and the interrogation of biological cells[24].[19] SECM has also been used for nano-gap studies,

evaluation of the shapes of nanometer-sized microelectrodes and single nanoparticle imaging.[9,17,25] Further details are discussed below.

Metal NPs have extraordinary physical and chemical properties, making them great for sensing and electrocatalysis.[26] They have uniquely high surface-to-volume ratio[17,22] and they can be cathodically charged with large populations of electrons.[27] Investigations have been carried out to intentionally control not only the size of NPs, but also their shape and surface properties to achieve higher efficiencies in their catalytic activities so that the efficiency of e.g. electrochemical energy conversion and storage processes would be improved. Higher efficiencies in electrocatalytic devices can be achieved only if the structure and reactivity relationship of the individual rather than an ensemble catalytic metal NPs is understood and then controlled; understanding can be achieved through SECM nanoscale resolution images.[17,22]

In Figure 1-2, the Mirkin group immobilized and characterised a gold NP on an inert surface in several experiments. In the first example in Figure 1-2 (a), the unbiased NP was acting as a bipolar electrode, since the regeneration of the redox species (reduction) was occurring at the top half of the particle close to the tip, and the opposite reaction (oxidation) was occurring at the lower part of the NP. The NP was seen to produce positive SECM feedback, resulting in an increase in measured tip current (Section 2.9.2), the degree of which depended on the ratio of the particle to the tip radii as well as the heterogenous charge-transfer kinetics. At as short as <2-3 nm distances, the NP was observed to behave as a part of the tip electrode, as electron tunnelling was initiated. Such a mode of SECM allows the investigation of heterogeneous reactions at a single NP level without the need to make a direct ohmic contact, as well as to explain NP/electrode interactions on the electrode surface or in the nanoimpact collision events.[28]

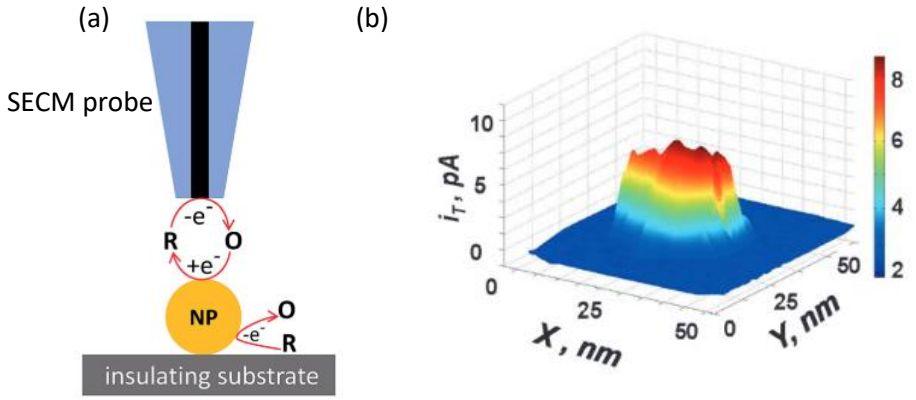

Figure 1-2. (a) Schematic diagram of the SECM probe above a single nanoparticle floating over the insulator surface. Positive feedback is observed between the tip and the upper part of the NP upon reduction, while oxidation occurs at the lower part of the NP upon interaction with the bulk solution.[28] (b) SECM image of a single gold NP on an HOPG surface.[22]

In Figure 1-2 (b), a single gold NP was immobilized on an inert highly ordered pyrolytic graphite (HOPG) surface. The SECM results allowed the investigation of the relationship between NP size, shape and orientation on the surface. The image clearly distinguishes between the significant positive and negative feedback (Section 2.9.2) over the NP and surrounding surface represented as red and blue colours in the image, respectively. The diameter of the NP from this image was observed to be close to the expected 20 nm value, unlike the 50 nm value obtained in an atomic force microscope (AFM) image taken during the same study. It was shown that SECM can be used to quantitatively probe an electrochemical reaction, such as an electron transfer (ET) at a single 20 nm NP, allowing the use of such approaches for characterization of the activities of NPs used as real-world macroscopic catalysts.[22]

The SECM technique has also been shown to be applicable in biosensing and bioimaging,[29] as both topography and electrochemical responses can be imaged.[30] Considerable progress has been made using SECM in the analysis of biological samples, including living cells and immobilized biomacromolecules such as enzymes, antibodies and DNA fragments.[31] Reduction-oxidation processes can be imaged and provide useful information about enzymatic activity, cellular functions, such as metabolism, and cell morphology, allowing the investigation of such important biological systems.[32,33] The activity of various cells can also be observed when monitoring oxygen consumption (oxygen reduction) at the tip, since oxygen concentration is related to cell respiration.[32]

Cells have been examined using different mediators, such as menadione. This is a synthetic form of vitamin K,[34] and it is a hydrophobic mediator which both oxidised and reduced forms can enter the cell and be regenerated at a measurable rate.[33] As a result, it was shown to result in a positive feedback in SECM imaging experiments, meaning that the tip current increased when scanning above the immobilized cell due to an intracellular oxidation of the reduced mediator species.[32,33] In a Bard study, SECM was used to study the uptake of menadione into yeast cells and its ejection as a glutathione complex; the SECM tip current was measured on yeast cells, suspended in the menadione-containing solution, allowing the measurement of the exported conjugate from cells with time.[35] The ultra-micro electrode (UME) tip was also positioned above the yeast cell aggregate, menadione was introduced and cyclic voltammograms were taken. Through the measurement of the tip current, concentration of the thiodione was measured. As this is the detoxification product released from yeast cells when they are stressed with menadione, this enabled an intracellular redox activity of yeast study.[35]

Electrochemical imaging is becoming more favourable for bio-imaging instead of standard fluorescence-based techniques due to simplicity, high speed, selectivity and the lower detection limit.[30] SECM also removes the need for labelling and allows for direct interrogation of the natural redox processes.[29]

There is the need for new electrocatalyst materials for energy conversion and SECM has been shown to be applicable in the assessment of oxygen reduction reaction (ORR) and hydrogen oxidation reaction (HOR) electrocatalysts for proton exchange membrane fuel cell (PEMFC) electrodes.[29] PEMFCs have attracted considerable attention in the scientific community in order to reduce the cost and improve the performance of these cells, which can be done if less costly (than Pt-based) electrocatalysts are found for the ORR in the acidic media.[36–38] Bard's group has compared ORR activity of various electrocatalysts using SECM; oxygen was generated at the tip via water electrolysis and the local ORR current was collected at the substrate.[29,36,38] SECM then allows a rapid scanning of catalyst spots, containing various mixtures of metals, and the identification of catalysts with relatively high activity for the ORR in acidic media.[36,38] This approach can yield a rapid screening method for testing large arrays of multicomponent, metallic electro-catalyst spots of varying compositions, which would significantly contribute to an effective way of discovering and evaluating alternative electrocatalysts for ORR in PEMFCs.[38] For example a Pd-Co electrocatalyst was found to show similar activity to Pt in strong acid.[38]

Challenges similar to those in electrocatalysis are experienced in photoelectrochemistry, where photoactive materials for solar energy harvesting and conversion are being developed.[29] Despite the progress made in understanding photoelectrochemical (PEC) systems, there is still the lack of practical, efficient, inexpensive and stable devices. There is an extensive number of metal combinations and dopants available for testing to achieve these desired characteristics, but a method allowing the synthesis and testing of these systems in a fast and efficient way is needed. SECM has been shown by Bard's group to be a suitable technique for this when the tip is replaced with an optical fibre which enables localized photoexcitation of the surface. The fibre is connected to a xenon lamp and rapidly scanned over the array, where the induced photocurrents are collected (as in the ORR current previously) at the substrate.[39] The light source illuminates each photocatalyst spot, whose activity gets determined from the generated photocurrent, as shown in Figure 1-3. The electrochemically active spots were imaged as high currents, while less active and non-active spots resulted in less intense positive feedback (hence lower feedback currents) and no sign of positive feedback at all, respectively.[39]

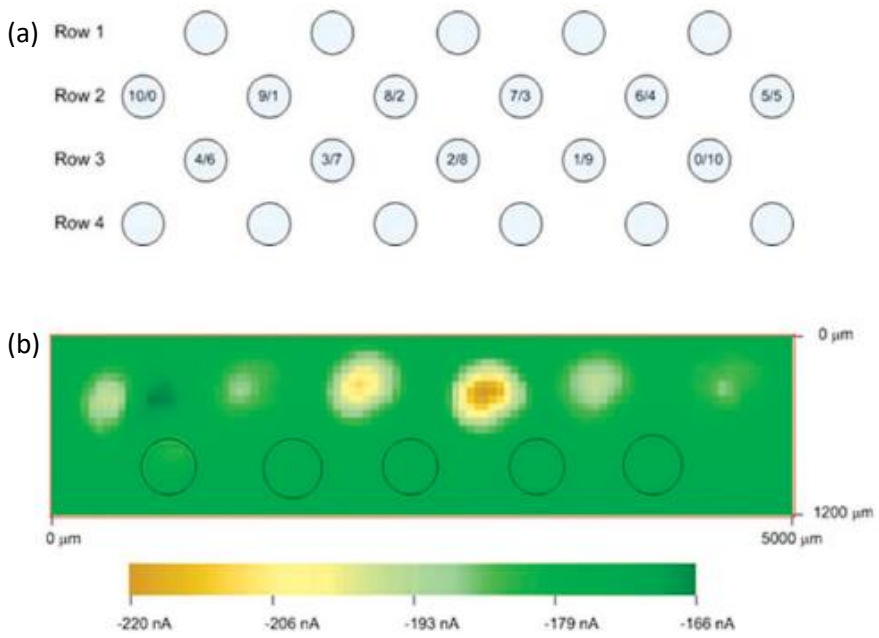

Figure 1-3. (a) Spots of photocatalysts in row 1-4, where rows 1 and 4 are 100 % Fe_2O_3 and rows 2-3 contain $Fe(NO_3)_3$ with Pd. Numbers in circles indicate number of drops of each, respectively. (b) SECM results of row 2 and 3 under UV-vis light illumination, showing that the two spots around the middle in the top row were the most photoelectrochemically active. (Images taken from reference[39].)

1.1.2 SECM developments to allow distance determination and control

SECM is used in a great variety of applications, as discussed above, but it is often lacking reliable quantitative distance determination and control. The measured current can be used to extract information about the tip-substrate distance, *d*, which is usually set using probe approach curves (PACs): the final value of *d* depends on the final measured tip current (Section 2.9.2). However, this can be challenging due to several reasons. If the tip electrode geometry is non-standard and hence lacking steady state expressions, or the underlying substrate is non-uniform, or the insulator surface isolated from the electrode is limited, or the distance is limited by the electrode and its sheath size, extracting *d* in a standard SECM set up becomes limited or even impossible.[19] Also, the SECM probe is typically a conductive electrode surrounded by an insulating glass, and a proper alignment between high fidelity probe and substrate surfaces is crucial.[10]

As a result of SECM coupling with other techniques through special combined probes, not only enhanced and complimentary information is collected to that available from SECM, but also the tip-substrate distance is determined more precisely.[19,40] Despite these special probes often being time consuming and difficult to fabricate, SECM variations have been introduced to obtain precise tip-substrate separation.[20,41,42] Tip positioning and distance control have been developed using SECM coupled with shear force[43], atomic force[44] and optical microscopy, as well as using a derived variation of SECM imaging modes[45,46].[11,19] This means that SECM can be either a complementary technique for other microscopies or new SECM imaging modes

can be introduced when using such non-standard imaging probes in order to introduce distance (feedback) control and to improve sensitivity.[20,41]

As SECM keeps advancing, more imaging probes also become available. One of such new probes is a micro pipette, filled with a liquid electrolyte containing neutral redox species and immiscible with the external solution, which allows the analysis of ionic reactants instead of redox species. As a result, another type of SECM mode, known as ion transfer (IT) or electron transfer/ion transfer (ET/IT) mode was introduced by Mirkin.[46] Neutral redox species are initially present only in the solution in the pipette but during the experiment the species partition from organic to aqueous phase. Upon bringing the pipette tip within a few tip radii from a conductive substrate surface, these neutral species diffuse to the surface and get oxidised. The resulting oxidation current corresponds to the local ET rate at the substrate surface facing the tip.[46] Such SECM variation allows for the same application of imaging surface topography and reactivity, only combining advantages of standard imaging modes of feedback (FB) and substrate generator-tip collector (SG-TC) (Section 2.9.2) while also removing their shortcomings.[46,47] The negative feedback response in ET/IT SECM is independent of the surface, unlike in standard SECM, and it can be used for the positioning of the pipette and importantly distance control.[46]

A constant-distance alternating current (AC) mode of SECM has been shown to be useful for imaging by Schuhmann.[16,48] In one of the studies, AC-SECM was used to image the metal/coating interface of lacquered tin plates, commonly used for manufacturing metal food containers, and the microscopic cracks and holes in the coating were visualized with high lateral resolution.[48] The mode is based on electrochemical impedance spectroscopy (EIS), which through the application of a sinusoidal excitation signal across the solid-liquid interface allows the measurement of the corresponding current or voltage response and the analysis of the data using AC theory.[48,49] The tip positioning is based on the application of high-frequency alternating voltage between two electrodes (SECM tip and counter electrode), and the AC current response is measured using a lock-in amplifier or frequency response analyser, thereby determining the system's impedance for analysis.[48]

Other types of microscopies, such as scanning ion conductance microscopy (SICM) and AFM can be coupled with SECM, allowing the use of SECM-SICM and SECM-AFM for more sophisticated analysis and imaging at the nanoscale.[50,51] For example, the SECM technique requires ultramicroelectrodes (UMEs), having dimensions of 1-25 μm,[52] for imaging the variation in electrochemical activity of a surface, covered by a redox mediator. However, the variations in topography are likely to distort results of electrochemical variations on the surface. Therefore, both electrochemical activity and high resolution topography of a surface can be simultaneously imaged when SECM is combined with SICM. [41,42,50,53]

SICM has been used for the studies of biological surface morphology at the nanoscale, and Figure 1-4 (a) shows a standard SICM setup.[50] SICM allows surfaces, covered by an electrolyte, to be probed by a glass pipette (d ≤ 100 nm), and an ion current is produced when one electrode is present at the pipette and another one – within the electrolyte solution covering the sample. The ion current decreases as the tip approaches the surface of the sample, hindering ion conduction, and so the immersed surface can be topographically mapped, since the ion current is used as a feedback parameter. The image is again therefore obtained in a non-contact regime.[50] A carbon nanoprobe double barrel tip in Figure 1-4 (b) can be used for SECM-SICM imaging of such substrates as nanopores and Pt interdigitated arrays (IDA), as shown in Figure 1-5 (a).[42]

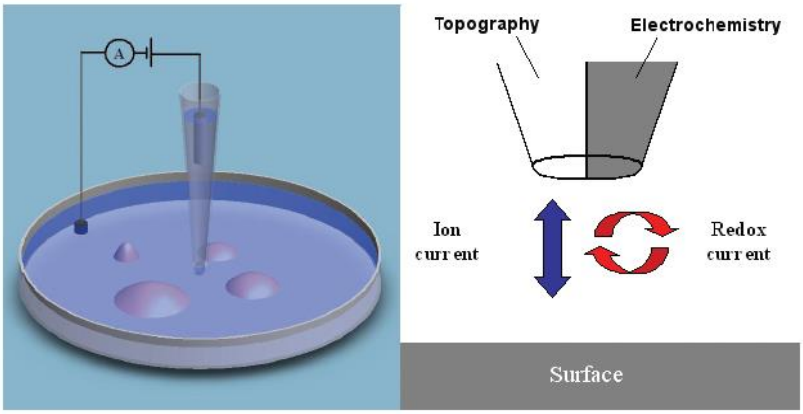

Figure 1-4. SICM setup (LHS) with a double barrel probe for SICM-SECM imaging (RHS). (Image taken from reference[50].)

In another study presented by Matsue, a Pt-based double barrel probe was used in SICM-SECM experiments for imaging of epidermal growth factor receptors on the membrane surface in Figure 1-5 (b).[41] Pt electrochemical deposition was performed on a carbon probe – nanoelectrode. The resulting spherical probe acted as an amplifier for electrochemical response, and the total flux of all electroactive species at the electrode surface was amplified. The probe was used for constant distance SECM-SICM imaging and higher electrochemical sensitivity was observed when compared to a bare carbon electrode of a nano size. This study for the first time demonstrated that a spherical electrode probe can be used for high-resolution electrochemical imaging.[41]

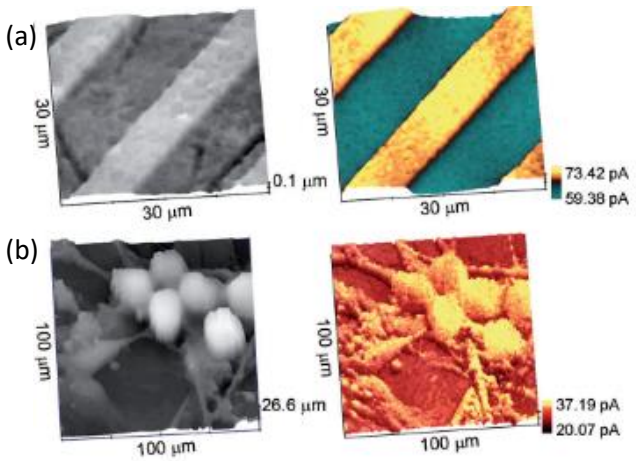

Figure 1-5. Simultaneous topographical (left) and electrochemical (right) images of (a) Pt-interdigitated electrode array and (b) living sensory neurons using SECM-SICM and a double barrel carbon nanoprobe. (Image taken from reference [20].)

SECM-AFM is another great tool for high-resolution electrochemical-topographical nanoscale imaging when using special probes, such as a Pt-coated AFM cantilever.[9,14,54] A feedback loop, controlled by a computer, allows for a constant cantilever amplitude, and hence a constant gap distance, while the tip is scanning the surface.[9] As such, SECM-AFM conductive tips have been used for simultaneous topographic and electrochemical property measurements of individual NPs, proteins on an individual virus,[9,55,56] nanopores,[57] and graphene and graphite substrates[9,51] to name but a few. However, one of the main disadvantages is the imperfect geometry of the tip, which means that quantitative electrochemical measurements are difficult.[9]

1.1.3 Quantitative SECM theory

SECM is an analytical technique, thus is it based on quantitative measurements. However, the probe system geometry is not as simple as in regular electrochemistry experiments. Even when a well described microelectrode tip is used in the simple positive and negative feedback PAC experiments, they are more challenging to be described with exact analytical expressions. Various general expressions or approximate analytical expressions are thus used instead to analyse steady-state feedback experiments.[58]

Analytical approximations have enabled generation of theoretical SECM dependencies and analysis of SECM experimental data. Most of these approximations are derived for a steady-state SECM response, because such quantitative studies are simpler than for non-steady-state responses, which depend on too many parameters complicating presentation of the experimental possibilities. Steady-state theory allows the usage of dimensionless working curves or analytical approximations.[10]

Kwak and Bard were the first ones to numerically calculate the dimensionless steady-state current-distance curves, known as probe approach curves (PACs), for a pure negative and a pure positive feedback (Section 2.9.2). The calculations assumed diffusion controlled redox species turnover, equal diffusion coefficients and an infinitely large substrate underneath the probe.[59] Based on these, other analytical expressions and approximations for various R_g values (Section 2.9.1) have been published.[60,61]

A disc geometry of microelectrodes used as SECM tips has been used the most widely, hence the approximate analytical and quantitative expressions and solutions have been derived mostly to disc geometry.[10,62] Analytical expressions for simulated data fitting are constantly improved and derived for other geometry probes as well to allow more effective and suitable modelling of various systems.[8,58,60] The lack of exact analytical descriptions of electrochemical responses means that modelling of experimental feedback curves is of a great importance. Zero tip-substrate separation point can be determined by fitting an experimental current-distance curve to the theory. This way the distance scale can be established which is essential for any quantitative SECM measurement.[10]

The PAC shape is dependent on the electron transfer rate at the substrate surface and there are two extremes.[63] The electron transfer rate can be zero or one when the probe is approaching an insulating or conducting surface, respectively, representing “pure negative feedback” and “pure positive feedback”.[8,63] A variety of curves are obtained for the intermediate electron transfer rate values,[28,63] such as in Figure 1-6. PACs are explained in more detail in Section 2.9.2.

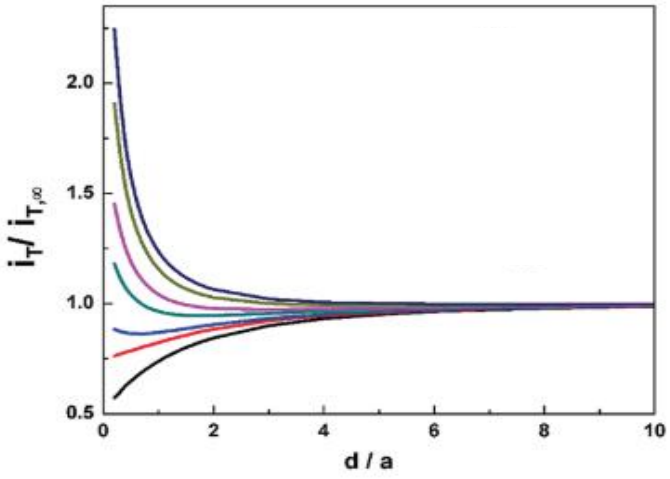

Figure 1-6. A variety of simulated PACs, representing varying electron transfer rate from ca. zero to ca. one. Both current and tip working distance have been normalized to bulk current and tip radius, respectively. (Image adjusted from reference[28].)

The SECM PACs are modelled using finite element model (FEM), built through COMSOL Multiphysics software, to achieve a quantitative insight into the imaging probe and underlying

substrate interaction. These are also typically modelled before any further, more complicated SECM system is modelled through COMSOL, such as 3D COMSOL modelling for the determination of live cell topography[64] or when probing passivating porous films[8]. Comparison between experimental and modelled curves also allows obtaining quantitative analysis of e.g. kinetic and physical properties of the sample.[65]

1.1.4 Issues with SECM standardised measurements

The development of different SECM probes and SECM combined with other techniques have enabled the imaging of smaller substrates. However, it does not fully solve the problem of the lack of standardised measurements and benchmarking substrate systems for SECM. Quantitative evaluation of whether the system is functioning as expected has not been fully developed and ways to better evaluate and account for imaging artefacts are still highly desired. Other microscopy techniques have some well-established standard systems for such measurements. For example, scanning tunnelling microscopy (STM) typically uses a gold grid of set dimensions[66] for initial imaging experiments or an HOPG graphite layer, freshly exposed for each measurement, allowing the imaging of hexagonal C planes[67].

Gold band arrays[65] have been used as a standard substrate of nominally defined dimensions for conventional SECM and SECM variation imaging.[53] Gold band arrays are easy to fabricate, have a defined spacing, are long and narrow, and are regularly placed hence it is known what dimension of results should be expected, making it a satisfactory standard.[68] However, there are also several characteristics that make them not the most desirable standard. They are known to be non-uniform in response across the electrode surface and to be lacking definition along the edges.[51] They typically suffer ageing, as the bands begin to delaminate at the edges after or during the use.[69,70] Fundamentally, they also produce time-variant current due to the cylindrical rather than steady-state hemispherical diffusion which is produced as a result of these long and narrow electrodes.[71,72] Together with a possibility of overlapping diffusion fields from the individual elements, this hinders quantitation in SECM measurements. Finally, gold band arrays are fragile, being susceptible to damage by simple handling errors or by the SECM tip if it hits the exposed electrode surface when imaging at smaller *d.*[69]

As such, SECM still would benefit from an easy to use and reliable standard. Our group has previously demonstrated the in-house photolithographic fabrication of rigid and robust Pt micro and nanoband edge electrodes.[73,74] Unlike gold band arrays or similar structures, these electrodes have high fidelity in terms of their geometry and dimensions due to the techniques used for their fabrication. The nanoband edge electrodes are readily and reproducibly obtained from the micro electrodes on etching through the metal, resulting in the electrode layer with an insulator layer top, preventing them from scratching and delaminating. Such electrodes show enhanced robustness and fidelity due to this recessed nature and their formation from the etching of selected areas of encapsulated thin film metal layers.[75,76] Quantitative reproducible

steady-state currents are obtained when under mass transport control.[71] This potentially allows the use of these electrodes not only for qualitative, but also for the quantitative analysis of imaging artefacts, related to the SECM technique. To the current knowledge, only kinetic studies have been shown to be quantified using SECM.[10]

1.2 MICROELECTRODES, MNEES AND ELECTRODE ARRAYS

1.2.1 Advantages of using micro versus macro electrodes in electrochemical experiments

Microelectrodes, also known as UMEs and also used as SECM tips,[77] due to a small electrode size have several different characteristics than macro electrodes.[52] In this section, microelectrodes, used for sensing instead of microelectrodes as SECM tips, that are spatially localised and measure a steady state current (see Section 2.9) are further discussed. First, linear diffusion transitions into more efficient hemispherical (radial) diffusion (Section 2.4), meaning that mass transport to/from the electrode surface of the redox species is faster, since the concentration gradients are very high.[78] This also means that less sensitivity to convection is experienced, and as the diffusion layer grows to the order of the electrode dimension, l, a steady-state current (Section 2.5) is recorded.[52] This never happens for a macro electrode due to the timescale and the effects of natural convection but happens in seconds or milliseconds for a microelectrode as this time ~ l^2/D (Section 2.4), given a typical diffusion coefficient, D, of 5×10^{-6} $cm^2\ s^{-1}$.[10]

Although the hemispherical diffusion results in the steady-state fluxes to the electrode surface (currents), the diffusion layer still grows with time.[10] As the double layer capacitance scales with electrode area (macro and microelectrode) but the Faradaic currents scale with radius (at the micro dimension and below), as the electrodes get smaller, at this scale the signal to noise gets bigger. Hence, microelectrodes have higher sensitivity than macro electrodes.[52,78] In addition, ohmic (iR) drop, a potential decrease at WE due to the resistance of the solution between reference and working electrodes when current flows in the electrochemical cell, is smaller. This means that some effects of this phenomena (peak signal shift in potential, decrease of the current and increased peak separation) are minimized in cyclic voltammogram experiments (Section 2.5).[77,79–83]

Microelectrodes definitely have become of real interest in modern electroanalytical chemistry, electrochemical studies and in many areas of science and technology, as predicted by Pletcher in the early 90s.[81,83] Electrodes even slightly larger than this still have the advantages for electroanalytical applications,[52] absent when using conventional, macro size electrodes. A combination of steady state behaviour, increased current density and improved signal to noise ratio (greater sensitivity) mean that microelectrodes are great electrochemical sensors.[52]

Small electrode size allows for the experiments in microscopic domains, and so microchemistry is applicable and benefits some of the technology application fields.[10,83] Electrodes can be incorporated in microelectronics, and they have been successfully incorporated in electrochemical devices for a variety of applications, including biosensing.[79,83] Electrochemistry became more useful in in vivo analysis as well as clinical treatment, since microelectrodes have low current flow due to their small size, meaning they are relatively non-invasive.[83]

Microelectrodes have been found to be applicable in many application fields and by far have showed better results than the standard macro electrodes in bioresearch, trace analysis and energy related areas.[81] Other applications include but are not limited to: high speed voltammetry, electrochemical experiments in highly resistive media, in vivo voltammetry.[80,81] There is a great potential to use them in imaging techniques to image diffusion fields and other electrodes, such as in SECM, which development also is strongly related to the development of the UMEs.[77] Fast mass transport allows to study fast processes such as fast-charge kinetics because the current is not as limited by how quickly redox species can diffuse to/from the electrode.[83,84]

1.2.2 Characteristics of nanoscale electrochemical systems

As the size of the electrode is further decreased past micro scale, the majority of the above discussed advantages further improve. This results in even more enhanced mass transport and further with this related advantages in sensing.[74]

At nano scale, the critical dimension of an electrode is of the same order as the size of the electrical double layer (EDL) (electrolyte-electrode interface[85]),[71] which has an effect on electron transfer (ET) reaction kinetics.[86] Since kinetics can be measured using steady-state experiments, it is expected that faster electrochemical and chemical reactions would be possible to study when using nano rather than microelectrode systems.[81]

While microchemistry and microelectrodes have been quite well understood and developed, nano materials have become of interest for further research and analysis in electrochemical applications.[87] Nanoband electrodes are expected to deliver even better results than microelectrodes in many areas, including 2D imaging. E.g., the resolution of the SECM image depends on the probe scale, and greater spatial resolution (useful electrochemical information about spatial differences in activity of the sample) is enabled when using nano probe.[78,88]

One of the main reasons why nanoband electrodes differ from microelectrodes is that experimental behaviour deviates from extrapolations of larger electrode's behaviour requiring further studies. At the band edges, the current density is expected to be the highest. The diffusion layer is the thinnest and migration is mostly contributing to the mass transport,

resulting in asymmetric current distribution.[71] This means that radial diffusion is dominant and negative effects of the solution resistance are decreased.[71,81,87]

There is a lot of ongoing work in order to show more advantageous behaviour of the nanoscale comparing to the bigger scale electrodes.[74] One of direct comparisons of electrochemistry arising from nano and macro scale is comparing Pt macro electrode with nanoband array having similar active Pt area. From the very initial CV experiment in KCl solution, it was observed that oxygen reduction wave below 0 V was much greater for microelectrode/microsquare nanoband edge electrode (MNEE), primitive nanoelectrode array system made by microfabrication, than for a macro electrode; hence more diffusion limited current has passed. Such experiment confirmed enhanced mass transport for nanoband electrode array, further backed up by a chronoamperometry experiment.[87]

1.2.3 Description of the electrode arrays

Micro- and nano- electrodes have increased mass transport and low ohmic drop compared to macro electrode. However, the reduced size of the electrode results in reduced currents, and obtained currents are tiny, and can be hard to measure with high fidelity, when measurement noise is greater than the signal. [41] If measured currents from single micro and nano electrodes are too small to work with and there is a requirement for higher sensitivity, electrode arrays can be used.[71,74,89] Such devices allow one to record higher currents which equal a product of the current from a single electrode multiplied by the number of the electrodes present in the array, *N*.[71,81]

Arrays can be interdigitated[65,90] (Figure 1-5 (a)), long band[71,72] (gold band) or MNEE.[71,74,89] The latter ones are robust, well defined and have been used in this thesis. Typical MNEE structure and design are shown in Figure 1-7. Array devices can be imaged using SECM, allowing evaluation of individual electrode activity as well as monitoring diffusion field expansion.

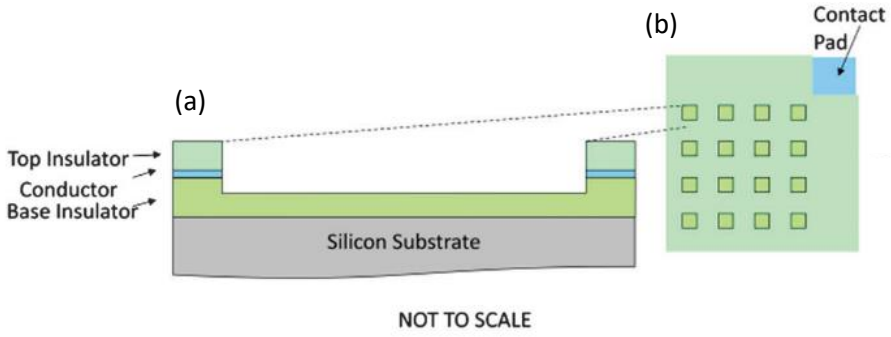

Figure 1-7. Schematic of an example of the MNEE array: (a) single square aperture in cross-section and (b) a plan view of the complete chip. (Image adjusted from reference[87].)

In order to preserve individual micro/nano electrode behaviour in any of the array type, it is important to prevent the hemispherical diffusion fields from individual electrodes overlapping.[71,82] Arrays must be designed so that appropriate distances between the electrodes are set to allow for each of the diffusion fields expansion. If overlap occurs, the resulting diffusion field can become linear, just like for macro electrodes, and so the characteristics of the system will also become similar to a macro electrode.[91] If that is prevented, all of the UME advantages such as high mass transport rates by hemispherical diffusion, resulting in a steady state behaviour and small charging times can be preserved while also recording higher currents which are much easier to measure and analyse.[91] As such, SECM can be used to image individual electrodes in the array devices to record visual proof if hemispherical diffusion fields are overlapping, and if so, to what extent and how much time is needed until the overlap is substantial, resulting in a macro electrode response.

1.2.4 Micro and nanoelectrode fabrication

As seen in the above sections, SECM probes and substrates tend to be of micro or nano scale. Depending on the electrode size, geometry and application, electrodes can be fabricated in various ways.[92] Micro electrodes (also used in this thesis) can be categorized as probe- or chip-based devices depending on their fabrication method.[93] Chip-based ones are usually obtained using photolithography technique.[52,92] Such microfabrication is an effective electrode fabrication method resulting in robust, well-defined electrodes and electrode arrays, where the size of individual elements as well as spacing between the elements are all controllable and highly reproducible.[71,74] Fabrication of the probe-based chips is usually specific by a fine metal being coated with an insulating material, e.g. glass or polymer. This way fabrication of probes for imaging techniques, such as SECM, is performed.[52,92]

An emerging way for microelectrode fabrication is screen-printing, which is more budget friendly and has advantages of simplicity as well as reproducibility, which is not always the case for photolithography-based technique, allowing for the mass production of the electrodes. However, there are also challenges, since depending on which method and materials are used, the screen-printed electrode array can be non-reproducible, meaning that electrodes can be of varying sizes and shapes.[52] Also, there might be leakage problems, which result in the loss of microelectrode behaviour, or electrochemical performance can get affected due to.[52] When dielectric layer, defining micro electrode size, is cured in the oven, efficient bonding to the carbon surface occurs, preventing above problems.[52] Further studies can be done to explore what sizes and geometry of the electrodes can be fabricated to compete with the photolithographic techniques.

There is a lot of concern regarding reproducibility of nano scale electrodes, which is the limitation regarding wider, industrial applicability.[87] Arrayed nanoelectrodes, resolving the low

signal issues, can be fabricated in several ways, some of which are briefly presented in this section.

Fabrication is relatively easy if there is no specific control of the inter-electrode spacing in the array devices, often referred to as ensembles. These can be produced by opening the pores in insulating layers deposited over conductive materials, hence exposing an ensemble of active electrode areas. This can be achieved using ultrasound or neutron track etching, templated growth in the nanopores of membranes or the imprinting of structures. However, large nanoelectrode arrays with systematic control of the size and separation of each electrode cannot be achieved in these ways. Instead, individual electrodes are likely to be affected by diffusional layer overlap from the neighbouring electrodes to variable extents as a function of time and there is heterogeneity of individual electrode response.[71]

Alternatively, ordered nanoscale arrays can be produced, but considerable expense and/or complexity is commonly encountered. Lower cost methods include micron resolution photolithography and reactive ion etch techniques. This way, arrays of individually addressable submicron band electrodes (e.g. 2 mm long with widths as small as 37 nm) can be fabricated. The electrodes are long and narrow, hence susceptible to line breakages during the fabrication process and/or operation. These electrodes also are not considered to produce steady-state response, desirable for some applications.[71,72]

The MNEE has been developed to address some of the above-mentioned issues. It is fabricated using reliable micron scale microfabrication techniques, including photolithography, which allows not only to control the size and shape of the electrode, but also the width of the nanoband.[73,74]

1.3 AIMS OF THIS THESIS

The SECM technique has been improved by introducing various different probes for scanning and combining with other imaging techniques. However, the original SECM set up is still widely used, and yet there is no standard set of measurements allowing ready evaluation of the sample and tip function as well as the presence and amount of imaging artefacts, ideally through quantitative analysis. The aim of this thesis is the qualitative and quantitative analysis of the SECM imaging of high fidelity micro electrodes and MNEEs and assessment of their suitability for standardised measurements and as a SECM benchmark system. Within the context discussed in this section, the main objectives of this thesis are to address the following:

- Fabrication of robust and well-defined single micro and nanoband-edge (MNEE) electrodes as well as micro electrode arrays using photolithographic techniques (Chapter 3).

- Use of analytical and numerical modelling to extract accurate SECM tip working distances (Chapter 4).
- Use of SECM for characterisation and diffusion field evolution imaging of the above-mentioned substrate samples in both disc and square geometry (Chapter 5-6, 8-9). Such analysis is only made possible through high fidelity substrate electrodes.
- Evaluation of diffusion field overlap in electrode array devices from SECM images (Chapter 5).
- Analysis of imaging artefacts and their dependence on imaging mode (Chapter 5-6, 8-9).
- Systematic study of the effect of the substrate size, the probe size, the imaging step and the imaging speed variation on SECM image resolution and artefacts (Chapter 8-9).
- Semi-quantitative and quantitative horizontal and vertical line profile analysis (Chapter 5-9).

1.4 REFERENCES

1. Cannes, C., Kanoufi, F. & Bard, A. J. Cyclic voltammetry and scanning electrochemical microscopy of ferrocenemethanol at monolayer and bilayer-modified gold electrodes. *J. Electroanal. Chem.* **547**, 83–91 (2003).
2. by Allen J. Bard (Editor), M. V. M. (Editor). *Scanning Electrochemical Microscopy, Second Edition*. (CRC Press, 2012).
3. Polcari, D., Dauphin-Ducharme, P. & Mauzeroll, J. Scanning Electrochemical Microscopy: A Comprehensive Review of Experimental Parameters from 1989 to 2015. *Chem. Rev.* **116**, 13234–13278 (2016).
4. Instruments, C. H. Scanning Electrochemical Microscope.
5. Stephens, L. I. & Mauzeroll, J. Altered Spatial Resolution of Scanning Electrochemical Microscopy Induced by Multifunctional Dual-Barrel Microelectrodes. *Anal. Chem.* **90**, 6796–6803 (2018).
6. Engstrom, R. C., Weber, M., Wunder, D. J., Burgess, R. & Winquist, S. Measurements within the Diffusion Layer Using a Microelectrode Probe. *Anal. Chem.* **58**, 844–848 (1986).
7. Bard, A. J., Fan, F.-R. F., Kwak, J. & Lev, O. Scanning Electrochemical Microscopy. Introduction and Principles. *Anal. Chem.* **61**, 132–138 (1989).
8. Kuss, C., Payne, N. A. & Mauzeroll, J. Probing Passivating Porous Films by Scanning Electrochemical Microscopy. *J. Electrochem. Soc.* **163**, 3066–3071 (2016).
9. Kai, T., Zoski, C. G. & Bard, A. J. Scanning electrochemical microscopy at the nanometer level. *Chem. Commun.* **54**, 1934–1947 (2018).
10. Sun, P., Laforge, F. O. & Mirkin, M. V. Scanning electrochemical microscopy in the 21st century. *Phys. Chem. Chem. Phys.* **9**, 802–823 (2007).
11. Takahashi, Y. *et al.* Multifunctional nanoprobes for nanoscale chemical imaging and localized chemical delivery at surfaces and interfaces. *Angew. Chem. Int. Ed. Engl.* **50**, 9638–42 (2011).

12. Ino, K. *et al.* Densified electrochemical sensors based on local redox cycling between vertically separated electrodes in substrate generation/chip collection and extended feedback modes. *Anal. Chem.* **86**, 4016–4023 (2014).

13. Zoski, C. G. Review—Advances in Scanning Electrochemical Microscopy (SECM). *J. Electrochem. Soc.* **163**, 3088–3100 (2016).

14. Macpherson, J. V., Unwin, P. R., Hillier, A. C. & Bard, A. J. In-situ imaging of ionic crystal dissolution using an integrated electrochemical/AFM probe. *J. Am. Chem. Soc.* **118**, 6445–6452 (1996).

15. Hampel, M., Schenderlein, M., Schary, C., Dimper, M. & Ozcan, O. Efficient detection of localized corrosion processes on stainless steel by means of scanning electrochemical microscopy (SECM) using a multi-electrode approach. *Electrochem. commun.* **101**, 52–55 (2019).

16. Eckhard, K., Etienne, M., Schulte, A. & Schuhmann, W. Constant-distance mode AC-SECM for the visualisation of corrosion pits. *Electrochem. commun.* **9**, 1793–1797 (2007).

17. Kim, J. *et al.* Electrocatalytic Activity of Individual Pt Nanoparticles Studied by Nanoscale Scanning Electrochemical Microscopy. *J. Am. Chem. Soc.* **138**, 8560–8568 (2016).

18. Kim, J., Shen, M., Nioradze, N. & Amemiya, S. Stabilizing nanometer scale tip-to-substrate gaps in scanning electrochemical microscopy using an isothermal chamber for thermal drift suppression. *Anal. Chem.* **84**, 3489–3492 (2012).

19. Sundaresan, V. *et al.* Visualizing and Calculating Tip-Substrate Distance in Nanoscale Scanning Electrochemical Microscopy Using 3-Dimensional Super-Resolution Optical Imaging. *Anal. Chem.* **89**, 922–928 (2017).

20. Takahashi, Y. *et al.* Multifunctional nanoprobes for nanoscale chemical imaging and localized chemical delivery at surfaces and interfaces. *Angew. Chemie - Int. Ed.* **50**, 9638–9642 (2011).

21. Kim, J., Xiong, H., Hofmann, M., Kong, J. & Amemiya, S. Scanning electrochemical microscopy of individual single-walled carbon nanotubes. *Anal. Chem.* **82**, 1605–1607 (2010).

22. Sun, T., Yu, Y., Zacher, B. J. & Mirkin, M. V. Scanning electrochemical microscopy of individual catalytic nanoparticles. *Angew. Chemie - Int. Ed.* **53**, 14120–14123 (2014).

23. Cao, F., Kim, J. & Bard, A. J. Detection of the short-lived cation radical intermediate in the electrochemical oxidation of N, N -dimethylaniline by scanning electrochemical microscopy. *J. Am. Chem. Soc.* **136**, 18163–18169 (2014).

24. Takahashi, Y. *et al.* Topographical and electrochemical nanoscale imaging of living cells using voltage-switching mode scanning electrochemical microscopy. *Proc. Natl. Acad. Sci.* **109**, 11540–11545 (2012).

25. Zoski, C. G. & Mirkin, M. V. Steady-State Limiting Currents at Finite Conical. *Anal. Chem.* **74**, 1986–1992 (2002).

26. Yu, Y., Sun, T. & Mirkin, M. V. Scanning Electrochemical Microscopy of Single Spherical Nanoparticles: Theory and Particle Size Evaluation. *Anal. Chem.* **87**, 7446–7453 (2015).

27. Murray, R. W. Nanoelectrochemistry: Metal Nanoparticles, Nanoelectrodes, and Nanopores. *Chem. Rev.* **108**, 2688–2720 (2008).

28. Sun, T., Wang, D. & Mirkin, M. V. Electrochemistry at a single nanoparticle: from bipolar regime to tunnelling. *Faraday Discuss.* **210**, 173–188 (2018).

29. Wain, A. J. Scanning electrochemical microscopy for combinatorial screening applications: A mini-review. *Electrochem. commun.* **46**, 9–12 (2014).

30. Matsue, T. Bioimaging with Micro / Nanoelectrode Systems. *Anal. Sci.* **29**, 171–179 (2013).

31. Felipe, C., Albert, S. & Wolfgang, S. Biological imaging with scanning electrochemical microscopy. *Proc. R. Soc. A Math. Phys. Eng. Sci.* **474**, 20180409 (2018).

32. Li, X. & Bard, A. J. Scanning electrochemical microscopy of HeLa cells – Effects of ferrocene methanol and silver ion. *J. Electroanal. Chem.* **628**, 35–42 (2009).

33. Liu, B., Cheng, W., Rotenberg, S. A. & Mirkin, M. V. Scanning electrochemical microscopy of living cells - Part 2. Imaging redox and acid/basic reactivities. *J. Electroanal. Chem.* **500**, 590–597 (2001).

34. EFSA. Scientific Opinion on the safety and efficacy of vitamin K 3 (menadione sodium bisulphite and menadione nicotinamide bisulphite) as a feed additive for all animal species 1. *EFSA* **12**, (2014).

35. Mauzeroll, J. & Bard, A. J. Scanning electrochemical microscopy of menadione-glutathione conjugate export from yeast cells. *Proc. Natl. Acad. Sci.* **101**, 7862–7867 (2004).

36. Fernández, J. L. & Bard, A. J. Scanning electrochemical microscopy. 47. Imaging electrocatalytic activity for oxygen reduction in an acidic medium by the tip generation - Substrate collection mode. *Anal. Chem.* **75**, 2967–2974 (2003).

37. Bing, Y., Liu, H., Zhang, L., Ghosh, D. & Zhang, J. Nanostructured Pt-alloy electrocatalysts for PEM fuel cell oxygen reduction reaction. *Chem. Soc. Rev.* **39**, 2184–2202 (2010).

38. Fernández, J. L., Walsh, D. A. & Bard, A. J. Thermodynamic guidelines for the design of bimetallic catalysts for oxygen electroreduction and rapid screening by scanning electrochemical microscopy. M-Co (M: Pd, Ag, Au). *J. Am. Chem. Soc.* **127**, 357–365 (2005).

39. Lee, J., Ye, H., Pan, S. & Bard, A. J. Screening of Photocatalysts by Scanning Electrochemical Microscopy. **80**, 1–2 (2008).

40. Amemiya, S., Bard, A. J., Fan, F. R. F., Mirkin, M. V. & Unwin, P. R. Scanning electrochemical microscopy. *Annu. Rev. Anal. Chem. (Palo Alto. Calif).* **1**, 95–131 (2008).

41. Şen, M. *et al.* Improving the Electrochemical Imaging Sensitivity of Scanning Electrochemical Microscopy-Scanning Ion Conductance Microscopy by Using Electrochemical Pt Deposition. *Anal. Chem.* 150223122321004 (2015). doi:10.1021/acs.analchem.5b00027

42. Takahashi, Y. *et al.* Multifunctional nanoprobes for nanoscale chemical imaging and localized chemical delivery at surfaces and interfaces. *Angew. Chemie - Int. Ed.* **50**, 9638–9642 (2011).

43. Kranz, C. Recent advancements in nanoelectrodes and nanopipettes used in combined scanning electrochemical microscopy techniques. *Analyst* **139**, 336–352 (2013).

44. Kranz, C. *et al.* Integrating an ultramicroelectrode in an AFM cantilever: Combined technology for enhanced information. *Anal. Chem.* **73**, 2491–2500 (2001).

45. McKelvey, K., Edwards, M. a. & Unwin, P. R. Intermittent contact-scanning electrochemical microscopy (IC-SECM): A new approach for tip positioning and simultaneous imaging of interfacial topography and activity. *Anal. Chem.* **82**, 6334–

6337 (2010).

46. Wang, Y., Kececi, K. & Mirkin, M. V. Electron transfer/ion transfer mode of scanning electrochemical microscopy (SECM): A new tool for imaging and kinetic studies. *Chem. Sci.* **4**, 3606–3616 (2013).

47. Shao, Y. & Mirkin, M. V. Probing Ion Transfer at the Liquid / Liquid Interface by Scanning Electrochemical Microscopy (SECM). *J. Phys. Chem. B* **102**, 9915–9921 (1998).

48. Katemann, B. B., Schulte, A., Calvo, E. J., Koudelka-Hep, M. & Schuhmann, W. Localised electrochemical impedance spectroscopy with high lateral resolution by means of alternating current scanning electrochemical microscopy. *Anti-Corrosion Methods Mater.* **4**, 134–138 (2002).

49. Diakowski, P. M. & Ding, Z. Novel strategy for constant-distance imaging using alternating current scanning electrochemical microscopy. *Electrochem. commun.* **9**, 2617–2621 (2007).

50. Pollard, A. J. *et al.* Development of a novel combined scanning electrochemical microscope (SECM) and scanning ion-conductance microscope (SICM) probe for soft sample imaging. *MRS Online Proc. Libr.* **1422**, No pp. given (2011).

51. Wain, A. J., Pollard, A. J. & Richter, C. High-resolution electrochemical and topographical imaging using batch-fabricated cantilever probes. *Anal. Chem.* **86**, 5143–5149 (2014).

52. Metters, J. P., Tan, F., Kadara, R. O. & Banks, C. E. Electroanalytical properties of screen printed shallow recessed electrodes. *Anal. Methods* 3140–3149 (2012). doi:10.1039/c2ay25512j

53. Ebejer, N., Schnippering, M., Colburn, A. W., Edwards, M. A. & Unwin, P. R. Localized High Resolution Electrochemistry and Multifunctional Imaging : Scanning Electrochemical Cell Microscopy. *Lett. to Anal. Chem.* **82**, 9141–9145 (2010).

54. Kueng, A., Kranz, C., Lugstein, A., Bertagnolli, E. & Mizaikoff, B. A FM-tip-integrated amperometric microbiosensors: High-resolution imaging of membrane transport. *Angew. Chemie - Int. Ed.* **44**, 3419–3422 (2005).

55. Huang, K., Anne, A., Bahri, M. A. & Demaille, C. Probing individual redox PEGylated gold nanoparticles by electrochemical-atomic force microscopy. *ACS Nano* **7**, 4151–4163 (2013).

56. Nault, L. *et al.* Electrochemical atomic force microscopy imaging of redox-immunomarked proteins on native potyviruses: From subparticle to single-protein resolution. *ACS Nano* **9**, 4911–4924 (2015).

57. Arrigan, D. W. M. Nanoelectrodes, nanoelectrode arrays and their applications. *Analyst* **129**, 1157–1165 (2004).

58. Lefrou, C. & Cornut, R. Analytical expressions for quantitative scanning electrochemical microscopy (SECM). *ChemPhysChem* **11**, 547–556 (2010).

59. Kwak, J. & Bard, A. J. Scanning Electrochemical Microscopy. Theory of the Feedback Mode. **1227**, 1221–1227 (1989).

60. Cornut, R. & Lefrou, C. A unified new analytical approximation for negative feedback currents with a microdisk SECM tip. *J. Electroanal. Chem.* **608**, 59–66 (2007).

61. R. Cornut, C. L. New analytical approximation of feedback approach curves with a microdisk SECM tip and irreversible kinetic reaction at the substrate. *J. Electroanal. Chem.* 178–184 (2008).

62. Compton, R. G., Wildgoose, G. G., Rees, N. V, Streeter, I. & Baron, R. Design, fabrication, characterisation and application of nanoelectrode arrays. *Chem. Phys. Lett.* **459**, 1–17 (2008).

63. Zhou, Q., Wang, Y., Tallman, D. E. & Jensen, M. B. Simulation of SECM Approach Curves for Heterogeneous Metal Surfaces. *J. Electrochem. Soc.* **159**, H644–H649 (2012).

64. Li, M. S. M., Filice, F. P. & Ding, Z. Determining live cell topography by scanning electrochemical microscopy. *J. Electroanal. Chem.* **779**, 176–186 (2016).

65. Filice, F. P., Li, M. S. M., Henderson, J. D. & Ding, Z. Three-Dimensional Electrochemical Functionality of an Interdigitated Array Electrode by Scanning Electrochemical Microscopy. *J. Phys. Chem. C* **119**, 21473–21482 (2015).

66. Womelsdorf, J. F., Ermler, W. C. & Sandroff, C. J. Imaging of colloidal gold on graphite by scanning tunneling microscopy: Isolated particles, aggregates, and ordered arrays. *J. Phys. Chem.* **95**, 503–505 (1991).

67. Gan, Y., Chu, W. & Qiao, L. STM investigation on interaction between superstructure and grain boundary in graphite. *Surf. Sci.* **539**, 120–128 (2003).

68. Thormann, W., van den Bosch, P. & Bond, A. M. Voltammetry at Linear Gold and Platinum Microelectrode Arrays Produced by Lithographic Techniques. *Anal. Chem.* **57**, 2764–2770 (1985).

69. Tian, H. *Tribology and Interfacial Delamination of Thin Film Systems*. (massachusetts Institute of Technology, Department of Mechanical Engineering, 1990).

70. *Handbook of Electrochemistry*. (Elsevier Science, 2006).

71. Schmueser, I. *et al.* A systematic study of the influence of nanoelectrode dimensions on electrode performance and the implications for electroanalysis and sensing. *Faraday Discuss.* **164**, 295 (2013).

72. Forster, R. J. Microelectrodes: New Dimensions in Electrochemistry. *Chem. Soc. Rev.* **23**, 289–297 (1994).

73. Damion K Corrigan, Justin P Elliott, Ewen O Blair, Simon J Reeves, Ilka Schmüser, A. J. W. and A. R. M. Advances in electroanalysis, sensing and monitoring in molten salts. *Faraday Discuss.* 351–366 (2016). doi:10.7488/ds/1338

74. Terry, J. G. *et al.* Nanoscale electrode arrays produced with microscale lithographic techniques for use in biomedical sensing applications. *IET Nanobiotechnol.* **7**, 125–134 (2013).

75. Blair, E. O., Corrigan, D. K., Terry, J. G., Mount, A. R. & Walton, A. J. Development and Optimization of Durable Microelectrodes for Quantitative Electroanalysis in Molten Salt. *J. Microelectromechanical Syst.* **24**, 1346–1354 (2015).

76. Li, P. Q., Piper, A., Schmueser, I., Mount, A. R. & Corrigan, D. K. Impedimetric measurement of DNA–DNA hybridisation using microelectrodes with different radii for detection of methicillin resistant Staphylococcus aureus (MRSA). *Analyst* **142**, 2849–2849 (2017).

77. Walsh, D. A., Lovelock, K. R. J. & Licence, P. Ultramicroelectrode voltammetry and scanning electrochemical microscopy in room-temperature ionic liquid electrolytes. *Chem. Soc. Rev.* **39**, 4185–4194 (2010).

78. Arrigan, D. W. M. Nanoelectrodes, nanoelectrode arrays and their applications. *Analyst* **129**, 1157–1165 (2004).

79. Prats-alfonso, E., Villa, R., Guimera, A. & Campo, F. J. D. E. L. *Development of*

Microelectrode- based Biosensors for Biomedical Analysis. (2016).

80. Wiley, J. Analytical Electrochemistry: The Basic Concepts References and Links. 1996–1997 (2009).

81. Kosuke, I. Electrochemistry. *Electrochemistry* **83**, 688–694 (2015).

82. Hwang, S. *et al.* CMOS microelectrode array for electrochemical lab-on-a-chip applications. *IEEE Sens. J.* **9**, 609–615 (2009).

83. Pletcher, D. Why Microelectrodes? in *Microelectrodes: Theory and Applications* (ed. Montenegro, Irene, Queirós, M. Arlete, Daschbach, J. L.) 3–16 (Springer Netherlands, 1991).

84. Woodvine, H. L. Development and Characterisation of Microelectrode and Nanoelectrode Systems. (The University of Edinburgh, 2012).

85. University of Cambridge Department of Chemical Engineering and Biotechnology. The Electrical Double Layer. *Teaching Notes* (2015). Available at: http://www.ceb.cam.ac.uk/research/groups/rg-eme/teaching-notes/the-electrical-double-layer.

86. Bae, J. H., Yu, Y. & Mirkin, M. V. Diffuse Layer Effect on Electron-Transfer Kinetics Measured by Scanning Electrochemical Microscopy (SECM). *J. Phys. Chem. Lett.* **8**, 1338–1342 (2017).

87. Freeman, N. J. *et al.* Comparison of the performance of an array of nanoband electrodes with a macro electrode with similar overall area. *Phys.Chem.Chem.Phys.* 8112–8118 (2013). doi:10.1039/c3cp50759a

88. Tomčík, P. Microelectrode arrays with overlapped diffusion layers as electroanalytical detectors: theory and basic applications. *Sensors (Basel).* **13**, 13659–13684 (2013).

89. Woodvine, H. L., Terry, J. G., Walton, A. J. & Mount, A. R. The development and characterisation of square microfabricated electrode systems. *Analyst* **135**, 1058–1065 (2010).

90. Partel, S. *et al.* Lift-Off Free Fabrication Approach for Periodic Structure with Tunable nano Gaps for Interdigitated Electrode Arrays. *ACS Nano* 1086–1092 (2016). doi:10.1021/acsnano.5b06405

91. Brady, C. L. . The Development and Characterisation of Microelectrodes for Extreme Environments. (The University of Edinburgh, 2013).

92. ŠTULÍK, K., AMATORE, C., HOLUB, K., MAREČEK, V. & KUTNER, W. MICROELECTRODES. DEFINITIONS, CHARACTERIZATION, AND APPLICATIONS. *Pure Appl. Chem.* **72**, 1483–1492 (2000).

93. Ino, K., Şen, M., Shiku, H. & Matsue, T. Micro/nanoelectrochemical probe and chip devices for evaluation of three-dimensional cultured cells. *Analyst* **142**, 4343–4354 (2017).

2 THEORY

2.1 ELECTROCHEMISTRY OVERVIEW AND APPLICATIONS

Electrochemistry has obviously been around for a long time. 'The roots of electrochemistry can be traced to Egyptian and Roman physicians who used the discharges of electric eels as a method of treatment.'[1] It is therefore no surprise that many basic electrochemical principles as well as relationships had been described before the discovery of the electron in 1893 by J. J. Thompson.[2] Electrochemistry is fundamentally a study of the interconversion between chemical and electrical energy.[3–5] In this work, it involves the monitoring of electron transfer at the interface between a metallic electrode and a solution (solid-liquid interface) containing redox active species.[2]

A wide range of research and applications involve understanding and controlling this form of electrochemistry. It can be used to determine and/or develop electrochemical properties of organic and inorganic materials, to develop enhanced fuel cells, battery technology and solar cells, to investigate electrocatalysis, to understand colloid science, electrochemical sensors, electrodeposition, corrosion, nanoscale effects, and to explore biochemical and biological systems, including nerves and enzyme reactions.[3–5] In this chapter, the basic terminology, methods and principles of electrochemistry relevant to the results shown in the following chapters is presented.

2.2 DEFINING TERMS

2.2.1 Thermodynamically driven redox reactions

Electrochemical experiments as defined in this thesis can be carried out only if electrochemically active species are present in the solution, also referred to as an electrolyte. An electrolyte is a solution containing solvent and supporting electrolyte (inert salt) ions, typically of high concentration for balancing the charge on the electrode through the formation of a thin double layer. The concentration of the dissolved salt also governs the conductivity of the solution, hence, high values minimize the solution electrical resistance to passage of current.[2,5] The electrochemically active species in such solutions undergo reduction/oxidation reactions, also known as redox reactions, unlike the supporting electrolyte. This means that an electron is transferred to/from the active species next to the electrode in solution (a local electron transfer), and this transfer occurs across the metal electrode-electrolyte interface. An example of one-electron electrochemically and chemically reversible redox couple (see Section 2.2.2) includes ferrocene/ferrocinium methanol ($FcMeOH/FcMeOH^+$) as shown in Equation (2.1).[5,6]

$$FcMeOH^+ + e^- \rightleftharpoons FcMeOH \quad (2.1)$$

Reduction reactions are typically presented when reading the reaction from left to right, and oxidation reactions are read from right to left.[2]

FcMeOH species are typically a choice for SECM experiments not only due to reversible redox reactions, but also due to fast kinetics during electron transfer processes (very efficient electron transfer rate).[7–9] Thus, it can be used for quantitative studies of the kinetics, such as the measurements of electron transfer rate constants.[7,8] FcMeOH also results in a well-predicted, of a sharp 'S' shape cyclic voltammogram under typical experimental conditions (Section 2.5). Since FcMeOH was used in all of the SECM experiments in this thesis, the oxidation reaction of Equation (2.1) is referred to in the results chapters and Figure 2-1 shows this reaction using chemical structures.

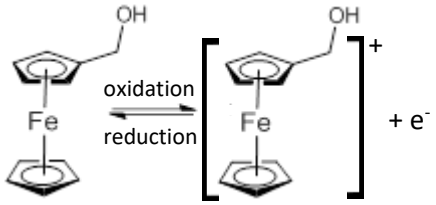

Figure 2-1 Chemical structures of ferrocenemethanol (left) and ferrocinium methanol (right) related by oxidation/reduction processes. This also represents redox reactions discussed in the results chapters of this thesis.

The driving force for these electrochemical reactions is thermodynamics, controlled by the change in free energy during such reactions. This can be explained though the change of Gibb's free energy, ΔG, which combines changes in enthalpy, ΔH, and entropy, ΔS, of the reaction as shown in Equation (2.2) below, either where these three parameters are under standard conditions (denoted by ^{0}) or not (no ^{0}) and T is temperature.[5,10]

$$\Delta G^0 = \Delta H^0 - T\Delta S^0 \quad (2.2)$$

The change in enthalpy reflects the heat change in the system during the reaction.[11] Entropy is a property of matter and it tells us how energy is dispersed within it.[11] The reaction is spontaneous (will occur) when ΔG is negative, meaning that the reaction does not require an energy input to occur.[2]

In electrochemistry, any redox reaction can be made to occur by changing the energy of the electron through changing the electrode potential. How this occurs can be explained by considering the energy levels of the electronic orbitals. When a potential (V) is applied to an inert electrode, usually made of gold, platinum, glassy carbon or mercury, the highest energy of the electrons in the electrode is controlled. At a certain potential, the highest occupied molecular orbital (HOMO) energy of the electrode (the Fermi level) is higher than the lowest

unoccupied molecular orbital (LUMO) or the lowest partially occupied molecular orbital of the redox species, as shown in Figure 2-2 (b). This leads to a thermodynamically spontaneous reaction where an electron transfer from the electrode to the redox species occurs (reduction), as shown in Figure 2-2 (c). The driving force for this reaction is the energy difference between the two orbitals, and the reduction is thermodynamically favourable (overall negative ΔG). As the Fermi level can be raised or lowered upon a change in the potential of the electrode (to more negative or positive potentials), a more positive potential will lead to this orbital of the electrode being below the molecular orbital of Fc in energy, and electron transfer from Fc to metal (oxidation) will be spontaneous.[5]

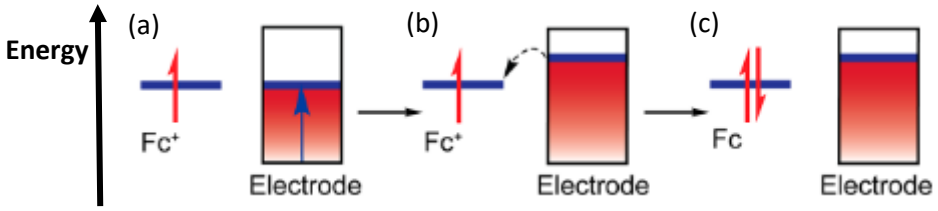

Figure 2-2. Schematic diagram showing highest occupied molecular orbital (MO) of ferrocinium and highest occupied molecular orbital (Fermi level) of the metal electrode (with red denoting the filled electron energy levels) when they are (a) at the same level and no net electron transfer occurs and (b) the electrode potential is made more negative (decreased), raising the Fermi level and causing the reduction of ferricinium (c). (Figure adjusted from reference.[5])

2.2.2 Kinetics and reversibility

If the forward and reverse reaction in Equation (2.1) is rapid, then equilibrium will be established at the electrode, as shown by the use of two-way half-headed arrows, which represent an electrochemically reversible reaction.[5] Electrochemical reversibility is possible when there is a low kinetic barrier to an electron transfer compared to the thermal energy.[5] Equation (2.1) is an example of such reactions, where minimal change in the configuration of the coordination shell of the molecule occurs on oxidation or reduction and where the added electronic charge is effectively delocalised around the reduced species.[5]

Depending on the slowest step of the reaction, it can be either mass transfer or charge transfer limited. Generally, both of these processes are required e.g. mass transfer of a reactant from bulk solution occurs prior to charge transfer. If the excess potential (known as overpotential) applied to the working electrode (WE) is large (positive or negative compared to the standard or formal potential, see Section 2.2.3), the charge transfer at the electrode-electrolyte interface is generally fast and the reaction is mass transfer limited. For an irreversible reaction, when a small excess potential (near the standard or formal electrode potential) is applied to the WE, charge transfer is often the slowest step, and hence the rate-determining step of the reaction.

Electrochemically reversible reactions are different to chemically reversible or irreversible reactions. Chemical irreversibility occurs when the product of an electrochemical reaction can

further react in a subsequent chemical reaction.[2,12] In other words, if a reduction process is chemically reversible, the product is sufficiently stable to be subsequently reoxidised.[2,5] This means that FcMeOH/FcMeOH$^+$ is also a chemically reversible redox couple.

2.2.3 Nernst equation

If the system is electrochemically reversible with fast kinetics, the Nernst equation relates the potential of the electrochemical cell (two electrodes) or a half cell (one electrode) to the activities (concentrations) at the surface of the electrode(s).[2] This equation is one of the most important equations in electrochemistry and it provides a powerful way to predict how a system will respond to or effect a change of redox species concentration at the electrode-solution interface due to electrode potential variation.[2,5] Thus the term 'Nernstian equilibrium' is used and it can be assumed to be established at the electrode surface essentially immediately upon any change in applied potential in such systems when there is a low barrier to an electron transfer.[5]

The Nernst equation is derived from thermodynamics. To be specific, from the Gibbs's free energy, *G*, as shown in Equations (2.3-2.5).[2,13]

$$\Delta G = -nFE_{cell} \quad (2.3)^{9}$$

$$\Delta G = \Delta G^0 + RT\ ln\ Q, \quad (2.4)^{2}$$

$$\Delta G^0 = -nFE^0_{cell} \quad (2.5)^{2}$$

Where n is the number of electrons involved in an electrode redox reaction, F is the Faraday's constant (96 485 C mol^{-1}), ΔG is the change in free energy for the process, $\Delta G°$ is the change in *G* for the process when reactants and products are in their standard states, *R* is the gas constant (8.314 J / (mol×K)), *ln Q* is the natural log of the reaction quotient (relative activities (concentrations) of products divided by the relative activities (concentrations) of reactants in the reaction[14,15]).[2,13] The cell voltage, E_{cell}, is the potential difference between the two electrodes in the cell at open circuit (no current flowing in the cell), and the potential of each electrode is also referred to as the open-circuit potential (OCP).[2,13]

For a reaction $O + e^- \rightleftharpoons R$, we solve for E_{cell} from Equation (2.3) while using ΔG from Equation (2.4) and ΔG^0 from Equation (2.5). The result is the Nernst equation, which relates potential measured at the cell and the concentration of the redox species at the surface of an electrode, as shown in Equation (2.6).[2,16]

$$E_{cell} = E^0_{cell} - \frac{RT}{nF}\ ln\ Q \quad (2.6)$$

E^0_{cell} is the voltage under standard conditions or simply the measured voltage when $Q = 1$.[11] If the concentrations of the reactants and products on both sides of the cell represent chemical

equilibrium, the cell cannot perform any electrical work, E_{cell} = 0 and there can be no net flow of electrons between the two sides of the cell. Then $Q = K$, meaning that the reaction quotient becomes the equilibrium constant, K.[13] In this case, at T = 25 ^{0}C the Nernst equation can be expressed as follows:[16,13]

$$E^0_{cell} = \frac{0.0591}{n} \ln K \tag{2.7}$$

Then, it is also possible to get the Nernst equation for a single electrode. By the substitution of K or Q for the activities of the products and the reactants Equation (2.6) becomes as follows:

$$E = E^0 + \frac{RT}{nF} \ln \frac{a_O}{a_R} \tag{2.8}$$

where E^0 is a standard potential of an electrode (not a cell as above). Since activities cannot be measured, they are assumed to be proportional to concentration of the redox species, c, which can actually be measured. The two terms are related via the activity coefficient, γ, measuring by how much solution activity is different from the ideal solution (γ = 1), as shown in Equation (2.9).[15,16]

$$a = \frac{\gamma c}{c^\circ} \tag{2.9}$$

where c^0 is the standard concentration (1 mol dm^{-3}). Since the standard potential is not often measured in the electrochemical cell, the formal potential, $E^{0'}$, against the reference electrode (RE) (under non-standard conditions) is measured and used in the equation instead. Such substitution is possible due to the following relationship:

$$E^{0\prime} = E^0 + \frac{RT}{nF} ln \frac{\gamma_O}{\gamma_R} \tag{2.10}$$

When $\gamma_O = \gamma_R$= 1, the concentration ratio of O and R is unity and all other concentrations are fixed; therefore, formal potential equals to standard potential. When n = 1, Equation (2.8) becomes as follows:

$$E = E^{0\prime} + \frac{RT}{F} ln \frac{[O]}{[R]} \tag{2.11}$$

Where E is a potential applied to (or measured at) the WE with respect to the RE. When substituting T = 25 ^{0}C, R and F for their values, this leads to the final one-electrode Nernst equation at:[5,13]

$$E = E^{0\prime} + 0.0591 ln \frac{[O]}{[R]} \tag{2.12}$$

2.2.4 Faradaic and non-Faradaic reactions

Faradaic and non-Faradaic processes, both occurring at the electrode, are distinguished by whether charge (electron) transfer across the metal-solution interface occurs.[2,17] The two processes represent fundamentally different modes of electrode behaviour.[17] In a Faradaic electrode process, charge transfer occurs and both product and reactant redox species are typically in the solution phase.[17] The current is proportional to the rate of electron transfer at the electrode surface and hence the rate of the redox reaction,[17] while the charge, *Q,* (the integral of the current with time) is proportional to the amount of a substance generated, as stated by the Faraday's law shown in Equation (2.13).[18]

$$Q = nFN \tag{2.13}$$

The amount of a substance consumed/deposited or liberated on an electrode during electrolysis (the number of moles, *N*) is therefore directly proportional to the total quantity of electric charge passed.[18]

Non-Faradaic currents are attributed to all the other processes that induce current. such as parasitic currents.[17] These are typically small and an example of undesired currents, including noise, which can occur as a result of the experimental set-up. A Faraday cage is typically used to minimise electrical noise. Another example of non-Faradaic currents is the charging current (electrical double layer) as is outlined in Section 2.2.5. In the experiments in this thesis (voltammetry and PACs), it is transitory and/or constant, and a small contribution to the overall current compared to the current due to the redox reactions, since the work has been done exclusively with microelectrodes and MNEEs. The overall contribution of non-Faradic currents can be neglected, and the currents measured in this thesis are mainly Faradaic.

2.2.5 Electrical double layer

The capacitance of the electrical double layer (C_{dl}) is the most important parameter which determines the double layer charging (non-Faradaic) currents. The double layer is a region of solution that is close to the electrode surface where electric fields exist as a result of the excess charge on the electrode.[19] The C_{dl} is proportional to the area of a macroelectrode and is independent of the scan rate.[20] The magnitude and variation of C_{dl} can be explained using the double layer models of the interfacial region between a macro electrode surface and an electrolyte solution (Section 2.2.1).

Such electrode/electrolyte interface was first considered by Helmholtz (1853), using a simple model, assuming that no electron transfer reactions (Faradaic processes) occur.[21] The model is shown in Figure 2-3 (a). Ions are either attracted or repelled electrostatically depending on the charge within the solution layer which is close to the electrode surface. This results in an excess of counterions (either anions (negatively charged ions) or cations (positively charged ions)) which build up at this interface to balance the charge on the electrode. These attracted

ions can typically approach an electrode to a minimum distance determined by the solvated size of the ion. The plane through the centre of this layer of ions is called the Outer Helmholtz Plane (OHP), which in this model completely balances the excess charge on the metal.[21] The corresponding potential drop (Section 2.2.6) across this metal surface-OHP interface is shown in Figure 2-3 (d). Helmholtz named this interface as an 'electrical double layer'. It is also equivalent to an electrical capacitor, since charge is stored in the two layers of ions, as on the plates of a capacitor.[21]

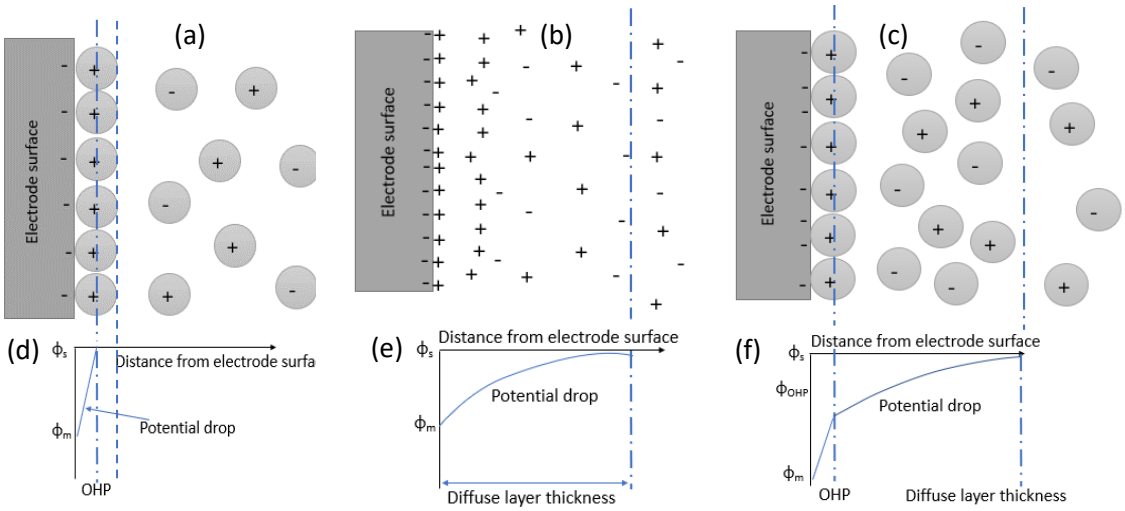

Figure 2-3. Schematic of (a) Helmholtz, (b) Gouy-Chapman, and (c) Stern electrical double layer and the corresponding plots of the surface potential versus distance from an electrode surface in (d-f) (reproduced from reference[21]).

Then, the double layer model was improved by Gouy and Chapman independently (Gouy-Chapman theory). This model in Figure 2-3 (b) uses point charges representing ions to enable a Boltzmann distribution of cations and anions in the electric field near the electrode, and the corresponding imbalance of charge to determine the evolution of this field with distance from the electrode. The charge density in the solution is thus contained within a 'diffuse layer', which is close to the electrode surface but is spread over a greater distance (more diffuse) than in the Helmholtz model. This is due to the Brownian motion and the kT (thermal energy) of the neighbouring molecules, which is the random thermal motion of molecules mathematically expressed as a function of probabilities.[22,23] It counteracts electrostatic attraction forces by providing enough energy to overcome the attractive forces to the electrode for some ions at the OHP and this means that the excess charge density in solution is present not only at the OHP.[21] As a result, the potential drop across this diffuse layer is less sharp than in the Helmholtz model, as some charge is also held further away from the electrode and the OHP. The net charge density decreases with increasing distance away from the electrode surface, as depicted in Figure 2-3 (e).[21]

Both models have problems, as the first neglects the thermal forces and the second neglects the ion size and assumes the ions can approach infinitely close to the electrode. These issues were addressed by Stern, who finalised the model in 1924, by combining the two models, as shown in Figure 2-3 (c).[21] The resulting (Gouy-Chapman-Stern) model considers two layers within the electrode-electrolyte interface: the first is a compact layer of ions strongly electrostatically adsorbed at the surface of the electrode – giving rise to the Helmholtz-like double layer capacitance (C_H); and the second is a diffuse layer, taking into account a continuous distribution of ions driven by thermal motion – the diffuse double layer capacitance (C_{diff}), where the attractive forces are lower and the ions compensate the charge over a larger distance in a Boltzmann distribution.[19,24,25] Therefore, the overall observed capacitance of the double layer (C_{dl}) is a combination of the two capacitances in series, as shown in Equation (2.14), and it is usually of the order of nanometres.[19]

$$\frac{1}{C_{dl}} = \frac{1}{C_H} + \frac{1}{C_{diff}} \tag{2.14}$$

The initial potential drop is sharp between the electrode and OHP and then it gradually falls to a value, which is characteristic of the bulk electrolyte at the edge of the diffuse double layer, which is further away from the electrode surface, as shown in Figure 2-3 (f).[21] When using smaller than macro electrode, the overall C_{dl} is reduced, resulting in smaller electrical double layer (EDL) effects on electron transfer (ET) reactions.[26,27] Therefore, capacitive effects typically become less important than Faradaic processes for microelectrodes. In other words, the enhanced mass transport (diffusion) at microelectrodes means the Faradaic currents become more dominant (Section 2.4). At smaller electrode scale depletion (diffusion) layer also starts approaching the size of the double layer and the two become interlinked.[19,28]

2.2.6 Three electrode system

Electrochemical experiments are a great tool to observe/detect/study specific species in the solution if Faradaic reactions are involved.[5,29] A standard set-up in electrochemistry involves a three-electrode system. It includes counter electrode (CE), reference electrode (RE) and working electrode (WE) as well as hardware, such as a potentiostat, required to control and monitor the system.[29] The potential, E (V), is typically set in the experiment and it is applied to the WE as a voltage (a measured potential difference between two electrodes) or simply measured (in the case of OCP measurements (Section 2.2.2)) with respect to the constant potential RE. Meanwhile, the CE is a current sink for the system, and it is used for supporting the resulting current at WE in order to ensure only current between CE and WE is measured; a large area CE is typically used.[2,29] As a result of the resistance of the solution between WE and RE, when current flows in an electrochemical cell the potential drop at a WE surface may be less than the applied potential. This phenomenon is described by Ohm's law in Equation

(2.15) and hence it is often called Ohmic drop or simply *iR drop*. This equation shows that this potential drop, V, is related to the measured current in the cell, *i*, multiplied by the solution resistance, R_s.[2,26]

$$V = iR_s \tag{2.15}$$

To ensure V is so small it can be neglected, R_s must be minimised. This is achieved by adding the background electrolyte (R_s is inversely proportional to *c*) and, additionally where this is not enough e.g. for non-aqueous solvents, placing the WE and RE close together. The latter is typically not done unless strictly necessary, as if the electrodes are too close together this will interfere with transport to the WE.[2] Another way to minimise the *iR* drop is to reduce the current, which means operating with as small a current as possible. This is done by simply using micro- and nano-electrodes, and reduced *iR* drop is one of the advantages of these electrodes.

It is possible for a second WE to be introduced, in which case the potential (E_2) and current (i_2) are then also controlled and measured between this WE and a common RE and CE respectively. This makes it a four-electrode system, an example of which is the SECM technique used throughout this thesis, in which the two WEs are the tip and the substrate.

2.2.7 Electrochemical windows

An electrochemical window of a solvent is the potential limits between which the solvent does not oxidise or reduce[4] and there are no electrolyte related Faradaic currents (the electrolyte is electrochemically inert).[4,30] A smaller electrochemical window within this solvent window is then chosen to study the reaction of choice in electrochemical experiments, allowing focus on redox characterisation at the electrode/electrolyte interface without interference from other electrochemical processes.[4,30]

2.3 MASS TRANSPORT TO THE ELECTRODE SURFACE

As mentioned in Section 2.2.4, Faradaic currents are dependent on a combination of two processes: mass transport, which is a rate at which redox species reach the electrode from the bulk solution, and charge transfer, which is the rate of electrons transferring across the electrode/electrolyte interface.[2,31] Therefore, it is important to understand mass transport, which has three mechanisms: diffusion, migration and convection. All three phenomena affect the movement of redox species and can contribute to the magnitude and evolution of a measured current. Typically it is desired to design an experiment in a way so that the effects of one or more transport processes of species are negligible, controlled and/or predictable.[10,31]

Diffusion is a spontaneous, random movement of species from regions of high to low concentration (or activity) of the same species. The rate of diffusion is dependent on the difference between the concentrations at the two points of interest (which is also known as the

concentration gradient) and on the diffusion coefficient, *D*. The latter has a specific value for each of the solution species at fixed temperature.[10,31,32] An uneven concentration distribution is equalised by diffusion, which at the same time maximises the system entropy.[11]

Migration is a movement of charged particles driven by electrostatic fields.[5,31,32] This means that positive ions are attracted to negative electrodes or vice versa unless effectively shielded such that there is no field. An addition of ions that make up a background electrolyte at a 10-100-fold excess with respect to the redox species concentration eliminates this migration effect (outside the double layer) through the double layer formation and shielding. This way an electric field arising due to a positive-negative charge attraction gets minimized, as electrolyte (of high concentrations) migrates to the electrode surface for a charge balance. An electric field between the two electrodes involved in the experimental measurement is then spread over more ions in the solution compared to when only redox species are present, as discussed in Section 2.2.5.[5,10,31,32]

Convection is a movement of species placed within a specific volume of hydrodynamically moving (stirred or agitated) solution.[10,31,32] This is driven by net hydrodynamic flow, and it represents the action of convective forces, such as stirring, thermal gradients which give rise to density fluctuations, or vibrations. Forced convection may be suppressed by simply not stirring and thermally equilibrating the solution but natural convection (although relatively inefficient) cannot be completely eliminated.[10,31,32]

Individual contributions from diffusion, migration and convection feature in the Nernst-Planck equation as a concentration gradient, an electric field and a hydrodynamic velocity, respectively.[31,32] This equation reveals that the total flux of species moving towards the electrode surface is proportional to either of the slopes of these terms, represented as a function of distance from the electrode surface.[31,32] Since current leads to local changes in concentration, diffusion is hard to be eliminated and thus it dominates mass transport in most electrochemical experiments. As a result, only diffusion controlled currents are analysed and modelled, as migration and major convection effects, as discussed above, can be removed and therefore excluded from the most commonly used theoretical treatments and modelling.[31,32] This means that most of the experiments can be designed in a way that mass transport would be only diffusion-controlled and modelled by Fick's 1st law of diffusion in one dimension, x, as shown in Equation (2.16).[10,31] This represents diffusion term in Nernst-Planck equation and more details on the other two terms can be found in the literature.[33,34]

$$J = -\frac{D_A \, \partial[A]}{\partial x} \tag{2.16}$$

where J is diffusive flux, D_A is the diffusion coefficient of species A, which can be either oxidant or reductant and d[A]/dx is the concentration gradient of A with respect to the distance from an electrode surface, x.[10,31]

2.4 DIFFUSION LAYER EVOLUTION

Diffusion governed mass transport results from reaction at an electrode such as the WE. Thus the diffusion/depletion layer is a region of electrolyte adjacent to the WE, where reactants are depleted and products accumulate and from this region redox species (reactants/products) diffuse to/from the bulk solution.[26] Redox species concentrations within this field differ from the bulk concentration, hence concentration gradients exist, as discussed in Section 2.3. Figure 2-4 shows the two mostly encountered types of diffusion of reactants, marked as arrows towards the electrodes. The mass transfer can approach such an electrode surface either normal to the electrode surface (linearly) or from/to the edge (radially). Hence the diffusion to the electrode surface can be either linear or radial (hemispherical), respectively.[26]

In this thesis, as a result of the diffusive flux and progressive diffusion of the reactant species, the diffusion layer thickness from an electrode surface, l, grows with time (or space between the tip and the substrate).[35] The characteristic relationship used in electrochemistry is shown in Equation (2.17), which can also be rearranged to a more relevant to this thesis expression in Equation (2.18).

$$t = \frac{l^2}{4D} \tag{2.17}$$

$$l = 2\sqrt{Dt} \tag{2.18}$$

Equation (2.18) allows one to calculate the diffusion length (the depletion layer thickness), l, depending on the diffusion coefficient of the redox species and time.[19,26,32] In other words, a semi-infinite electrochemical diffusion layer thickness can be obtained.[36] Such l, t and D relationship has also been shown by Einstein to be related to Brownian motion (a random walk process), showing that diffusion and random walk share the same mathematical represantation.[20] The numerical value in front of D was shown different in the original paper by Einstein (possibly representing linear diffusion).

Macro electrode, described as having at least millimetre (mm) size critical dimension (which determines the electrochemical response of the electrode[38]), has a large area, hence the thickness of the diffusion layer at any time is relatively small compared to the electrode dimensions. Mass transport to the electrode surface is linear with negligible edge contribution,

as shown in Figure 2-4 (a). Since the edge contribution (edge effect), also known as radial diffusion, is tiny compared to the linear diffusion, the latter dominates.[39]

Smaller dimension electrodes such as microelectrodes or nanobands, where at least one of the characteristic dimensions needs to be on the micro or nano scale, experience different diffusion controlled mass transfer.[35] When the electrode is this small, diffusion from the edges of the electrode rapidly becomes more significant than linear diffusion, and radial diffusion contributes more to the mass transport of redox species.[26,35] This results in an overall hemispherical diffusion field, as shown in Figure 2-4 (b)[26] as soon as the diffusion layer thickness is comparable in size to the electrode dimension, *a*, and at longer times (Equation (2.18), with *a* substituted for *l*).[40]

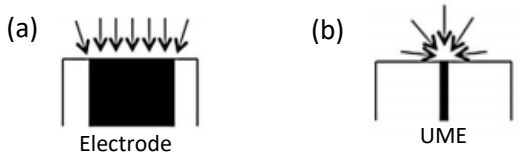

Figure 2-4. Illustrations of (a) a linear diffusion to a macro electrode surface where radial diffusion to the corners of the electrode are negligible and (b) a radial diffusion to an UME where linear diffusion is negligible. (Figure adjusted from reference[26].)

Square electrodes have a very specific diffusion profile, which is a combination of three diffusional modes: linear, edge and point diffusion. Linear diffusion exists initially over the majority (central) electrode area, while edge diffusion is seen at the edges and point diffusion takes place at the corners. The concentration gradient is the greatest at the corners, meaning that the current density is also the greatest initially and in this area the diffusion layer increases at the fastest rate.[35,41] However, when dimension of the square electrode is microns or smaller, it has been shown by modelling theoretically and through impedance analysis[32] that as the diffusion layer grows with time, an overall near hemispherical diffusion layer rapidly forms, just like for a micro disc or an ultra-micro disc electrode. It is typical to distinguish UMEs from microelectrodes in order to emphasize the smaller size of the former's dimensions, as they are within a specific 1-25 µm range.[26] Although the diffusion field evolution for both disc and square electrodes has been modelled and the results predict that both diffusion fields are hemispherical,[32] consistent with electrochemical measurements, this remains to be observed and confirmed by SECM imaging (see Chapter 5).

2.5 CYCLIC VOLTAMMETRY RESPONSES

One of the most commonly encountered experiments in electroanalytical studies of a WE system is cyclic voltammetry (CV). It is a dynamic experiment where an applied potential to a WE is varied linearly with time at a constant sweep (scan) rate, as shown in Figure 2-5 and

then the sweep is reversed to return, resulting in a triangular potential cycle.[21] For an oxidation, the CV experiment is set to start sweeping at the leftmost point of the desired electrochemical window limits E_1 and in the forward (initial) scan. The potential E is swept positively from the starting point until it reaches the switching potential E_2 and it generates an anodic (oxidising) current. At this point the scan direction is reversed, hence the potential is swept negatively until the same starting point, inducing the re-reduction of the oxidised product, and the resulting signal is cathodic.[5,21]

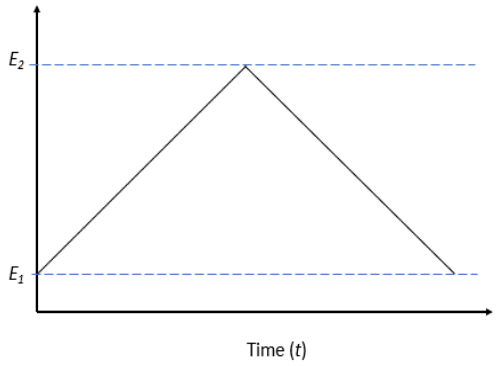

Figure 2-5. Applied potential versus time in a typical CV experiment when studying an oxidation. E_1 is a potential applied at the start of the experiment, E_2 is a switching potential. Standard (formal) reduction potential is between E_1 and E_2. (Reproduced from reference[18].)

The resulting data are plotted as cyclic voltammograms, which are plots of the generated current (the response) versus the applied potential (the parameter imposed on the system).[4,5] The response reflects three stages of the redox reactions occurring at the electrode surface: an electroactive species traveling towards the surface of working electrode (WE), the species getting reduced/oxidised, and the resulting product of this reaction moving away into the bulk solution from the electrode surface.[29]

In this thesis, all recorded cyclic voltammograms are from reversible one electron transfer reactions, providing typical responses as shown in Figure 2-6. The generated cyclic voltammograms give characteristic shapes for macro, micro and nano scale electrodes.[42] These shapes (and currents) are governed by diffusion-controlled mass transport processes in the solution.[10] Both the peaks and sigmoidal responses in cyclic voltammograms arise from Faradaic currents, consistent with electron transfer redox processes taking place.[17]

Macro electrodes have their peak-shaped signals shown in Figure 2-6 (a) due to linear diffusion. The signal is often referred to as a duck (body and beak) shaped signal.[5,26,39] As the potential is swept from an initial point towards the switching potential, it reaches values that can induce oxidation of the redox species, resulting in a measured current increase. As more positive potential values are reached, the current rise slows down and a maximum value of

the anodic peak, i_{pa}, at the maximum peak potential, E_{pa}, is reached as mass transport becomes limiting.[21]

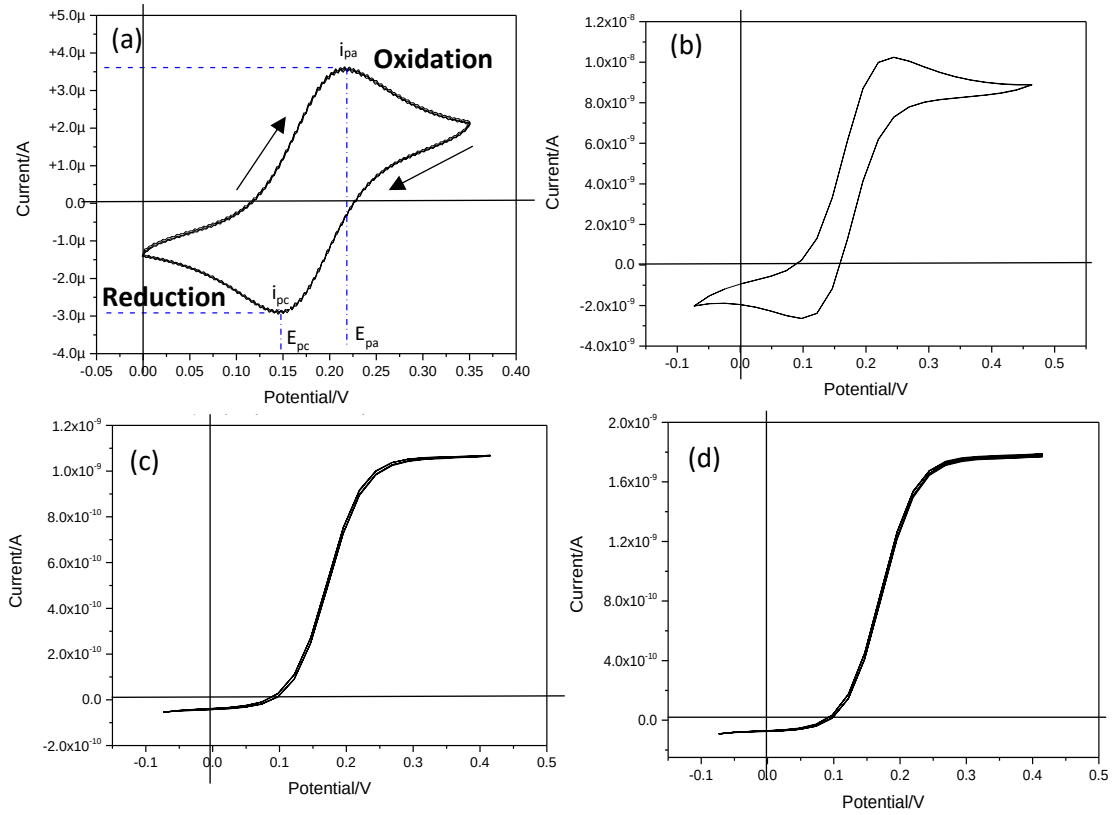

Figure 2-6. Typical cyclic voltammograms for different size electrodes: (a) a Pt macro electrode CV, where i_{pc} is the cathodic peak current, i_{pa} is the anodic peak current, E_{pc} is the cathodic peak potential, E_{pa} is the anodic peak potential, arrows show forward and backward reactions; scan rate 0.1 V s $^{-1}$; (b) Pt micro disc, r = 50 µm, scan rate 0.1 V s $^{-1}$; (c) MNEE (50 nm Pt band thickness), r = 10 µm, scan rate 0.01 V s $^{-1}$; (d) micro disc electrode, r = 15 µm, scan rate 0.01 V s $^{-1}$. All experiments were performed in KCl (100 mM) and FcMeOH (a) 1 mM, (b-d) 0.5 mM) solutions in DI water with 2 % EtOH (b-d). For all experimental details see Chapter 3. Horizontal black lines indicate zero on current axis.

Then, the current starts falling off with increasing potential (time) as a result of the growing dominance of the effect of diffusion of the reactant species at the electrode surface. This is the increase of the thickness of the diffusion layer (Section 2.4).[43] In this region, current becomes governed by the rate of reactant species delivery via diffusion from the bulk solution as the thickness of the diffusion layer increases and the concentration gradient decreases, as shown by Fick's first law (Equation (2.17)). The volume of the product species at the electrode surface continues growing throughout the scan, leading to ever shallower diffusion gradients and slowing down the mass transport of the reactant species to the electrode surface. The mass transfer of the reactant species to the electrode surface is slower, as the species need to travel from further away. [5,26]

Upon reaching the switching potential, potential scan is reversed, and currents are observed in the reverse direction (reduction) and so the process occurs in the reverse direction. The product species which were produced in the diffusion layer are now the reactant species. As the reduction potentials are applied, the measured reduction current starts increasing again, and the re-reduction process is observed. This results in another, cathodic peak, i_{pc}, at a maximum potential value, E_{pc}. Once the diffusion layer is depleted, current decreases again.[5,26]

Diffusion controlled reversible reactions at macro electrodes have the characteristic that the peak current is directly proportional to the concentration and it increases with the square root of the scan rate (v/V s^{-1}).[16,20,44,45] The exact relationship is described by the Randles-Sevcik equation in Equation (2.19).[46]

$$i_p = 0.4663nFAc\left(\frac{nFvD}{RT}\right)^{\frac{1}{2}} \quad (2.19)$$

where i_p is the peak current, either anodic or cathodic, and A is the electrode area.

Scan rate is therefore an important parameter in CV as it defines the experimental timescale and hence the extent of reactant depletion.[5] If the process is diffusional, peak current against the square root of the scan rate should give a straight line.[41]

As the electrode size decreases, the peaks disappear and are replaced by a wavelike, time-independent response, as shown in Figure 2-6 (c-d) when using e.g. an UME or a MNEE. Unlike for a macro electrode, in these cases the diffusion layer thickness rapidly becomes relatively large compared to the electrode dimension and the diffusion field becomes hemispherical (Section 2.4). The resulting CV signal is therefore different from that at a macro electrode. There are no observable peaks as there is a time independent mass transfer by diffusion to the electrode as hemispherical diffusion is established. As radial diffusion is more efficient than linear diffusion, the rate of mass transport to the electrode is always able to exceed the rate of electron transfer, so depletion is balanced by diffusion of fresh redox species to the electrode and the diffusion profile becomes constant with time (steady state). The resulting signal is sigmoidal and it represents a steady-state current.[26] At bigger electrodes, the amount of redox species exchanging electrons at the electrode surface is higher than those that diffuse from the bulk of the solution; hence, equilibrium cannot be established.[40]

Although the average diffusion rate across the electrode is constant, the hemispherical diffusion field is not uniform over the whole microelectrode e.g. disc surface, resulting in a non-uniform current density. This is because the diffusion rate is always higher at the edge of the electrode than at the centre. For a MNEE it can be considered that there is only edge hence

the mass transport limited current density is even higher. As the current is measured over the entire electrode both diffusion rate and the resulting current density are normally calculated as space-averaged quantities by integration over the entire electrode area.[44] Such spatial variations are suitable to be analysed through imaging, as shown in Chapters 5-9.

Figure 2-6 shows that for an individual microelectrode whether or not one obtains the characteristic CV shape depends not only on the size of the electrode, but also on the scan rate.[20] This governs the timescale of the experiment and whether there is time for hemispherical diffusion to be established. For example, the CV signal from a disc electrode of 30 µm diameter at a scan rate of 0.01 V s^{-1} in (d) is equivalent to the MNEE nanoelectrode signal in (c) at the same scan rate[42,16,31], while a 100 µm diameter micro electrode generates a signal somewhere in between the characteristic macro and microelectrode responses when using a faster 0.1 V s^{-1} scan rate.[20] Larger micro electrodes (compared to UME) will therefore deliver a characteristic sigmoidal signal at slower scan rates but at faster scan rates the signal will most likely start to contain peak-like characteristics of the macroelectrode CV, indicative of the growing contribution of linear diffusion as the diffusion layer becomes thinner.

Scan rate also has an impact on a micro and nano electrode array signals. As discussed in Section 1.2.3, a CV on a micro electrode array can result in either peak or sigmoidal signal, depending on the design of the array. The diffusion field grows with time (Section 2.4); hence when the scan rate is too slow, even though hemispherical diffusion has been established it is likely that the neighbouring hemispherical diffusion fields overlap when the diffusion layer thickness, determined by $(2Dt)^{1/2}$ becomes comparable to or greater than the neighbouring electrode separation. They combine to produce linear diffusion across the entire array, resulting again in a peak-shaped signal, which can also result if scanning is performed too fast. Therefore, not only electrode size and separation but also the scan rate has to be considered when designing and using the array.[22] Because of this a single electrode is sometimes preferable over an array if the experimental set up and application allows it. But imaging of arrays would be informative to not only asses the relative response of different electrodes, but to probe this developing diffusional overlap.

2.6 MASS TRANSFER LIMITED CURRENT EQUATIONS TO MICRO AND NANOELECTRODES

A steady-state, i_{SS}, also known as bulk, i_{bulk}, current expression in Equation (2.20) is used as a common practice to check if a recorded CV signal corresponds to the theoretical value under mass transport limited conditions when the electrochemical reaction is relatively fast, and the reactant concentration is zero at the electrode surface. Since the current is diffusion controlled, the expression involves the diffusion coefficient specific to the reactant, which is the redox species initially present in the solution.[47,48]

$$i_{SS} = BNnFDcL \quad (2.20)$$

Here, *N* is the number of electrodes if it is an array; *L* is the electrode size (radius of a single disc or length of a single square side) and *B* is the numerical factor dependent on a WE geometry and size. This equation is applicable to an array at scan rates where electrodes can be considered to be acting independently; hence there is no diffusional overlap from neighbouring electrodes.

Then, *B* = 4 for a disc microelectrode; *B* = 2.34 for a square microelectrode; *B* = 0.96 for a square nanoband.[26,29,32,44,49] Since there was no specific *B* value for disc nanoband reported at the time this thesis work commenced, it was modelled using a 3D finite element model (FEM) in COMSOL and found to be 1.44 (Dr Ilka Schmueser, UoE). The reported value of *D* for FcMeOH in the literature varies from 7.8 x 10^{-10} m^2 s^{-1} to 6.1 x 10^{-10} m^2 s^{-1} [50–52], as the diffusion coefficient is known to vary with the temperature and solution composition and SECM experiments are often not temperature-controlled.[53,54] In this thesis, a specific value for this data set (at room temperature) was determined in Section 4.3.1.

2.7 RECESSED VERSUS INLAID ELECTRODES

Depending on the electrode fabrication technique, electrodes can be inlaid, also known as co-planar, or recessed, as shown in Figure 2-7 (a-b), respectively. In this case, the limiting current for a recessed microdisc electrodes is slightly different from Equation (2.20) due to the linear diffusion profile within the recess, and can be estimated from Equation (2.21).[41,55,56]

$$i_L^{recess} = 4nFDcr\left(\frac{\pi r}{4G + \pi r}\right) \quad (2.21)$$

where *G* is the depth of the electrode recess for a single microdisc (for which *B* = 4 and *N* = 1 in Equation 2.20).

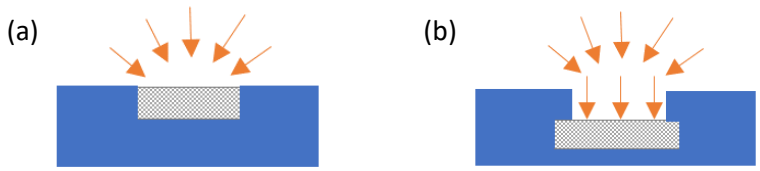

Figure 2-7. Graphical presentation of a cross section of (a) an inlaid and (b) a recessed micro electrode, where metal is shown as grey and the surrounding insulator is presented as blue. Orange arrows represent diffusion to the electrode in the solution.

At the interface of the electrode and insulator there is an increased current density, known as an edge effect, which leads to more complicated numerical simulations.[41,57] To model a recessed microdisc response, a FEM is used commonly, where more mesh points are required at the edge and directly above the active metal area.[58] For the recessed electrodes used in this thesis (Chapter 3), it has been shown by Woodvine[59] that inlaid electrode approximations

are valid, simplifying the analysis and numerical modelling in the following chapters.[35] Therefore, an inlaid electrode Equation (2.20) was used, since the recess of 0.5 µm was found to be relatively small and insignificant for such steady state calculations, allowing to neglect the recess.

2.8 CHRONOAMPEROMETRY

Chronoamperometry (CA), also known as a potential step voltammetry, is a technique in which the potential applied to the WE is changed from one value to another in steps and the resulting current is monitored as a function of time for the diffusion controlled processes (Section 2.3).[2,10,60,61] As shown in Figure 2-8 (a), the time at which the potential step is initiated is considered as the zero time (t = 0), and at this time the reactive species concentration at the electrode surface is zero. The chosen step potential values usually span across the region where redox processes occur, often starting at a value E_1 where the redox species are electrochemically inactive (no Faradaic currents are observed).[10,60] In general, this 'zero current' potential condition is also used to start CV experiments.[10] The step potential E_2 at t = 0 is often chosen to be sufficiently large to ensure mass transport limited oxidation or reduction.[61] The WE is then held at this potential value for a chosen amount of time usually starting from several seconds.

Since a measurable current is generated as shown in Figure 2-8 (b-c), chronoamperometry is an amperometric technique.[62] Apart from very short times, where the current is dominated by the non-Faradaic double layer charging process (Section 2.2.5), CA gives information about the Faradaic current response of the electrode.[10,60] When the step potential is such that mass transport limited reaction of a species A occurs at a macroelectrode, the Cottrell equation in Equation (2.22) below shows the relationship between the magnitude of the current response and time[21] as the diffusion layer thickness evolves with the square root of time (Section 2.4).[60]

$$|i| = \frac{nFAD^{\frac{1}{2}}[A_{bulk}]}{\pi^{\frac{1}{2}}t^{\frac{1}{2}}} \qquad (2.22)$$

For both macro and micro (as well as nano) electrodes, at t = 0 the current sharply increases as a result of a double layer charging, and then drops, as shown in Figure 2-8 (b-c). However, a difference between the two is observed at longer times, reflecting the same differences observed in the CV responses (Section 2.5). When using a macro electrode, the current decreases and approaches zero current value as the time approaches infinity as shown in (b), unlike when using a micro (or nano) electrode, at which mass transfer is time independent and current approaches a steady state current instead, as shown in (c). The latter is applicable to work in this thesis, since PAC experiments are similar in principle to such CA experiments.

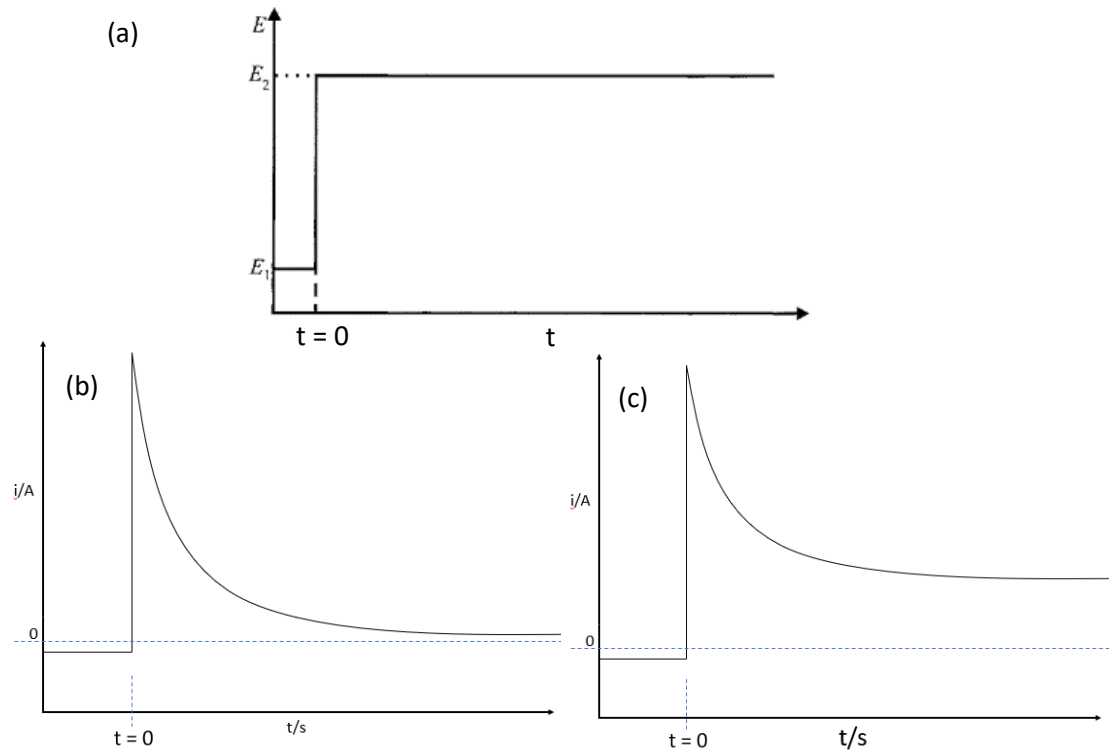

Figure 2-8. (a) A typical potential step experiment waveform and (b) the resulting chronoamperometry signal for a macro and (c) a micro (or nano) electrode. (Figure adjusted from reference[10,63].)

2.9 SCANNING ELECTROCHEMICAL MICROSCOPY (SECM)

2.9.1 SECM tip current

Fabrication of a typical SECM tip (also referred to as probe) usually involves heat-sealing of a conductive microdisc of a metal (microwire of Pt or carbon fibre or similar) with sheath glass or polymer and making a connection to a larger wire on the back side.[64,65] The sealed side of the probe has to be exposed to the solution and manually polished. Critical dimensions are the radius of the exposed metal disc, *a*, and the total tip radius, referred to as insulating sheath radius, r_g. These are used to obtain the dimensionless R_g ratio,[65] which is the ratio of the radius of the entire tip to the disc electrode radius, as shown in Equation (2.23) and in a schematic representation in Figure 2-9 (b).[64,65]

$$R_g = r_g/a \tag{2.23}$$

Depending on the R_g value, the steady-state tip current, also referred to as the tip bulk current, i_T^{bulk}, varies.[64,65] A commonly encountered value is $R_g \leq 10$,[26,66] for which diffusion of the redox species from the back of the tip starts playing a significant role, as shown in Figure 2-9 (a). The transition from linear to radial diffusion occurs and the diffusion field extends beyond the outer edge of the insulating shield. [65,67] This means that the flux to the inlaid electrode is enhanced by diffusion from behind the plane of the electrode when the insulating sheath

thickness is of comparable dimension to the electrode radius, and the most extreme example is when R_g is close to 1.[67] When R_g ≥ 10, this effect is smaller, as shown in Figure 2-9 (b). In both cases, the expanding hemispherical diffusion field is affected, and Equation (2.20) must be adjusted to reflect this current increase, as follows:[43,64,67]

$$i_T^{bulk} = 4nFDcr\beta \qquad (2.24)$$

where β is the beta factor, quantifying the enhanced diffusion due to the glass insulator around the Pt wire. This phenomena for a micro disc probe was observed first in 1984, and has been considered since.[64,67] With decreasing R_g, β and hence i_T^{bulk} increase, resulting in a significant difference between a simple micro disc electrode (Equation (2.20)) and a probe steady state currents (Equation (2.24). When R_g is large (e.g. 1000), the tip behaves as an inlaid disk and Equation (2.20) can be used.[68] β = 1.02 for R_g = 10 (applicable to this thesis) was demonstrated in 2002 by Zoski and Mirkin using the following equation:[67]

$$i_{disk}^{ss}(\mathrm{R}_g)/i_{disk}^{ss} = 1.0000 + \mathrm{B}(\mathrm{R}_g - C)^D \qquad (2.25)$$

where i_{disk}^{ss} is the disk steady state current, B = 0.1380, C = 0.6723, and D = -0.8686.[67] Thus β = 1.02 was used.

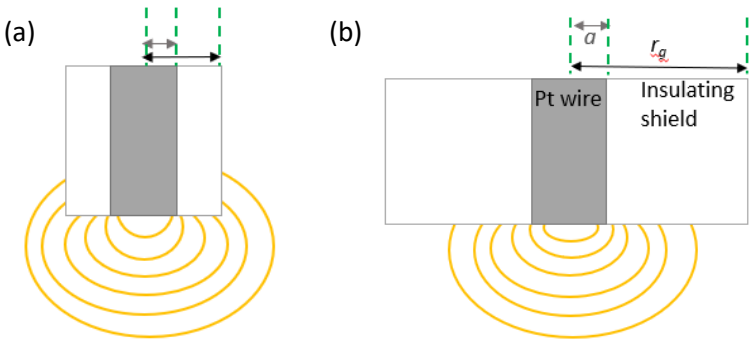

Figure 2-9. Schematic representation of micro disc probes and the resulting diffusion fields for (a) R_g ca. 2 and (b) R_g greater than 10. Note the drawing in (b) is not to scale.

2.9.2 Description of SECM imaging modes

There are two typical SECM imaging modes: feedback (FB) and generator-collector (G-C), shown in Figure 2-10. G-C mode in general is used for tip-substrate separation distances, *d*, not greater than ten radii of the tip electrode,[69] and it can be in either a tip generator-substrate collector (TG-SC) or substrate generator-tip collector (SG-TC) configuration.

In TG-SC, the tip electrode is used to perturb the surface in order to induce an electrochemical reaction, sensed by the substrate as a collected current. The tip is held at a potential which allows $O + ne^- \rightarrow R$ reaction to occur, where R is the reduced, and O is the oxidised species. Meanwhile, the substrate is held at a different potential where this product will rapidly react ($R \rightarrow O + ne^-$) (get collected) at the substrate. Since the tip is usually much smaller than the

substrate, a collection efficiency, measured by i_S/i_T, where i_S is the substrate current, is essentially 1 (100 %) for a stable tip-generated product.[47,48,70] TG-SC imaging mode is usually used for kinetic measurements, one of which is the rate constant determination for a homogeneous reaction, as i_S/i_T ratio becomes smaller with increasing d, or for screening electrocatalysts.[70]

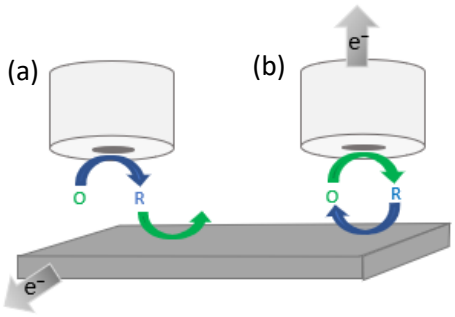

Figure 2-10. Types of SECM imaging modes: (a) tip generator-substrate collector and (b) feedback, where the substrate surface is conducting. (Figure recreated from reference[48].)

SG-TC mode is the opposite to TG-SC, as the potentials of tip and substrate are reversed, such that reaction of the bulk species (product generation) is driven at the substrate and probed (collected) by the tip. During the scan in x*y*-plane, local changes in concentration of the electroactive product species are sensed by the tip. In other words, when the tip is scanning across the substrate surface, the tip determines spots where substrate reaction occurs at a higher rate, through higher currents.[47,48,70] A diffusion layer is generated by the substrate and the tip is typically travelling and scanning within this thin diffusion layer. The collection efficiency then often can approach zero particularly when there are very large electrode size differences, giving a relatively small ratio of i_T to i_S. SG-TC mode also benefits from low background currents as there is no R in solution to react and so there is no current unless the substrate is detected below. This mode has often been used to scan unbiased surfaces, for electrocatalysts examination,[47,48,70] for monitoring enzymatic reactions, corrosion and similar heterogeneous processes taking place at the substrate surface. [47] However, if the substrate is very large, the use of SG-TC has been limited, since non-steady state processes result in significant *iR* drop and low collection efficiency.[47]

The most frequently used SECM imaging mode is FB mode. It is a special tip-collection mode used for analysing reversible redox reactions, where only the tip current is monitored.[69,70] When the tip is relatively far away from the substrate (more than several tip diameters), there is a general (essentially bulk) diffusion of electroactive species, which get reduced at the tip, as discussed in Section 2.9.1 and shown in Figure 2-11 (a). However, when the tip-substrate separation is reduced, the presence of the substrate perturbs the tip current and depending on what type of substrate is (conducting substrate electrode or insulator), the current increases

or decreases.[26,47,70–73] The effect is either negative or positive feedback due to the local presence of an insulating surface or conducting electrode as a substrate, respectively.

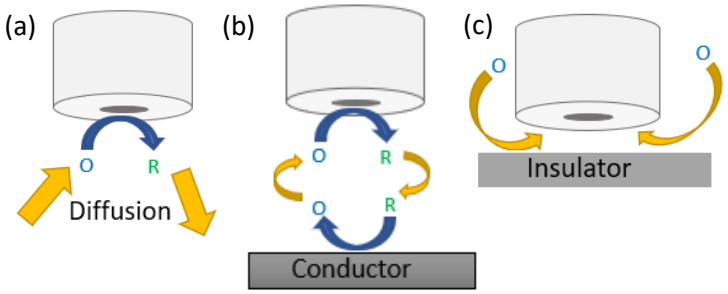

Figure 2-11. Diffusion (orange arrows) of reactant (O) and product (R) species, when SECM imaging probe in FB mode is: (a) above the substrate at a large d, resulting in a steady-state tip current; (b) above the conductor surface at a moderate height from the substrate, resulting in a positive feedback; (c) above the insulator surface close to the substrate, resulting in a negative feedback.[26,47,66]

If the tip at the oxidising potential is above a substrate which is a conducting electrode, diffusion of the product species, R, results in conversion back to the reactant species, O, at this conductive surface, as shown in Figure 2-11 (b). This results in enhanced flux of O to the tip, hence an increasing tip current and a term 'positive feedback' is used, where the tip current is greater than the bulk current, being $i_T > i_T^{bulk}$. In contrast, if the tip is placed close to a substrate which is an insulator surface, diffusion of the species from the bulk towards the tip becomes hindered/blocked by the narrow channel between the substrate and the sheath of the tip, shown in Figure 2-11 (c). This results in hindered diffusion and a decrease of the tip current, known as 'negative feedback', where $i_T < i_T^{bulk}$. Positive and negative feedback responses can readily be presented as curves in Figure 2-12 obtained in probe approach curve (PAC) experiments where position above the surface is fixed (fixed x, y coordinate) and the tip is moved towards the surface (z-direction).[26,47,70–73]

In these PACs both experimental currents and distances are typically normalized to i_T^{bulk} and probe radius, *a*, respectively. The tip approach towards a conducting or insulating surface is then clearly reflected by currents higher or lower than 1, when the normalized distance, $L = d/a$, becomes smaller than around 4. Such normalisation allows one to directly compare measurements performed using different probes and imaging settings, and eliminates the need to worry about time dependent tip currents, which may affect experiments to a different extent.[74]

All in all, tip currents in FB mode are more sensitive to changes in *d* than the ratio of currents (substrate and tip) in G-C modes. FB mode also tends to be more experimentally challenging and occasionally suffers from microelectrode passivation over the timescale needed to perform an experiment.[47,48] Nevertheless, experiments in FB mode make use of extremely fast

mass transport, useful for a rapid electron-transfer kinetics analysis at both tip and substrate surfaces.[64,75] A fuller discussion of PACs and their theory is to be found in Chapter 4, while FB and SG-TC mode further analysis and comparison is discussed throughout Chapters 5-9.

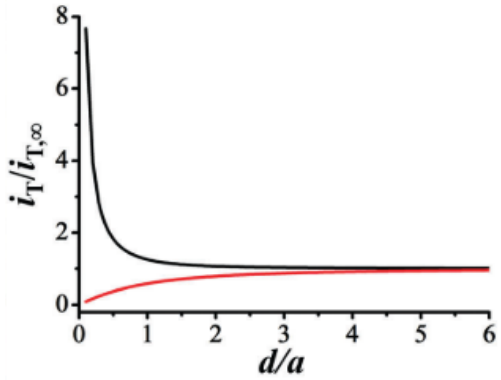

Figure 2-12. Positive (black line) and negative (red line) feedback curves, where both currents and tip working distances were normalized.

2.10 REFERENCES

1. Chapter 5. Bioelectrochemistry. Available at: http://www.phattimes.com/myoglobin/chapter5.htm. (Accessed: 5th April 2019)
2. Ciobanu, M., Wilburn, J. P., Krim, M. L., Cliffel, D. E. & Electrochemistry, C. I. N. Chapter 1. Fundamentals. in *Handbook of Electrochemistry* (ed. Zoski, C. G.) 3–29 (2006).
3. Wain, Andrew J., M. O. Multi-Scale Electrochemical Imaging. *NPL* (2007). Available at: http://www.npl.co.uk/science-technology/electrochemistry/research/electrochemical-imaging. (Accessed: 13th June 2016)
4. Hayyan, M., Mjalli, F. S., Hashim, M. A., AlNashef, I. M. & Mei, T. X. Investigating the electrochemical windows of ionic liquids. *J. Ind. Eng. Chem.* **19**, 106–112 (2013).
5. Elgrishi, N. *et al.* A Practical Beginner's Guide to Cyclic Voltammetry. *J. Chem. Educ.* **95**, 197–206 (2018).
6. Vasilescu, I., Eremia, S. A. V, Radoi, A., Radu, G. & Litescu, S. Lipid hydroxide determination on a ferrocenemthanol modified electrode. *Anal. Methods* **5**, 2013–2019 (2013).
7. Sun, P. & Mirkin, M. V. Kinetics of electron-transfer reactions at nanoelectrodes. *Anal. Chem.* **78**, 6526–6534 (2006).
8. Lovelock, K. R. J. *et al.* On the diffusion of ferrocenemethanol in room-temperature ionic liquids: An electrochemical study. *Phys. Chem. Chem. Phys.* **13**, 10155–10164 (2011).
9. Cannes, C., Kanoufi, F. & Bard, A. J. Cyclic voltammetry and scanning

electrochemical microscopy of ferrocenemethanol at monolayer and bilayer-modified gold electrodes. *J. Electroanal. Chem.* **547**, 83–91 (2003).

10. Bond, A. M. *et al. Electroanalytical Methods. Guide to Experiments and Applications*. (Springer, 2010). doi:10.1007/s100080050001
11. The LibreTexts. 6.6: Enthalpy and Entropy. *Chemistry* (2019). Available at: https://chem.libretexts.org/Bookshelves/Organic_Chemistry/Map%3A_Organic_Chemistry_(Smith)/Chapter_06%3A_Understanding_Organic_Reactions/6.06_Enthalpy_and_Entropy.
12. Attia, P. M. Chemical and electrochemical reversibility. (2018). Available at: https://petermattia.com/cyclic_voltammetry_simulation/reversibility.html. (Accessed: 4th June 2019)
13. Department of Chemistry, the University of California, S. C. Lab 13 - Electrochemistry and the Nernst Equation. *WebAssign* (2011). Available at: http://www.webassign.net/labsgraceperiod/ucscgencheml1/lab_13/manual.html.
14. The reaction quotient Q. *Khan Academy* (2019). Available at: https://www.khanacademy.org/science/chemistry/chemical-equilibrium/factors-that-affect-chemical-equilibrium/a/the-reaction-quotient.
15. Electrochemistry. *Khan Academy* Available at: https://www.khanacademy.org/test-prep/mcat/physical-processes/intro-electrochemistry-mcat/a/electrochemistry.
16. Chapter 3 Electrochemistry. Available at: http://www.phattimes.com/myoglobin/chapter3.htm. (Accessed: 3rd March 2016)
17. Biesheuvel, P. M. & Dykstra, J. E. The difference between Faradaic and Nonfaradaic processes in Electrochemistry. 1–10 (2018).
18. Faraday's First Law of Electrolysis. *Tutor Vista* (2013). Available at: https://www.youtube.com/watch?v=sZ8Z54E4WXI.
19. Dickinson, E. J. F. & Compton, R. G. Influence of the diffuse double layer on steady-state voltammetry. *J. Electroanal. Chem.* **661**, 198–212 (2011).
20. University of Cambridge Department of Chemical Engineering and Biotechnology. Linear Sweep and Cyclic Voltametry: The Principles. (2015). Available at: https://www.ceb.cam.ac.uk/research/groups/rg-eme/Edu/linear-sweep-and-cyclic-voltametry-the-principles. (Accessed: 4th February 2016)
21. Fisher, A. C. *Electrode Dynamics*. (Oxford University Press, 1996).
22. Compton, R. G., Wildgoose, G. G., Rees, N. V, Streeter, I. & Baron, R. Design, fabrication, characterisation and application of nanoelectrode arrays. *Chem. Phys. Lett.* **459**, 1–17 (2008).
23. Benoit Cushman-Roisin. Chapter 2. Diffusion. *School of Engineering at Dartmouth* Available at: http://www.dartmouth.edu/~cushman/courses/engs43/Chapter2.pdf.
24. Gao, Q. Optimizing carbon / carbon supercapacitors in aqueous and organic electrolytes. (University of Orleans, 2013).

25. Araki, J. Electrostatic or steric? – preparations and characterizations of well-dispersed systems containing rod-like nanowhiskers of crystalline polysaccharides. *Soft Matter* **9**, 4125–4141 (2013).
26. Walsh, D. A., Lovelock, K. R. J. & Licence, P. Ultramicroelectrode voltammetry and scanning electrochemical microscopy in room-temperature ionic liquid electrolytes. *Chem. Soc. Rev.* **39**, 4185–4194 (2010).
27. Bae, J. H., Yu, Y. & Mirkin, M. V. Diffuse Layer Effect on Electron-Transfer Kinetics Measured by Scanning Electrochemical Microscopy (SECM). *J. Phys. Chem. Lett.* **8**, 1338–1342 (2017).
28. Watkins, J. J. & White, H. S. The Role of the Electrical Double Layer and Ion Pairing on the Electrochemical Oxidation of Hexachloroiridate(III) at Pt Electrodes of Nanometer Dimensions. *Langmuir* **20**, 5474–5483 (2004).
29. Hwang, S. *et al.* CMOS microelectrode array for electrochemical lab-on-a-chip applications. *IEEE Sens. J.* **9**, 609–615 (2009).
30. Ong, S. P., Andreussi, O., Wu, Y., Marzari, N. & Ceder, G. Electrochemical windows of room-temperature ionic liquids from molecular dynamics and density functional theory calculations. *Chem. Mater.* **23**, 2979–2986 (2011).
31. Wiley, J. Analytical Electrochemistry: The Basic Concepts References and Links. 1996–1997 (2009).
32. Prats-alfonso, E., Villa, R., Guimera, A. & Campo, F. J. D. E. L. *Electrochemical Strategies in Detection Science. Chapter 2: Development of Microelectrode-based Biosensors for Biomedical Analysis*. (2016). doi:10.1039/9781782622529-00019
33. Pabst, M. Analytical solution of the Poisson-Nernst-Planck equations for an electrochemical system close to electroneutrality. *J. Chem. Phys.* **140**, (2014).
34. Maex, R. Nernst-Planck Equation. *Encyclopedia of computational neuroscience* (2014). doi:10.4249/scholarpedia.1286
35. Woodvine, H. L., Terry, J. G., Walton, A. J. & Mount, A. R. The development and characterisation of square microfabricated electrode systems. *Analyst* **135**, 1058–1065 (2010).
36. Zhang, C. & Park, S. moon. Simple Technique for Constructing Thin-Layer Electrochemical Cells. *Anal. Chem.* **60**, 1639–1642 (1988).
37. Kleijn, S. E. F., Lai, S. C. S., Koper, M. T. M. & Unwin, P. R. Electrochemistry of nanoparticles. *Angew. Chemie - Int. Ed.* **53**, 3558–3586 (2014).
38. Arrigan, D. W. M. Nanoelectrodes, nanoelectrode arrays and their applications. *Analyst* **129**, 1157–1165 (2004).
39. Selzer, Y. & Mandler, D. Scanning electrochemical microscopy. Theory of the feedback mode for hemispherical ultramicroelectrodes: Steady-state and transient behavior. *Anal. Chem.* **72**, 2383–2390 (2000).
40. Orozco, J., Fernandez-Sanchez, C. & Jimenez-Jorquera, C. Ultramicroelectrode

array based sensors: A promising analytical tool for environmental monitoring. *Sensors* **10**, 475–490 (2010).

41. Metters, J. P., Tan, F., Kadara, R. O. & Banks, C. E. Electroanalytical properties of screen printed shallow recessed electrodes. *Anal. Methods* 3140–3149 (2012). doi:10.1039/c2ay25512j
42. Compton Group. The microdisc electrode. Available at: http://compton.chem.ox.ac.uk/john/Thesis/9/9.html.
43. Shao, Y. & Mirkin, M. V. Probing Ion Transfer at the Liquid / Liquid Interface by Scanning Electrochemical Microscopy (SECM). *J. Phys. Chem. B* **102**, 9915–9921 (1998).
44. Pletcher, D. Why Microelectrodes? in *Microelectrodes: Theory and Applications* (ed. Montenegro, Irene, Queirós, M. Arlete, Daschbach, J. L.) 3–16 (Springer Netherlands, 1991).
45. Introduction. Available at: http://web.nmsu.edu/~snsm/classes/chem435/Lab13/intro.html. (Accessed: 3rd March 2016)
46. Randles, J. E. B. A cathode ray polarograph.The current-voltage curves. *Trans. Faraday Soc.* **44**, 327–338 (1948).
47. Instruments, C. H. Scanning Electrochemical Microscope.
48. Wain, A. J. Scanning electrochemical microscopy for combinatorial screening applications: A mini-review. *Electrochem. commun.* **46**, 9–12 (2014).
49. Schmueser, I. *et al.* A systematic study of the influence of nanoelectrode dimensions on electrode performance and the implications for electroanalysis and sensing. *Faraday Discuss.* **164**, 295 (2013).
50. Filice, F. P., Li, M. S. M., Henderson, J. D. & Ding, Z. Three-Dimensional Electrochemical Functionality of an Interdigitated Array Electrode by Scanning Electrochemical Microscopy. *J. Phys. Chem. C* **119**, 21473–21482 (2015).
51. Dauphin-Ducharme, P. *et al.* Corrosion Product Formation Monitored Using the Feedback Mode of Scanning Electrochemical Microscopy with Carbon Microelectrodes. *J. Electrochem. Soc.* **162**, C677–C683 (2015).
52. Liljeroth, P., Johans, C., Slevin, C. J. & Quinn, B. M. Micro ring – disk electrode probes for scanning electrochemical microscopy. *Electrochem. commun.* **4**, 67–71 (2002).
53. Krynicki, K., Green, C. D. & Sawyer, D. W. Pressure and temperature dependence of self-diffusion in water. *Faraday Discuss. Chem. Soc.* **66**, 199–208 (1978).
54. Raju, M., Ananth, M. V. & Vijayaraghavan, L. Influence of temperature on the electrochemical characteristics of MmNi3.03Si0.85Co0.60Mn0.31Al0.08 hydrogen storage alloys. *J. Power Sources* **180**, 830–835 (2008).
55. Bond, A. M., Luscombe, D., Oldham, K. B. & Zoski, C. G. A comparison of the

chronoamperometric response at inlaid and recessed disc microelectrodes. *J. Electroanal. Chem. Interfacial Electrochem.* **249**, 1–14 (1988).

56. Aguiar, F. A. *et al.* Conical recessed gold microelectrode arrays produced during photolithographic methods: Characterisation and causes. *Electrochem. commun.* **9**, 879–885 (2007).
57. Gavaghan, D. J., Gillow, K. & Su, E. Adaptive Finite Element Methods in Electrochemistry. *Langmuir* **22**, 10666–10682 (2006).
58. Bartlett, P. N. & Taylor, S. L. An accurate microdisc simulation model for recessed microdisc electrodes. *J. Electroanal. Chem.* **453**, 49–60 (1998).
59. Woodvine, H. L. Development and Characterisation of Microelectrode and Nanoelectrode Systems. (The University of Edinburgh, 2012).
60. Brady, C. L. . The Development and Characterisation of Microelectrodes for Extreme Environments. (The University of Edinburgh, 2013).
61. Bard, A. J., Denuault, G., Friesner, R. A., Dornblaser, B. C. & Tuckerman, L. S. Scanning electrochemical microscopy: theory and application of the transient (chronoamperometric) SECM response. *Anal. Chem.* **63**, 1282–1288 (1991).
62. Guy, O. J. & Walker, K.-A. D. Chapter 4. Graphene Functionalization for Biosensor Applications. in *Silicon Carbide Biotechnology (Second Edition)* 85–141 (2006).
63. Nirmaier, H. P. & Henze, G. Characteristic Behavior of Macro-, Semimicro- and Microelectrodes in Voltammetric and Chronoamperometric Measurements. *Electroanalysis* **9**, 619–624 (1997).
64. Lefrou, C. & Cornut, R. Analytical expressions for quantitative scanning electrochemical microscopy (SECM). *ChemPhysChem* **11**, 547–556 (2010).
65. Souto, R. M., Lamaka, S. V & González, S. Uses of Scanning Electrochemical Microscopy in Corrosion Research. in *Microscopy: Science, Technology, Applications and Education, A. Méndez-Vilas and J. Díaz (Eds.)* 1769–1780 (2010).
66. Sun, P., Laforge, F. O. & Mirkin, M. V. Scanning electrochemical microscopy in the 21st century. *Phys. Chem. Chem. Phys.* **9**, 802–823 (2007).
67. Zoski, C. G. & Mirkin, M. V. Steady-State Limiting Currents at Finite Conical. *Anal. Chem.* **74**, 1986–1992 (2002).
68. Amphlett, J. L. & Denuault, G. Scanning Electrochemical Microscopy (SECM): an investigation of the effects of tip geometry on amperometric tip response. *J. Phys. Chem. B* **102**, 9946–9951 (1998).
69. Zoski, C. G. Review—Advances in Scanning Electrochemical Microscopy (SECM). *J. Electrochem. Soc.* **163**, 3088–3100 (2016).
70. Kai, T., Zoski, C. G. & Bard, A. J. Scanning electrochemical microscopy at the nanometer level. *Chem. Commun.* **54**, 1934–1947 (2018).
71. Wain, A. J., Pollard, A. J. & Richter, C. High-resolution electrochemical and topographical imaging using batch-fabricated cantilever probes. *Anal. Chem.* **86**,

5143–5149 (2014).

72. Scanning electrochemical microscopy. *Wikiwand* (2016). Available at: http://www.wikiwand.com/en/Scanning_electrochemical_microscopy. (Accessed: 9th June 2016)
73. Eckhard, K. & Schuhmann, W. Alternating current techniques in scanning electrochemical microscopy (AC-SECM). *Analyst* **133**, 1486–1497 (2008).
74. Polcari, D., Dauphin-Ducharme, P. & Mauzeroll, J. Scanning Electrochemical Microscopy: A Comprehensive Review of Experimental Parameters from 1989 to 2015. *Chem. Rev.* **116**, 13234–13278 (2016).
75. Sundaresan, V. *et al.* Visualizing and Calculating Tip-Substrate Distance in Nanoscale Scanning Electrochemical Microscopy Using 3-Dimensional Super-Resolution Optical Imaging. *Anal. Chem.* **89**, 922–928 (2017).

3 MATERIALS AND METHODS

3.1 INTRODUCTION

This is an experimental chapter regarding single and array platinum (Pt) electrode fabrication and their usage for SECM imaging. The discussion includes the electrode fabrication process, cleaning protocols and electrode characterisation using simple CV experiments. A variety of electrode arrangements used for the experimental work in this thesis, as well as experimental and set-up details for the electrochemical and SECM experiments are presented.

3.2 ELECTRODE FABRICATION

Pt electrodes were used as WEs in CV experiments and substrates in SECM. They were fabricated in-house (Scottish Microelectronics Centre (SMC), University of Edinburgh (UoE)) using standard photolithography techniques, as published in more detail elsewhere[1–5] and briefly presented below. Machinery and equipment used were standard for such clean room facilities. Single and array electrode fabrication process steps, recorded in the run sheet, were identical. The time spent on steps, such as etching, was altered in order to optimise the process. Devices of interest were disc and square geometry micro and nanoband edge single and array electrodes. The individual arrangement of electrodes in the latter was either honeycomb (hexagonal) or square; this difference only becomes important when considering the analysis of the diffusion profile overlap, as discussed in Section 5.3.

3.2.1 Fabrication of single electrodes

The established typical electrode fabrication process was as follows. An SiO_2 insulator layer (500 nm) was grown on Si wafers (of 3'' diameter), followed by a deposition of a thin (approximately 5 nm) titanium (Ti) adhesion layer and Pt metal layer (approximately 45 nm). AFM experiments determined the actual step height between SiO_2 and the combined Ti and Pt layers as 48 nm, as shown in Figure 3-1. It was not possible to determine what the precise individual thicknesses of each of the two deposited metals were, as deposition of Ti and Pt metals occurs one after another, without exposure of the wafer to the environment for measurement in between these two depositions.

The deposited metal was then patterned by selective exposure, and dissolution of positive photoresist (SPR 220 – 3) activated by heat (at 110 °C) was completed. Chemical etching of Pt by Argon (Ar) ion milling (or wet etch) and photoresist removal in an ultrasonic bath was performed, followed by deposition of the top insulator of silicon rich nitride (SiRN, thickness 500 nm). A second step of photoresist patterning and activating followed, etching through the top insulator layer to expose recessed Pt micro electrodes with specific, edge length (square)

or diameter (disc) as determined by the mask. Further Pt etching using the Ar ion mill was employed to generate a deeper (550 nm) cavity, maintaining the desired electrode dimension with the Ti/Pt nanoband (approximately 50 nm in height) located at the base of the internal periphery. The resulting micro and nanoband edge electrodes were therefore recessed by 500 and 550 nm, respectively due to removal of the top insulating nitride layer. Wafers were then immersed in ACT stripper at 50 ^{0}C to remove all remaining photoresist layers. Finally, wafers were covered with an easy to remove sprayable photoresist. This step ensures protection of the surface from small particles and dust, which may contaminate the electrode surface during the dicing process and from any overall possible damage to the metal during dicing. Diced and framed wafers were packed and transported to the chemistry laboratory. Before using, each electrode was individually washed with acetone, methanol and deionised water to remove this photoresist layer and dried with nitrogen (N_2) gun.

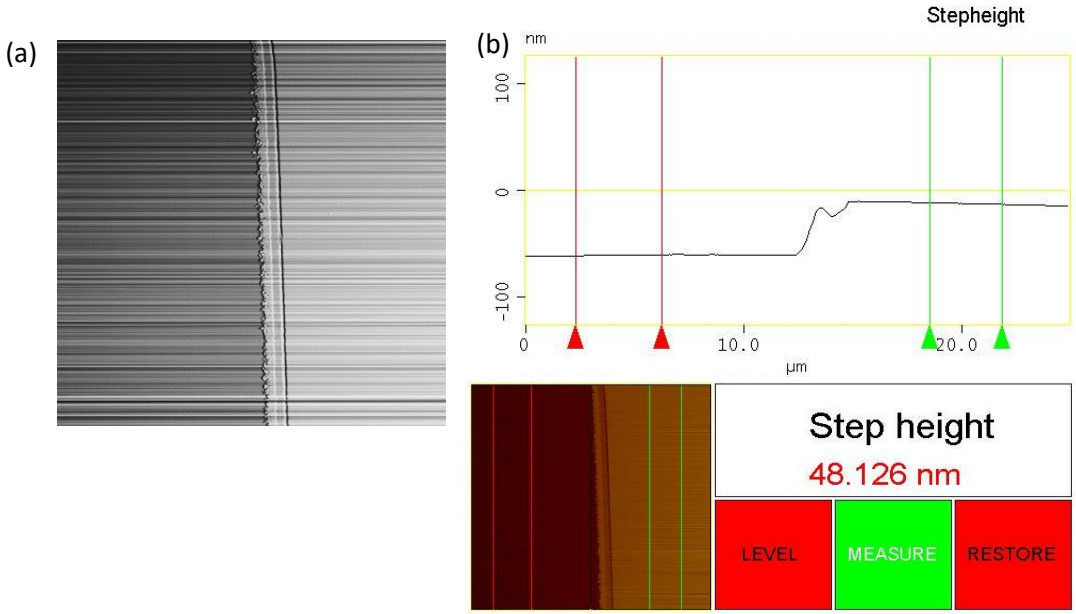

Figure 3-1. AFM (a) image and (b) levelling data to determine the step height between insulator and metal layers. (Dr Camelia Dunare, UoE.)

Figure 3-2 summarizes the results of this process, containing images of a framed wafer, separated and cleaned chip devices and a cross-sectional view of the micro and nanoband devices. Two batches, each consisting of 4 wafers each of which contained one kind of electrode (micro electrode or MNEE) and geometry (disc or square) were fabricated using the procedure as explained above. Micro disc, micro square, nanoband edge disc and nanoband edge square devices of 10, 20, 30, 50 and 100 µm diameter and edge length, *L*, for a disc and square, respectively, were the resulting fabricated devices. As a result of analysis of the first produced batch, fabricated electrodes from the first batch in Figure 3-3 were found to have corrugated cavity edges due to the use of a dirty mask. Occasionally such masks were found to require harsh cleaning using concentrated acid solutions to remove accumulated

photoresist or similar chemical residues and dust, which have become stuck on the mask and compromise electrode definition. As a result, electrode features were affected, resulting in devices with varying and not precisely known active area, and hence unknown expected performance (e.g. limiting currents). From Figure 3-3, smaller electrodes (*L* = 20 µm) were affected to a greater extent than large (*L* = 100 µm) electrodes.

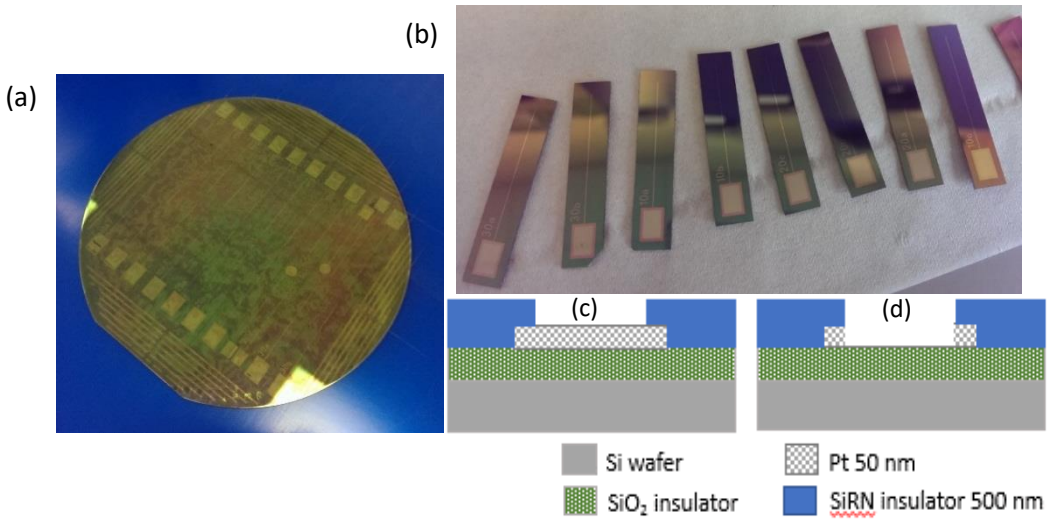

Figure 3-2. (a) Fabricated wafer of diced Pt electrode chips covered with the sprayed photoresist layer. (b) Pt electrode chips removed from the frame, washed with acetone, methanol and deionised water and ready to be used for the experiments. Each chip has width of 0.7 cm and length of 3.5 cm. (c) Schematic figure of the cross sectional view of the micro and (d) nanoband edge electrodes to show the layers of different materials used during fabrication process (note: the relative thicknesses of the layers are not drawn to scale).[3]

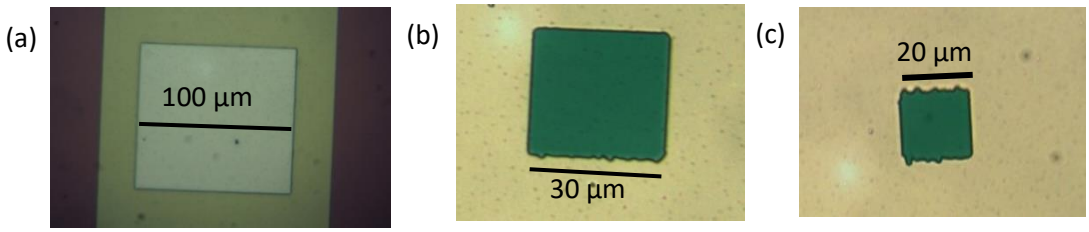

Figure 3-3. (a) Micro and (b-c) nanoband edge square electrodes from the first batch with the edge length of (a) 100 µm, (b) 30 µm, (c) 20 µm. Curvy edges were the consequences of dirty masks, used for the electrodes patterning, and they were more visible on smaller electrodes. Resulting electrodes are challenging to use for quantitative analysis as precise area and edge length are unknown.

To ensure such unwanted devices were fabricated only once, along with this mask cleaning more control steps during the fabrication process were introduced, collecting further microscope images during processing to ensure high fidelity production. Wet etching for Pt and Ti layer removal outside of the bond pads and tracks using an acid mixture solution (3:2:1 HCl (37 %):DI water:HNO_3 (70 %) at 60 ^oC) was used instead of the previously performed dry etching using JLS machinery. Such an etching method was expected to be more reliable and precise when removing metal from unwanted areas. However, this resulted in the uneven edge around the remaining metal area observed from the AFM image in Figure 3-1. The features

were not visible from optical images unlike for the first batch, confirming that the effect was of a negligible scale and the actual electrode size, area or performance were not affected. The electrodes from this batch were used for the qualitative and quantitative analysis in the following chapters.

3.2.2 Fabrication of the array devices

All array devices used in this thesis were fabricated by Dr Ilka Schmueser and Dr Ewen Blair, UoE, SMC, not exclusively for this thesis. Array devices of different size, shape, arrangement and electrode-to-electrode separation were fabricated using different masks but the same process as above. Two chip designs and an optical image of the micro square electrode array arranged in a square geometry, where each electrode was of 30 µm edge length and the edge-to-edge separation distance was 3*L* = 90 µm, are shown in Figure 3-4. This array was of the 'old' design layout presented in Figure 3-4 (a), which is no longer favoured in the group due to identified connection disadvantages in the conventional set-up for the electrochemical experiments, as discussed in Section 3.3.3.

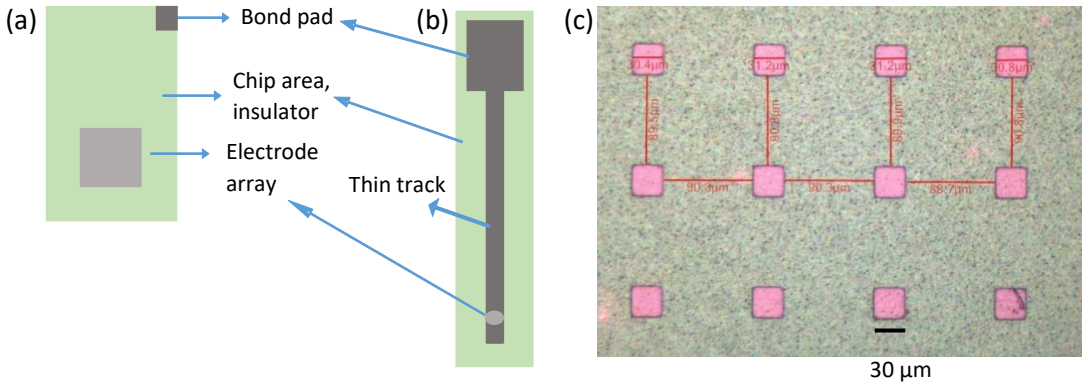

Figure 3-4. (a) Old chip design with an electrode array in the middle[6] *and (b) an improved electrode design – 'thin track' – chip. Both schemes are not to scale. (c) Optical image of a subset of the electrode array, where the square electrodes are arranged in a square geometry, the edge length is 30 µm and edge-to-edge separation between electrodes is 90 µm.*

Subsequent in-house fabricated array electrodes were of a different design, where a narrow metal track was found and the chip was longer and narrower than in the old design; hence, the name 'thin track' electrodes, as shown in Figure 3-4 (b). Another electrode design used in some experiments in this thesis (Section 3.6.8.3) was 'super thin track', similar to the one showed in Figure 3-4 (b). The track width at the top is the same as in the 'thin track' design, and then the track becomes slightly thinner further down. The 'thin track' design allows the fitting of a larger number of electrodes on one wafer compared to the old design, making this a preferable choice for fabrication efficiency as well as for ease of establishing electrode connection.

3.3 EXPERIMENTAL

The following experimental details were used in the standard electrochemical experiments performed for this thesis to validate the electrode cleanliness and ensure they were functioning as expected.

3.3.1 Chemical reagents and experimental conditions

All chemicals were used as purchased without further purification and all solutions were prepared using deionized (DI) water with a resistivity of 18.2 MΩ cm. Electrochemical experiments were performed in 0.5 mM FcMeOH (97%, Sigma-Aldrich) aqueous solutions, containing 100 mM KCl (99.0+%, Sigma) as background electrolyte, prepared in 98:2% DI water:ethanol (EtOH, 95%, Sigma-Aldrich) in order to improve FcMeOH solubility.[7] For complete and faster FcMeOH dissolution, the mixture was placed in a sonicating bath for 15-25 minutes.

3.3.2 Instrumentation

All initial electrochemical experiments were temperature controlled, using an in-house made water bath (T = 25 ^{0}C). Experiments were carried out on AutoLab potentiostats, controlled on a PC by NOVA software (Metrohm), with integrated data analysis. Further data processing was performed using Origin software (MicroCal).

3.3.3 Electrochemical testing set-up

Figure 3-5 shows a typical set-up used for those experiments in this thesis which involved a three-electrode cell. The in-house fabricated substrate (Pt) chip electrodes were used as the working electrodes (WEs), saturated calomel electrode (SCE) or Ag/AgCl/KCl (sat.) electrode as the reference electrode (RE), and a Pt gauze or an electrode chip with a physical vapor deposition (PVD) blanket deposited uniform Pt layer was the counter electrode (CE). All potentials are reported with respect to the relevant RE. The WE was connected via a crocodile clip, which had an insulating ceramic substrate placed underneath the chip to minimize the chances of breaking the thin brittle chip, as shown in Figure 3-5 (c). A metal ball-bearing on top of the electrode was used in order to protect the WE surface, to prevent scratching of the bond pad by the crocodile clip “teeth” and as a further prevention against breaking the chip. As seen from Figure 3-5 (b), one crocodile clip “tooth” was bent to create some space for the ball-bearing and assure that it was fixed in place. Such a connection method was applicable to thin track electrodes showed in Figure 3-4 (b), allowing easy connection and handling of these chip devices. (The alternative electrode design in Figure 3-4 (a) was not used for any of these control experiments.) Using such a set-up, CV scans were obtained between +0.45 V and 0.00 V to obtain one electron reversible oxidation-reduction wave of 0.5 mM FcMeOH/FcMeOH$^+$.[8]

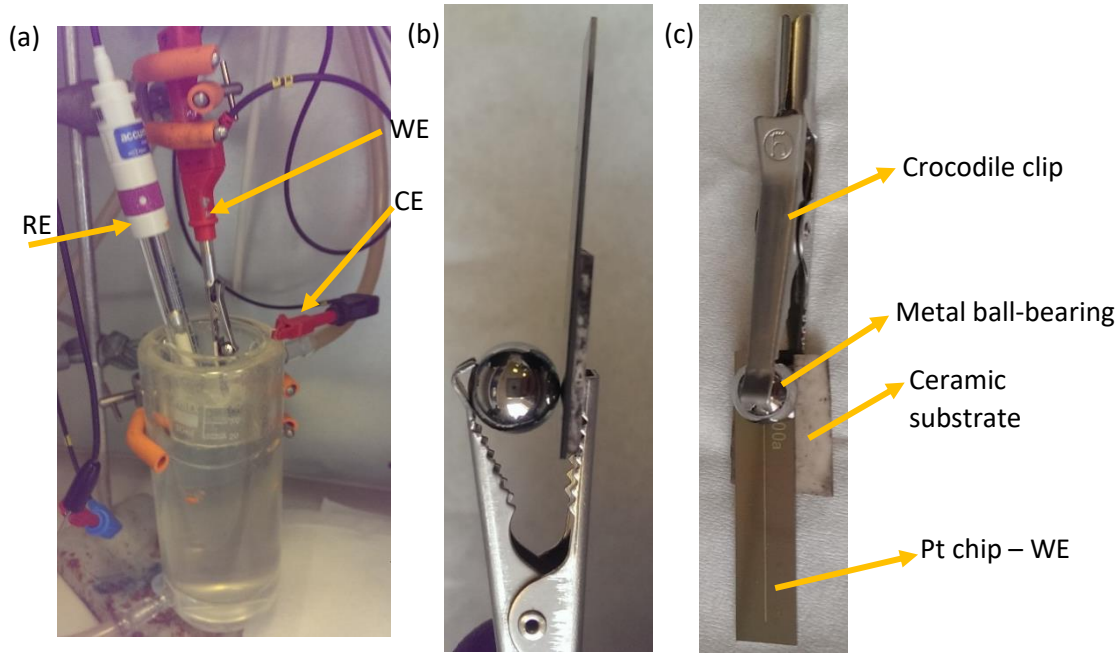

Figure 3-5. (a) Electrochemical experiments set-up, showing WE, RE and CE; (b) side view of the WE clipped with a crocodile clip: ceramic substrate is underneath and a metal ball bearing on top of the WE; (c) top view of (b).

3.4 ELECTRODE CLEANING

Metals, including Pt, readily form oxide layers (Pt oxide) either during the electrode fabrication processes or in the air, or in the oxygen rich aqueous solutions.[9] The requirement of cleaning these in-house fabricated electrodes comes from the need to remove these metal oxide layers that inhibit electrode surface and hence the electrochemical signal (e.g. limiting current). Cleaning protocols of micro electrodes and MNEEs differ from macroelectrodes.[10] Physical polishing often used for the latter cannot be employed for such significantly smaller and more fragile devices; instead, electrochemical cleaning has been shown to be an effective method. Some small organic material residues from the fabrication process are also likely to get removed during this process; however, if the residues on the electrode surface were significant and visible from the optical images, electrodes required further investigation and more aggressive cleaning than described below.

Electrochemical cleaning was initially performed by cycling within the upper potential limit of +1.6 V and the lower limit of -0.32 V in sulphuric acid (100 mM) solution. Then, cycling in the experimental solution containing FcMeOH within the electrochemical window of the redox species where the peak features are typically observed (between +0.4 V and -0.05 V for FcMeOH) followed. When cycling in sulphuric acid, a Pt micro square electrode, L = 30 µm, was rinsed with DI water in between cleaning and characterisation in experimental redox solution (Section 3.3.1), but it was observed that the solution changed colour from pale yellow to light blue. This suggests that there was a strong acid contamination and a chemical reaction.

If cycling in sulphuric acid solution, it is advised to leave the WE immersed in DI water for a significant period of time to ensure no contamination, and only consider solutions that are fine and have not gone blue. Sulphuric acid was observed to cause more trouble than deliver improved results and so an alternative electrode cleaning process was used.

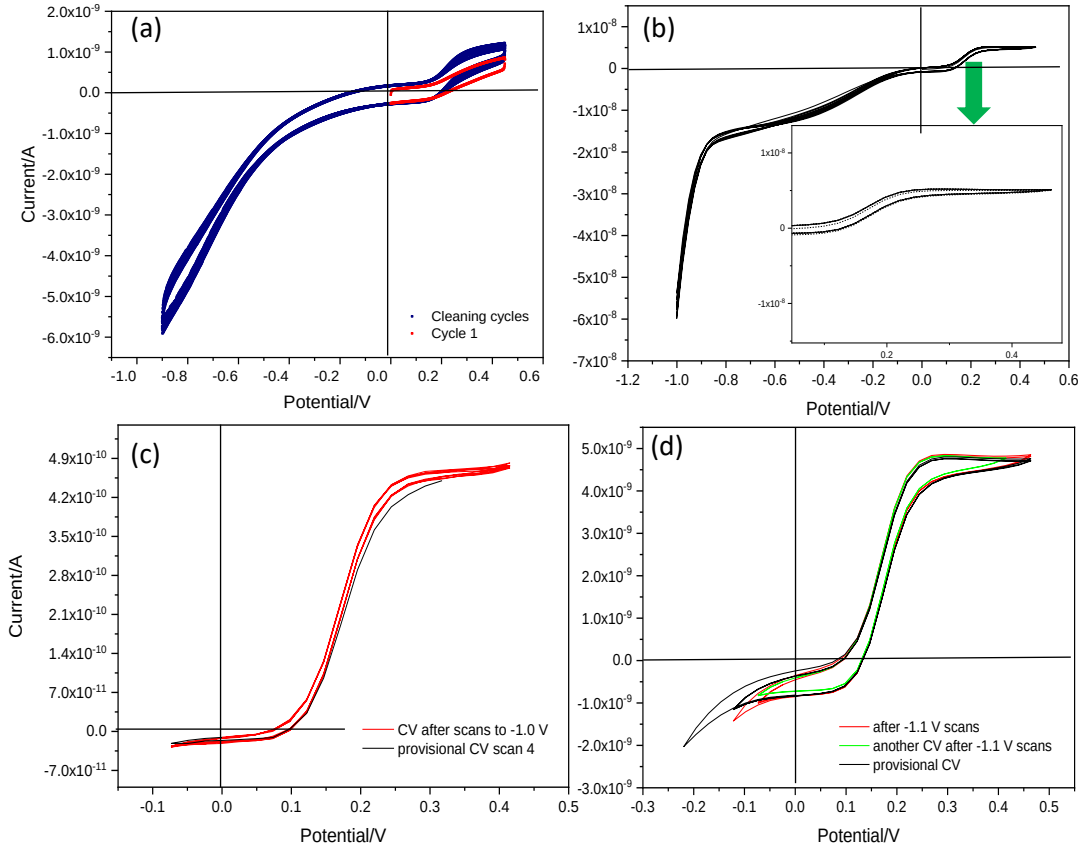

Figure 3-6. Electrochemical cleaning in FcMeOH solution (Section 3.3) at 0.1 V $s^{-1}$of the following: (a) MNEE, L = 50 µm, where the first cycle (red) generated a 45^0 angle-like almost linear response but cycling to a more negative potential (such as -0.9 V) likely reduced Pt oxide on the electrode surface, and an improved CV response was recorded (navy). (b) MNEE, where scanning between -1.1 V and +0.45 V was performed and almost no difference in the response shape before and after such scanning was observed. (c) MNEE, d = 30 µm, where the 4^{th} scan of the provisional CV (before cleaning) and a scan after cycling to -1.0 V are shown; some improvement in an oxidative peak is observed. (d) MNEE, d = 100 µm, where provisional CV response and CV responses after the first and second rounds of cleaning show improvement in the reductive end.

A typical electrochemical cleaning protocol of micro electrodes and MNEEs was developed by Piper.[9] Depending on the electrode cleanliness, some or significant signal improvement was observed after several full scans between a more negative potential (approximately -1.0 V) and a standard positive potential (e.g., 0.45 V for FcMeOH) when cycling in the experimental redox solution.[9] An example of such variation in the initial response is shown in Figure 3-6. An example in (a) shows the signal that started with the response indicating that metal layer is hindered (cycle 1), as the initial signal was resistive and resembling a 45^0 angle line. However, the signal significantly improved after one full scan and then gradually improved with the

following full scans, indicating that the electrode was getting cleaned (oxide layer removal). Some electrodes showed a clean electrode response from the beginning of the electrode cleanliness inspection, such as in (b), and some electrodes showed some improvement of the signal on the oxidative or reductive end in (c) and (d), respectively.

Cycling to a more negative potential value allows the reduction of PtO_2 which may form on the surface of the electrode when it is left in contact with the air, resulting in hindering active electrode surface. Such results showed that current flowing through the electrode increased and the electrode got cleaner. Most importantly, this electrochemical cleaning was done in the same solution, which is used for general electrochemical experiments, eliminating the need of tedious and time-consuming set-up changes. For the consistency of this work, 15 full scans were mostly used for cleaning each electrode. More scans could be used, and more detailed analysis of the procedure could be carried out but for the purposes of this project, such a cleaning protocol was satisfactory and hence was used with occasional modifications in negative potential values and/or scan number throughout the work. The cleaning process was always continued until (c-d) responses were obtained, ensuring a clean electrode. If the response was not achieved, the electrode was not used for the following SECM experiments.

3.5 ELECTRODE CHARACTERISATION

From each wafer a significant number of chip devices (electrodes) were tested using CV experiments. A scan rate of 0.1 V s^{-1} was considered as a standard, and occasionally a full range of scan rates (0.01; 0.05; 0.1; 0.2; 0.3; 0.4 and 0.5 V s^{-1}) was used to collect a set of data to observe changes in the peaks as a result of the scan rate variation, as shown in Figure 3-7 (a). As expected, at faster scan rates, such as 0.5-0.3 V s^{-1} the microelectrode CVs typically produced peaks (Section 2.5). Starting at 0.2 V s^{-1}, the peaks started diminishing and the shape became sigmoidal, which is specific to MNEEs at relatively fast scan rates and micro electrodes at progressively slower scan rates due the steady state currents when under hemispherical diffusion.[11,12] An example of this is shown in Figure 3-7 (b-c), where little difference is observed between the shape of the CV responses from the MNEE of 10 µm diameter at 0.1 V s^{-1} and a 30 µm diameter micro disc electrode at 0.01 V s^{-1}.

As discussed in Section 3.4, once distinctive micro or nanoband electrode features were revealed, often after electrochemical cleaning, then, measured and expected limited currents (Equation (2.20)) of the electrodes were compared to finalize the evaluation of the cleanliness of the electrode. In the examples showed in this thesis, electrodes behaved as expected generating well defined CV responses where limiting currents were within a reasonable error from the theoretical currents, suggesting that fabrication was successful, and cleaning of the electrodes was performed to a satisfactory level for the work in this thesis.

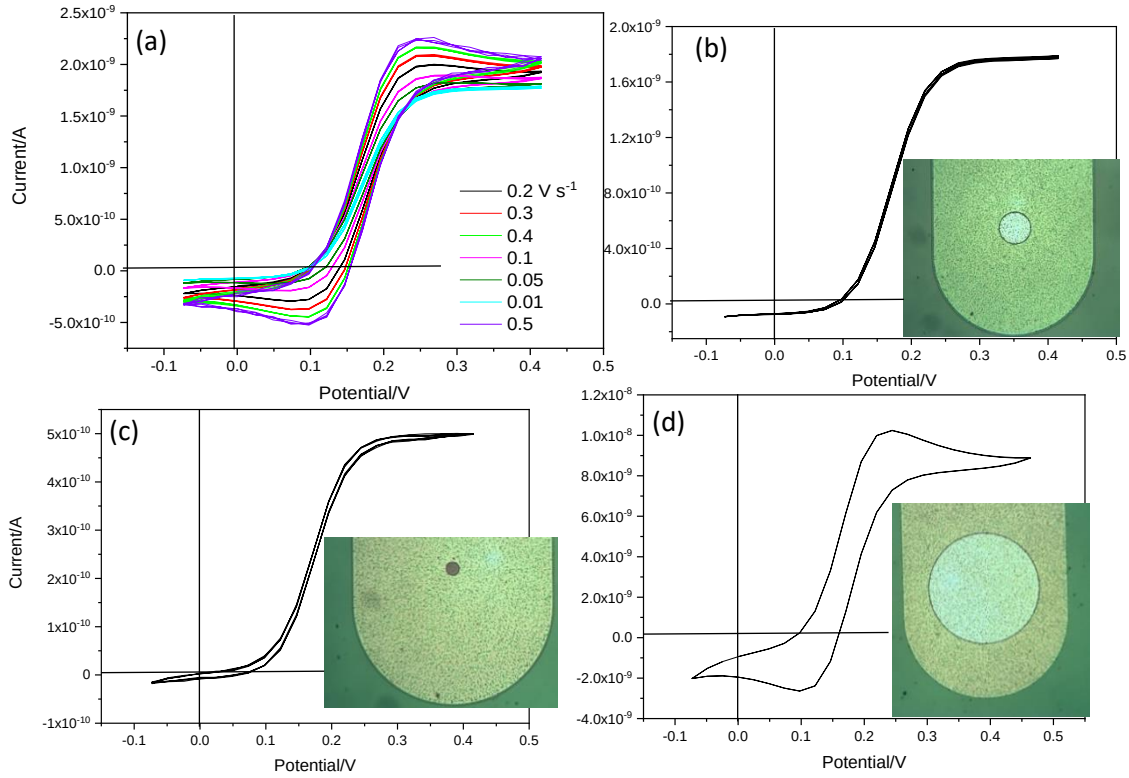

Figure 3-7. CV signal of (a) a micro disc electrode, d = 30 µm, at scan rates of 0.5-0.05 V s^{-1}; (b) a micro disc, d = 30 µm, at 0.01 V s^{-1} showing that at slower scan rates micro electrode CV signal becomes sigmoidal; (c) a MNEE, d = 10 µm, at 0.1 V s^{-1}; (d) a micro disc, d = 100 µm, at 0.1 V s^{-1}. Inserts in the graphs show optical images of the electrodes.

3.6 SECM EXPERIMENTS

3.6.1 Experimental

All SECM experiments were performed in an aqueous solution of 0.5 mM FcMeOH (97%, Sigma-Aldrich) containing 100 mM KCl (99+%, Sigma) as a background electrolyte prepared in 98:2% DI water:ethanol (EtOH, 95%, Sigma-Aldrich) in order to improve FcMeOH solubility (same experimental redox solution as in Section 3.3.1).[7]

3.6.2 SECM set-up

SECM experiments were performed at the National Physical Laboratory (NPL) using a bipotentiostat (CHI900B SECM) instrument. Experiments were carried out without temperature control, at room temperature (22−25 °C) in a Faraday cage. SECM imaging and electrochemical data were exported and analysed using CHI900B or CHI920D and Origin software. The set-up included Ag/AgCl/KCl (sat.) RE, a Pt coil or an electrode chip with a PVD blanket deposited uniform Pt layer used as a CE and two working electrodes: WE1 being the tip and WE2 the substrate electrode. All potentials, *E*, are quoted with respect to this RE unless otherwise stated.

The standard SECM set-up is shown in Figure 3-8. A personal computer (PC) is connected to a bipotentiostat and a three-dimensional positioner consisting of three stepper motors for coarse movement and a piezo positioner for fine movement. The substrate electrode is immersed in the electrochemical solution positioned parallel to the tip, and both are connected to the potentiostat, producing a four-electrode electrochemical cell.[13,14]

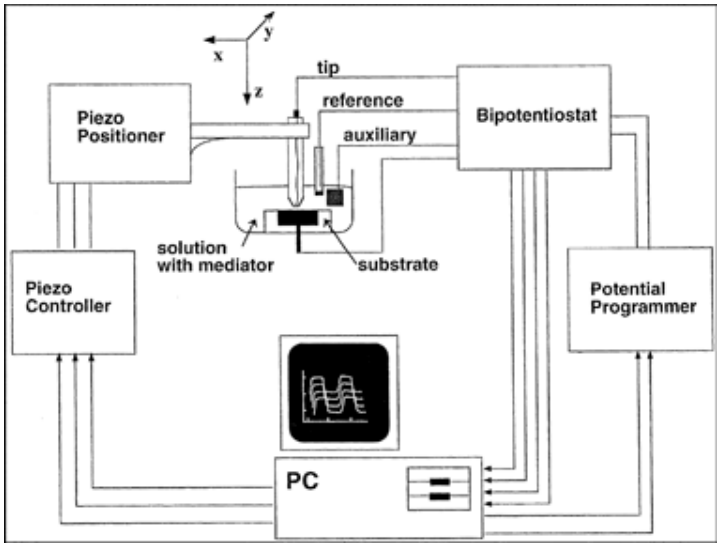

Figure 3-8. The block diagram of the SECM set-up, where 'tip' is the tip electrode, 'reference' is a RE, 'auxiliary' is a CE, 'substrate' is a substrate electrode, 'solution with mediator' is the experimental solution (containing FcMeOH). (Figure taken from reference[13].)

3.6.3 SECM operation

Conventional SECM imaging typically involves scanning an UME tip at a constant height above the sample, defined by the tip-substrate distance (separation), *d*. The tip is designed to induce measurable electrochemical reactions and/or collect the response when scanning the surface. Regarding the possible tip geometries, which include hemispherical, cylindrical, microband, and microring, the disc shaped microelectrode has been preferred due to easier data analysis resulting from the symmetry of the disc. The advantages of UMEs observed in general electrochemistry are exploited in SECM. These include low ohmic drop, fast steady-state response, and small tip size, which enables SECM to investigate micro- or nano- scale environments.[13,15]

An FcMeOH oxidation potential of +0.45 V or reduction potential of 0 V was always applied to the tip and the underlying substrate electrode, depending on the imaging mode, to ensure mass transport limited oxidation or reduction. Currents were measured at both electrodes but only the tip currents were analysed in this thesis. Since two SECM modes will be used throughout the work, it is worthwhile explaining how they differ in this specific system using FcMeOH as a redox species.

A solution phase redox mediator such as ferrocene methanol (FcMeOH) was used to probe the surface electrochemical activity through feedback, as shown in Figure 3-9. In what is commonly called feedback (FB) mode, the SECM tip current is measured as the tip is held at a potential sufficient to oxidize FcMeOH to $FcMeOH^+$ under diffusion control, as shown in Figure 3-9 (a). The measured current is dependent on the tip-substrate separation and the nature of the sample: if the tip is brought close to an insulating sample, the hindered diffusion to the tip results in a decrease in current (negative feedback), whereas if the sample is conducting and is set to a potential to rereduce $FcMeOH^+$ to FcMeOH under diffusional control, the resulting redox cycling leads to an augmented current (positive feedback) (Section 2.9.2). Alternatively, in substrate generation-tip collection (SG-TC) mode in Figure 3-9 (b), the potential is set such that FcMeOH is now completely oxidised at the conducting substrate, and the collector tip electrode is held at a potential where complete reduction of $FcMeOH^+$ occurs, again under mass transport control.[16,17,18] It is worth noting that redox cycling occurs in both modes, with the difference being the additional effect of transport of FcMeOH from the bulk solution to the substrate and tip, respectively.

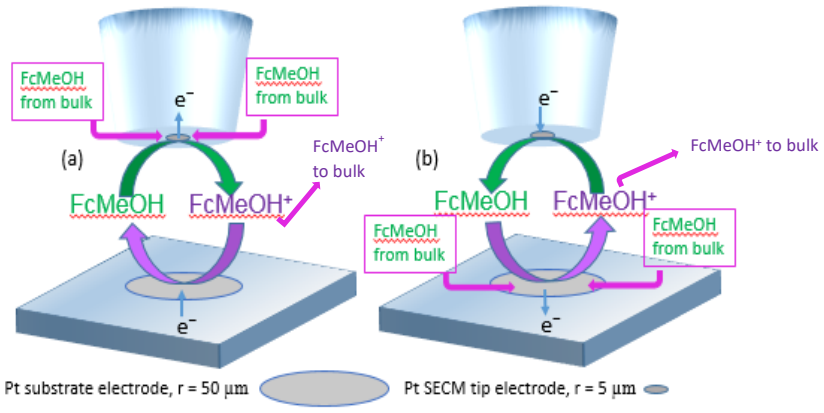

Figure 3-9. Schematic diagram of SECM modes over a conducting substrate surface with FcMeOH redox species undergoing one electron transfer, where micro disc, r = 50 µm, and tip dimensions result in R_g = 10: (a) FB mode, showing positive feedback and (b) SG-TC mode.

3.6.4 SECM imaging

All images were collected as the tip scanned the substrate surface horizontally in successive lines from left to right (long move = x-axis) starting from the top and moving towards the bottom of the image (y-axis). Specifically, the movement pattern, referred to as a raster scan, was so that the probe moves slowly from left to right according to the step size and increment time, records the current during this movement and then quickly returns to x = 0 without recording the current, before starting the next scan line. A precondition time (also referred to as 'quiet time'), during which the potentials are applied to the tip and substrate before the probe movement is initiated. This was varied for different experiments depending on tip current stability, but the most common value was 60 s. The scanning speed was determined by a

combination of the step size and the increment time (time that the tip spends at each pixel before moving to another one) settings, when either of the two was varied. An increment step of 5 µm and an increment time of 0.2 s were used as the benchmark settings, so unless stated otherwise, these settings were used. Another typical SECM imaging setting, in this case only relevant to approach curves, was the 'max increment' (set to 1 µm) which specifies the fastest rate of probe movement in the z direction. During approach curves the SECM software automatically decreases this increment size as the tip current begins to increase or decrease towards the current setpoint. Total x and y imaging distances were 400 µm and 200 µm for 100 µm and 50 µm electrodes, respectively. Other specific details can be found in the Figure legends or in the Experimental section of the results chapters.

3.6.5 SECM probe cleaning

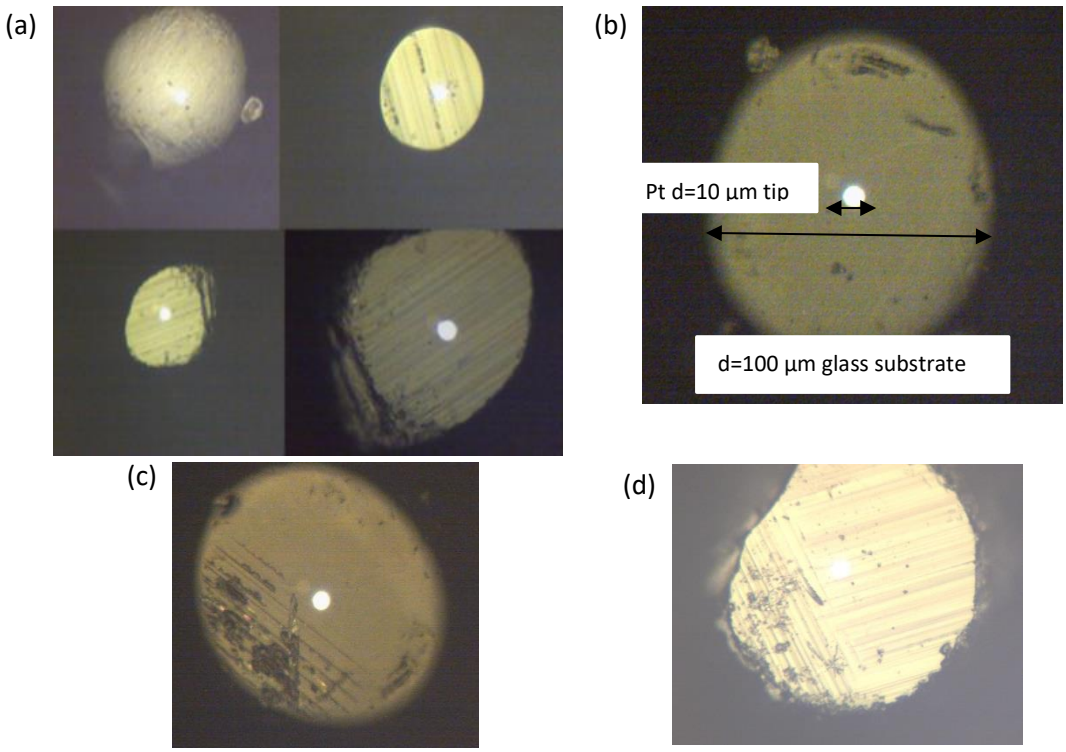

Figure 3-10. (a) Variation of the glass insulator surrounding Pt tip after polishing performed in between the experiments. All images are of the same tip, where r_{tip} = 50 µm, r_{Pt} = 5 µm, R_g = 10. (b) Polished and ready to use Pt probe and (c) the same probe after some experiments, requiring polishing. (d) 1 µm Pt probe, R_g = 15 before polishing.

SECM probes with a Pt disc radius, *r*, of 5 µm (CH Instruments) and 0.5 µm (Heka Elektronik, Germany) and R_g of approximately 10 and 15, respectively, were used to collect SECM images in this thesis. Each probe was examined under the microscope to ensure fidelity, e.g. see Figure 3-10, and polished prior to use. Throughout the text, the tip size will be defined as either 10 µm or 1 µm, referring to the Pt diameter value. Tip polishing was performed using a 0.05 µm

aqueous alumina slurry using manual polishing and/or a semi-automatic system, when the tip is polished on micro polishing wheel, adding DI water to keep the surface of the wheel damp.

During scanning experiments the tip may become damaged or dirty, resulting in lower currents; hence, the tip was examined again under the microscope and repolished. The amount of polishing required depended on the extent of scratching. Several optical images of damaged and clean probes are also presented in Figure 3-10. When comparing the same probe before and after some experiments, it was clear that it needed to be refreshed to remove some dirt and scratches that appeared during immersion in the solution and possibly through touching the substrate surface. During the setup (including the surface alignment to the tip), tip crashing to some extent was possible, which would result in such visible scratches on the probe surface.

3.6.6 SECM set-up evaluation prior to imaging

Following experimental set-up for SECM imaging, simple CVs were performed on both WEs (tip and substrate) to make sure both were functioning as expected and to evaluate if further cleaning was required. CV scans were performed between +0.45 V and 0.00 V to obtain one electron reversible oxidation-reduction wave of 0.5 mM $FcMeOH/FcMeOH^+$ at 0.1 V s^{-1}. Electrochemical cleaning was performed on the substrates, as described in Section 3.4.

The substrate alignment to the tip was evaluated using the line scans. They were performed across the insulating regions of the surface in both x and y directions to get the tip current as stable as possible, which would mean that the substrate tilt is minimal. As discussed in the results chapters, sometimes this was not completely successful.

3.6.7 Extraction of the middle line profiles

In this thesis, horizontal (H) and vertical (V) middle line profiles extracted from the SECM images were used for quantitative analysis (Chapters 5-9). They were chosen through the evaluation of the images: the electrode centre and edges were located through symmetry and through corresponding middle left and right or top and bottom edge electrode image values, as shown in Figure 3-11. These edge coordinates (either for disc or square geometry), x (yellow) and y (purple), were then confirmed visually and the middle values were found for both V and H line profiles respectively. The absolute values varied within different electrodes, due to some variation in centring of the image.

Selected line profiles were extracted from the images by collecting the current values in an Excel spreadsheet for each pixel, at given x (row) and y (column) values. For H line profiles, the required data row was selected with increasing y value, representing the left to right tip movement in these experiments. For V line profiles, the required column of data was selected, and the data were rotated. Neighbouring line profiles were also extracted and compared to confirm an effective middle line profile selection in both directions.

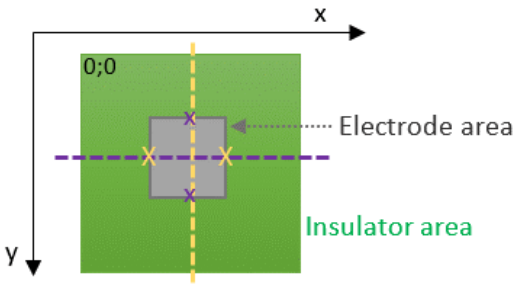

Figure 3-11. H (purple) and V (yellow) middle line profiles, derived using middle coordinates of the electrode edges for a square (or equivalent approach for a disc).The initial (0;0) coordinate is at the top left corner.

3.6.8 Substrate samples in the SECM set-up

The SECM set-up usually includes a cell with an o-ring, which is placed on top of the sample clamped with sufficient surface pressure to make sure the liquid does not escape. Some adjustments to this system were required to fit in-house fabricated electrode designs, introduced in Section 3.2. Four sample configurations were used for single and array electrode chips used to collect data for this thesis, requiring creativity in adjusting the set-up as well as SECM set-up versatility to a variety of the substrate samples.

3.6.8.1 SECM set-up for the old design chip substrate

The Pt micro square electrode array of the old design (Figure 3-4) was used as a substrate. The relatively wide chip dimension was small enough to be immobilized in a small petri dish (of approximately 3 cm diameter) using AIB epoxy mixture B:A (100:27), as shown in Figure 3-12. Connection to the bond pad was achieved by fixing a wire on the electrode using silver loaded epoxy adhesive and hardener (approx. 1:1 ratio) and this was then insulated from the solution by covering with further AIB epoxy. Electrical connection to the other end of the wire was then easily achieved with a crocodile clip via a piece of copper tape. The petri dish was filled with the experimental solution and RE, CE and probe were placed within the petri dish and connected to enable imaging.

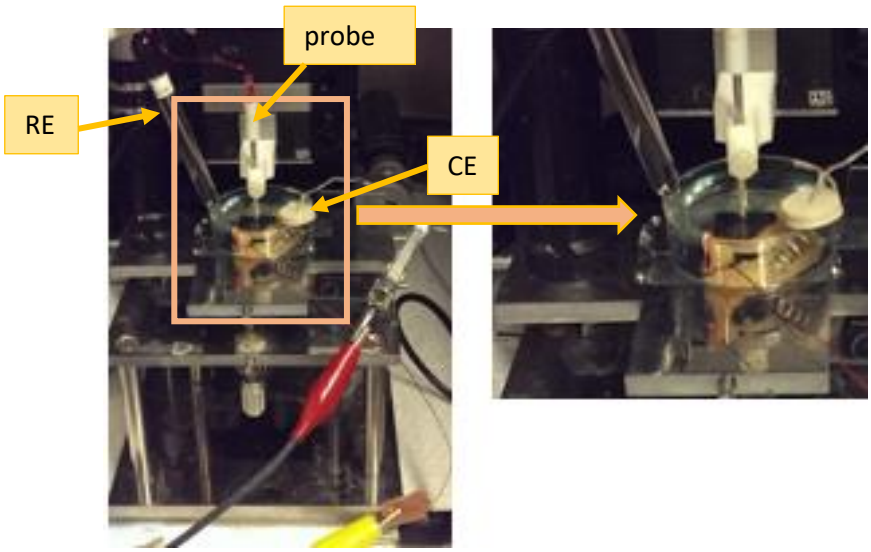

Figure 3-12. (a) SECM set-up when the substrate was an old design array, which was immobilized in a petri dish. Yellow clip connects WE placed in the petri dish on the stage, red clip connects CE.

3.6.8.2 SECM set-up for thin track chips

A plastic substrate with a cavity of the dimensions of the electrode was laser cut by Anthony Buchoux (SMC) to fit a single 'thin track' design electrode. Some polytetrafluoroethylene (PTFE) tape was placed at the base of the cavity, and an electrode was placed in this custom-built cell, as shown in Figure 3-13 (a). An original o-ring seal was placed on top, Figure 3-13 (b), and the final assembly was checked for leakage with and without the externally attached crocodile clip. CE, RE and probe electrode were placed within the o-ring and connected.

This set-up was confirmed to be suitable to use for SECM imaging, allowing a reusable cell to be used for as many electrodes as needed, without damaging the electrodes. However, the PTFE tape did not always ensure complete insulation and protection of the bond pad and the crocodile clip against water leakage. The set-up was therefore regularly controlled to check that water did not leak and reach the bond pad. Due to such leakage problems, a different approach was developed.

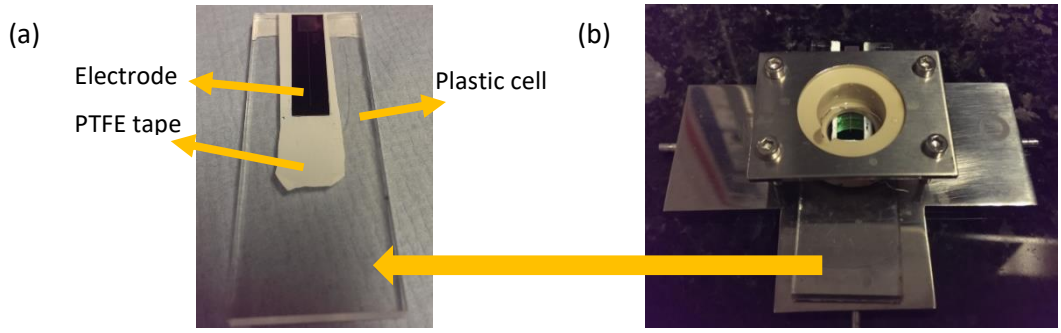

Figure 3-13. (a) Reusable plastic cell, 'case', with an inserted WE and PTFE tape on the base to prevent solution leaking in the final set-up in (b), where the case is fixed to the stage with a double-sided sticky tape and the electrode area of interest is sealed with an o-ring on top of it (set-up using 4 screws).

A different substrate set-up was made for the single 50 µm MNEE devices of thin track design (Chapter 8-9), as shown in Figure 3-14, with the help of Mr David Paden (School of Chemistry Mechanical Workshop). The set-up required more preparation than in the above example, but it was robust and prevented leaking at all times during the experiments. First, a slot in the wall of a small petri dish (approximately 3 cm diameter) was cut out just wide enough for the electrode chip to be placed through and into the dish, as shown in Figure 3-14 (a). The chip was placed flat in the dish and its end with the electrode was positioned so that it would be placed approximately in the middle of the dish. In this position, the chip was glued using an araldite mixture (fast drying, 1:1 ratio) to hold it in place, and the sides around the cut-out space were also sealed with this araldite mixture. Sticky tape was then used to create a new wall in that area and araldite was used to make it solid, as shown in Figure 3-14 (b). The overall finish of this design clearly shows it has been custom made in-house, but it proved to be easy to handle during the experimental work. Although the electrode could not be recovered from the dish it could be continuously used for other electrochemical experiments using a small RE and a CE, both placed in the dish just like for the SECM experiments, as shown in Figure 3-14 (c).

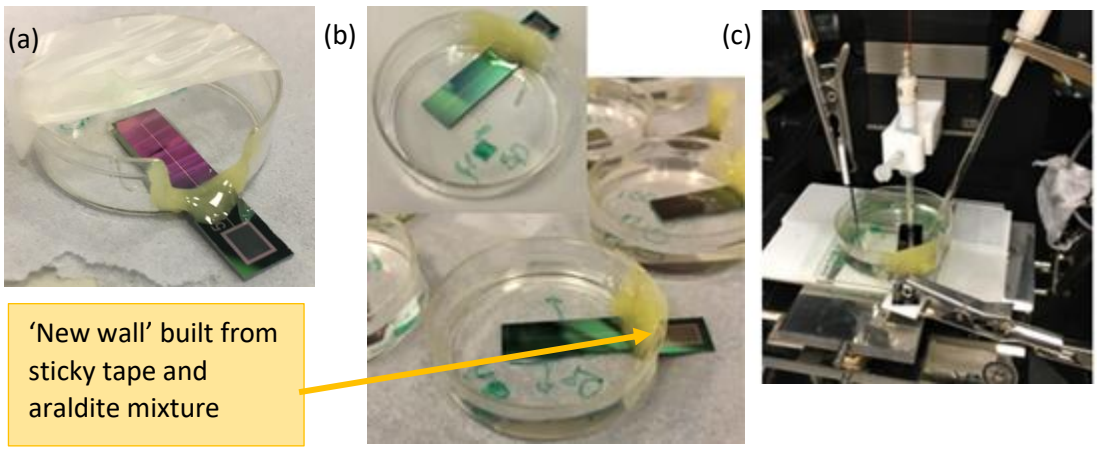

Figure 3-14. Thin-track chip set-up progress: (a) a petri dish with a cut-out wall, so that the bond pad of the glued electrode chip would be outside of the dish. Some araldite around the cut-out space reassured good sealing and parafilm above the electrode area prevented accidental araldite drops to the electrode area; (b) petri dishes with glued electrodes and fully built new walls made using sticky tape and araldite mixture. (c) Full SECM set-up using this substrate design, where RE, CE and probe electrode were immersed in the petri dish filled with the experimental solution.

3.6.8.3 SECM set-up for a super-thin track chip

A reusable cell for the thin track electrode was made, using a silicon multi-well replaceable superstructure (Nexterion ® IC-16s), which was modified to fit our design, as shown in Figure 3-15. The structure contained 16 chambers but due to it being made from a soft material, it was easily cut to have 12 chambers and two of the separation bars in the structure were cut out, making some space for CE and RE. The WE chip was slit in through the two H cuts made in the separation bars to have it parallel to the surface. The structure comes with a sticky side which was used to adhere it on a microscope slide, which was positioned on the SECM stage

using double-sided tape. SECM requires little solution for the experiments, hence the height of this structure was sufficient, and all four electrodes, including the probe, which could move above the defined surface without any constraints, were immersed in the solution.

The problem with this set-up was related to the crocodile clip connection. When in a near horizontal, rather than vertical position often used for the electrochemical experiments, the clip weighs significantly more than the rest of the system, which occasionally produced cell lifting despite the sticky tape. Some blue tack was eventually placed under the clip to prevent such movement. In the future, a stronger adhesive could be used to ensure resistance to leverage induced by the crocodile clip weight or a different connection to the electrode should be made. The structure made of silicon is however still soft, suggesting further issues in holding the electrode in place. In case of the future experiments, a set-up similar to the one in Figure 3-14 could be used for these electrodes instead.

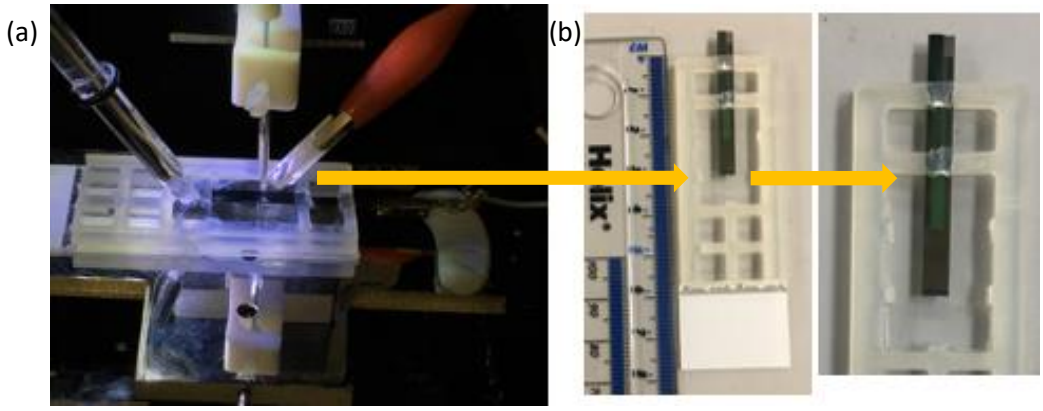

Figure 3-15. (a) Silicon multi-well structure with all 4 electrodes in place on the SECM stage. (b) A closer look of the super-thin track electrode substrate positioned in the silicon multi-well cell.

3.7 REFERENCES

1. Terry, J. G. *et al.* Nanoscale electrode arrays produced with microscale lithographic techniques for use in biomedical sensing applications. *IET Nanobiotechnol.* **7**, 125–134 (2013).
2. Schmueser, I. *et al.* A systematic study of the influence of nanoelectrode dimensions on electrode performance and the implications for electroanalysis and sensing. *Faraday Discuss.* **164**, 295 (2013).
3. Blair, E. O., Corrigan, D. K., Terry, J. G., Mount, A. R. & Walton, A. J. Development and Optimization of Durable Microelectrodes for Quantitative Electroanalysis in Molten Salt. *J. Microelectromechanical Syst.* **24**, 1346–1354 (2015).
4. Woodvine, H. L., Terry, J. G., Walton, A. J. & Mount, A. R. The development and characterisation of square microfabricated electrode systems. *Analyst* **135**, 1058–1065 (2010).
5. Woodvine, H. L. Development and Characterisation of Microelectrode and Nanoelectrode Systems. (The University of Edinburgh, 2012).
6. Terry, J. G. *et al.* Nanoscale electrode arrays produced with microscale lithographic

techniques for use in biomedical sensing applications. *IET Nanobiotechnology* **7**, 125–134 (2013).

7. Shafiee, S. A. How do you prepare FcMeOH? *Research Gate* (2014). Available at: http://www.researchgate.net/post/How_do_you_prepare_FcMeOH. (Accessed: 6th June 2016)

8. Vasilescu, I., Eremia, S. A. V, Radoi, A., Radu, G. & Litescu, S. Lipid hydroxide determination on a ferrocenemthanol modified electrode. *Anal. Methods* **5**, 2013–2019 (2013).

9. Piper, A. Electrochemical characterisation of microsquare nanoband edge electrode (MNEE) arrays and their use as biosensors. (University of Edinburgh, 2017).

10. Jacobse, L., Raaijman, S. J. & Koper, M. T. M. The reactivity of platinum microelectrodes. *Phys. Chem. Chem. Phys.* **18**, 28451–28457 (2016).

11. Wiley, J. Analytical Electrochemistry : The Basic Concepts References and Links. 1996–1997 (2009).

12. Wightman, R. M. Microvoltammetric electrodes. *Anal. Chem.* **53**, 1125A–1134A (1981).

13. Sun, P., Laforge, F. O. & Mirkin, M. V. Scanning electrochemical microscopy in the 21st century. *Phys. Chem. Chem. Phys.* **9**, 802–823 (2007).

14. Kai, T., Zoski, C. G. & Bard, A. J. Scanning electrochemical microscopy at the nanometer level. *Chem. Commun.* **54**, 1934–1947 (2018).

15. Instruments, C. H. Scanning Electrochemical Microscope.

16. Zoski, C. G. Review—Advances in Scanning Electrochemical Microscopy (SECM). *J. Electrochem. Soc.* **163**, 3088–3100 (2016).

17. Partel, S. *et al.* Lift-Off Free Fabrication Approach for Periodic Structure with Tunable nano Gaps for Interdigitated Electrode Arrays. *ACS Nano* 1086–1092 (2016). doi:10.1021/acsnano.5b06405

18. Kwak, J. & Bard, A. J. Scanning Electrochemical Microscopy. Theory of the Feedback Mode. **1227**, 1221–1227 (1989).

4 ANALYSIS OF EXPERIMENTAL AND NUMERICALLY DERIVED PROBE APPROACH CURVES

4.1 INTRODUCTION

Prior to SECM imaging, probe approach curves (PACs) are used to determine and set the tip working distance, *d*. It is therefore important to establish the appropriate PAC calibration for the system. In this work, PACs were recorded above an insulator surface and the centre of micro electrode and microdisc/microsquare nanoband edge electrode (MNEE), as well as the edge of the electrode. COMSOL Multiphysics was used to model equivalent PACs to pure insulator and conductor surfaces at specific *d* values. The experimentally recorded PACs for several substrate electrodes are compared with numerically modelled data, both of which are then fitted with the approximate analytical expressions reported in the literature. The latest approximate analytical expressions by Lefrou *et al.*[1] are tested to determine their validity compared to the other models. All of this is required to enable the determination of real tip working distances (in µm) from the tip current values measured during PAC experiments. Knowing these values is important for quantitative SECM image data analysis in the following chapters.

4.2 EXPERIMENTAL PROBE APPROACH CURVES

4.2.1 Experimental details

Both substrate and probe electrodes used in this thesis have dimensions in the 1-100 µm range so they can be well-defined by electrochemical methods and establish steady state currents on typical experimental timescales. This is unlike electrodes of macroscopic dimensions which are too large to establish steady state signals on such timescales.[2] A mass transport limited steady state current is a requirement for establishing the tip working distance in a repeatable manner, which is conventionally achieved by recording PACs over a region of the substrate surface with known electrochemical properties. In this thesis, the region of the substrate surrounding the electrode area is known to be a pure insulator, so this region was used for probe positioning using negative feedback.

When the tip electrode is relatively far above the substrate, FcMeOH redox species diffuse from the bulk towards the tip and are oxidised by the tip. This results in a steady state current described in Section 2.6 and referred to as the bulk tip current, i_T^{bulk}, in the SECM context. As the probe approaches the surface (leading to a decrease in *d*), the tip current decreases as a result of a greater negative feedback due to a hindered diffusion. This means that tip working distances can be measured and defined according to the measured current as a fraction of i_T^{bulk}, often referred to as the setpoint. In this work, this setpoint was varied between 0.9 and

0.7, typically using working distances of d = 0.7i_T^{bulk}, 0.8i_T^{bulk} and 0.9i_T^{bulk}. The aim of this chapter is to convert these current percentages into absolute working distances, measured in µm.

The substrate electrode was located by imaging with SECM and the probe was moved to the desired position for PAC analysis. For more complete initial studies which can be confidently built on for a further analysis using approximate analytical expressions, PACs were also recorded over the middle of the substrate electrode. This area is conducting for a micro electrode and insulating for a microdisc/microsquare nanoband edge electrode (MNEE). PACs over the conductor area result in increasing positive feedback (Figure 2-12). PACs over the insulator area in the middle and edge of the electrode of the MNEE were also collected for additional analysis. Except where otherwise stated, the electrodes used for all of the data collection in this chapter, were micro and nanoband edge single Pt electrodes of 100 µm diameter and single edge length for a disc and square geometry, respectively. All experimental details are presented in Section 3.5.1.

4.2.2 Typical normalized probe approach curve responses

In this section, examples of normalized approach curves above an insulator, a conductor and an electrode edge are presented in Figure 4-1 (a). A schematic figure depicting above which areas in the electrode chip PACs were recorded is shown in Figure 4-1 (b). Current values from the experimental PACs were normalised to the first recorded current value in each curve, which in fact is i_T^{bulk}, since the first current point was recorded at a large d value.[3] PAC normalization was used to remove the effect of changes due to varying concentration and temperature between experiments. As expected, over the insulating surface a decrease in tip current, i_T, was recorded with decreasing d, reflecting a negative feedback response (black squares), while an increase in i_T, known as positive feedback (red circles), was recorded over the conducting substrate electrode (Section 2.9.2).

The PAC recorded over the band edge (blue triangles) in Figure 4-1 exhibits a mixed conductor and insulator-type response. As the tip approached the substrate surface, it initially generated a positive feedback, while at smaller d, the currents decrease with decreasing d, as seen for an insulator surface. Individual positive and negative feedback responses have been reported extensively before and they are relatively well understood.[4,5] A mixed response in this case reflects the trade-off between an unhindered diffusion path between the tip and the band electrode at intermediate distances and blocked diffusion caused by the presence of the electrode recess at short distances. At very short distances, a very small region of the nanoband electrode is probed, and in this case the probe electrode is much larger than the “substrate”. This suggests that the latter cannot keep up with the electron transfer at the tip, hence a negative feedback.

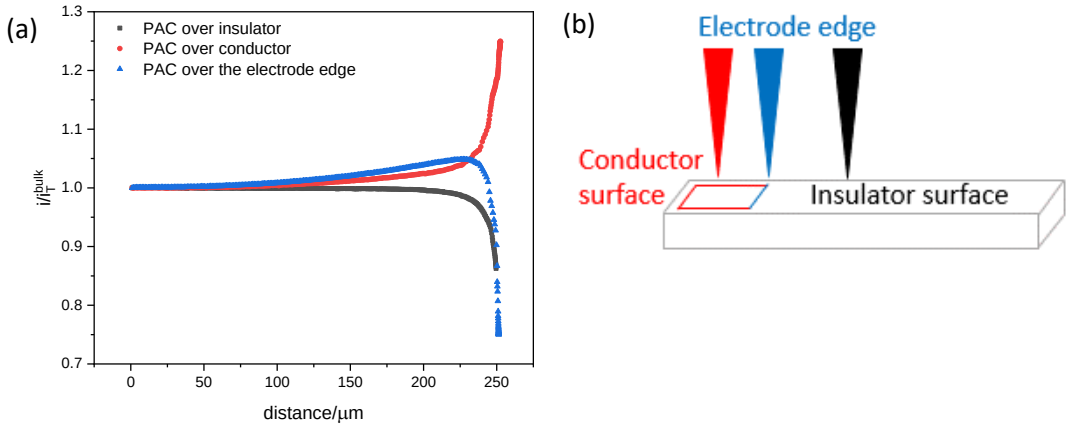

Figure 4-1. (a) PACs recorded above an insulating (black squares), a micro electrode substrate (red circles), which is a conducting surface, and an edge of the substrate electrode (MNEE) (blue triangles). Currents were normalized to i_T^{bulk} and distance (x axis) is "z-d" where z is the starting position which was arbitrarily set at 250 μm from the surface (i.e. d = 0 μm is the electrode surface). (b) Schematic presentation of the electrode chip, showing where all three PACs were performed, using the same colour code as in (a).

4.2.3 Analysis of insulator probe approach curve currents

Following the initial PAC behaviour presented above, unnormalized current values from experimental PACs are compared to evaluate if the data was indeed as expected and reproducible. The i_T^{bulk} values at large tip-substrate distances above the insulator were recorded as the first current value of each PAC, and the values are presented in Table 4-1. The average initial current across all measurements was 0.635±0.036 nA, which is within experimental error from the theoretical steady state tip current of 0.638 nA. This value was calculated using Equation (2.24), which is a variation of the widely accepted analytical expression in Equation (2.20) for a microdisc electrode. When the diffusion coefficient of the redox species, $D = 6.48 \times 10^{-10}$ m^2 s^{-1} (Section 4.3), $i_T^{bulk} = 0.638$ nA. Temperature, T, was not controlled, allowing for a diffusion coefficient variation, to some extent affecting i_T^{bulk}. Such i_T^{bulk} comparison shows a good correlation between experimental and theoretical values.

	$0.9i_T^{bulk}$ PAC	$0.8i_T^{bulk}$ PAC	$0.7i_T^{bulk}$ PAC
	i_T^{bulk}/nA	i_T^{bulk}/nA	i_T^{bulk}/nA
Microdisc	0.595	0.613	0.698
Microsquare	0.582	0.603	0.611
Nanoband disc	0.620	0.645	0.651
Nanoband square	0.656	0.654	0.693

Table 4-1. The first recorded tip current, i_T^{bulk}(nA), from PACs set to stop at $0.7i_T^{bulk}$, $0.8i_T^{bulk}$ and $0.9i_T^{bulk}$ above the insulator surface of four substrate electrodes listed on the left. Average i_T^{bulk} from all measurements = 0.635 ± 0.036 nA.

Experimental i_T^{bulk} variation between 0.582 and 0.698 nA in Table 4-1 can be explained as follows. After the first PAC was recorded to a setpoint of $0.9i_T^{bulk}$ over an insulator surface, an SECM image of the electrode was collected (time taken per image was approximately 15 min), followed by a retraction of the probe by a constant value (250 μm) from the electrode surface.

Another PAC to a setpoint of $0.8i_T^{bulk}$ and the SECM image were recorded, followed by the same procedure regarding $0.7i_T^{bulk}$ PAC and the image. This shows that there was some control over the experimental work, but such approach also resulted in increasing i_T^{bulk} with a decreasing setpoint. This could be due to the initial trace amounts of $FcMeOH^+$ in solution (e.g. from aerial oxidation) that gets gradually reduced by the substrate electrode over time (since it is biased at 0 V). Hence, there is more FeMeOH in bulk solution in the later approach curves resulting in a greater i_T^{bulk} with time.

Another possibility is that more tip area was getting exposed to the solution, as the tip may have been getting cleaned due to constantly applied positive potential of +0.45 V, resulting in an increasing current. However, this is unlikely, since such positive potential values were not used for cleaning processes at any point, as discussed in Section 3.4. Such current increase due to product species accumulation could be an important factor in time-dependent experiments, such as corrosion monitoring.[6] Such current increase over time due to other than the underlying substrate changes reasons could significantly affect the results and lead to misinterpretations. In this work, tip bulk currents are within acceptable, experimental error, as the substrates were not sensitive to time spent in the solution.

It was also checked if the SECM instrument stopped the tip at the correct values in the PAC experiments above. This was done by comparing the final i_T from PACs over four different samples at three setpoints, as shown in Table 4-2. In such experiments, the type of electrode should not matter as the tip is approaching an insulator surface which is at a reasonable distance away from the electrode area. Therefore, final current values in each column are expected to be the same within experimental error, since i_T^{bulk} is the same in all cases. The values are as expected, within experimental error in each column, reflecting acceptable functioning of the system (piezo controllers) and data reproducibility.

Electrode type	*$0.9i_T^{bulk}$/nA*	*$0.8i_T^{bulk}$/nA*	*$0.7i_T^{bulk}$/nA*
Microdisc	0.536	0.490	0.489
Microsquare	0.523	0.481	0.427
Nanoband disc	0.558	0.515	0.456
Nanoband square	0.590	0.522	0.485

Table 4-2. Comparison of the final current values in PACs set to stop at three i_T^{bulk} setpoints over the insulator surface outside the different electrodes.

These final current values, i_T, from Table 4-2 were normalized to the initial current values, i_T^{bulk}, from Table 4-1. Such current normalization (i_T/i_T^{bulk}) in Table 4-3 allows verification that the software stopped PAC correctly at the set position. In all cases, it is confirmed that the settings did not deviate, delivering ratio values of 0.9, 0.8 and 0.7 as expected, within an acceptable ±1% variation independent of the substrate type. This confirms that any time or temperature dependent variations in tip current can be successfully removed by the normalization process.

i_T^{bulk} ratio	i_T/i_T^{bulk}	i_T/i_T^{bulk}	i_T/i_T^{bulk}	i_T/i_T^{bulk}
	Microdisc	Microsquare	Nanoband disc	Nanoband square
0.9	0.90	0.90	0.90	0.91
0.8	0.81	0.80	0.80	0.81
0.7	0.69	0.70	0.70	0.71

Table 4-3. Normalized final current values (i_T) from insulator PACs to i_T^{bulk}. The resulting i_T/i_T^{bulk} reflect the PAC setpoints: 0.9, 0.8 and 0.7.

4.2.4 Graphical presentation of the current variation in experimental probe approach curves

Initial and final current values from PACs were shown to be mostly as expected, and the full curves are shown in Figure 4-2 to evaluate data reproducibility further. Several PACs over the middle of the electrode were collected together with the ones over the insulating surface on the side of the electrode. Normalized PACs above the insulator surface are shown in (a), while PACs above the middle of each electrode are presented in (b).

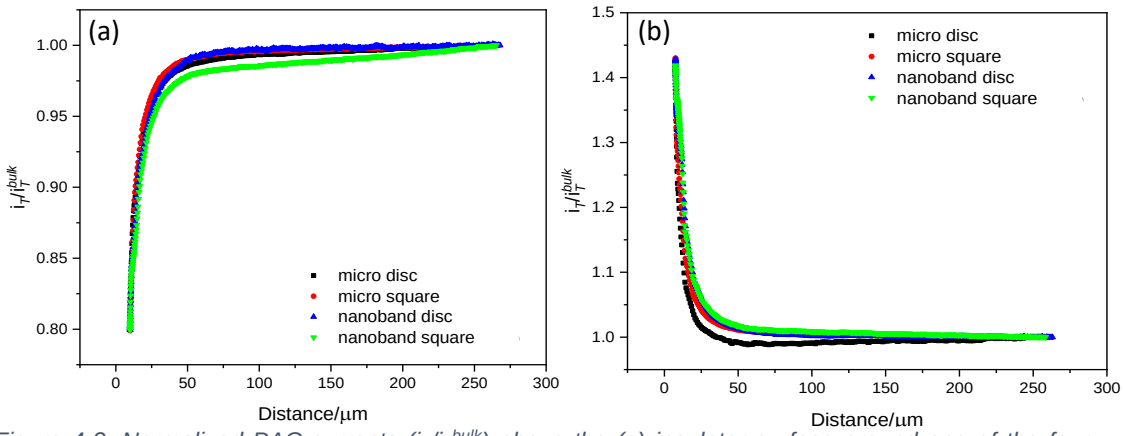

Figure 4-2. Normalized PAC currents (i_T/i_T^{bulk}) above the (a) insulator surface around one of the four electrodes at $0.8i_T^{bulk}$, where i_T^{bulk} is a tip current value at a large tip-substrate distance, (b) middle of the four substrate electrodes at $0.7i_T^{bulk}$.

Insulator PACs in Figure 4-2 (a) are broadly as expected for negative feedback. Although, some variation is observed in the case of the nanoband square substrate, in which the current exhibits a gradual decay from the beginning of the PAC. This suggests that the tip current was not completely stable when the PAC started, possibly due to the tip passivation or contamination processes over time. Such time-dependent tip currents also impact SECM imaging data (see Chapter 6). In the case of PACs, this can usually be minimised by applying a tip pre-conditioning step (also referred to as “quiet time”) before the tip movement begins. Such pre-conditioning may have been insufficient in the case of the nanoband square PAC.

Interestingly, the PAC response recorded at the middle position of the substrate electrodes in Figure 4-2 (b) exhibit positive feedback for both micro and nanoband edge electrodes. The middle of the latter is an insulator, so negative feedback might be expected, but when the tip begins to block the diffusion to the electrode recess, the hemispherical diffusion field from the band electrodes must extend sufficiently to give a positive feedback response. On close

inspection of Figure 4-2 (b), the current values at intermediate distances (green box) vary slightly for all electrodes. As with the insulator PACs, this likely reflects time-dependent tip currents.

4.3 EXTRACTION OF THE DIFFUSION COEFFICIENT

Before proceeding with COMSOL modelling and PAC fitting using approximate analytical expressions, it was important to determine diffusion coefficient, D, value specific for these experiments. Whilst the nominal tip radius was 5 µm, throughout this work it was observed that the value of i_T^{bulk} varies considerably across experiments, which can be attributed to changes in the apparent tip radius, a, which can vary due to a number of experimental factors. First, probe electrode passivation or contamination over time typically causes a gradual decay in the tip current, which can be accounted for by assuming an apparent loss of electrode size. Second, it is a standard procedure to manually polish imaging probes before and in between some of the experiments due to vast imaging, as explained in Section 3.5.5. Extensive polishing will not only affect the absolute value of a, but will eventually affect the R_g value, which governs i_T^{bulk} related to the value of β.

Since the experiments were not temperature controlled, the value of a = 5 µm was assumed to be correct for the calculations regarding D.

Since most of the COMSOL modelling was performed for a microdisc electrode, PAC experimental data also from a microdisc electrode was used in this analysis section. At $0.8i_T^{bulk}$ tip working distance, i_{tip} over the insulator area was 0.497 nA, which approximates to 0.5 nA. This value is 80% of the i_T^{bulk}, so i_T^{bulk} = 0.625 nA. This value was used in Equation (2.21) to obtain the diffusion coefficient, $D = 6.48\times10^{-10}$ m^2 s^{-1}, which falls within the cited literature values between 7.81×10^{-10} m^2 s^{-1} and 6.1×10^{-10} m^2 s^{-1} at room temperature.[7–9] Equivalent COMSOL simulated $0.8i_T^{bulk}$ value using this value of D was 0.477 nA, resulting in i_T^{bulk} of 0.621 nA, which is comparable to the experimentally extracted value and confirms the reliability of the results. Both D values from experimental and COMSOL calculations were similar, hence the experimental one was further used throughout this work.

4.4 COMSOL MODELLING OF THE TIP CURRENTS

After experimental PACs over conductor and insulator surfaces were collected and analysed, a COMSOL model was developed to obtain equivalent theoretical data in order to determine the absolute values of d that correspond to the setpoints of $0.7i_T^{bulk}$, $0.8\,i_T^{bulk}$ and $0.9i_T^{bulk}$ used throughout this thesis. Only final current values over each surface at specific tip working distances were numerically derived, as these were the most relevant to vertical probe positioning. The model was used to generated flux values, which were integrated across the

tip surface and converted to currents. These values were normalized by the tip current calculated at a large *d* approaching infinitely large insulator area and compared to the normalized values obtained from experimental PACs.

4.4.1 Description of the numerical model

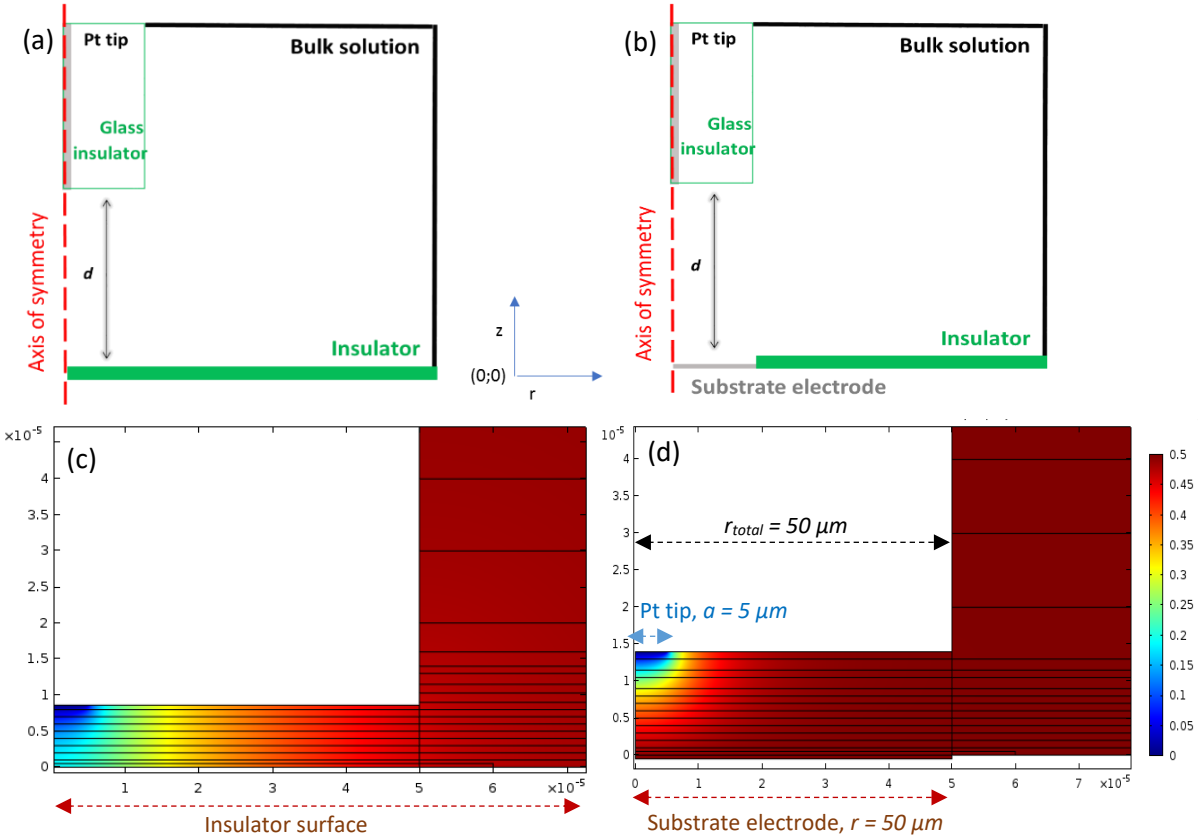

Figure 4-3. Schematic representation of COMSOL 2D axially symmetric model depicting SECM tip over (a) an insulator surface outside electrode area and (b) the middle of the substrate electrode, which is a conductor for micro electrodes and an insulator for nanoband electrodes. Substrate electrode is recessed by 500 nm, r = 50 µm, Pt tip a = 5 µm, R_g = 10. Dimensions of the figure are not to scale. Equivalent COMSOL generated surface concentration models (mol m^{-3}) for (a) when d = 23 µm and (b) when d = 14 µm are in (c) and (d). The latter was modelled for a microdisc electrode, allowing to use the highest symmetry possible. For both (c-d), t = 100 s and the scale on the right of (d) applies.

COMSOL 5.1 Multiphysics was used for diffusional simulations using 2D-axially symmetric finite element method (FEM) for a microdisc substrate electrode with a radius of *r* = 50 µm and a probe electrode radius of *a* = 5 µm. Figure 4-3 shows a schematic representation of the model used, where the tip is situated above either: (a) the pure insulator (negative feedback); or (b) the middle of the disc microelectrode (positive feedback), as set by the appropriate boundary conditions. As substrate electrodes are recessed by 0.5 µm (Section 3.2.1), the tip-substrate distance is increased by this value over the middle of the electrode, referred to as a conductor. Final current values over pure insulator and conductor at seven and six *d* values, respectively, were modelled, and examples of the resulting 2D concentration profiles is shown in Figure 4-3 (c-d). Since the disc has such a high symmetry, only a line in 2D needs to be

modelled, as rotation around the central axis generates a complete picture of the model, as shown in Figure 4-4.

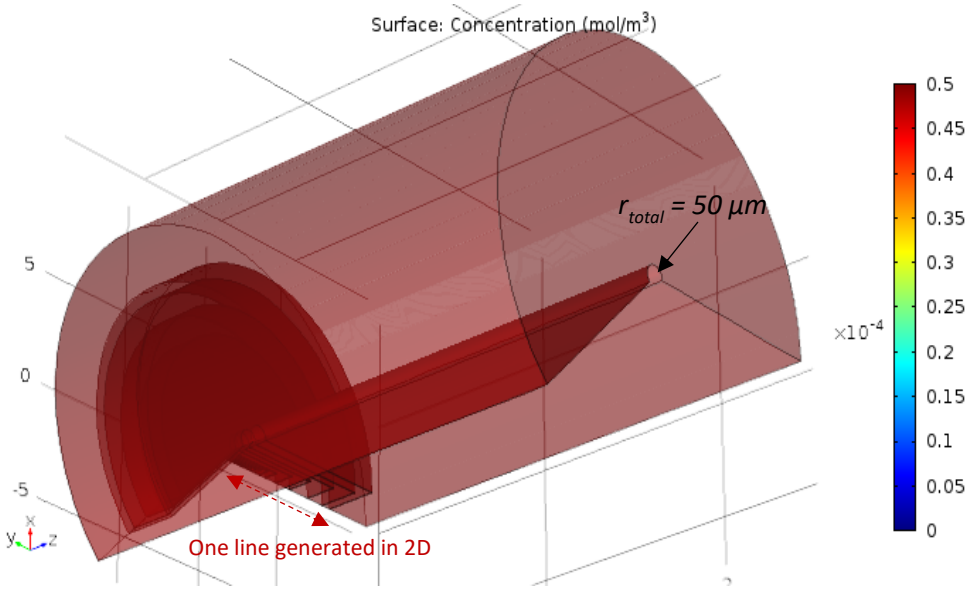

Figure 4-4. 3D representation of a COMSOL-generated concentration profile surface (mol/m^3) for a disc electrode, created using 2D lines and boxes.

The model was set-up as follows: a simulation box, such as in Figure 4-3 (c-d), was created by drawing lines and boxes to reflect electrode and probe dimensions from Figure 4-3 (a-b). As shown in Figure 4-3 (c-d), the solution part of the box (coloured) was filled with a mesh, required to enable diffusion modelling. A relatively high mesh density value (3000-10 000 domain elements), compared to approximately 100 for boxes further away from the electrodes, was used near both tip and substrate electrode surfaces and around their edges to reflect the greater diffusional gradients, as suggested by the literature.[10] Either mesh density or mesh size was increased or decreased, respectively, in a model until less than a 0.001 nA (<1%) difference was observed in simulated steady-state current values for each *d*, just like in the previously published examples.[11] The mesh size used from the list in the model was 'coarse' or 'fine', both giving similar results, and more than 760,000 degrees of freedom (DOF) were solved for in each model.

Other important set-up details include the boundary conditions and concentration values. A no flux boundary (or barrier boundary), where the concentration gradient is zero, was set at the insulating surfaces (in green, Figure 4-3), while the FcMeOH bulk concentration (c = 0.5 mM) was fixed at the semi-infinite diffusion boundaries (black lines, Figure 4-3) and the substrate electrode surface. The FcMeOH concentration at the tip electrode was set to c = 0 mM, representing redox species oxidation under mass-transport (diffusion) limited conditions.

Mechanical agitation, thermal and forced convection and migration effects were assumed to be insignificant and were not included in the model.[12]

The box dimensions are height (h) = 0.25 cm, width (w) = 0.1 cm. These values are enough to prevent the hemispherical diffusion field reaching the edges of the box when using diffusion time of t = 100 s for the simulations. From Equation (2.17), for D = 6.48 x 10^{-10} m^2 s^{-1} it would take over 770 s to reach the shorter edge of the simulation box.

Time-dependent and stationary Fick's first and second laws of diffusion in Equation (4.1) and (4.2), respectively, were used to simulate time-dependent and steady state currents.

$$\boldsymbol{N}_i = -D_i \nabla c_i \tag{4.1}$$

$$\frac{\delta c_i}{\delta t} = D_i \nabla^2 c_i \tag{4.2}$$

where $\boldsymbol{N}_i$ is the molar flux (mol m^{-2} s^{-1}), D_i is the diffusion coefficient (m^2 s^{-1}), ∇ is a nabla mathematical operator and c_i is the concentration (mol m^{-3}) of the diffusing species, i. The generated normal diffusive flux values (mol/s) were multiplied by Faraday's constant to obtain current values.

Initial numerical modelling was validated by comparing theoretical i_T^{bulk} with the modelled value, obtained using a large tip working distance (d = 1.5 mm) above an insulating surface, similar to Figure 4-3 (a). Importantly, the calculated COMSOL tip current was i_T^{bulk} = 0.641 nA, which is within 0.5 % of the value determined by Equation (2.20), i_T^{bulk} = 0.638 nA. This is well within previously reported errors of up to 2% in COMSOL modelling.[13] Such close agreement between theoretical and COMSOL modelling values suggests that concentration profiles were successfully solved in this model, and that the input parameters such as diffusion coefficient (Section 4.3), are valid. This also shows that in this case the presence of the recess of 0.5 µm was insignificant for the steady state (limiting) current calculations, agreeing with Woodvine[11], who showed that recess at this scale is insignificant for the determination of the limiting current. Otherwise, a greater difference between the values would be observed, as Equation (2.20)[14] is derived for an inlaid electrode (Section 2.7). The calculated value of i_T^{bulk} = 0.638 nA was used for the current normalization processes in the following sections.

4.4.2 COMSOL prediction of PAC final normalized currents

As presented in the above section, COMSOL 2D rotational symmetry model was used to generate final PAC current values over an insulator surface at three tip working distances. The initial values used were d = 14.00, 9.95 and 7.55 µm, representing approximately $0.9i_T^{bulk}$, $0.8i_T^{bulk}$ and $0.7i_T^{bulk}$, respectively, obtained from one of the first literature entries for such tip working distances calculations based on analytical expressions for negative feedback (Section 4.5.1).[15] These initially selected values were known to be imprecise for the tip electrode size

and geometry (Section 4.5.1) but were still used to obtain some current values, which are later related to more precise tip working distances.

Table 4-4 shows the tip current, i_T, calculated at the three defined *d* values using COMSOL at two values of time, *t* = 100 s and *t* = 300 s, to assure that a steady state signal was achieved (Section 4.4.1). Since all of the generated values differ by 0.001 or 0.002 nA, which is less than 0.2%, it suggests that 100 s was sufficient to establish i_T^{bulk}.

i_T^{bulk} *setpoints*	*d*/µm	*COMSOL* i_T*/nA (t = 100 s)*	*COMSOL* i_T*/nA (t = 300 s)*	*COMSOL* i_T *(t = 100 s) normalized to* i_T^{bulk} *(0.638 nA)*
0.7	7.55	0.405	0.404	0.635
0.8	9.95	0.462	0.461	0.724
0.9	14.00	0.522	0.520	0.818

Table 4-4. Tip current values (i_T) values that were modelled by COMSOL using t = 100 s and 300 s at three d values. COMSOL (t = 100 s) values were normalized and used in the following sections for the extraction of the nominal d values.

Generated current values at selected *d*, based on the early published analytical expression for negative feedback at *t* = 100 s, were normalized to i_T^{bulk} = 0.638 nA and compared with the setpoint values. All normalized COMSOL values are lower than the expected values based on the selected setpoint values of 0.7, 0.8 and 0.9, in all cases by approximately 10%, as shown in the last column of Table 4-4. These uniformly lower values suggest that the absolute tip working distances derived from the early analytical expression were not accurate, resulting in an offset in normalized currents. At the end of this chapter, more accurate *d* values are extracted with the aid of a more appropriate analytical expression.

COMSOL 2D simulations were also performed to predict current values representing the last i_T values from PACs over a conductor surface at the same tip working distances as used for the insulator PACs. COMSOL generated values were normalized to the same i_T^{bulk} = 0.638 nA, as shown in Table 4-5.

d/µm	i_T^{bulk} *setpoint*	*COMSOL* i_T */nA*	*COMSOL* i_T/i_T^{bulk} *(0.638 nA)*
7.55	0.7	0.839	1.315
9.95	0.8	0.784	1.229
14.0	0.9	0.735	1.152

Table 4-5. The values of i_T modelled by COMSOL and normalized to i_T^{bulk} = 0.638 nA at three tip working distances representing final current values from PACs over the conductor surface.

4.5 APPROXIMATE ANALYTICAL EXPRESSIONS FOR DATA FITTING

In order to extract specific tip working distances valid for this work, COMSOL generated values were further validated using more recent approximate analytical expressions derived in the literature than in Section 4.4.2. First, experimental insulator and conductor PACs were fitted to specific for negative and positive feedback approximate analytical expressions, respectively, to confirm that the expressions are valid for data in this chapter. Then, constructed curves

from COMSOL modelled current values over insulator and conductor surfaces at several tip working distances were fitted to the same analytical expressions to extract more accurate absolute values for the $0.9i_T^{bulk}$, $0.8i_T^{bulk}$ and $0.7i_T^{bulk}$ tip working distances. All data were fitted using the least squares regression method (Origin software).

4.5.1 Approximate analytical expressions for negative and positive feedback

The first analytical approximations for the tip currents above conductor and insulator surfaces shown in Equation (4.3) and (4.4), respectively, were proposed by Mirkin et al.[16] Both expressed as a function of *L*, the distance between the probe and a substrate normalized to the tip radius (=*d*/*a*), and were created specifically for a disk-shaped tip steady-state currents over infinite insulator and conductor surfaces.[1,15] These expressions have been shown to be valid only as far as *L* = 100.[16]

$$i_T^{cond}/i_T^{bulk} = 0.68 + \left(\frac{0.78377}{L}\right) + 0.3315 * \mathrm{EXP}\left(-\frac{1.0672}{L}\right) \quad (4.3)$$

$$i_T^{ins}/i_T^{bulk} = 1/\left(0.292 + \frac{1.5151}{L} + 0.6553 * \exp\left(-\frac{2.4035}{L}\right)\right) \quad (4.4)$$

where i_T^{cond} and i_T^{ins} refer to the tip currents approaching a conductor and insulator, respectively.

Several groups have since derived expressions with improved accuracy, also including the tip geometry and R_g factor. In the previous models the latter was omitted, presumably for simplicity or because the impact of its variation on the tip current was not fully appreciated. The latest literature considers that R_g greatly varies within different probes and as a result of this different expressions have been developed not only for different R_g values, but also for different geometry probes.[1,6] One example of this is shown in Equation (4.5), which was derived by Lefrou *et al.* to describe negative feedback,[16] and has been reported as valid for R_g between 1.3 and 62. In this study, the probe has R_g value of approximately 10, since r_{total} = 50 µm, *a* = 5 µm, which should allow the use of this equation for fitting of the experimental and modelled data.

$$i_T = 1 + \left(\frac{-4.2 + 2.3 * \ln\left(R_g + 6.65\right)}{L^{\left(0.34+0.81*\mathrm{atan}\left(R_g{}^2\right)\right)}}\right)^{0.6} \quad (4.5)$$

Equation (4.6) was shown to be even more precise. It was also presented by Lefrou *et al.* and it is based on the above equation.[1,16] However, the accuracy was quoted as better than 1% for all *L* and values of R_g < 200.[1,16] Being specific for microdisc electrodes with finite R_g values,[1,16] it was considered to be the most recent and appropriate, hence it was used for the fitting of experimental and COMSOL PAC data over an insulator surface.

$$\frac{i_T^{ins}}{i_T^{bulk}} = \left[\frac{2.08}{R_g^{0.358}}\left(L - \frac{0.145}{R_g}\right) + 1.585\right] * \left[\frac{2.08}{R_g^{0.358}}\left(L + 0.0023 * R_g\right) + 1.57 + \frac{lnR_g}{L} + \frac{2}{\pi R_g} ln\left(1 + \frac{\pi R_g}{2L}\right)\right]^{-1} \quad (4.6)$$

There has been significantly less discussion in the literature regarding fitting data from positive feedback PACs than negative feedback PACs. One approximate analytical expression is shown in Equation (4.7), also derived by Lefrou *et al.*[1] It was specifically designed for positive feedback and also takes into account the R_g value.

$$\frac{i_T^{cond}}{i_T^{bulk}} = \alpha(R_g) + \frac{1}{\beta(R_g)}\frac{\pi}{4atanL} + \left(1 - \alpha(R_g) - \frac{1}{2\beta(R_g)}\right)\frac{2}{\pi}atanL \quad (4.7)$$

$$\alpha(R_g) = ln2 + ln2\left(1 - \frac{2}{\pi}acos\left(\frac{1}{R_g}\right)\right) - ln2[1 - (\frac{2}{\pi}acos\left(\frac{1}{R_g}\right))^2] \quad (4.8)$$

$$\beta(R_g) = 1 + 0.639\left(1 - \frac{2}{\pi}\text{acos}\left(\frac{1}{R_g}\right)\right) - 0.186[1 - \left(\frac{2}{\pi}\text{acos}\left(\frac{1}{R_g}\right)\right)^2] \quad (4.9)$$

4.5.2 Evaluation of negative feedback approximate analytical expressions

Experimental PACs over an insulator surface were fitted to the newest expressions in Equations (4.5) and (4.6) to verify their suitability for interpreting the PAC data. Throughout this chapter it has been shown that collected insulator PACs are very similar, in that the hemispherical diffusion field emerging from the electrode has been shown not to affect the location where the PACs were recorded, which can be considered as purely insulating. To be more consistent with the fitting approach, only values below d = 100 µm were used, and this value was considered the maximum tip-substrate distance, also used for the current normalization. Such selection allows the fitting to focus on the area where current values are decreasing due to the negative feedback.

The data from an example experimental PAC recorded over an insulator surface is presented in Figure 4-5 along with its fits produced using both Lefrou *et al.* Equations (4.5) and (4.6). The first simpler Lefrou *et al.* Equation (4.5) in (a) does not fit well as seen from the mismatching experimental (black squares) and analytical expression values (red line). Meanwhile, Equation (4.6) is more effective as shown by the greater overlap between the experimental and modelled data in (b) and obtained higher R^2 values. Hence, it was concluded that Equation (4.6) is more suitable than Equation (4.5) for interpreting the PACs generated in this work.

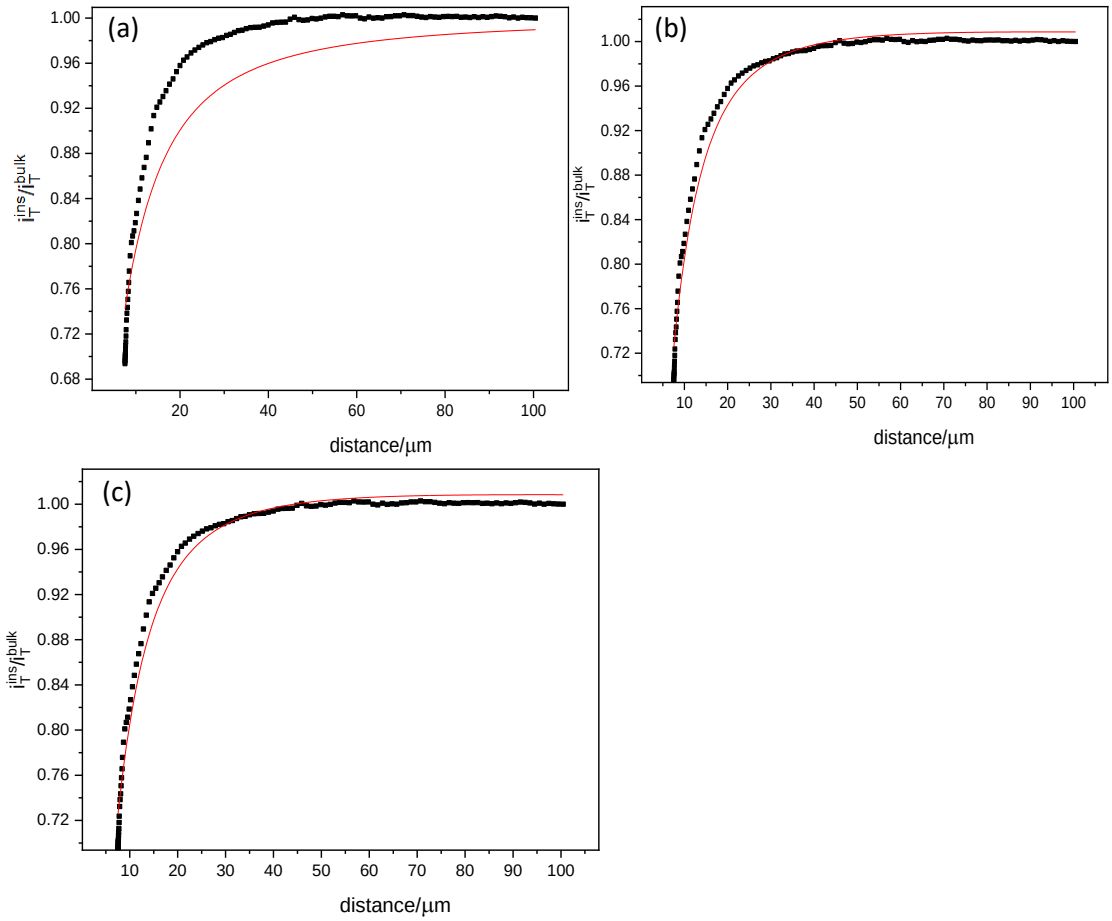

Figure 4-5. The PAC over an insulator surface (microdisc electrode) (black squares) fitted (red line) with (a) a simpler Equation (4.5) when R_g = 10, a = 5 were fixed values, resulting in R^2 = 0.898 and (b) the most recent Lefrou expression in Equation (4.6) when R_g = 10, a = 5 were fixed values and (c) only a = 5 was fixed, resulting in R_g = 9.83. PAC values were normalized to the specific for each PAC current value at d = 100 µm.

	Example 1		*Example 2*		*Example 3*	
	Fixed both variables		Fixed *a*		Fixed *Rg*	
Parameter	Value	Standard Error	Value	Standard Error	Value	Standard Error
x_{off}	0.187	0.00386	0.183	0.0149	0.180	0.012
R_g	*10*	*0*	9.825	0.620	*10*	*0*
a	*5*	*0*	*5*	*0*	4.923	0.115
R^2	0.985		0.985		0.985	

Table 4-6. Values and their standard errors generated from an experimental PAC fitting to Lefrou et al. analytical expression designed for an insulator PAC in Equation (4.6). Values in green and italics were fixed during the fitting process.

Next, data from fitting using the more recent Equation (4.6) was further evaluated. Initially, the experimental PAC data was fitted by fixing the parameters R_g = 10 and *a* = 5. This resulted in a successful iterative fit, as presented in Figure 4-5 (b) and a high R^2 value of 0.985, as shown in Table 4-6 (example 1). Then, the effect of allowing one of these parameters to be varied during the iterative fitting was explored, whilst keeping the other parameter fixed, thus allowing the varied parameter to be determined. Both parameters were examined in this way, and

generated values of R_g = 9.83 and a = 4.92 µm are close to the expected values of 10 µm and 5 µm respectively. The same high R^2 values of 0.985 were obtained, as shown in Table 4-6 (example 2 and 3). The quality of one of these fits can also be seen in Figure 4-5 (c). This confirmed that the fitting model was efficient for this type of data and it built confidence in using it for fitting COMSOL modelled data, shown in the following sections.

4.5.3 Positive feedback experimental data fitting using approximate analytical expression

Equivalent fitting using expression in Equation (4.7) was performed to the PACs over the middle of a microdisc electrode (r = 50 µm), known as a conductor surface. Again, it is enough to discuss only one PAC, such as in Figure 4-6, since it is expected that PACs above all conductor surfaces would be similar. In this case, the PAC data to the microdisc electrode was used.

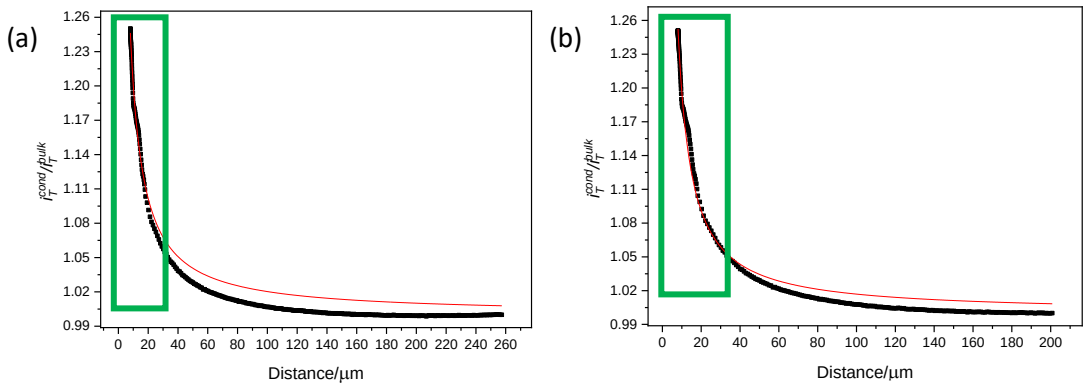

Figure 4-6. Experimental PAC over the middle of the micro electrode (black squares) fitted to Lefrou et al. analytical expression in Equation (4.7) (red line) when (a) R_g = 10 and a = 5 were fixed, resulting in R^2 = 0.987, and when (b) R_g = 10, generating a = 4.11 and R^2 = 0.992. Green box emphasizes that the fitting was the most effective at small d values.

	Example 1		*Example 2*	
	Fixed both variables		Fixed R_g	
Parameter	Value	Standard Error	Value	Standard Error
x_{off}	-2.006	0.0507	-0.0337	0.168
R_g	*10*	*0*	*10*	*0*
a	*5*	*0*	4.106	0.0768
R^2	0.987		0.992	

Table 4-7. Values and their standard errors generated from an experimental PAC fitting to Lefrou et al. analytical expression designed for a conductor PAC in Equation (4.7). Values in green and italics were fixed during the fitting process.

First, in Figure 4-6 (a), both R_g and tip radius parameters were fixed to their expected values of 10 and 5 µm, respectively, generating a fit with R^2 = 0.987, as shown in Table 4-7. This value is as high as in the above section, showing effectiveness of the fitting. However, a relatively poor fit was observed at >20 µm tip working distances from Figure 4-6 (outside the green box), unlike in the insulator data fitting. Then, it was evaluated if expected R_g = 10 and

a = 5 values were suitable for this data fitting, and one parameter at a time was fixed in the same way as for the insulator PACs. When R_g = 10 was fixed, the determined a value was 4±0.1, resulting in fitting in Figure 4-6 (b) and higher R^2 = 0.992 than in (a) (Table 4-7). When both R_g and a were allowed to vary within reasonable boundaries, the fitting model suggested values of 8 and 4, respectively. Together with relatively high associated errors, this reflects difficulty in fitting experimental data with Equation (4.7). The results of a = 4 and R_g = 8 suggest that the model did not fit experimental data well, and these values are outside experimental error from the expected values unlike in the insulator data fitting. There is motivation for a better equation to be used for fitting conductor data.

Interestingly, data from the expression seems not to reach the normalised current value of 1. This could suggest that longer distances are needed to achieve bulk current; however, it is unexpected to be true, especially since the normalization in both experimental and analytical expression data were effective in the insulator case when d = 100 µm. Then, either fitting to the conductor surface is overall more challenging due to reasons such as additional currents over the middle of the electrode than fitting to the insulator surface, or the approximate analytical expression in Equation (4.7) was not particularly effective for this data, or it is a combination of both. Most likely, this shows a limitation of the analytical expression (i.e. the accuracy becomes insufficient at larger values of d).

4.5.4 Evaluation of the positive feedback approximate analytical expression

Since experimental conductor data fitting with the latest Lefrou *et al.* expression in Equation (4.7) was not as effective as expected, it was further evaluated. The expression was used to generate normalized tip currents at several values of d, which were then compared with the values obtained from one of the first such positive feedback expressions presented by Mirkin in Equation (4.5)[15] and with numerically derived values using COMSOL (Section 4.4.3). It was evaluated if i_T^{cond}/i_T^{bulk} extracted from the analytical expressions differed from the COMSOL data.

In Table 4-8, six tip working distances and corresponding normalized tip current values are shown. The former in µm (used for COMSOL modelling) and dimensionless ratios L (used in the expressions) are shown in columns [1-2]. Normalized tip current values from COMSOL, Equation (4.3) and Equation (4.7) are shown in columns [3-5]. For comparison, normalised current values calculated from COMSOL were divided by i_T^{cond}/i_T^{bulk} values obtained from Equations (4.3) and (4.7) at each d to reflect the difference between the values from these analytical expressions in columns [6-7]. COMSOL values are in a better agreement with the ones from the latter equation, since the ratios in column 7 are on average 0.993 compared to 0.969 in column 6. The difference between COMSOL and Equation (4.7) values is less than

1% at all *d* values compared to more than 2% when comparing to the values from Equation (4.5).

Both expressions were designed for inlaid electrodes, while the electrodes used in this study and in the modelling were recessed by 0.5 µm. The above agreement with the COMSOL generated data suggests that such a recess for 100 µm edge length or diameter electrodes should not have significant impact on the measured current. This agrees with the previous measurements on recessed microelectrodes of this aspect ratio.[14] This allows the model to be kept as simple as possible, using the approximation for an inlaid electrode.

The above data comparison shows that even though Equation (4.7) did not fit the experimental PAC data well, especially at larger than 20 µm distances (Section 4.5.3), it seems to be a reasonable choice for fitting COMSOL data at smaller *d*. Thus, comparison of the results with those from the insulator data fitting is possible. Equivalent extensive comparison between analytical expressions for the insulator data was unnecessary since experimental data agreed well with the analytical expression values, and all COMSOL values were off by approximately 10%, suggesting that the initial *d* values employed require further refinement (Section 4.5.2).

1	*2*	*3*	*4*	*5*	*6*	*7*
d/µm	*L*	i_T^{cond}/i_T^{bulk} *COMSOL*	i_T^{cond}/i_T^{bulk} *Eq. (4.3)*	i_T^{cond}/i_T^{bulk} *Eq. (4.7)*	*COMSOL/Eq. (4.3)*	*COMSOL/Eq. (4.7)*
8.05	1.61	1.315	1.338	1.320	0.983	0.997
9.10	1.82	1.271	1.295	1.277	0.981	0.996
10.45	2.09	1.229	1.254	1.236	0.980	0.995
12.15	2.43	1.189	1.216	1.198	0.978	0.993
14.50	2.90	1.152	1.180	1.162	0.977	0.992
18.20	3.64	1.114	1.143	1.126	0.975	0.990
				Average	**0.979**	**0.993**

Table 4-8. Conductor PAC normalized final current values modelled using COMSOL and extracted using Equation (4.3) and Equation (4.7) (column 3-5) at six tip working distances (columns 1-2). COMSOL values were divided by the values from the two equations (column 7-8), showing that Equation (4.7) generated data more similar to COMSOL than Equation (4.3).

4.5.5 COMSOL generated values fitted to analytical expressions

Finally, COMSOL tip current values above an insulator and conductor surfaces modelled at several tip-substrate distances between 0.7-0.95i_T^{bulk} were plotted against *d*. More than three experimentally used values were modelled in both cases to have more data points for a more accurate line fitting, also allowing to extract smaller *d* values if needed. Data points were fitted using approximate analytical expressions in Equation (4.6) and Equation (4.7), tested in the above sections. If the COMSOL modelled values are effectively fitted, the real tip working distance values applicable to the experiments with a Pt probe, where a = 5 µm and R_g = 10, can be extracted.

The resulting graphs are presented in Figure 4-7. The fit was generally effective in both insulator and conductor cases, indicating good agreement between numerically simulated

data points and the models. High values of R^2 were obtained for the insulator (R^2 = 0.999) and conductor (R^2 = 0.993) surfaces. A slightly better correlation for the insulator case compared to the conductor can be attributed to errors in the analytical expressions which are accurate to within 1% and 2% for the insulator and conductor cases, respectively.[1] Closer inspection of the data in Figure 4-7 (b) shows that the fit deviates the most at higher *d* values (> 12 µm), which possibly relates to the presence of the electrode recess, which is not accounted for in the analytical expression. The insulator scenario may also be easier to model since it does not include complications due to diffusion field interactions between the two electrodes. Similar ineffectiveness of the model was present when fitting experimental conductor PACs in Figure 4-6 (Section 4.5.3), suggesting that Equation (4.7) was fine at shorter distances but it started deviate at larger distances.

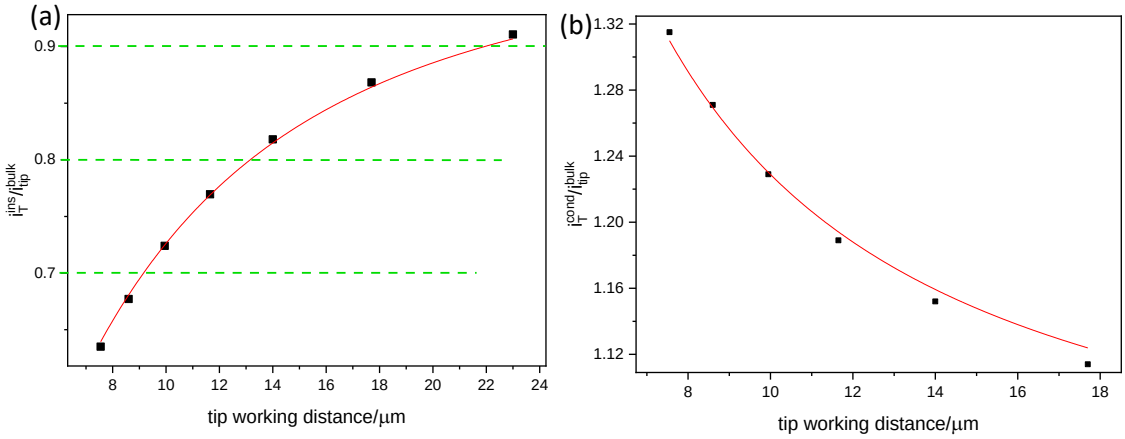

Figure 4-7. Normalized tip currents (black squares) at several d values (µm). Current values were numerically derived using COMSOL models (Figure 4-3) and were normalized to i_T^{bulk} = 0.638 nA. These values were fitted using approximate analytical expression in (a) Equation (4.8) for the insulator and (b) Equation (4.9) for the conductor surface. Experimentally used tip working distances were extracted from the fitting curves, where green dashed lines in (a) intercept with the red fitting curve.

Since the analytical expression for an insulator (Equation (4.6)) has been shown to be effective at all *d*, experimental tip working distances were extracted using this data. The green dashed lines in Figure 4-7 (a) indicate experimentally employed setpoints of $0.7i_T^{bulk}$, $0.8i_T^{bulk}$ and $0.9i_T^{bulk}$, which correspond to the tip working distances of 9.2 µm, 13.2 µm and 22.1 µm, respectively, found at the intersections between the red fitting line and horizontal green dashed lines. Since Pt substrate electrodes used in this work were recessed by 0.5 µm, the corresponding experimental values of *d* over the Pt region should in principle be adjusted to 9.7 µm, 13.7 µm and 22.6 µm, respectively. A full comparison of all *d* values in µm corresponding to tip bulk current fractions of $0.9i_T^{bulk}$, $0.8i_T^{bulk}$ and $0.7i_T^{bulk}$ encountered in this chapter is tabulated in Table 4-9.

d related to i_T^{bulk}	*d from Equation (4.3)/µm*	*d from Figure 4-7 (a) graph/µm*	*d from Figure 4-7 (a) plus recess for the conductor surface/µm*
$0.7i_T^{bulk}$	7.55	9.2	9.7
$0.8i_T^{bulk}$	9.95	13.2	13.7
$0.9i_T^{bulk}$	14.00	22.1	22.6

Table 4-9. Comparison of tip working distance values used in this chapter, when Pt tip of a = 5 µm and R_g = 10 was used.

4.6 CONCLUSIONS

Experimental and numerically modelled PACs were used to extract tip working distances in µm contributing towards the quantitative analysis of the SECM images discussed in the following chapters. Both insulator and conductor experimental PACs were as expected, showing increasing negative and positive feedback, respectively, with decreasing *d*. Negative feedback PACs were used to confirm reproducibility of the PAC experiment, as the recorded i_T^{bulk} was consistent within an experimental error at all times. Normalized final current values from such PACs also confirmed that the electronics were working as expected, stopping the probe when a set fraction of i_T^{bulk} was reached. Diffusion coefficient of 6.48×10^{-10} m^2 s^{-1} applicable to the experiments in this thesis was extracted using experimental data.

Final PAC tip current values above the insulator and conductor surfaces were numerically derived using COMSOL and normalized to i_T^{bulk} = 0.638 nA. The former values were 10% lower than the experimental ones at all *d*, mostly because the initial estimates for the currents based on the nominal setpoints were up to 10% too high. Experimental insulator PACs were fitted using the latest at the time approximate analytical expression, suggesting that the expression was also suitable for COMSOL data fitting at all selected *d* values. An effective overall fit was achieved, allowing determination of $0.7i_T^{bulk}$, $0.8i_T^{bulk}$ and $0.9i_T^{bulk}$ distances in µm (Pt probe, where *a* = 5 µm and R_g = 10) as 9.2 µm, 13.2 µm and 22.1 µm, respectively. When holding the tip above the electrode area, these values were adjusted to 9.7 µm, 13.7 µm and 22.6 µm, respectively, due to 0.5 µm electrode recess.

Fitting of the experimental conductor PAC was not as effective as for the insulator PAC. At *d* > 12 µm (equivalent to *L* = 2.4) current values from the selected approximate analytical expression did not show as effective agreement with the experimental values as at smaller *d*. The same expression was used for fitting a set of COMSOL derived values, and fitting was less effective than fitting to the insulator surface data. This suggests more analytical work is needed to understand and model conductor response, and possibly even another analytical expression might be required to ensure effective experimental conductor data fitting.

4.7 REFERENCES

1. Lefrou, C. & Cornut, R. Analytical expressions for quantitative scanning electrochemical microscopy (SECM). *ChemPhysChem* **11**, 547–556 (2010).

2. Polcari, D., Dauphin-Ducharme, P. & Mauzeroll, J. Scanning Electrochemical Microscopy: A Comprehensive Review of Experimental Parameters from 1989 to 2015. *Chem. Rev.* **116**, 13234–13278 (2016).

3. Kuss, S., Kuss, C., Trinh, D., Schougaard, S. B. & Mauzeroll, J. Forced convection during scanning electrochemical microscopy imaging over living cells: Effect of topographies and kinetics on the microelectrode current. *Electrochim. Acta* **110**, 42–48 (2013).

4. Lindsey, G., Abercrombie, S., Denuault, G., Daniele, S. & De Faveri, E. Scanning electrochemical microscopy: Approach curves for sphere-cap scanning electrochemical microscopy tips. *Anal. Chem.* **79**, 2952–2956 (2007).

5. Zhou, Q., Wang, Y., Tallman, D. E. & Jensen, M. B. Simulation of SECM Approach Curves for Heterogeneous Metal Surfaces. *J. Electrochem. Soc.* **159**, H644–H649 (2012).

6. Souto, R. M., Lamaka, S. V & González, S. Uses of Scanning Electrochemical Microscopy in Corrosion Research. in *Microscopy: Science, Technology, Applications and Education, A. Méndez-Vilas and J. Díaz (Eds.)* 1769–1780 (2010).

7. Filice, F. P., Li, M. S. M., Henderson, J. D. & Ding, Z. Three-Dimensional Electrochemical Functionality of an Interdigitated Array Electrode by Scanning Electrochemical Microscopy. *J. Phys. Chem. C* **119**, 21473–21482 (2015).

8. Dauphin-Ducharme, P. *et al.* Corrosion Product Formation Monitored Using the Feedback Mode of Scanning Electrochemical Microscopy with Carbon Microelectrodes. *J. Electrochem. Soc.* **162**, C677–C683 (2015).

9. Liljeroth, P., Johans, C., Slevin, C. J. & Quinn, B. M. Micro ring – disk electrode probes for scanning electrochemical microscopy. *Electrochem. commun.* **4**, 67–71 (2002).

10. Bartlett, P. N. & Taylor, S. L. An accurate microdisc simulation model for recessed microdisc electrodes. *J. Electroanal. Chem.* **453**, 49–60 (1998).

11. Woodvine, H. L. Development and Characterisation of Microelectrode and Nanoelectrode Systems. (The University of Edinburgh, 2012).

12. Ngamchuea, K., Eloul, S., Tschulik, K. & Compton, R. G. Advancing from Rules of Thumb: Quantifying the Effects of Small Density Changes in Mass Transport to Electrodes. Understanding Natural Convection. *Anal. Chem.* **87**, 7226–7234 (2015).

13. De Smet, L. C. P. M. *et al.* Diffusion in porous silicon: Effects on the reactivity of alkenes and electrochemistry of alkylated porous silicon. *Electrochim. Acta* **47**, 2653–2663 (2002).

14. Woodvine, H. L., Terry, J. G., Walton, A. J. & Mount, A. R. The development and characterisation of square microfabricated electrode systems. *Analyst* **135**, 1058–1065 (2010).

15. Mirkin, M. V, Fan, F.-R. F. & Bard, A. J. Scanning electrochemical Part 13. Evaluation microelectrodes microscopy size of the tip shapes of nanometer. *J. Electroanal. Chem.* **328**, 47–62 (1992).

16. Cornut, R. & Lefrou, C. A unified new analytical approximation for negative feedback currents with a microdisk SECM tip. *J. Electroanal. Chem.* **608**, 59–66 (2007).

5 SECM IMAGING OF SINGLE AND ARRAY MICRO ELECTRODES

5.1 INTRODUCTION

In this chapter, SECM images of Pt micro-fabricated single and array micro electrodes are evaluated and compared in terms of SG-TC and FB modes and several tip working distances used for imaging. Single electrode devices of interest were designed as a disc and square, of 100 µm diameter and a single edge length, respectively, and their images are discussed individually and then compared to each other, also evaluating differences between FB and SG-TC modes. Then, horizontal (H) (tip measurement along the x-axis of image, resulting from one tip scan) and V (tip measurement at selected x along the y-axis of the image, constructed from successive horizontal tip scans) middle line profiles across the electrode area extracted from these images. They are used for a further qualitative and semi-quantitative analysis of the imaging artefacts, such as sample tilting, convection and time-dependent tip currents, which repeatedly appear within data in this thesis. Such data analysis demonstrates that high fidelity and easy to handle micro electrodes are a suitable benchmark system for SECM probe response validation and method development and optimisation. As a further step to show SECM versatility for imaging different substrates, SECM images of array electrodes are also briefly introduced and discussed in terms of the expanding hemispherical diffusion field and its overlap by the neighbouring electrodes within the array.

5.2 SECM IMAGES OF SINGLE MICRO ELECTRODES

5.2.1 Qualitative analysis of SECM micro electrode images

In this section, SECM images of single microdisc and microsquare electrodes are qualitatively evaluated regarding image resolution and imaging related artefacts. All images were collected using a 10 µm diameter Pt probe with identical imaging settings (Section 3.5). Figure 5-1 shows (a) SG-TC and (b) FB mode images of microdisc and (c-d) microsquare electrode 2D images collected at the smallest experimentally used tip working distance of d = 9.2 µm ($0.7i_T^{bulk}$) (Section 4.5.5). In all images, the tip currents, as expected, were positive for FB mode and negative for SG-TC mode (as a result of the oxidation/reduction resulting from the potential applied to the tip[1]). For a direct comparison between the modes, the same colours for high and low magnitude currents in the colour map should be used, so the positive magnitude of the FB mode is used, using a modulus on the SG-TC mode currents.

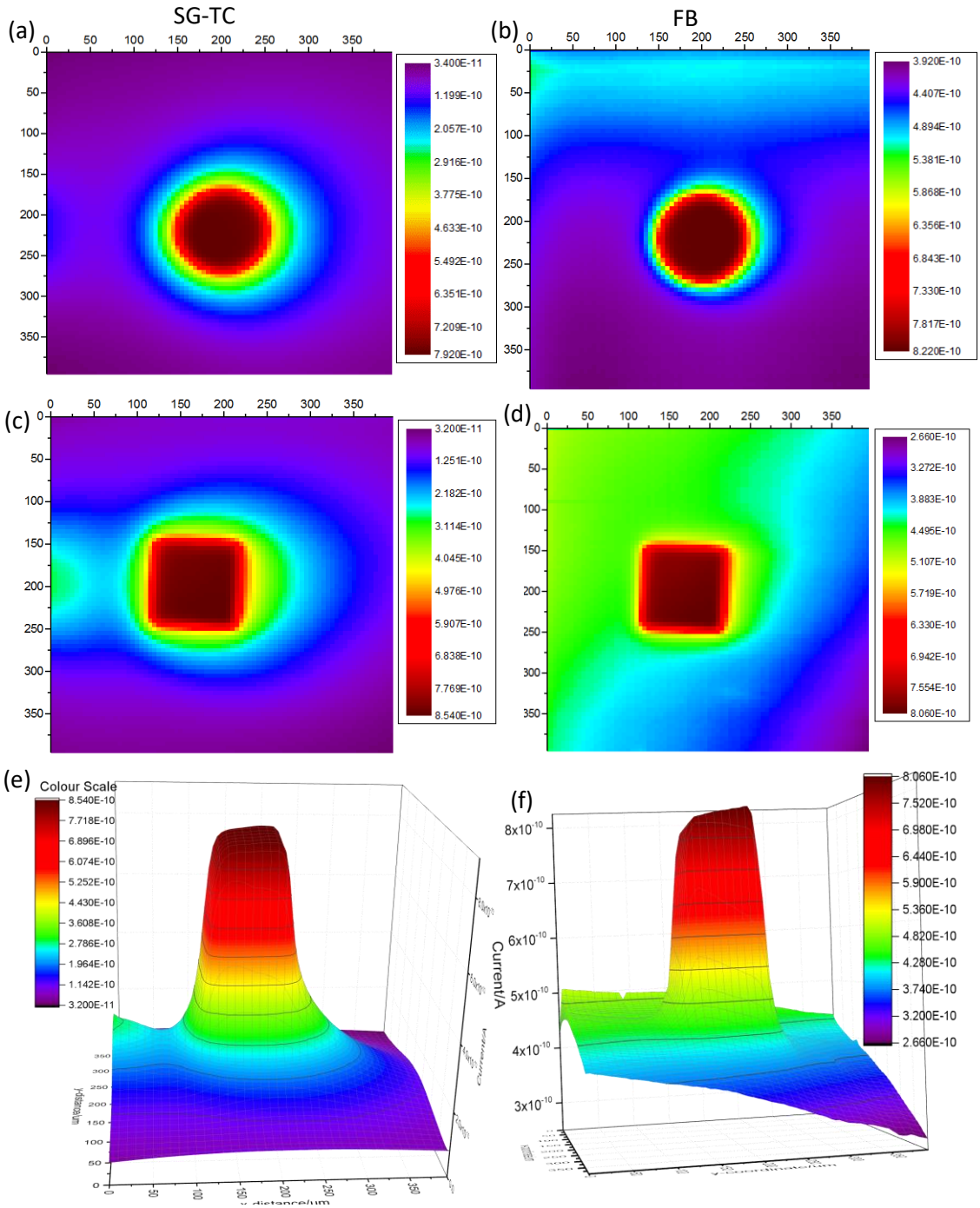

Figure 5-1. SECM 2D images over 400x400 µm area collected at d = 9.2 µm and containing micro electrodes in (a) disc geometry in SG-TC and (b) FB mode and (c) square geometry in SG-TC and (d) FB mode. (e) A 3D image of a microsquare electrode in SG-TC and (f) FB mode, generated using 2D images data to emphasize imaging artefacts. A current scale map is on the side of each image. (Note: current in SG-TC and FB modes are absolute tip currents in Amps for a direct comparison between the modes. Original SG-TC currents were negative.)

In all images in Figure 5-1, electrodes have well-defined geometry and uniform currents across the electroactive regions. An increase in tip currents, i_T, presented as a dark red colour, is observed over the microdisc/square electrode area, as expected due to an increase in positive feedback (Section 2.9.2). The insulator area, mostly presented as a blue/purple colour, around

the electrode is also uniform, with no visible pin holes, which would be a result of failed fabrication processes. It is clear from the images that there is some variation in current across the insulating regions of the sample, indicating the presence of imaging artefacts, which could be one of the following:

- Sample tilting resulting in a variable tip-substrate separation across the image;
- Convection effects caused by the tip dragging redox-active species along with it;
- Time-dependent tip currents resulting from gradual passivation of the tip electrode over time.

These imaging artefacts will be briefly identified from the images in this section and then discussed in a greater detail with more explanations using more images and extracted middle line profiles from these images throughout this chapter.

SG-TC mode images in Figure 5-1 (a, c) are evaluated first. The insulator area is mostly uniform, presented by a clear dominance of dark blue/dark violet colours, unlike in FB mode images discussed below. The spatial expansion of the hemispherical diffusion field is clearly reflected by circles of progressively lower currents, around the outside of the electrode area of the highest currents. As seen in the colour maps, the current decrease is gradual, eventually settling at the extremes of the surrounding insulator area at the top and bottom of the electrode area. At greater than 9.2 µm tip working distances, it is expected to see that the hemispherical features are visible to a greater extent, having larger circles of different currents surrounding the electrode area (Section 5.2.2).

In both SG-TC mode images in Figure 5-1 (a, c), the currents are higher on the left side of the substrate electrode than on the right. This is unlikely to be due to time-dependent tip currents, since current decay is not continuous across the entire image. The current increase only occurs at the beginning of the middle scan lines which pass through the micro electrode, so this observation likely results from convection. In SG-TC mode, an oxidation potential of +0.45 V is constantly applied to the substrate electrode so a diffusion field of $FcMeOH^+$ is established at the surface. Therefore, the probe, travelling above the substrate electrode, could be responsible for some of the $FcMeOH^+$ from this diffusion field being dragged from right to left during the probe's return to the left side in order to begin another scan line. Then, at the beginning of the next scan line some residual $FcMeOH^+$ remains, as reflected in a non-zero current which takes some time to settle.

These residual currents on the left side are higher in the microsquare than microdisc image and thus the currents take longer to settle before the probe reaches the electrode area. We attribute this difference to the larger total area of the 100 µm square electrode compared to the equivalent 100 µm diameter disc electrode area, which leads to a greater quantity of $FcMeOH^+$ being dragged along by the tip.

The diffusion field over the microsquare electrode itself is also perturbed by the probe's left to right movement, as indicated by the asymmetry of the electrode shape in the H-direction. This is thought to be due to $FcMeOH^+$ being dragged along with the tip during scanning, resulting in a current "tail" to the right hand side of the electrode. Such asymmetry is expected to be more apparent from the line profile analysis presented later in this chapter.

FB mode images of microdisc and square electrodes are also compared in Figure 5-1 (b, d). Horizontal line profiles of higher currents (light blue) compared to the surrounding insulator surface (violet) were recorded at the top part of the disc image in (b). These higher currents are present until approximately 100 µm from the electrode top but, importantly, the currents settle before the electrode area and do not seem to affect it. The fact that the current eventually stabilises suggests that in this case the tip current experienced a time-dependent artefact, in which the tip current decays over time. The cause of such effects is unclear but may relate to the tip electrode passivation either due to chemical contaminants in the solution, or physical contaminants (e.g. dust particles) picked up from the substrate surface by the tip.

Convection effects in FB mode are less significant than in SG-TC mode. Although, some evidence of solution dragging is indicated by the fact that the electrode in Figure 5-1 (b) is not perfectly round (green and light blue circles). This difference is to be expected: in FB mode, the oxidation potential is constantly applied to the tip and so the measured current reflects the overlap of the tip and the substrate diffusion fields. When the tip is not present, there is no electrochemical process happening at the electrode, so there is no diffusion field for it to disturb. As a result, the same colour was seen immediately surrounding all the electrode area, unlike in SG-TC mode, where Figure 5-1 (c) is a great example.

The microsquare FB mode image in Figure 5-1 (d) is affected by an artefact that does not exhibit the character of convection and time-dependent tip currents. The insulator surface appears almost diagonally divided in two, having higher currents, presented as green colour, on the left and lower currents, presented as shades of blue, on the right. From this it appears that the left side is further away from the probe, resulting in higher currents due to a more available space for the redox species to diffuse between the probe and the substrate, hence less negative feedback over the insulator surface. The right side is then closer to the tip than the left side, hence lower currents over the insulator area. Therefore, it is suspected that some sample tilting, further discussed throughout this chapter, is present in microsquare FB mode image in Figure 5-1 (d), resulting in different currents on the top left and bottom right of the image.

In both modes, microsquare electrode images are more affected by the imaging artefacts, which are further highlighted in the equivalent 3D images. The SG-TC mode microsquare image in Figure 5-1 (e) emphasizes higher currents on the left side of the image due to convection. The insulator surface overall is uniform but additional currents are also visible

towards the right side of the image and to some extent towards the right side of the peak. These effects are smaller over the electrode area than over the insulator area immediately surrounding the electrode, resulting in a slightly distorted cone base in the 3D image in (e). Meanwhile, the FB mode 3D image of a microsquare in Figure 5-1 (f) clearly confirms a tilting artefact.

Overall, all SECM FB and SG-TC mode images of microdisc and square electrodes are prone to different imaging artefacts, occurring to different extent. However, all images are of high resolution and data from them are used for the semi-quantitative analysis in the following sections.

5.2.2 Effect of tip working distance on image resolution and artefacts

Some of the above discussed imaging artefacts as well as image spatial resolution can also be evaluated as a function of the tip working distance. Microdisc and microsquare electrodes were imaged using three tip working distances, presented as tip bulk currents of $0.7i_T^{bulk}$, $0.8i_T^{bulk}$ and $0.9i_T^{bulk}$ which from Section 4.5.5 are known to correspond to the distances of 9.2 µm, 13.2 µm and 22.1 µm, respectively. In Figure 5-2 and Figure 5-3, electrode images in FB and SG-TC modes collected at these tip working distances are presented on a uniform current scale, derived for each set by choosing the smallest and the greatest current values from across the three images. These images are of a different colour scheme than in Figure 5-1, in which the images were constructed using different software (Origin). It was decided that these original images, extracted directly from the SECM imaging software, effectively convey the message of this work and so this method of data presentation was adopted for the remainder of this thesis.

All images in Figure 5-2 and Figure 5-3 present clear and expected trends. With increasing tip working distance (left to right), the spatial resolution of the micro electrode gradually decreases, reflecting diffusional broadening deeper into solution. This fading is more gradual in SG-TC than in FB mode, which is more sensitive to changing *d*, as established in qualitative image evaluation in the above section. Resolution of the electrode geometry remains clear in all cases, but at the largest tip working distance the current contrast is the poorest, as expected. In FB mode the current measured over the insulator region increases with increasing *d*, which reflects the fact that less negative feedback is experienced at longer tip working distances. In contrast, in SG-TC mode the current over the insulator region appears to be constant since this is expected to be close to zero irrespective of working distance. This effect is further evaluated in Section 5.2.3.

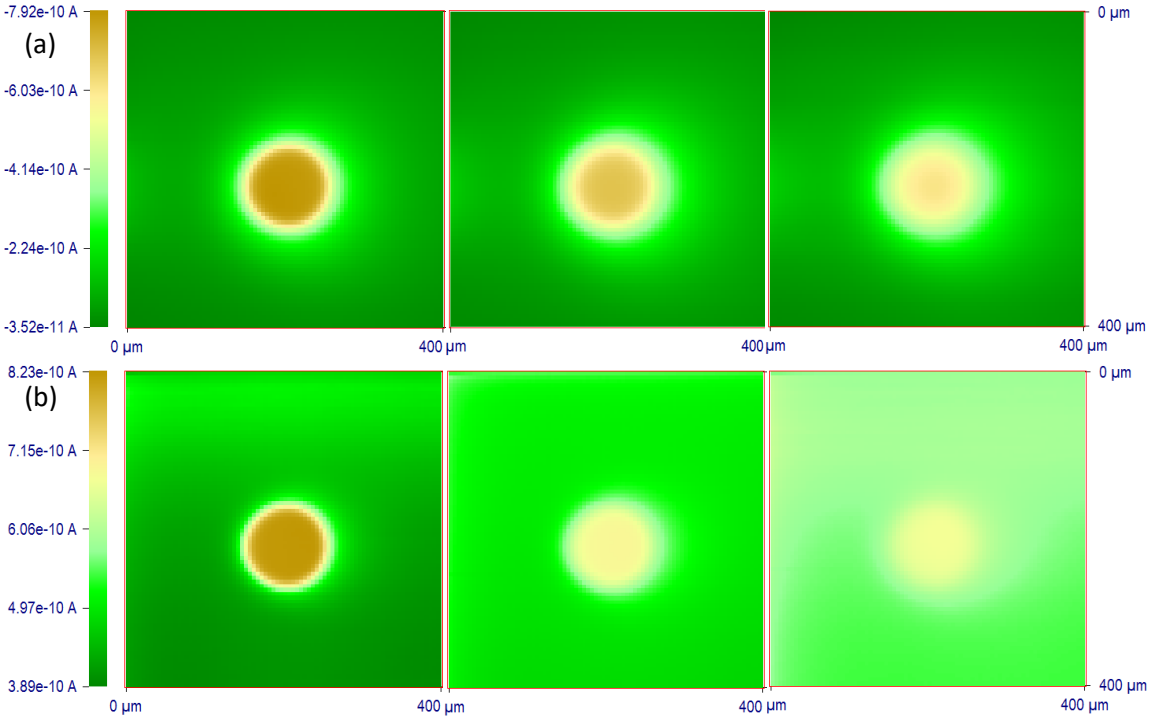

Figure 5-2. SECM images of microdisc electrode at $0.7i_T^{bulk}$, $0.8i_T^{bulk}$ and $0.9i_T^{bulk}$ tip working distances increasing from left to right in (a) SG-TC and (b) FB modes. In each mode, the images were placed on a uniform current scale, derived from the three images when selecting the overall lowest and the highest current values in that set.

There are some differences in the observed convection effects of these SECM images of the different geometry electrodes. In Figure 5-2, convection effects in SG-TC mode are minimal and constant over the microdisc electrode area at all *d*, while in FB mode on the left side of the image together with time-dependent tip currents at the top part of the image become the most significant to the image collected at $0.9i_T^{bulk}$. In the microsquare electrode images in Figure 5-3, convection artefacts in the SG-TC images appear more apparent. The extent of the convection effect appears to increase with increasing *d*. In Figure 5-3 (a), the tip movement effect from left to right is significantly more pronounced in $0.8i_T^{bulk}$ and $0.9i_T^{bulk}$ images, resulting in a diffusion field over the electrode that appears rather elliptical in the horizontal direction. Currents on the left side of the H scan lines which pass through the electrode area are also higher at $0.9i_T^{bulk}$ than at $0.7i_T^{bulk}$, again due to more significant convection effects at longer tip working distances. This is possibly because a small gap between the tip and the sample restricts the convective flow introduced by the tip movement, so the diffusion field appears less distorted.

In FB mode, significant convection effects are absent at all tip working distances, as discussed above, confirming that this mode is less sensitive to solution dragging or displacement. However, the images in Figure 5-3 (b) indicate tilting, presented as higher currents towards the top left and lower currents towards the bottom right side of the image, in the $0.7i_T^{bulk}$ and $0.8i_T^{bulk}$ images, but at $0.9i_T^{bulk}$ the insulator surface appears more uniform. This suggests that

the extent of tilting was relatively small compared to the imaging distance, hence still allowing collection of both high quality and resolution SECM images.

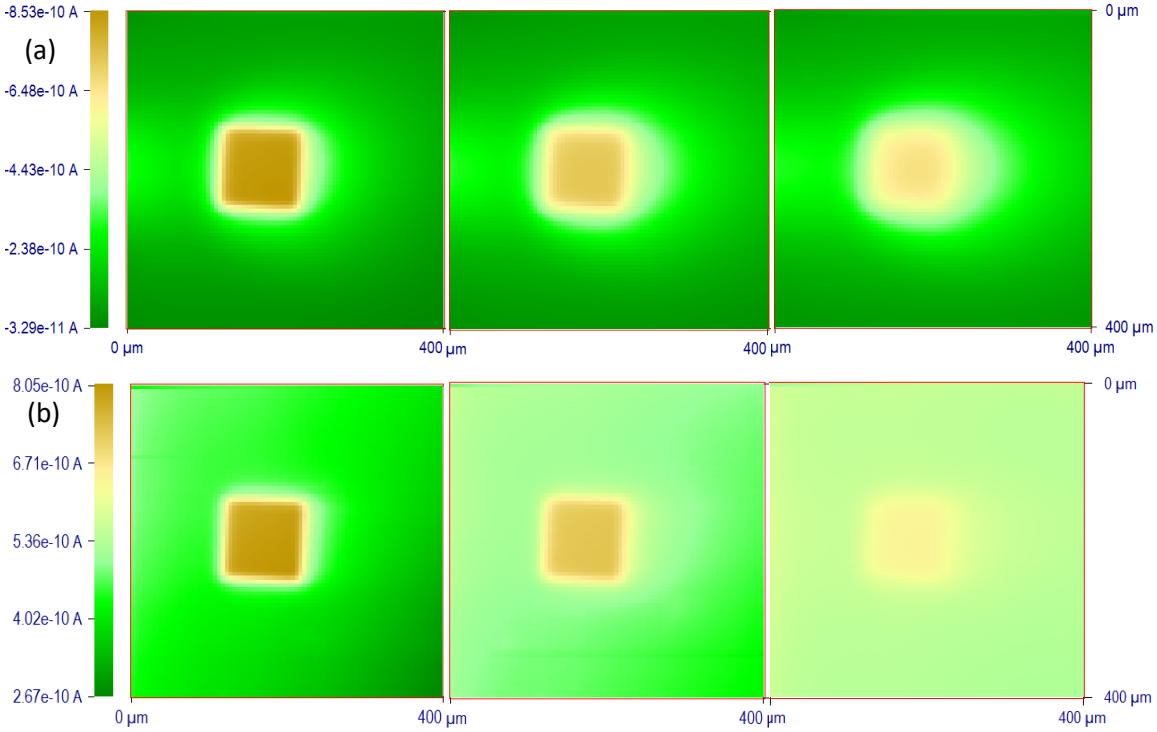

Figure 5-3. SECM images of microdisc electrode at three tip working distances of $0.7i_T^{bulk}$, $0.8i_T^{bulk}$ and $0.9i_T^{bulk}$ increasing from left to right in (a) SG-TC and (b) FB modes. In each mode, the images were placed on a uniform current scale, derived from the three images when selecting the overall lowest and the highest current values in that set.

5.2.3 Semi-quantitative horizontal middle line profile analysis

Having discussed micro electrode image spatial resolution and a variety of the artefacts present in these SECM FB and SG-TC mode images, semi-quantitative analysis follows. H line profiles going through the middle of the electrode were extracted from the images collected at three tip working distances ($0.7i_T^{bulk}$, $0.8i_T^{bulk}$ and $0.9i_T^{bulk}$) and are plotted in Figure 5-4. The middle line profiles were chosen deliberately to have as much symmetry as possible for a more simplified analysis. Current values were relatively normalized, dividing each value by the smallest current value at the top part of the image, before the electrode area was reached, i_{min}. In SG-TC mode, the tip is constantly biased at a reducing potential (0 V), resulting in close to zero current value in the original image. In contrast, in FB mode an oxidizing potential (+0.45 V) is constantly applied to the tip, resulting in a diffusion limited current value resulting from the oxidation of FcMeOH. As a result, i_{min} in FB mode is significantly greater and normalized tip current in FB mode is on average 3.85 times smaller than in SG-TC mode.

In Figure 5-4, H central line profiles at three *d* values for a microdisc in (a-b) and a microsquare electrode in (c-d) in both modes are presented. As expected, currents over the middle of the

electrode increase with decreasing tip working distance, as a result of the increasing positive feedback over the conductor area. This corresponds to the highest contrast and definition, also observed from the qualitative SECM images analysis. For both microdisc and microsquare electrodes the diffusion field begins to exhibit hemispherical shape with increasing *d*, as indicated by the more pronounced rounding of the current in the middle of the electrode. This agrees well with the literature[2,3], which suggests that the diffusion field evolving from both geometry electrodes should be hemispherical.

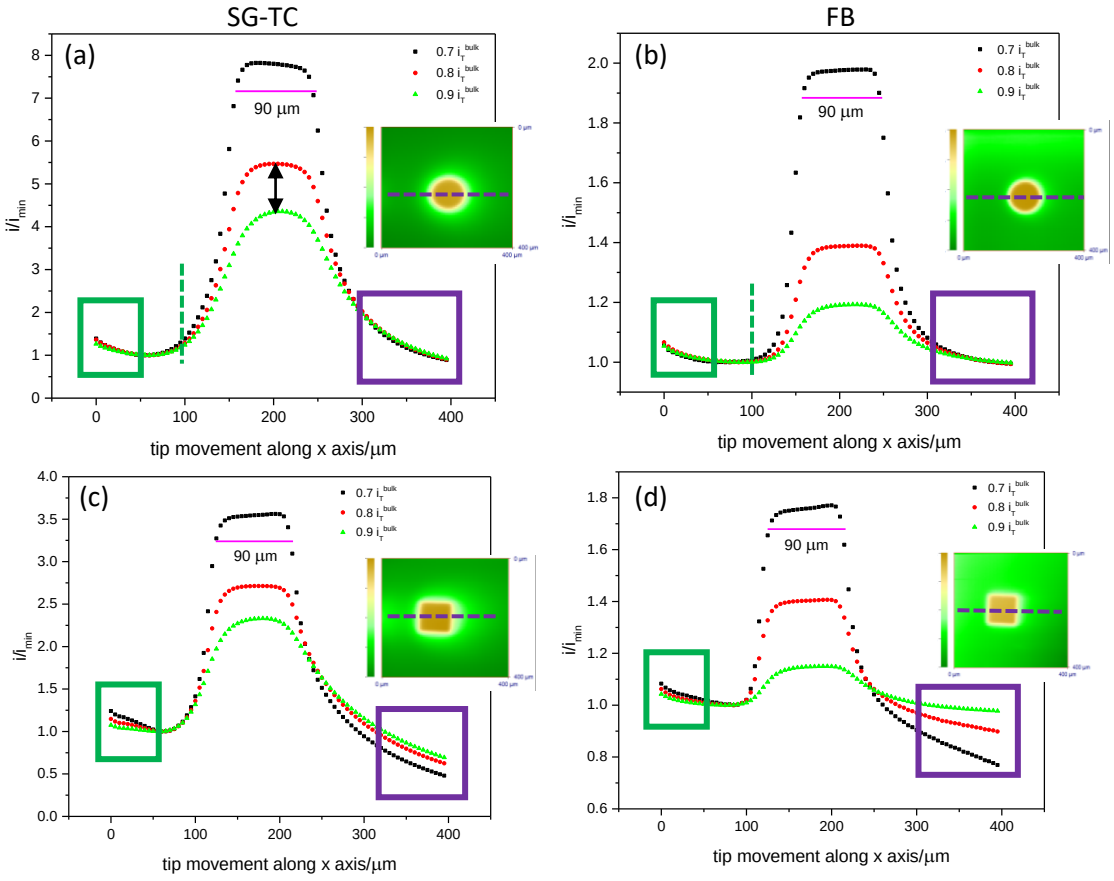

Figure 5-4. H middle line profiles through micro (a) disc electrode in SG-TC and (b) FB modes and (c) square electrode in SG-TC and (d) FB modes at tip working distances of $0.7i_T^{bulk}$, $0.8i_T^{bulk}$ and $0.9i_T^{bulk}$ presented as black squares, red circles, and green triangles, respectively. All currents were normalized to i_{min} and 90 µm pink bar measures peak width over the flat top of the peak. Inserts are electrode SECM images, having a dashed line representing a line profile across the middle. V green dashed lines in (a-b) mark 100 µm on x axis allowing to compare initial line profiles between the modes. Green and purple boxes mark the beginning and end of the line profile for the discussion in text. Black V double-headed arrow in (a) emphasizes difference in magnitude between the two lines.

Even though electrode diameter or edge length was 100 µm, at the shortest working distance, the flat top of maximum enhanced current over the electrode itself was approximately 90 µm wide, as marked in each graph in Figure 5-4. The slightly smaller measured value can be explained by considering the two electrodes in the imaging set-up. The probe electrode of 10 µm diameter is above the substrate electrode of 100 µm critical dimension and the probe is

moving horizontally in 5 µm increments. For the full enhancement of the current the whole probe electrode needs to be directly above the substrate. Thus, for 5 µm on both sides of the substrate electrode the maximum current may not be reached, resulting in a total apparent substrate width of 90 µm.

When comparing middle line profiles from microdisc images in SG-TC and FB modes in Figure 5-4 (a-b), at all imaging distances FB mode in (b) provides line profiles of sharper corners. This is because SG-TC mode is recording the hemispherical diffusion profile established at the substrate electrode, while FB mode represents the overlap of the tip electrode diffusion field with the substrate electrode, and thus to a greater extent captures features of the substrate. This is also visible from microsquare middle line profiles in Figure 5-4 (c-d). The differences of the two line profile (flat top) edges are relatively small at $0.7i_T^{bulk}$ and $0.8i_T^{bulk}$ but at $0.9i_T^{bulk}$ the peak in SG-TC mode in (c) is significantly more rounded than in FB mode in (d).

Then, from all graphs in Figure 5-4, the magnitude of the FB response is clearly more sensitive to the tip working distance than in SG-TC mode. When comparing the gap between two neighbouring lines (V black arrow in (a)), such as $0.7i_T^{bulk}$ and $0.8i_T^{bulk}$ as well as $0.8i_T^{bulk}$ and $0.9i_T^{bulk}$, the drop in the peak currents with increasing *d* is more substantial in FB mode. In this mode, the flat top is also becoming considerably smaller and less distinctive at greater *d*, while in SG-TC mode all tops are relatively well defined and significantly further away from emerging into a line (due to low peak currents). This effect in FB more is exaggerated as a result of normalization and plotting all three line profiles in one graph, yet it still presents the mode being more sensitive to varying *d.* More differences between the graphs are present, but they are related to imaging artefacts and hence are discussed in the following sections.

5.2.4 Comparison of imaging artefacts in horizontal middle line profiles

The images presented thus far are broadly as expected. However, there are subtle observations that encourage further discussion about possible imaging artefacts in FB and SG-TC modes already briefly initiated in the above sections. Various phenomena, such as image sharpness depending on the mode, sample tilt, time-dependent tip currents or convective effects are discussed in this section in a greater detail using Figure 5-4 and referring to Figure 5-1.

To start with, in SG-TC mode, the “baseline” current over the insulator regions should be 0 nA. However, in the images, this baseline was always greater than zero, and was approximately 0.067 nA on average (calculated from (0;0) coordinate). This is due to trace amounts of $FcMeOH^+$ present in bulk solution, presumably from oxidation during extensive imaging experiments or from areal oxidation by dissolved oxygen. The extent of this oxidation is presumed to be relatively small so that baseline current is constant, but even small changes in this could have an impact on the normalised current.

Then, from Figure 5-4 (a-b), the flat top of the current maxima at $0.7i_T^{bulk}$ in the two modes are different. In SG-TC mode, the left side of the microdisc peak is visibly of higher currents, while in FB mode the right side is of only slightly higher currents. Fabrication-related artefacts are not likely to be present, as discussed in the Introduction. Tilting could have slightly affected the LHS which would be closer to the tip resulting in a more positive feedback. However, usually such tilting would also result in the insulator surface on the left side being presented as lower currents than the right side due to a greater negative feedback. However, this was not the case.

This artefact most likely reflects slight differences in the convection effects in FB and SG-TC modes (Section 5.2.1). In FB mode in Figure 5-4 (b), left to right probe's movement may have resulted in subtle convection effects and hence slightly higher currents on the right side of the peak. But convection is minimal on the left side of the line profile (beginning of each line profile within the green box area), as also seen in Figure 5-1. In SG-TC mode in Figure 5-4 (a), the residual currents at the beginning of the H line profiles may be the cause for the higher currents on the left side of the peak. In other words, the current may not have fully settled to the baseline value before the electrode area in SG-TC mode. In FB mode, as discussed above, these effects are minimal.

The convection artefact in the microsquare data in Figure 5-4 (c-d) is also evaluated. In SG-TC mode in (c), there is more current variation and disturbance in the measured signal at the beginning of the line profile (area within the green box). This reflects decreasing convection effects with the increasing tip working distance. As discussed in Section 5.2.2, from the images it looks like convection gets worse with increasing tip working distance, whereas the residual currents appear higher in the line profiles for the shorter working distances. This is probably because in the images the residual currents appear small compared to the electrode size (L = 100 µm).

In Figure 5-4 (c-d), the right side of the line profile (area within the purple box) is of lower currents than the left side (area within the green box), showing significant current decrease from left to right. This absence of symmetry is likely to be due to sample tilting, because in FB mode the positive feedback current over the electrode slightly increases from left to right, consistent with a decrease in tip-substrate separation. The difference between the ends of the line profiles (purple box) also varies to a greater extent in FB than SG-TC mode, since FB mode is more sensitive to tip-surface separation and hence more susceptible to tilting effects.

5.2.5 Convection evaluation from horizontal and vertical middle line profiles

In this section, convection is evaluated by comparing middle line profiles in both H and V directions from both microdisc and microsquare electrodes in FB mode. This mode has been shown to generate more electrode features rather than hemispherical diffusion field as well as

to be more sensitive to the variation of the tip working distance. Since the probe scanned the substrate surface from left to right (horizontally), it is expected that convection artefacts should be minimized in V middle line profiles extracted from the images. This comparison therefore allows a better assessment of convection effects, which have been shown to be more subtle in the case of FB mode. In Figure 5-5, an arrow in (a) indicates the start of the peak, which corresponds to the electrode area, and numbers 1-2 mark the end of the electrode area in V (red) and H (black) line profiles, respectively, from microdisc in (a) and microsquare electrode in (b).

From both graphs in Figure 5-5, convection effects are observed in the H line profile. At position 1, the line is narrower and more symmetric (resembling the LHS of the line profile) than at position 2, indicating that the V middle line profile is indeed significantly less affected by convection artefacts. The H line profile at position 2 exhibits a current "tail", as discussed above, which suggests that the left-to-right movement of the probe is stirring the electrolyte solution in the gap between the tip and the substrate, leading to additional current measured at the tip. The difference between V and H lines at x = 320 in (a), when the difference is the greatest, is 0.024 nA, approximately 4.7 %. This may be used as an approximate measure of how much convection is involved in this set of data.

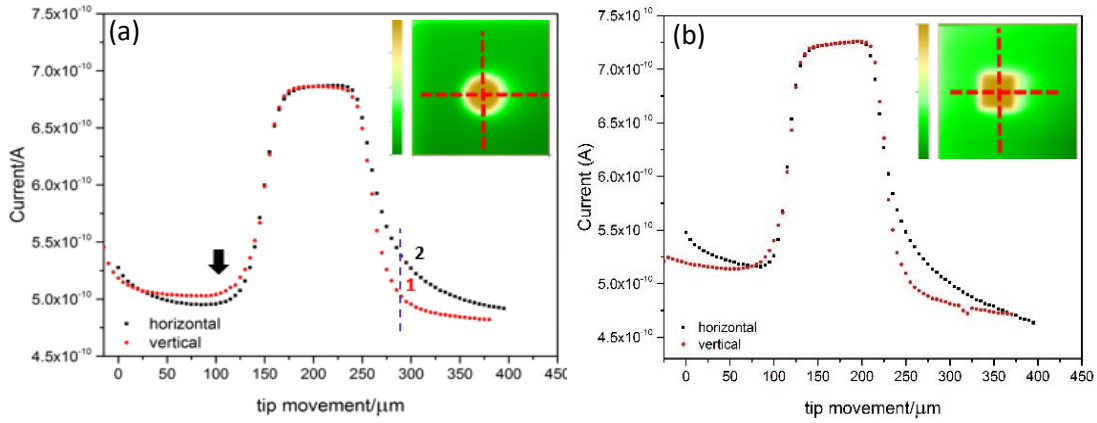

Figure 5-5. H (black) and V (red) middle line profiles from SECM images (inserts) of the (a) microdisc (V dashed line marks x = 320 µm) and (b) microsquare electrodes, both imaged in FB mode at d = 13.2 µm. Inserts contain red dashed lines representing middle line profiles; V black arrow and numbers 1-2 in (a) mark areas of focus for comparison between the two line profiles to evaluate convection effects.

The sample tilt has been discussed and mentioned in almost every section thus far. Yet the most obvious example is evident in microsquare data in Figure 5-5 (b). The negative FB current baseline decreases from left to right, whilst the positive FB in the middle of the electrode shows an increase from left to right in both, H and V, middle line profiles. This indicates that sample tilting is present in both x and y directions of the image. During the set-up of the experiment this artefact is, of course, aimed to be minimized, but in this case it was not removed completely.

Overall, the direct comparison of H and V middle line profiles for the same substrate, imaging mode and tip working distance has provided a convenient means to evaluate the extent of convection effects. This approach will be used in the following results chapters to establish if convection effects vary when changing substrate, probe or imaging settings.

5.2.6 Construction of a conductor approach curve from SECM images

Quantitative analysis of the currents recorded over the conductor was achieved by using the currents recorded at the three different *d* to construct a quasi-PAC (analysis shown in Table 5-1). From each image a current value over the middle of the electrode was normalized to i_T^{bulk}, extracted using one of the current values over the insulator surface at the beginning of the image and the tip setpoint value. The very first current value at (0;0) has been observed from the SECM images as always being higher than expected and the rest of the current values over the insulator surface due to the tip current conditioning effects. Therefore, currents at (0;50) coordinate (H scan line) from 400×400 µm images were used for this purpose. The tip at this location is relatively far away (in x- and y-axis) from the substrate, and so higher currents due to the influence from the hemispherical diffusion field from the electrode are expected to be non-existent or minimal. However, current variation across the image provides additional challenges when deciding which experimental current value should be used for the most effective current normalization. Depending on which value was used, normalized current value will change.

i_T^{bulk} *setpoint*	i_T *at (0;50) coordinate*	*Extrapolated* i_T^{bulk}	i_T *from the SECM image/nA*	i_T / i_T^{bulk}	*d/µm*	i_T *from Equation (4.7)*
0.7	*0.470*	0.671	0.821	1.223	9.7	1.257
0.8	*0.545*	0.681	0.687	1.009	13.7	1.173
0.9	*0.598*	0.665	0.673	1.013	22.6	1.099

Table 5-1. The values of i_T over the middle of the microdisc electrode from SECM images at three i_T^{bulk} setpoints. These values were normalized to i_T^{bulk} extracted from i_T at (0;50) coordinate from the SECM images. Equivalent i_T values at selected d (Section 4.5) were extracted from Equation (4.7).

Therefore, such experimental data taken from the SECM images allows to construct a quasi-PAC, which contains several differences from the typical PAC current values. In addition to unclear normalization tip current, the tip instead of being gradually brought towards the substrate at slow velocity like in PAC experiments was doing work (imaging the substrate). This means that some additional imaging artefacts, such as convection, are present to a more significant extent. These steps reflect how many variables there are to be considered, when constructing a PAC from experimental imaging data.

For comparison, Table 5-1 also contains tip current values for the conductor surface extracted from the approximate analytical expression in Equation (4.7). Normalized i_T values from Table 5-1 together with the actual experimental conductor PAC are plotted in Figure 5-6, allowing a

comparison of the quasi-PAC, the true PAC and the theoretical PAC. Only normalized experimental current values at distances <90 µm are shown, since the other two sets of data contain values within a narrow *d* range. As shown in Chapter 4, experimental PAC data agrees with the values derived from the approximate analytical expression at short distances. However, the difference between these and the quasi-PAC is small only at the smallest *d*. the other two data points are significantly off-set from both experimental and analytical expression data. This reflects that conductor data is more challenging to model and compare with the experimental data extracted in such a way.

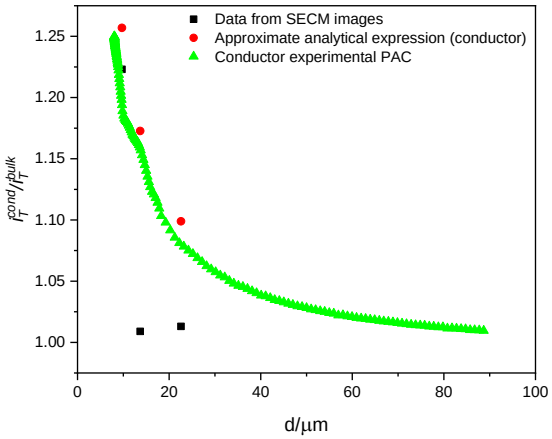

Figure 5-6. Comparison of normalized tip current values from: SECM images (quasi-PAC) (black squares) and approximate analytical expression derived for the conductor surface (theoretical PAC) (red circles) at three d values as well as experimental conductor PAC (green triangles) at d<90 µm.

5.3 ARRAY CHARACTERISATION USING SECM

To further show versatility of the SECM technique, some of the array electrodes were characterised using SECM. This work is the first to characterise such in-house Pt micro fabricated array electrodes[4] in terms of their localised electrochemical performance in solution during redox reactions. Two types of Pt electrode arrays were examined: hexagonal (honeycomb) and square arrangement arrays. In the first case, each disc electrode is 30 µm diameter and the electrode arrangement is hexagonal so that the centre-to-centre electrode separation is 100 µm or the edge-to-edge distance is 70 µm to all neighbours. A large area close to the edge of the array and an area of eight electrodes which are close to but not at the edge were imaged using SECM FB and SG-TC modes. The scanning scan speed was varied either by changing the increment size (step size) between 2 and 5 µm or the increment time from 0.05 to 0.1 s, and the tip working currents (distances) of $0.6i_T^{bulk}$ and $0.7i_T^{bulk}$ were used. The second array consists of microsquare electrodes of 30 µm edge length, *L*, where the separation between the nearest neighbours from centre-to-centre is 120 µm (edge-to-edge separation of 90 µm) and between the diagonal neighbours the distance (centre-to-centre) is approximately 170 µm. Images were collected at increasing tip working distance over a large

area of electrodes, over nine and two electrodes. All of this allows evaluation of image resolution and artefact occurrence upon variation of imaging settings and diffusion field overlap from individual electrodes in FB and SG-TC modes at different tip working distances for both array types.

5.3.1 Effect of imaging settings on a hexagonally arranged microdisc array spatial resolution

First, the hexagonally arranged Pt microdisc electrode array is evaluated through SECM images of a large area of 500×500 µm over the edge electrodes in SG-TC and FB modes at $0.7i_T^{bulk}$ imaging current, as shown in Figure 5-7. The electrodes are again clearly localised, of the expected size and separation and surrounded by a uniform insulator surface, indicating that good spatial resolution SECM images of the electrodes within the array were obtained, just like the individual electrode images in Section 5.2. Also, the diffusion field overlap at this hexagonal electrode array at this distance appears to be minimal. A hemispherical diffusion field is to some extent observed as pale green circles surrounding the electrodes, but they do not appear to reach the field of the neighbouring electrode.

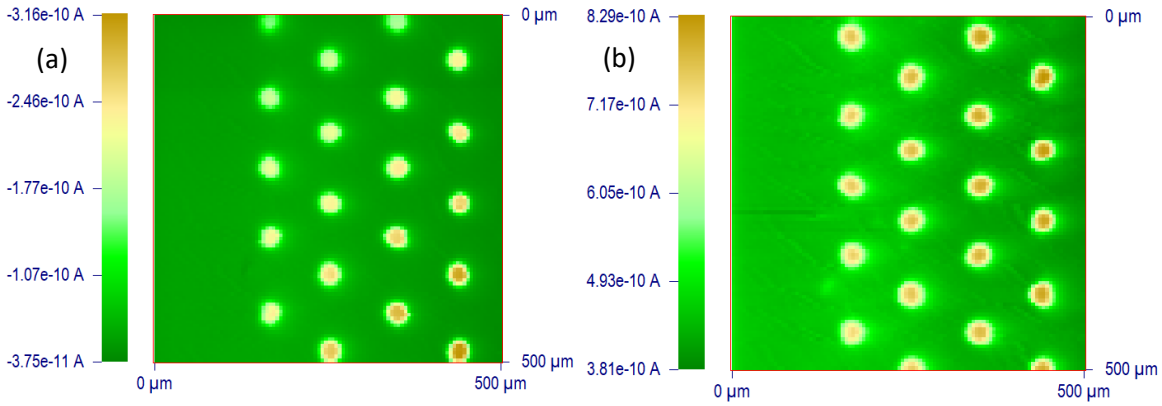

Figure 5-7. SECM (a) SG-TC and (b) FB mode images of edge electrodes over 500×500 µm area at $0.7i_T^{bulk}$. Microdisc electrode array of r = 15 µm, 70 µm side-to-side spacing. Long move x, max increment 1 µm, 5µm step, 0.5 s step time, 10 s quiet time.

In SG-TC mode image in Figure 5-7 (a), some tilting is observed. The electrodes at the bottom right of the image appear more active (indicated by their darker brown colour) than the electrodes at the top left of the image, which are more blurred and of lower currents. Furthermore, the electrodes on the right side seem to be slightly higher in current than on the left. This would suggest that the bottom right was slightly closer to the probe during imaging, resulting in a greater positive feedback (Section 2.9.2). Alternatively, such a current variation could be a real reflection of the electroactivity of the electrodes, in which some variation may

be possible due to passivation of the surface. However, in this case, the current variation is not random but shows a gradual change, hence a tilting artefact is more likely.

Meanwhile, FB mode equivalent image in Figure 5-7 (b) was collected after the substrate was realigned in order to fix the tilting. As a result, the imaged electrodes are mostly uniformly active and only minor current variations are present. Electrodes on the right remain slightly more active than the ones on the left; however, the extent of differences is smaller than in Figure 5-7 (a). In addition, as major tilting has been fixed, convection effects due to probe's movement to the right are also now observed in this image, indicated by the horizontally distorted diffusion field, similar to those seen for single electrodes (Section 5.2). It is also worth noting that in this image some features are observed on the insulator regions, highlighting the sensitivity of this mode to surface topography.

Images of a smaller area of 260×260 µm containing only eight electrodes were collected using a variation of imaging settings to further evaluate image spatial resolution in both modes and diffusional overlap effects. Over a larger area subtle changes might be less visible; hence the smaller area was used. From SG-TC images collected at $0.6i_T^{bulk}$ and $0.7i_T^{bulk}$ in Figure 5-8, electrodes in both images are sharp and well localized, with their diffusion fields not overlapping with the neighbour diffusion fields, nor visibly distorted by the convection. At the bottom of the V middle row, there is a hint of the ninth electrode, suggesting that SG-TC mode captures hemispherical diffusion field to a great extent, hence the diffusion field from an additional, not fully imaged electrode is sensed. In this mode it is expected to see broader diffusional fields than in FB mode, just like from a single electrode imaging.

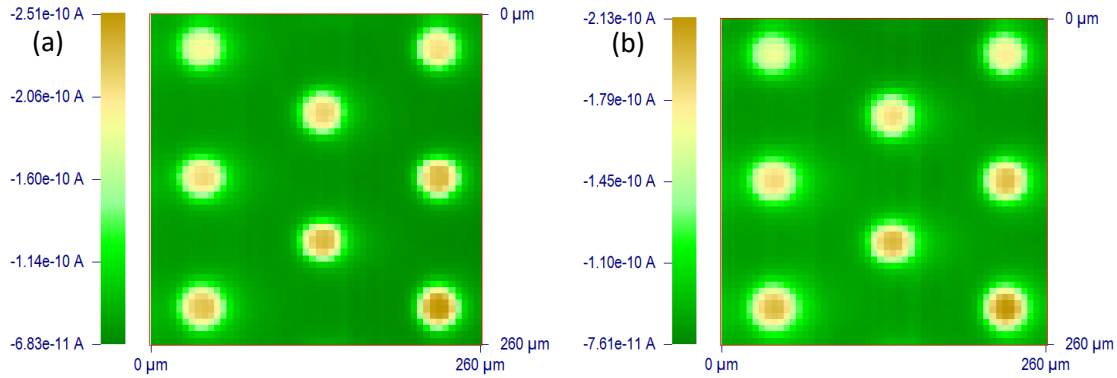

Figure 5-8. SECM SG-TC mode images of eight near the edge electrodes over 260×260 µm area from microdisc electrode array of r = 15 µm, 100 µm centre-to-centre spacing, using the following settings: 0.05 s increment time, 10 s quiet time, 5 µm step size, (a) $0.6i_T^{bulk}$ and (b) $0.7i_T^{bulk}$.

The image collected at the shortest imaging distance in (a) is characteristic of clear electrode features, just like for the single electrodes. With increasing tip working distance the hemispherical diffusion field expands, which is expected to result in less resolved electrode features. However, when the probe was lifted from $0.6i_T^{bulk}$ (Figure 5-8 (a)) to $0.7i_T^{bulk}$ (Figure 5-8 (b)), no significant changes were observed, suggesting that the image resolution is not

sensitive to such a change in SG-TC mode at very short working distances. In addition, from Figure 5-8, it seems that the bottom part of both images was closer to the imaging probe than the top, suggesting a minor tilting effect.

FB mode images of the same 30 µm diameter microdisc array electrodes in Figure 5-9 were collected using several different imaging settings. Electrodes in all images are clearly resolved but variation of the step size, increment time and imaging distance result in some differences between the images. When contrasting 5 µm and 2 µm step size images collected at $0.6i_T^{bulk}$ in Figure 5-9 (a-b), both images show localized diffusion fields around each of the eight electrodes. The image collected using a 2 µm step size is less pixelated than that using a 5 µm step size, as expected, thus giving the perception of a higher quality image. However, the smaller step size results in the electrodes in the lower part of the image being of lower currents and the insulator being of higher currents than in the upper part. This suggests that the lower part could have been further away from the probe due to tilting. Since the sample tilt was not intentionally adjusted between recording the images in (a) and (b), this suggests that decreasing the step size (and consequently the scan speed) makes the SECM more sensitive to sample tilt effects.

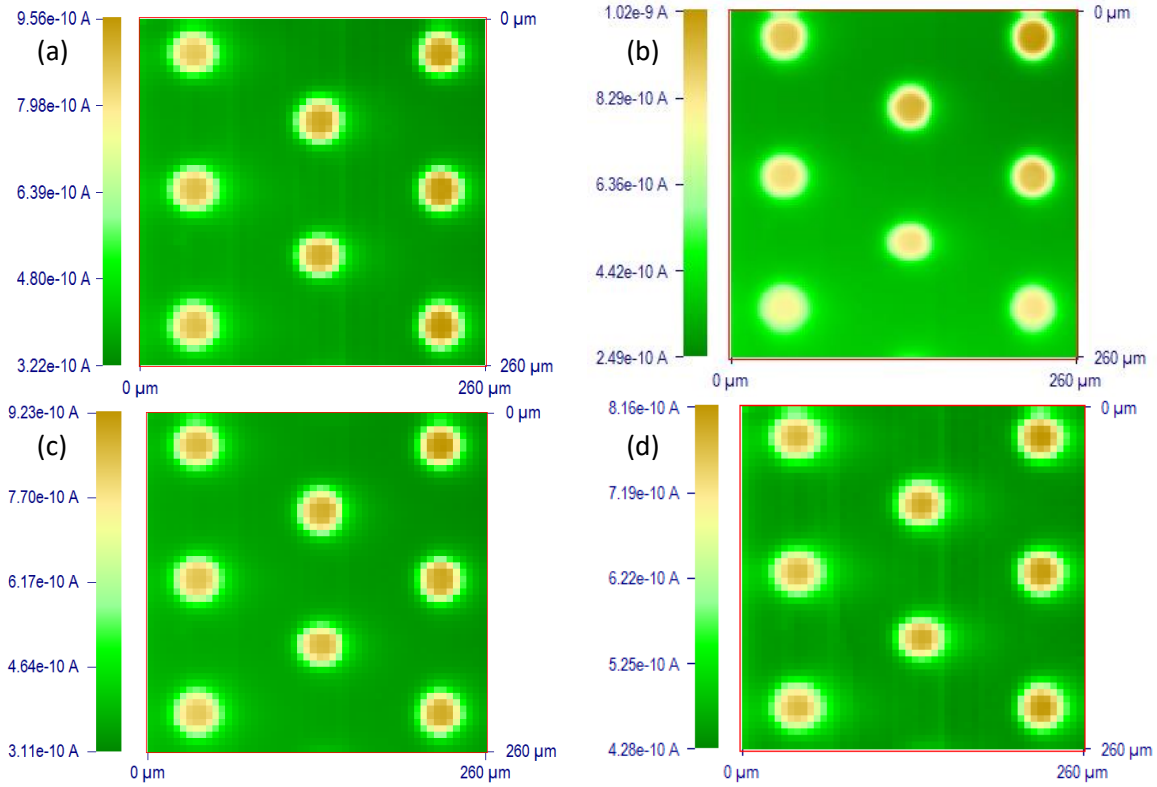

Figure 5-9. The same as in Figure 5-8 260×260 µm area from a hexagonal microdisc electrode array of r = 15 µm, 70 µm side-to-side spacing but imaged using SECM FB mode and the following settings: (a) $0.6i_T^{bulk}$, 5 µm step size, 0.05 s increment time, 10 s quiet time, (b) $0.6i_T^{bulk}$, 2 µm step size, 0.05 s increment time, 30 s quiet time; (c) $0.6i_T^{bulk}$, 5 µm, 0.1 s, 10 s, (d) $0.7i_T^{bulk}$, 5 µm, 0.05 s increment time, 10 s quiet time.

These images show the difficulty in imaging electrodes close to the edges of the image without the sufficient insulator area to allow for the imaging artefacts on the edges, unlike in Section 5.2. As such, whilst we have attributed this minor effect to tilting, it is possible that time dependent tip currents or convection are also playing a role. It was shown that it is challenging to clearly explain such differences only from the qualitative analysis. Semi-quantitative or quantitative analysis would allow more confident evaluation of these images. Nevertheless, all eight electrodes in both 2 µm and 5 µm step size images in Figure 5-9 (a-b) are well resolved and of relatively uniform activity across the area. Slightly higher resolution of the electrodes was achieved with a smaller step size, achieved at the expense of imaging time (approximately 2.5 min versus approximately 14 min).

The effect of increment time (scanning speed) and tip working distance on image resolution and artefacts on the array electrodes in FB mode was evaluated next. Figure 5-9 contains images collected at 0.1 s increment time in (c) rather than 0.05 s in (a) and an image collected at a greater tip working distance of $0.7i_T^{bulk}$ in (d) than $0.6i_T^{bulk}$ in (a). The longer increment time of 0.1 s in Figure 5-9 (c) resulted in slightly reduced visual artefacts, appearing in the form of vertical lines down the image in (a), possibly related to step motor movement. Despite this, the resolution or occurrence of artefacts appeared unchanged. Then, increasing the tip working distance from $0.6i_T^{bulk}$ in Figure 5-9 (a) to $0.7i_T^{bulk}$ in (d) resulted in slightly more observable convection effects in the latter due to probe scanning left to right in H direction, but this change did not significantly alter the overall appearance of the image.

Overall, this qualitative analysis of the individual hexagonally arranged array elements has revealed similar observations as from single electrode images. Further, the importance of an additional insulator area on the edges of the image was found to be important to allow for the various artefacts, which otherwise are more challenging to identify.

5.3.2 SECM images of a square-arranged microsquare array

5.3.2.1 Effect of tip working distance on image spatial resolution

SECM images of nine electrodes from the microsquare electrode array, where L = 30 µm, and side-to-side separation between the closest neighbours is 90 µm, were collected at different heights to compare sensitivity of FB and SG-TC modes in this differently arranged array compared to Section 5.3.1. The tip working distance was initially set at $0.75i_T^{bulk}$, representing the distance, d, of 10.9 µm (Section 4.5.5). The probe was then lifted up by 5 µm at a time in order to see how far up the tip can be lifted until blurred, low resolution images of the electrode features are observed. All images were placed on a uniform current/colour, specific to each mode, derived using the overall lowest and the overall highest current values from that set of data, to more effectively evaluate resolution decrease with increasing tip working distance. A 380×380 µm area was imaged, containing three lines of three electrodes each.

Sets of images in FB and SG-TC modes are presented in Figure 5-10 and Figure 5-11, respectively. As observed before, at smaller tip working distance images collected in FB mode are of a greater spatial resolution than in SG-TC mode. In all SG-TC mode images, the diffusion fields are wider and starting to overlap unlike in FB mode, reflecting the hemispherical diffusion fields adjacent to the electrodes, just like in single electrode images. Nevertheless, at greater *d* values the electrodes in both modes become significantly more blurred as the resolution decreases together with the expanding hemispherical diffusion fields from the electrodes, which at some point inevitably start overlapping. At *d* = 35.9 µm, only the silhouettes of the electrodes are visible in FB mode, while in SG-TC mode in Figure 5-11 the electrodes are still relatively well defined.

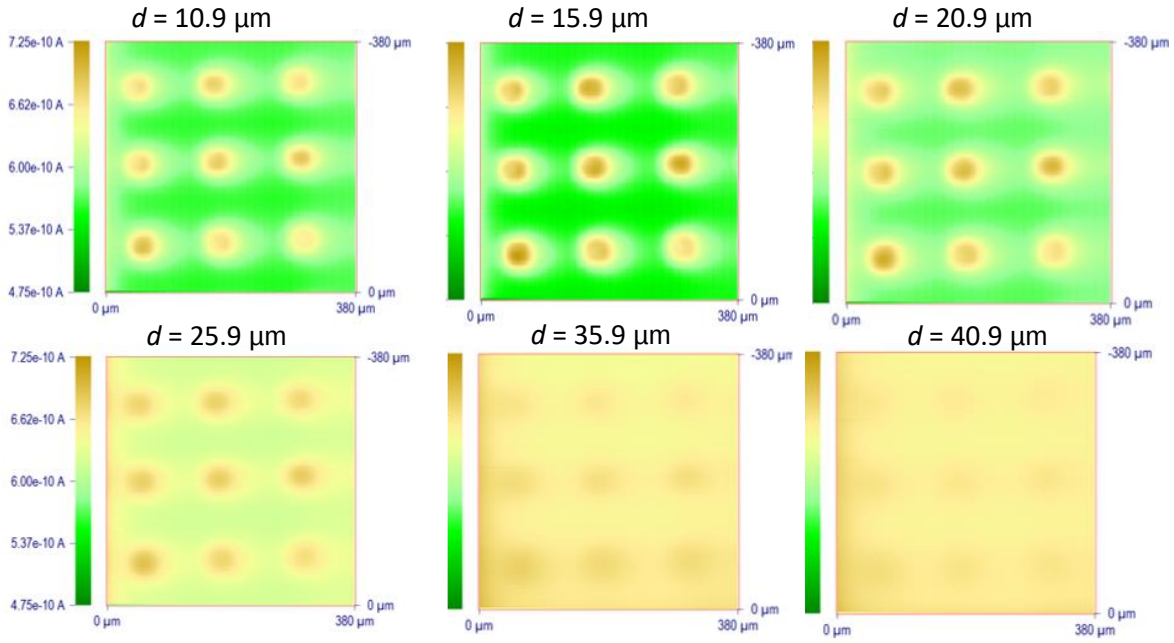

Figure 5-10. A set of SECM images over 380×380 µm area to check sensitivity of FB mode. Tip working distances are shown above each image and z-axis values were fixed on each image to 0.725-0.475 nA scale to compare tip working distance effect on image resolution. Initial tip working distance was set as $0.75i_T^{bulk}$, corresponding to 10.9 µm.

At *d* = 40.9 µm, FB mode images exhibit very little current contrast and the spatial resolution is poor. Meanwhile, in SG-TC mode the tip was lifted to a greater *d* of 60.9 µm. The image is certainly affected by the increased *d*, but it is still possible to identify that nine electrodes are present. This image comparison confirms that SG-TC mode delivers poorer resolution images when the tip is close to the substrate, as further discussed in the following chapters, but then this mode is less sensitive to the increasing tip working distance than FB mode. More images at greater tip working distances could be collected to establish at what tip working distances the underlying electrodes are no longer resolved.

The above discussed hexagonally arranged array at similar *d* has not reached diffusion overlap between individual electrodes unlike the one arranged in a square in Figure 5-10 and

Figure 5-11. Hemispherical diffusion fields emerging from all nine electrodes formed H lines of pale green colour alternating with bright green colour over the areas without the electrodes. Within these lines it is also clear that convection effects are present in both modes, as indicated by the elongated electrode appearance in the H direction and the absence of this pattern in the V direction. The presence of these convection artefacts makes it difficult to be certain about the extent of diffusional overlap between electrodes from these images.

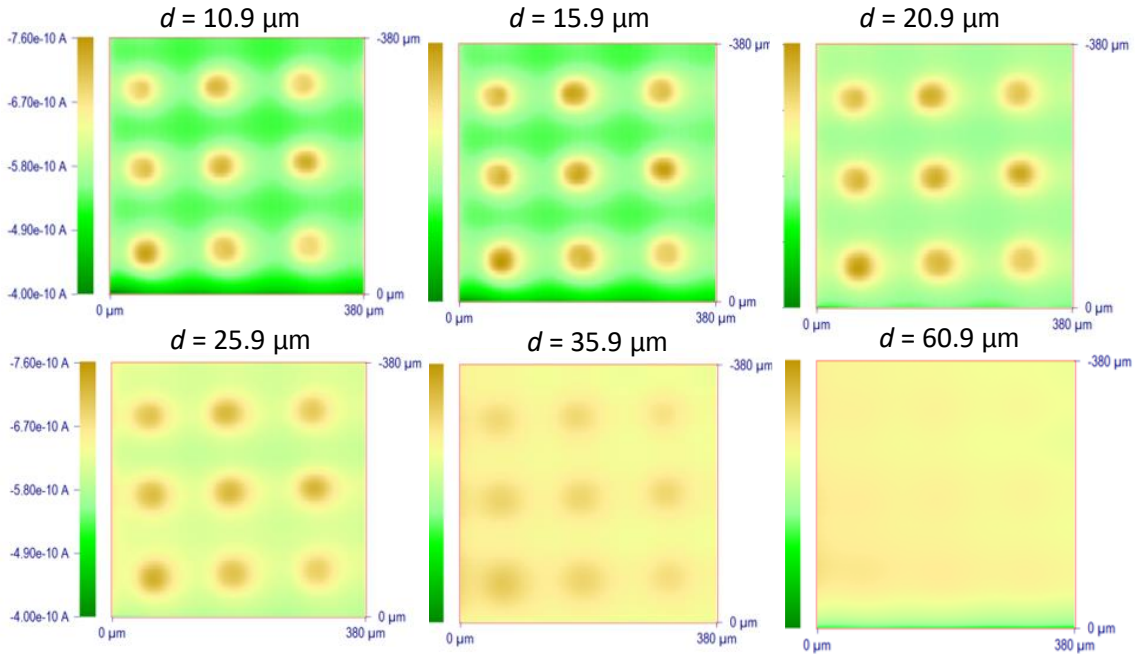

Figure 5-11. A set of SECM images to check sensitivity of SG-TC mode. Tip working distances are shown above each image and z-axis values were fixed to -0.760-0.400 nA on each image to compare tip working distance effect on image resolution. Initial tip working distance was set as $0.75i_T^{bulk}$, corresponding to 10.9 µm.

Finally, it is interesting that in both modes in Figure 5-10 and Figure 5-11 the electrodes seem to be of a disc geometry, while from the microscope images it is known that they were of a square shape (Figure 3-4). This suggests that hemispherical diffusion rather than precise electrode features is captured when imaging under these conditions. In Section 5.2, a larger electrode was imaged at a smaller *d*, making it easier to visualise the true square electrode geometry than in the present case.

5.3.2.2 More detailed analysis of the square array

One of the above presented images of 380×380 µm area containing 9 electrodes collected in FB mode is analysed in a greater detail in this section. Since the area is relatively small, differences between individual electrodes are possible to be observed. To start with, a smaller increment size of 2 µm was used to collect the image in Figure 5-12 but the resulting image barely changed from the previous one collected using a 5 µm step size. This suggests that

such setting variation had little influence on image spatial resolution and minimizing of the imaging artefacts, such as convection and time dependent tip currents.

Nevertheless, there is some variation in the electrode activity. From Figure 5-12, there is no obvious variation pattern, since some electrodes on the right and some on the left are of a greater activity. This suggests that tilting is unlikely to be the reason for such observations. The image suggests minor inconsistency of electrode activity within the array and the reason could be defects related to fabrication or passivating contaminants covering electrode surface, that were not fully removed before imaging experiments (Section 3.4). The difference was found to be approximately 0.05 nA (approximately 8%), which is small, but clearly within the sensitivity limit of the SECM technique. Convection effects at the beginning of each H scan line and on the right side of each electrode are also present, similarly as in Figure 5-10.

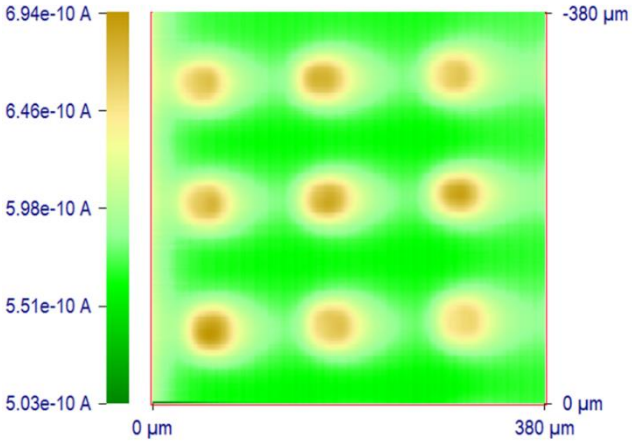

Figure 5-12. Area containing nine microsquare electrodes from the array, imaged using FB mode at $0.75i_T^{bulk}$ tip working distance. Increment distance 2 µm, incr. time 0.04 s, quiet time 10 s.

Next, the area of the image was decreased and only two randomly selected electrodes from the array were imaged in SG-TC mode within a 250×140 µm area in Figure 5-13. The increment distance was decreased to 1 µm and there was more imaged insulator area surrounding the electrodes. Nevertheless, convection effects were still observed, and the electrode's geometry remained resembling a disc rather than a square.

Interestingly, a clear difference in the activity of the two electrodes, indicating either the presence of a defect in the array or the occurrence of electrode passivation, was observed. The electrode on the left in Figure 5-13 is active, showing high current over Pt area, while the one on the right seems to be significantly less active. It would be an interesting experiment to check the activity of all electrodes in the array, allowing evaluation of the cleanliness and uniformity of the array. These array SECM images are the first step towards such array evaluation using visual and quantitative data.

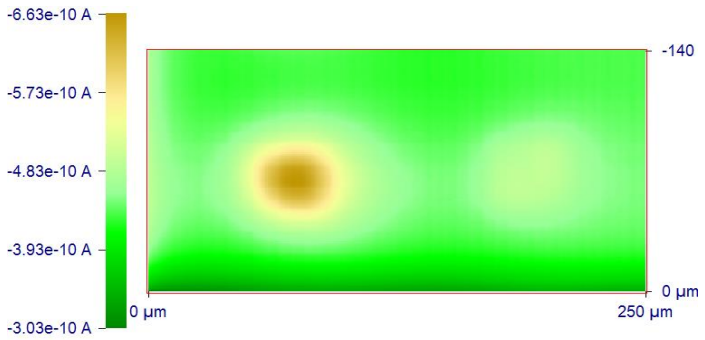

Figure 5-13. Two electrodes imaged over a randomly chosen 250×140 µm area using SECM SG-TC mode at $0.7i_T^{bulk}$. Increment distance 1 µm, incr. time 0.05 s, and quiet time 30 s.

5.3.2.3 Diffusional field overlap effects in SECM images over a large area

Several images over a large area (2000×2000 µm) of the same microsquare electrode array were obtained using both SG-TC and FB modes to further evaluate diffusional field overlap effects. In Figure 5-14, a large increment size of 10 µm was used in order to be more proportional to the imaging area and to obtain an image within a reasonable time. In both images, the electrodes are visible, relatively well defined, apparently working uniformly, and there are no random spots of significantly different currents compared to the rest of the electrodes. In both cases there is a narrow region of low current (dark green) on the right hand edge of the image, which represents pure insulator layer, too far away from the active electrode area to be affected by the diffusion or it is believed to be an artefact that occurs during fast scans at the end of each scan line.

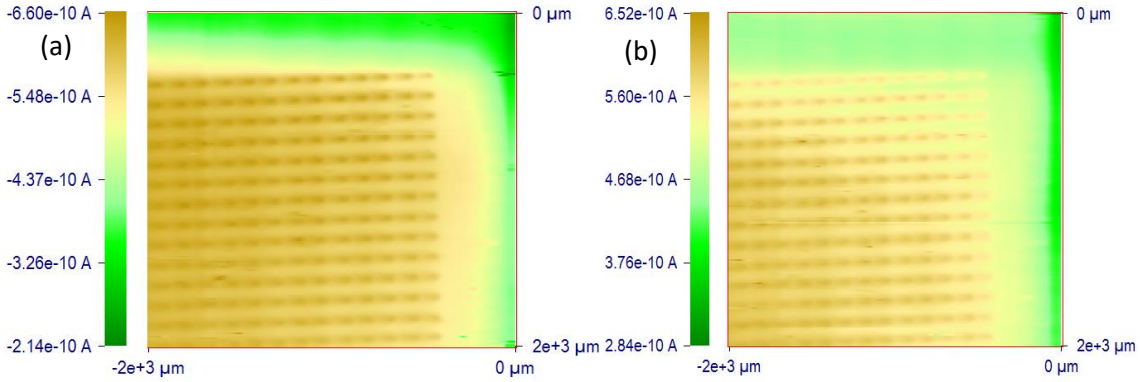

Figure 5-14. 2000x2000 µm area of electrode array imaged using (a) SG-TC and (b) FB mode at $0.8i_T^{bulk}$, increment distance 10 µm, incr. time 0.02 s, and quiet time 30 s.

SG-TC mode image in Figure 5-14 (a) suggests that expanding diffusion fields from individual electrodes appear to have overlapped and expanded to reach the insulator region beyond the array on the right side of the image. Diffusion fields from each micro electrode in SG-TC mode are broader and giving impression of a more diffusional overlap at this *d* than in FB mode. This reflects the fact that SG-TC mode captures more of a diffusion field profile rather than the

features of the substrate electrode, agreeing with the previous such comparison between the imaging modes.

FB mode in Figure 5-14 (b) results in a sharper spatial resolution image of the features of the substrate, which is reflected by smaller diffusion field profiles and the imaged electrodes being more defined. This is especially noticeable from the electrodes on the top right corner. Over the middle of the array there is more current than over the corner, where the electrodes also start to look slightly fused, just like in SG-TC mode. This is likely due to the diffusion field surrounding the probe electrode communicating with multiple substrate electrodes when in the middle of the array. The overlap observed in SG-TC mode suggests this array would deliver a macro electrode CV response (linear diffusion) of a higher magnitude than theoretically predicted signal for an array of isolated electrode, and it might not be the priority choice for the sensing applications, requiring all the advantages micro electrodes usually offer (Section 1.2.1). These SECM images show that there is a difference between edge and middle electrodes, and, again, quantitative analysis, such as middle line profile extraction and fitting, similarly as seen in Section 5.2.3, would allow a further evaluation of these observations.

5.3.2.4 2D and 3D SECM images of hemispherical diffusion fields

Overall, in all SECM images of the array electrodes the hemispherical diffusion field of the individual electrodes can be seen by the gradual decline in current around the electrode edges. In some cases, due to the probe's left to right scanning and resulting convection effects the circle was observed to be elongated in the H direction. This effect could be removed or reduced by changing imaging settings, probe size or substrate size, as discussed in a greater detail in Chapters 8 and 9.

Using Origin and CHI software, both used for 2D images extraction throughout this thesis, a hemispherical diffusion field evolving from the array electrodes can also be visualised by presenting the current map in 3D. In Figure 5-15, one of the 2D images in Section 5.3.2.1 is plotted in 3D using two different data analysis packages, which result in the same electrode presentation. The current map images show that the whole electrode well is of the same current as expected for a micro electrode. However, electrodes are indeed presented as having hemispherical profile rather than square geometry. This means that at these imaging settings hemispherical diffusion field overcame actual shape of the electrode. Each electrode shows up as a cone of varying height across the area of interest. Some inconsistency of the currents at the electrodes is more obvious and emphasized in a 3D representation, as different height cones rather than different shades of colour in 2D image may be more easily compared. Such current differences are numerically minor, yet they still exist and show how sensitive and powerful SECM technique is to detect such feature variation.

The results are also interesting regarding the actual current values for FB and SG-TC modes. FB mode provides results as expected, as the background current, measured with the tip at 0.4 V, was approximately 0.5 nA. This current was increased as the tip was moved across the electrode array due to the positive feedback (Section 2.9.2). Meanwhile, the background current measured in SG-TC mode with the tip at 0 V, which is typically expected to be close to zero nA, was actually closer to -0.5 nA, which is technically equivalent to the FB mode value (when in modulus). Since this is a cathodic current, such a current value is possible only if almost all of the present FcMeOH between the tip and the substrate was oxidised to $FcMeOH^+$ by the substrate electrode. Therefore, a further increase in the current as the tip was moving across the electrodes has to be due to an additional feedback effect. In this imaged array case, diffusion fields of adjacent electrodes must have been overlapping so that a complete mediator conversion occurred at the working distances used for these experiments. Finite element model (FEM) using such software as COMSOL of such array arrangement would be of interest to compare with the collected experimental data.

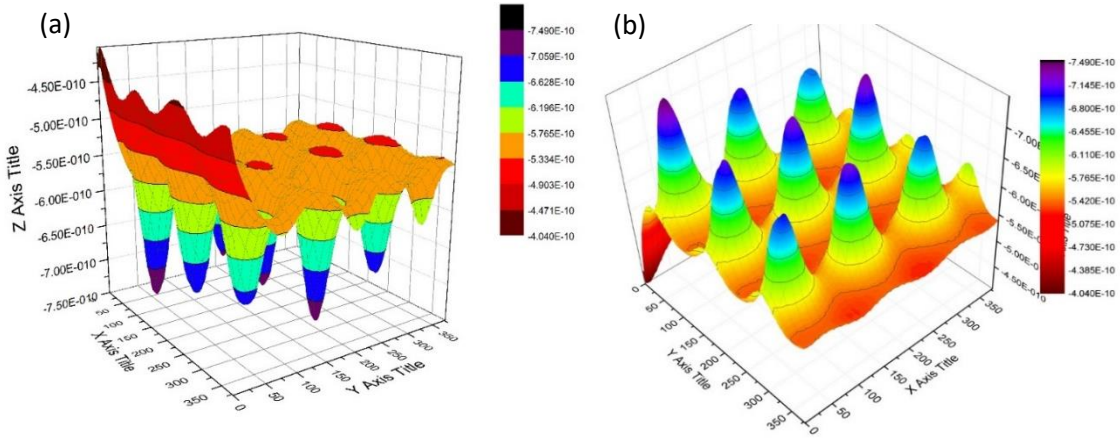

Figure 5-15. 3D presentation of one of the array images from Section 5.3.2.1 using (a) CHI software and (b) Origin software.

5.4 CONCLUSIONS

SECM images of single and array micro electrodes were collected at several *d*, and FB mode images were of a better spatial resolution than in SG-TC mode in all cases. The latter to a greater extent captured hemispherical diffusion field evolving from the substrate, to which the oxidation potential was constantly applied. As a result, convection effects were more likely to affect images in SG-TC mode due to the tip's left to right movement within this field and the resulting stirring. This is unlike in FB mode, where the probe's diffusion field gets affected by the presence of the substrate only when directly above it. From qualitative image analysis convection effects were observed to generally increase with increasing tip working distance in both modes, and it was possible to approximate them in H line profiles from the comparison

of H and V middle line profiles. The latter were more symmetrical than the H ones as a result of the minimized convection. From such analysis, FB mode was shown to be more sensitive to the variation of *d* and the images contained some additional imaging artefacts compared to SG-TC mode. The examples are time-dependent tip currents at the top part of the image and tilting, which was observed to decrease with increasing tip working distance due to a smaller percentage change of the currents. It is important to image the area of interest whilst including some additional space around it to allow for imaging artefacts to die away; otherwise, it is likely that the artefacts will overlap with the substrate's response, causing imprecise and challenging quantitative analysis.

Images of square and hexagonal-arranged microsquare and disc, respectively, electrode arrays of similar electrode separation distances imaged using SECM in FB and SG-TC modes confirmed a successful electrode fabrication, as the electrode surface was generally homogenous in all cases. The effect of scanning speed by varying a step size and an increment time on image spatial resolution and diffusion field overlap from neighbouring electrodes in the array was evaluated. From a qualitative analysis of the individual array elements similar observations as from single electrode images were obtained, but since there was less electrode-surrounding insulator area on the edges of the image, imaging artefacts and substrate response were occasionally more difficult to be separated. The square arranged array was imaged with overlapping diffusion fields at selected *d*, while hexagonally arranged array at the same *d* preserved localized diffusion fields which did not exhibit significant overlap. The hemispherical diffusion field was shown to evolve not only from the disc, but also from the square micro electrodes, overcoming the geometry of the electrode and resulting in circular electrode presentation in the images. The microsquare of 30 µm edge length was too small to preserve the square features in most of the images.

Overall, SECM is a powerful technique for imaging micro fabricated Pt single and array electrodes. The collected data was successfully used for comparison between different electrodes and imaging modes, allowing to progress to a structured benchmarking system of the SECM results. Continuing with this purpose, SECM images of nanoband edge electrodes and their qualitative, semi-quantitative and quantitative analysis is presented in the following chapters.

5.5 REFERENCES

1. Heinze, J. Cyclic Voltammetry - 'Electrochemical Spectroscopy'. *Angew. Chem. Int. Ed.* **23**, 831–847 (1984).

2. Fleischmann, M. & Pons, S. The behavior of microelectrodes. *Anal. Chem.* **59**, 1391A–1399A (1987).

3. Forster, R. J. Microelectrodes: New Dimensions in Electrochemistry. *Chem. Soc. Rev.* **23**, 289–297 (1994).

4. Damion K Corrigan, Justin P Elliott, Ewen O Blair, Simon J Reeves, Ilka Schmüser, A. J. W. and A. R. M. Advances in electroanalysis, sensing and monitoring in molten salts. *Faraday Discuss.* 351–366 (2016). doi:10.7488/ds/1338

6 SECM IMAGES OF SINGLE NANOBAND EDGE ELECTRODES

6.1 INTRODUCTION

In this thesis, the term “qualitative spatial resolution” describes the sharpness of the image, based on the known dimensions of the substrate electrode. In the previous chapter, single micro electrodes were imaged using SECM and the images were evaluated with respect to qualitative spatial resolution and the occurrence of imaging artefacts. In this chapter, SECM is used to image and qualitatively as well as semi-quantitatively analyse high fidelity microfabricated platinum (Pt) nanoband edge electrodes, also of controlled design, shape and dimension just like in Chapter 5. These single microsquare/microdisc nanoband edge electrodes (MNEEs) are of 100 µm edge length/diameter, respectively. Images were collected at three fixed tip working distances, *d*, to probe, quantify and mitigate the impact of effects such as convection, sample orientation and changes in the response of the SECM tip with time. Convective artefacts are evaluated by comparing H and V middle line profiles, and data collected in FB and SG-TC modes are compared and contrasted.

6.2 SECM IMAGES OF THE MNEES IN FB AND SG-TC MODES

6.2.1 Resolution dependency on imaging mode

Disc and square nanoband edge electrode images in SG-TC and FB modes are shown in Figure 6-1 on the left and right, respectively. For a direct comparison, like in Chapter 5, the magnitude of the FB mode tip currents and SG-TC mode currents were compared as the modulus was used. All images exhibit high currents around the conducting band edges (dark red) with lower currents in the middle (mostly red-yellow) and outside the edges (blue-violet) above the insulator as expected for nanoband edge electrodes. This confirms that Pt metal was successfully fully removed from the electrode wells during the fabrication process to reveal MNEEs.

The images are first compared to evaluate the image spatial resolution in the two modes. Above the insulator cavity, the imaging currents are higher than above the surrounding insulator area in both modes due to the expected establishment of the hemispherical diffusion field above the Pt band[1]. But it is interesting that in SG-TC mode image in Figure 6-1 (a) the tip current measured at the centre of the electrode well is only slightly lower than that measured at the edges, as indicated by a uniform red colouration. In contrast, in FB mode Figure 6-1 (b), the tip current drops more significantly at the centre of the well (indicated by yellow in the image) suggesting that FB mode better captures the band nature of the electrode than SG-TC mode. Since both images were collected at the same tip working distance (at $0.7i_t^{bulk}$ which in

Section 4.5 is determined to be d = 9.2 µm) such direct comparison is possible. Similarly, in Chapter 5, FB modes images were also of a better spatial resolution than SG-TC mode images.

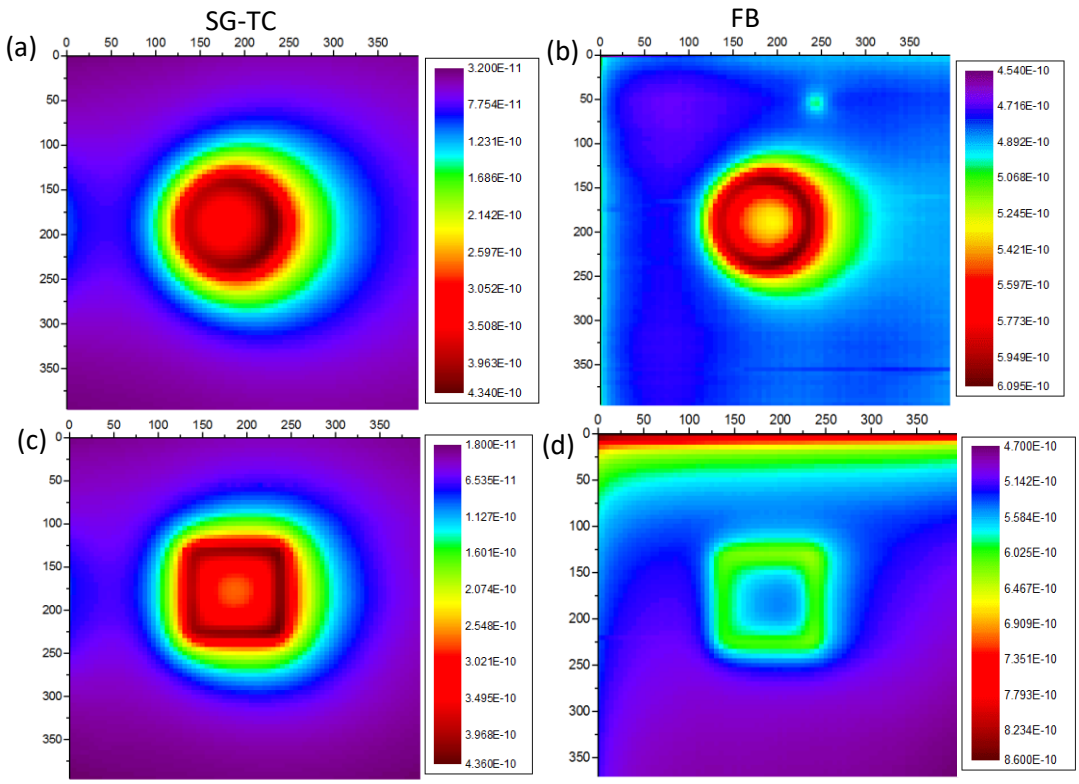

Figure 6-1. SECM images of (a) a nanoband edge disc electrode in SG-TC and (b) FB modes at d = 9.2 µm and images of (c) a nanoband edge square electrode in SG-TC at d = 9.2 µm and (d) FB mode at d = 13.2 µm. On the side of each image there is a current scale map. Note: current in SG-TC and FB modes are absolute tip currents in Amps for a direct comparison between the modes. (Images were produced using Origin software.)

In FB mode, each circular band in the image (representing different current ranges) is relatively narrower, and the region of current contrast is confined to a smaller fraction of the image area. This is also indicative of sharper changes in current, hence sharper colour contrast than in SG-TC mode. These observations reflect differences between the diffusion fields of the two electrodes, as shown in Figure 6-2. In FB mode in (a), the 10 µm diameter tip is set to the mass transport limited FcMeOH oxidation potential (+0.45 V) at all times. Its hemispherical diffusion field is therefore relatively small and compressed, compared to the near hemispherical diffusion field established in SG-TC mode across the 100 µm diameter MNEE substrate (also biased at +0.45 V) in (b). Depending on d, the extent of the overlap of the diffusion field from the sides of the band is expected to vary, as shown in Figure 6-2 (b).

Thus, SG-TC mode tends to result in images depicting the overall diffusion field of the substrate electrode, while FB mode delivers images of localized details, as also discussed in

Section 5.2.1. Whilst these observations are as expected,[2] it is important to demonstrate that such electrode and corresponding diffusion field size differences are fully reflected in the experimental images recorded at these high fidelity substrate electrodes.

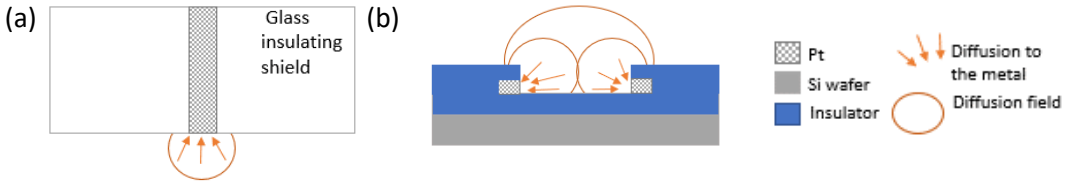

Figure 6-2. Diffusion field differences in (a) FB and (b) SG-TC modes, reflecting that it depends to which electrode oxidation potential of +0.45 V is applied. Diffusion field overlap from the band sides over the insulator cavity in the middle of the electrode varies with d, as shown in (b).

As mentioned above, the overlap is such that in SG-TC mode the imaging current above the middle of the cavity is only slightly lower than that above the Pt band, making it more challenging to resolve from the image whether it is a microelectrode or a nanoband edge electrode. Such diffusion field size effects on image sharpness are even clearer, when considering that the SG-TC nanoband square image in Figure 6-1 (c) was collected at d = 9.2 µm, while FB image in Figure 6-1 (d) was collected at the greater working distance, d = 13.2 µm. This means that SG-TC mode generated a less sharp image at a smaller working distance compared to the FB mode image collected at a greater d. Consequently, the square MNEE corners look more rounded in Figure 6-1 (c) than in FB mode in Figure 6-1 (d). The insulating area in the middle of the electrode is also more clearly visible in FB mode.

Overall, both nanoband disc electrode images contain less resolved insulator surface in the middle of the electrode than nanoband square images. When considering qualitatively the principle differences between the expected contributions of different parts of the square band and the disc band, it is worth first considering the current along the middle line of the image, as depicted in Figure 6-3. The middle line from the square (either H or V) should have equal contributions from the two parallel sides (either top and bottom horizontal or left and right vertical) at all points on the line, as the distance is the same from any point to each side wall. This is unlike the middle line of a disc band, where there is slightly more contribution from the two “walls”, due to their closer proximity and their rounding outside the middle plane. This effect was of a smaller importance in Chapter 5 due to the electrodes being significantly larger (micro versus nanoband). These geometry differences explain why in FB mode the insulator cavity of the nanoband edge disc electrode in Figure 6-1 (b) is not as precisely defined in the image as in a square in Figure 6-1 (d). In the latter, the middle area is obviously an insulator, as it is of the same colour (blue) as the surrounding insulator. Meanwhile, in the disc image, the cavity middle is of lower currents (yellow) than the band (red) but still of higher currents than the surrounding insulator (blue), as the diffusion field from the edges extends to a greater scope into this cavity than in a square electrode. This image still clearly shows a nanoband

edge electrode of a disc geometry, but if the disc diameter were smaller, at the same tip working distance as in Figure 6-1 (b), the image would most likely more resemble a microelectrode, rather than a nanoband edge electrode.

The differences between SG-TC mode images are smaller. The centre of the disc in Figure 6-1 (a) exhibits a uniform current in the range of 3.0-3.5×10^{-10} A, while the current at the centre of the square in Figure 6-1 (c) certainly drops below 3.0×10^{-10} A, as indicated by the hint of orange colour above the very middle of the cavity. Thus, the geometry of the electrode has less impact on SG-TC images on this scale. These effects will be further quantitatively analysed in Section 6.3.7 and throughout Chapter 7.

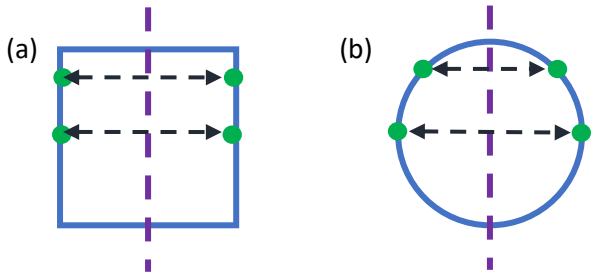

Figure 6-3. (a) Square and (b) disc electrode geometries with the middle line profiles are drawn as vertical dashed line. With respect to these middle lines, the contribution of the diffusion field from the walls of the electrode in the disc geometry is greater than in the square geometry, where the contribution from the walls is constant at all times.

6.2.2 Qualitative assessment of imaging artefacts

SECM images in Figure 6-1 are of high spatial resolution as the middle of the electrode clearly contains an insulator cavity. However, several typical SECM imaging artefacts are still observed, as in Chapter 5. Examples include convection effects that make the shape of the substrate electrode appear distorted in the H direction from left to right and the tip current decay effects that make the image appear tilted, when in fact it is level. Unlike some other systems such as gold band arrays (Section 1.1.4), high-fidelity images of electrodes (substrates) are required to provide some confidence in rationalising the artefacts as well as any additional and unexpected surface features.

Since electrode features are better resolved in FB mode, observation of a more electroactive spot on the insulator surface was possible only in this mode. In Figure 6-1 (b), at the top right of the disc nanoband image, there is a significant size region of higher currents. In Figure 6-4 (a), the same image is presented in 3D, where the axis has been rotated away from its original position to reveal and further emphasize this, captured as a current peak in the purple box. Such higher currents seem to originate from more than one line profile; hence, this suggests a real surface feature, not an artefact. It could have appeared due to a pinhole or the thinning of the insulator surface which is not sensed in SG-TC mode. The electrode area is not affected, and it is also absent from the middle line profile analysis in Section 6.3.

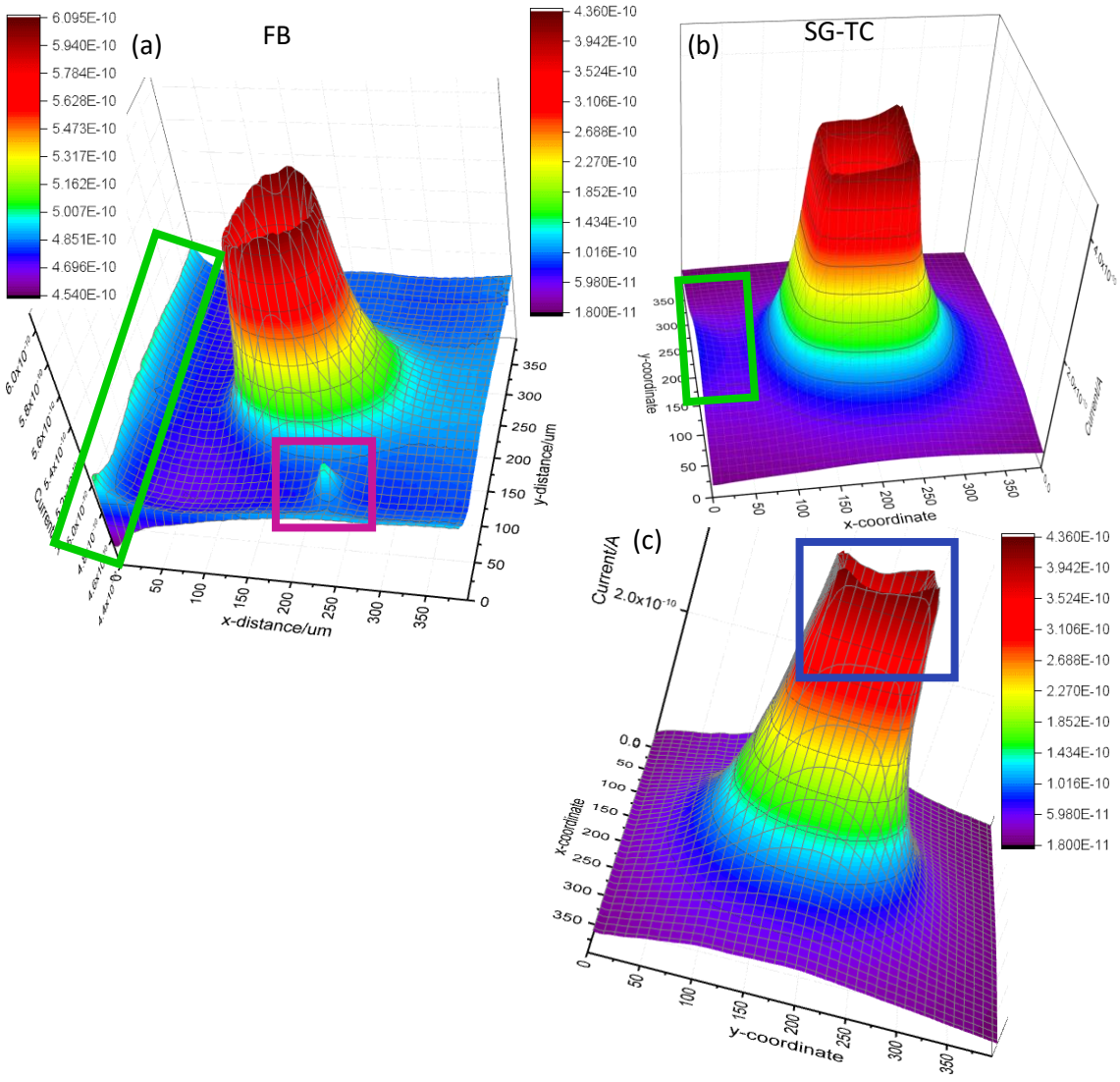

Figure 6-4. 3D SECM images of (a) a nanoband edge disc electrode in FB mode and (b) a nanoband square electrode in SG-TC mode, which (c) has been rotated to more clearly show an insulator profile (blue) within the conductor area and the corners of the square electrode, both of which are within the blue box. All images were collected at d = 9.2 µm, and these 3D representations are equivalent to images in Figure 6-1 (b-c). Green box in (a) emphasizes convection artefacts in FB mode and the smaller purple box focuses on an artefact on the insulator surface.

The 3D representations also enable a clear observation of another artefact in FB mode. In the equivalent 2D image in Figure 6-1 (b), this appears as a narrow line of higher currents presented as a light blue colour on the very edge of the left side of the image. And in a 3D image this is presented more clearly as indicated by the (green) box on the left edge of the image in Figure 6-4 (a). This is likely a consequence of the solution being stirred by the SECM tip[3] upon its returning rapidly from right to left to resume scanning after it has completed a horizontal scan line. Upon returning to the original x-coordinate one scan line lower, the tip appears to cause local stirring, which results in an additional convective transport of the redox species from the bulk to the tip and hence an increase of these initial current values. Enhanced currents at the beginning of each line profile show effective convection initially but within a few

points in the x-direction the current decreases towards a stable value, presumably because the scan speed during data collection (left to right) is significantly slower than the return scan speed (right to left). As long as these convection effects die down well before the electrode area, this does not disturb the collected data, allowing effective quantitative analysis.

The effect of imaging artefacts in the two imaging modes is evaluated from the comparison of two electrode images in Figure 6-4 (a-b). The convection effects due to the rapid scanning back from right to left (discussed in the above paragraph) are significantly more present in FB than in SG-TC mode. In the latter, the green box in Figure 6-4 (b) captures convection-related artefact at the front of the H line profiles. The effect is more localized than in FB mode, being only at the start of the H line profiles which involve crossing the nanoband electrode area, unlike in FB mode where all lines were affected. Since the redox couple oxidation potential (+0.45 V) is now applied to the substrate, this is because the tip, upon rapid scan back, drags some of the $FcMeOH^+$ generated at the substrate to the left side of the image, where it gets reduced and results in a higher current seen on the subsequent scan. When the tip is scanning over the area without the nanoband electrode, this affect is absent; thus, although both FB and SG-TC images indicate convection effects on the left edge of the scan, they arise from different processes.

When further evaluating these 3D images in Figure 6-4 (a-b), not only there is more current variation across the insulator area in FB mode, but also the cone, representing the active band, is more distorted. The right side of the cone at the base is elongated towards the right and the top profile of this cone is also of higher currents on the right side, as indicated by a darker red colour. In SG-TC mode, the right side of the nanoband square peak is also of higher currents than the left side, but the current increase is smooth, resulting in a relatively gradual slope. In FB mode, the slope is significantly steeper. It is not easy at this stage to explain why the currents immediately to the right of the nanobands are higher than they should be in both modes. It could be minor Pt band activity difference on the sides of the electrode or also convection-related artefact. Semi-quantitative analysis of these artefacts in the following sections of this chapter allows a further evaluation.

These higher currents on the sides of the electrode area result in an asymmetric (from left to right) presentation of the nanoband electrode images. This effect is more pronounced in the case of the nanoband disc, which appears elongated (egg-shaped), rather than perfectly circular. The fact that these effects are absent in the *y*-direction are a good indication that they are due to convection. Overall, FB mode has been shown to deliver greater spatial resolution images, but it also has been shown to be more affected by some of the typical SECM imaging artefacts than SG-TC mode.

The 3D figures clearly show the nature of the substrate electrode, as they visually establish that the imaged electrode is a MNEE in a more convincing manner than equivalent 2D images.

Specifically, for the nanoband disc 2D image in SG-TC mode from Figure 6-1 (a) it would need to be considered whether it is a band or a micro electrode without further analysis and comparison with the other images. When presented in 3D in Figure 6-4 (a), a high current band with an insulator area within it is revealed, as represented by the hollow centre of this band. This is also applicable to the square geometry. In addition, in Figure 6-4 (c), the square electrode area is highlighted by a blue box to emphasize that the corners appear to be more active. This, again, was not noticeable from the 2D image, and is potentially an example highlighting the enhanced effects of corner diffusion previously discussed in the literature.[1,4]

A further imaging artefact can be seen at the very top of the image in Figure 6-1 (d). It is clear that there is an area formed by H lines of significantly higher currents, which differs from the rest of the insulator surface. To demonstrate this effect more clearly, the current scale has been limited to a maximum upper value of 0.69 nA in Figure 6-5 (a), allowing the actual square electrode to be fully revealed while removing the focus on those upper H scan lines. This shows that the lines are of significantly higher currents for this insulator area in such images, and when evaluating currents from the newly generated scale, it is clear that the current is progressively dropping with successive H scans in this region. These changing currents gradually settle with time and line profile number. However, when comparing this FB mode image with the one from SG-TC mode in (b), the effect clearly has not fully settled before the electrode area. The electrode-surrounding insulator area is of varying currents across the whole surface.

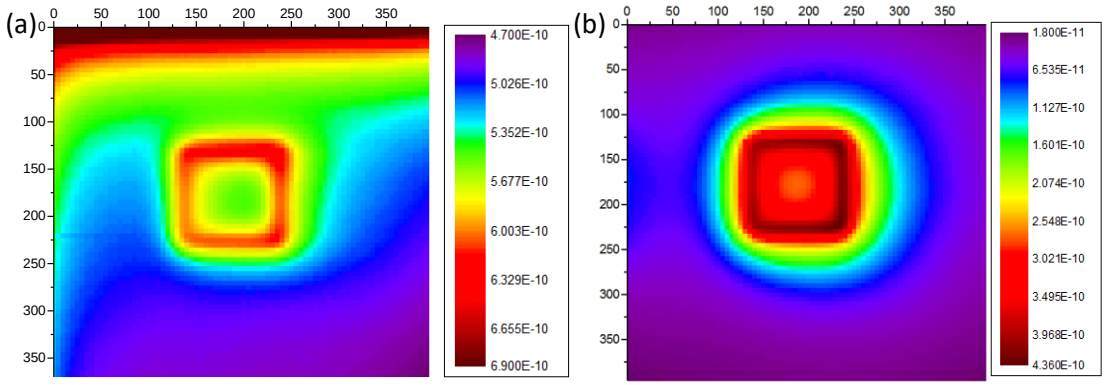

Figure 6-5. The same (a) FB and (b) SG-TC mode SECM square nanoband edge electrode images as in Figure 6-1(c, b). In FB mode, the current scale has been fixed to a maximum value of 0.69 nA to allow the focus of the image to be on the square rather than the H scan lines at the top of the image.

The reason for the occurrence of this time-dependent artefact could be an initial dragging of some kind of an electroactive particle under the tip. This would result in abnormally high currents at the beginning of the imaging, but then it also would be maintained if there was a current path to the underlying substrate (which there is not), and so it is hard to explain a gradual decrease in this current with scan number and time. Also, as a result of the presence

and then absence of the particle, the difference between high and low currents would be significantly sharper rather than gradual.

An overall tilt of the MNEE electrode can also be eliminated. In case of tilting, higher currents over the insulator at the top of the image would suggest that the tip was further away from the substrate, allowing smaller negative feedback. The tip would be closer to the substrate at the bottom part of the image allowing for a greater negative FB response. However, when evaluating currents over the band area, the opposite dependency on *d* is observed, as the top line of the square is of slightly higher currents, suggesting if anything greater positive feedback and a closer distance than for the bottom line. Therefore, tilting cannot consistently explain this response. The rest of the band electrode image is as expected in FB mode and the equivalent image in SG-TC mode in Figure 6-5 (b) is also not affected (although topography effects are known to be less pronounced in SG-TC mode compared to FB mode).

Therefore, it is most likely that this is an artefact related to the tip electrode conditioning. The currents decrease in a smooth manner, and similar high current profiles have been observed in other images, although normally the current stabilised much more quickly (i.e. within a few scan lines). This unusual behaviour may either indicate some early chemical contamination of the SECM tip or the time-dependent decrease in response of an unusually clean tip. Such effects are normally removed due to the preconditioning potential applied to the tip, but in this case, this was clearly not effective. This observation demonstrates the importance of the imaging of the insulator around the electrode to first establish and then potentially account for the effect of artefacts. The image was also used for a further discussion of semi-quantitative analysis, as presented later on in this chapter.

6.2.3 Electrode resolution dependency on the tip working distance

The following discussion focuses on imaging of the diffusion field as a function of the tip working distance. Nanoband disc and square electrode images were collected in SG-TC and FB modes at three nominal tip working distances of *d* = 9.2; 13.2 and 22.1 µm, as derived in Section 4.5.5. The images are grouped in four sets as shown in Figure 6-6 (nanoband disc) and Figure 6-7 (a-b) (nanoband square) and they are plotted on the same current range in Amps, derived using the smallest and the highest current values prevailing in each set. In both figures, part (a) and part (b) show the data recorded in SG-TC mode and FB mode, respectively. Images are presented in different colour schemes than above to show that either of the two software packages (Origin and CHInstrument) can be used to present and analyse data. Since the FB mode images of the square nanoband edge electrode in Figure 6-7 (c) are significantly affected by the tip conditioning artefact (Section 6.2.2), in Figure 6-7 (b), these images are zoomed in, so that this top area of the image is cropped out. This again emphasises the importance of identifying and, if possible, removing the effect of artefacts.

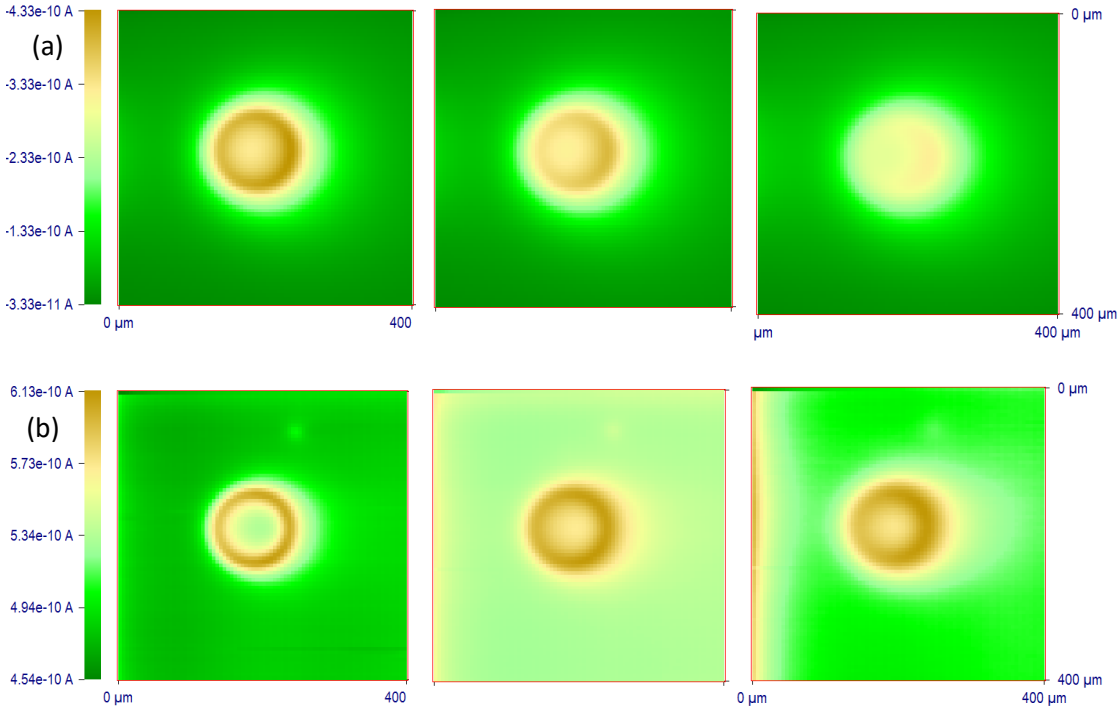

Figure 6-6. SECM images of r = 50 µm Pt nanoband edge disc using (a) SG-TC and (b) FB modes. Step size = 5 µm, step time = 0.2 s. Images were placed on the same current range in Amps in each mode for direct observations how variation of d (increasing from left to right) affects image spatial resolution. Images were produced using CHInstrument software.

In Figure 6-6 and Figure 6-7, the left images were collected at the smallest out of three *d* and the tip working distance increases towards the right. These MNEE images, as expected, clearly show that increasing *d* results in successively lower spatial resolution of the electrode features in both modes for both disc and square electrodes due to diffusional broadening. Despite this, both electrodes in FB mode in Figure 6-6 (b) and Figure 6-7 (b, c) are clearly seen to be band electrodes (MNEEs). FB mode MNEE images are consistently of a higher electrode feature resolution than in SG-TC mode at all *d*. Even at *d* = 22.1 µm in Figure 6-6 (b), it is clear a nanoband disc is being imaged. In SG-TC mode at the same *d* the diffusion field from the substrate has evolved into the insulator cavity and become nearer to hemispherical for both disc and square, as shown by the near circular disc-shaped image obtained for both disc and square electrodes in this mode.

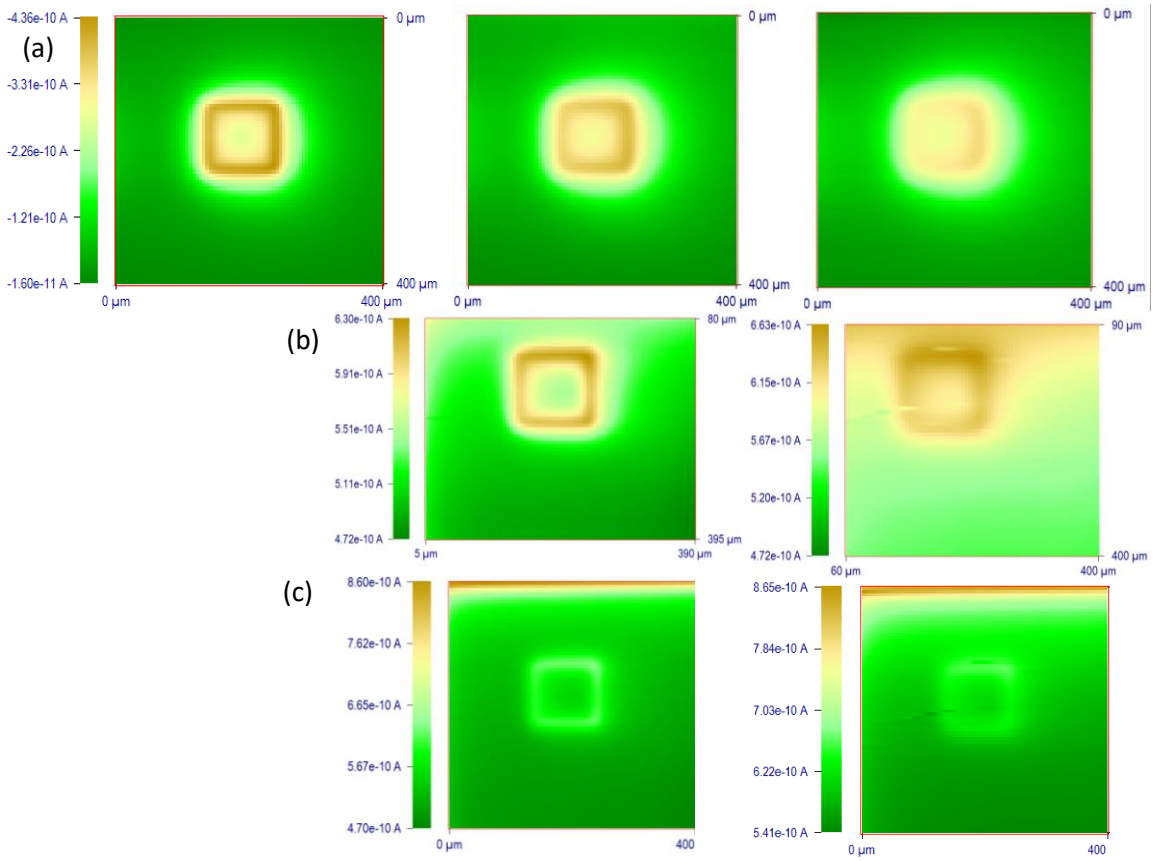

Figure 6-7. SECM images of L = 100 µm Pt square nanoband edge electrode at increasing tip working distance from left to right (d = 9.2, 13.2 and 22.1µm) in (a) SG-TC, where images were placed on a uniform current range for direct observations of how d affects spatial resolution and (b-c) FB mode, where original images in (c) were disturbed by time-dependent artefacts, which were removed by cropping the image in (c).

At *d* = 22.1 µm, it was still possible to distinguish between disc and square electrode geometry in both modes. But in SG-TC mode, the nanoband nature of the electrode is less apparent for the disc in Figure 6-6 (a) compared to the square in Figure 6-7 (a). In the latter, it is much clearer that a band was imaged, emphasizing that the geometry of the electrode is important. The development of the expanding hemispherical diffusion field depends on the nature of the electrode, which dictates how far above the surface the tip should be placed in order to fully resolve the electrode. The nanoband disc electrode images in SG-TC mode in Figure 6-6 (a) capture hemispherical profile to a great extent due to the greatest diffusional overlap from the band sides, which also means that at tip working distances greater than the diameter of the probe (10 µm) in SG-TC mode it is difficult to identify if it is a nanoband or a micro disc.

These sets of images at the three tip working distances allow evolution of diffusion for both geometries of the electrode. It has been predicted that both MNEEs will produce overall hemispherical diffusion fields (Section 2.4) at large enough times and distances, and from these images it is clearly seen that a hemispherical diffusion field evolves from both disc and

square nanobands within these experimental time and length scales. The hemisphere-like diffusion field has started to overcome the square geometry of the electrode, similarly as in Chapter 5. The hemispherical diffusion field was reached at a shorter distance by the disc than the square: the disc band shape more naturally leads to a hemispherical diffusion due to a circular geometry, and diffusional overlap from all parts of the band electrode as a function of height occurs more rapidly than for the square (Figure 6-3).

Since the tip currents vary from experiment to experiment due to various factors such as minor probe fouling and contamination, each image has a slightly different current range. It is interesting that the image collected at d = 9.2 µm shows the largest current range (also referred to as current contrast) in FB mode whilst the image at d = 22.1 µm shows the smallest. This is because the effects of negative feedback at the insulator (hindered diffusion to the tip) and positive feedback at the band electrode (reduction of the tip-generated redox species at the band) both become more pronounced with decreasing d, leading to a greater current contrast.

In contrast, the corresponding SG-TC images in Figure 6-6 (a) and Figure 6-7 (a) show a reduced current range. This can be seen to be primarily due to the invariance of the current over the surrounding insulator with d. There is no $FcMeOH^+$ redox species in the bulk to be affected by hindered diffusion and little detectable species from the MNEE electrode. Comparison of images after arranging them to be on the same current scale therefore really allows the comparison of the current ranges and relative resolution of the electrode features as a function of the changing tip working distance and between the measurement modes.

In conclusion, the nanoband disc electrode image at d = 9.2 µm in FB mode is the best of the three distances for qualitative spatial resolution of the electrode. It not only depicts a high-resolution circular band image with a clear, well established insulator area in the middle but also contains little impact from artefacts further discussed in this chapter. The corresponding square nanoband image suffers a tip conditioning artefact. Together these demonstrate how MNEE images can be used to demonstrate and account for these counterbalancing effects.

6.3 SEMI-QUANTITATIVE ANALYSIS OF THE MIDDLE LINE PROFILES

The relative effects of imaging artefacts and tip working distance variation in FB and SG-TC modes are further evaluated by comparing H and V line current profiles across the electrode area in the images. The three tip working distances used in these experiments were d = 9.2; 13.2 and 22.1 µm ($0.7i_T^{bulk}$, $0.8i_T^{bulk}$, $0.9i_T^{bulk}$, respectively) like in Chapter 5. Since only specific parts of the line profiles were analysed, this is a semi-quantitative analysis.

6.3.1 Horizontal line profile analysis in FB mode

In this section, only the nanoband edge disc electrode was fully analysed, as similar analysis was already performed on a micro disc and a micro square electrode in Section 5.2.3. H line profiles from these images collected at three *d* values are compared in Figure 6-8. Both raw and normalised currents are presented with three sections within these line profiles, highlighted for a more structured analysis: initial tip currents (green box); area containing two peaks present due to Pt electrode band (blue box); and final tip currents (purple box).

From the raw current line profiles, as expected, initial tip current increases with increasing tip working distance due to a less negative feedback at the insulating region of the substrate and the middle line profiles fall into an arrangement presented in Figure 6-8 (a). At *d* = 22.1 µm, the initial tip current has the highest value of the three lines, which is expected due to the smallest negative feedback: tip and substrate are separated by the greatest distance, allowing the greatest mass transport limited diffusion to the tip. It is worth mentioning that these images were collected at the greatest *d* first and there was a significant time frame between images, tiny currents and large solution volumes, which removes the possibility that the tip current is higher due to the $FcMeOH^+$ species gathering in the solution with time.

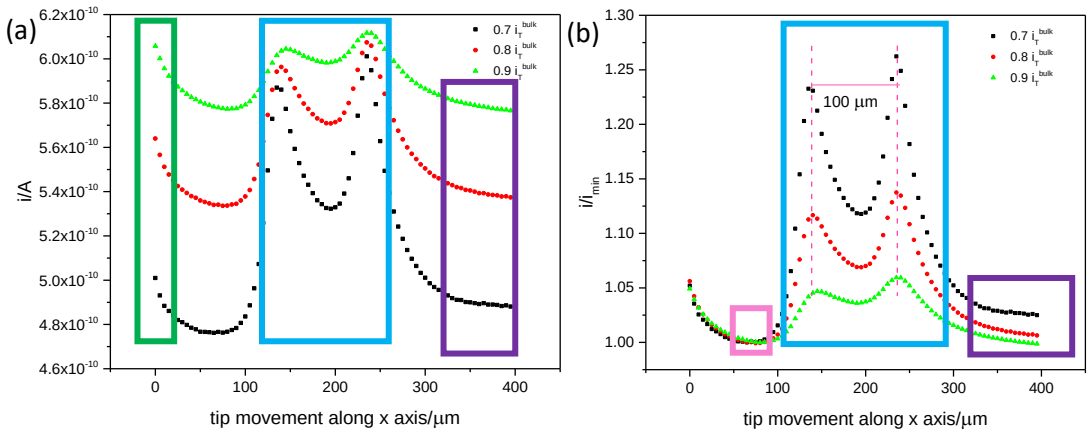

Figure 6-8. (a) Raw current and (b) normalized to i_{min} H middle line profiles from nanoband disc (r = 50 µm) FB mode images collected at the three tip-substrate distances. Dotted pink lines in (b) mark peak separation with regards to $0.7i_T^{bulk}$ line and a pink H bar represents 100 µm, which is a diameter of the electrode. Coloured boxes mark areas of interest discussed in the text.

An effective comparison of line profiles was enabled by dividing, 'normalizing', currents by i_{min} (defined as the smallest current value at the top part of the image over the insulator before the electrode area was reached), as shown in Figure 6-8 (b). This approach seemed to be the most effective for this type of analysis, allowing the line profiles to be arranged at approximately the same initial position. As a result of the convection effects discussed above, the first current values recorded in each line are always higher than the minimum current value in FB mode. This shows how much time – distance into the image – was needed until the

current stabilised, ideally before the electrode area was reached. It also shows if the current after the electrode area decreased, increased or remained at the similar level, allowing a better insight into some of the convection artefacts present in the images.

After normalization, H middle line profiles across the nanoband edge disc electrode in FB mode are stacked as presented in Figure 6-8 (b). Interestingly, the normalized current response at the beginning of each of the middle line profiles appears to overlay each other, independent of the tip working distance (pink box). This shows that the time taken for the disappearance of the convection artefacts is independent of the tip height and consistent with a diffusional process of the redox species. The line profile data also shows that with increasing tip working distance, the current over the peaks (blue box) decreases due to decreasing positive feedback. Furthermore, as more space between the tip and the substrate becomes available, the diffusional gradient between the tip and the substrate electrodes is reduced, allowing product species to diffuse into the bulk before being converted at the tip. As such, a broader tip diffusion field is experienced by the substrate, and both qualitative resolution and peak intensity decrease. This results in the sharpest and the highest peaks at $0.7i_T^{bulk}$, (d = 9.2 µm), where the peak separation is also the most distinctive due to the combination of sharp peaks and a relatively lower current dip between those peaks.

In Figure 6-8 (b), the peaks in the line profiles are consistently higher on the right band electrode than on the left, and an effect is the most pronounced at the shortest tip working distance. This could be due to minor tilting of the substrate, present in all three line profiles. This would mean that higher current value could represent greater positive FB over the conductor area, meaning that the right-hand band was closer to the tip. However, there is no obvious sign of tilting in the insulating regions of the image, suggesting that this is unlikely to be the cause of the differing levels of positive FB observed for the two bands. The more likely explanation is that convective mixing occurs, as discussed in Section 6.2. With decreasing tip working distance the current difference between before and after electrode area – marked with pink and purple boxes in Figure 6-8 (b) respectively – was found to increase. Thus, when the tip is closer to the substrate, there is more effect from the tip's left to right movement when scanning the surface during imaging. Specifically, the right peak and the end of the line profile (purple box) are both of higher currents compared to the left peak and the initial current (pink box), respectively. The amount by which the peak on the right is of a higher current than that on the left is comparable to the difference between left and right extremes of the line profile. Such combination of current differences is a strong indication that convection rather than tilting is present in the line profiles.

Finally, vertical dashed lines through the peaks in Figure 6-8 (b) represent position of the bands separated by 100 µm, which is the nominal value of the MNEE diameter. When examining line profiles more closely, the peak separation is 100, 95 and 90 µm from the

smallest to the greatest imaging distances. From this and from visual representation, the peak separations are indeed 100 µm with an experimental error, consistent with the step size during SECM imaging of 5 µm. The deviation at longer tip working distances likely arises due to an additional current contribution towards the centre of the cavity, where the band diffusion fields begin to overlap. These peak positions are discussed further in Section 6.3.6. At higher *d*, the hemispherical diffusion field profile has grown the most, and, as expected, this results in the two peaks starting to coalesce. However, the nanoband features presented by the distinct peaks are still present. These H middle line profiles show more clearly than the 2D images that the nanoband features are preserved in all three images, including the one collected at the greatest *d*.

6.3.2 Horizontal line profile analysis in SG-TC mode

Equivalent raw and normalized to i_{min} H middle line profiles at the three tip working distances in SG-TC mode are presented in Figure 6-9. During the normalization process, the currents were adjusted to be positive, enabling a clear comparison between the line profiles and also between the two imaging modes.

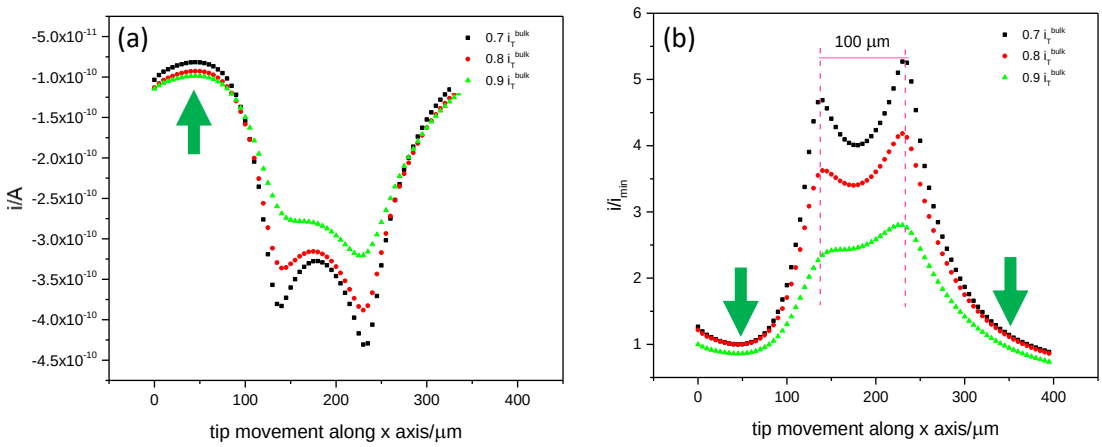

Figure 6-9. Nanoband disc H middle line profiles in SG-TC mode at the three tip-substrate distances in (a) raw and (b) normalized to i_{min} forms. Dotted lines in (b) mark peak separation with regards to $0.7i_T^{bulk}$ and the bar represents 100 µm (diameter of the MNEE). Green arrows mark areas of interest discussed in the text.

An important difference from the FB mode line profiles in Section 6.3.1 is seen in the raw current line profile comparison in Figure 6-9 (a). First, the initial profiles (green arrow) over the insulator are at approximately the same values for all imaging distances without the need to normalize them. However, this apparently changed less steeply than in FB mode. It should be remembered that the mass transport limited oxidation potential is constantly applied to the substrate rather than the tip electrode, hence the tip current is due to the reduction of $FcMeOH^+$. In theory, this current should be zero over the insulator due to the absence of any

$FcMeOH^+$ at a significant distance from the nanoband electrode. However, in practice a small reductive current is still observed at the tip due to residual $FcMeOH^+$ present in solution near the electrode (either generated by the band electrode and diffusing laterally during previous experiments or due to aerobic oxidation of FcMeOH due to the presence of oxygen), similarly as in Chapter 5.

In the normalized (i/i_{min}) line profiles in Figure 6-9 (b), the arrows mark initial and end profiles of the line profiles (before and after the peaks), respectively, which, differ much less compared to the FB mode. This is because in SG-TC mode there is no/little current over the insulator due to the absence of any product (generated on the substrate electrode) in the bulk and the hindered diffusion of product from the substrate that scales with *d*. In FB mode, the edge current values are higher due to the species being oxidised and being present in abundance (0.5 mM), resulting in smaller normalized relative currents. Further, both sides of the normalized line profiles are more similar in current values in SG-TC mode, supporting the observations from the image analysis that the convective effects are less important in SG-TC mode.

Similarly, as in FB mode, the current measured over the right-hand band electrode in Figure 6-9 is higher than on the left. However, the peak current values differ by a greater extent in SG-TC mode than in FB mode. From H line profiles, the right-hand peak is between 12-16 % higher than the left peak, which may be due to an enhanced convective effect within the relatively large substrate's diffusion field. It is shown that this convective effect is emphasized over the electrode area but is not carried further on to the area outside the electrode, while in FB mode, convection effects are present on both the right-hand peak and end profile of the line profile. In SG-TC mode, the tip significantly affects the substrate's hemispherical diffusion field, displacing some $FcMeOH^+$ species generated at the left-hand band electrode with the possible addition of feedback effects further enhancing the currents. This effect appears to be less pronounced in FB mode where the small diffusion field at the tip is affected by the underlying substrate electrode only when directly above it.

With increasing tip working distances the peak currents decrease due to the concentration of $FcMeOH^+$ species becoming diluted with distance from the band electrode as the diffusion field extends deeper into solution. At shorter tip working distances there may be added contribution of positive feedback effects due to the regenerated FcMeOH at the tip diffusing to the substrate and becoming oxidised again. But the peaks are still less sharp than in FB mode, which has been shown be generate higher spatial resolution images of the electrodes and hence sharper peaks at all *d* in the middle line profiles.

The peaks are close to 100 µm separation (H dashed lines in Figure 6-9 (b)), but when examining the peak values from the graph in a greater detail, the peak separation includes more than the experimental error of 5 µm observed in FB mode. The peak separation values

are 90, 90 and 80 µm at *d* = 9.2; 13.2 and 22.1 µm, respectively, (Section 6.3.6) suggesting that the band features are less resolved at comparable distance and the establishment of hemispherical diffusion over the substrate is more rapid, due to $FcMeOH^+$ species emerging from the opposing band beginning to contribute to the measured current. This is not unexpected and is consistent with the other observations established throughout this chapter that SG-TC mode generates images of less localized features and more effectively maps the onset of substrate diffusion profiles. As the tip working distance is increased, the peaks start to both overlap and get closer together, reflecting progressive development of a complete hemispherical diffusion field over the substrate electrode. An overall trend of increasing resolution of the peaks, presented as increasing currents, with decreasing tip working distance is present in both modes.

6.3.3 Evaluation of convection effects from FB mode middle line profiles

In Figure 6-10, H and V middle line profiles were extracted from both nanoband edge disc and square electrode images collected at *d* = 13.2 µm in order to evaluate differences between the directions of the line profiles in FB mode. This allows evaluation of convection effects, the variation of which with distance along the profile is expected to be fully eliminated in these V line profiles since the tip movement when scanning the surface was from left to right, rather than top to bottom (V direction). Such a convective mixing effect is an imaging artefact, which should be minimised and at least understood to simplify and assist in the data analysis process.

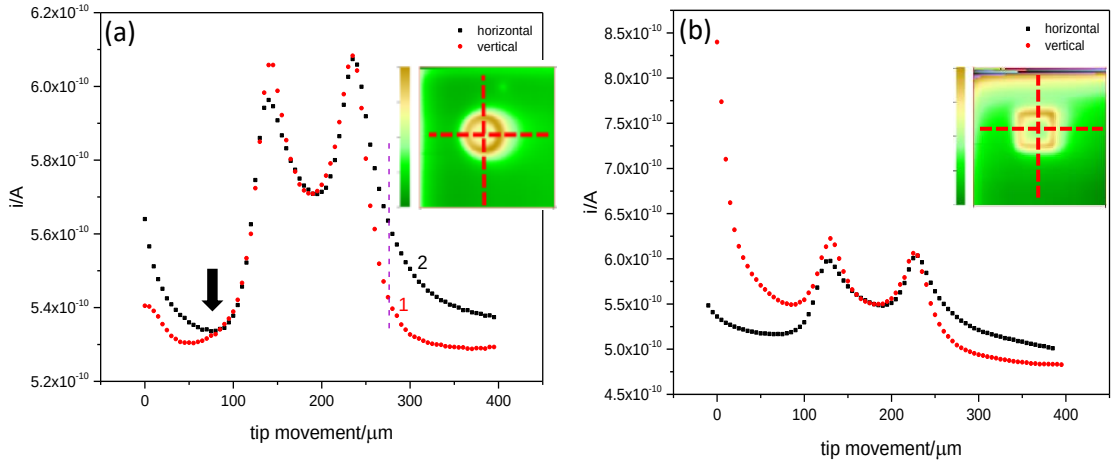

Figure 6-10. H (black squares) and V (red circles) middle line profiles, represented as red dashed lines in the inserts of the SECM electrode's image collected at d = 13.2 µm in FB mode: (a) nanoband disc (dashed vertical line marks x = 275 µm), (b) nanoband square. Vertical arrow and numbers 1-2 in (a) mark areas of focus for comparison between the two line profiles, applicable to both graphs.

In Figure 6-10 (a), a nanoband edge disc electrode image and its H and V middle line profiles are shown in FB mode. An arrow indicates the area where the first peak (electrode area) starts, and numbers 1-2 mark the end of the second peak (electrode area) in V and H line profiles, respectively. The initial current in the V line profile is lower than in H line profile, since the

former is composed from middle points of each H line profile, while the latter is an original scan line, in which the currents were still stabilising at the beginning of the line (due to the convective effects). Hence, higher currents are the result of the local stirring at the tip. The V line profile also shows some decreasing tendency of the initial currents, but this is due to the common observation of higher tip current values over the first few (H) line profiles due to gradual tip conditioning at the beginning of the image. Therefore, both line profiles contain artefacts, but they differ in their origin.

As the line profiles reach the 100 µm position, marked with a black arrow in Figure 6-10 (a), both currents overlap, as expected, showing that the differences between the two line profiles at this point are minimal. This correspondence in current broadly continues through the middle area between the two bands and even just after the second band. The peaks in the V line profile are of the same current value, suggesting symmetry and absence of convection effects, unlike in H line profile, where the left-hand peak is of lower currents than the right-hand one, as discussed above, being diagnostic of a convection effect.

On the right side of the bands, convection effects can also be clearly observed and quantified by comparing the H line profile with the V line profile. At position 2 in Figure 6-10 (a), the line is at much higher currents than when it was at the position marked with the arrow. When comparing positions 1 and 2, it is obvious that the V line profile is narrower and more symmetric. Here, position 2 indicates a much wider H profile due to a convection artefact. The greatest difference between V and H lines at x = 275 is 0.0208 nA, meaning that the V line profile point is at 3.7% lower current than the equivalent H profile. The convective effect is therefore relatively small but, given that the maximum peak currents are only approximately 15% above the baseline current, this value is over 20% of the peak response and therefore quite significant.

In Figure 6-10 (b), the V line profile from the nanoband square image is rather disturbed due to higher currents at the top of the image, discussed in the above sections. Thus, data analysis is seen to be challenging, and it could lead to misleading conclusions and imprecise estimation of the convection contribution. A comparison between the two images and their middle H and V line profile in Figure 6-10 shows the importance of having collected a good resolution and tip conditioning artefact-free images, which allows logical evaluation of the presence of convective effects. Using this knowledge, other images can be evaluated in a more controlled and confident manner to prevent inaccurate quantitation when comparing such line profiles. Such affected data also shows the need for consideration of convective effects and extraction of V profiles for quantitative analysis, as presented in Chapter 7. This allows a full evaluation of experimental line profiles after allowing for the effect of any imaging artefacts.

6.3.4 Evaluation of convection from the line profiles: SG-TC versus FB mode

SG-TC mode H and V middle line profiles across the nanoband edge disc and square electrode images collected at d = 13.2 µm are presented in Figure 6-11. Convection effects and other artefacts, as discussed in the above section regarding FB mode data, can again be seen in SG-TC mode, which data are compared with the equivalent FB mode data.

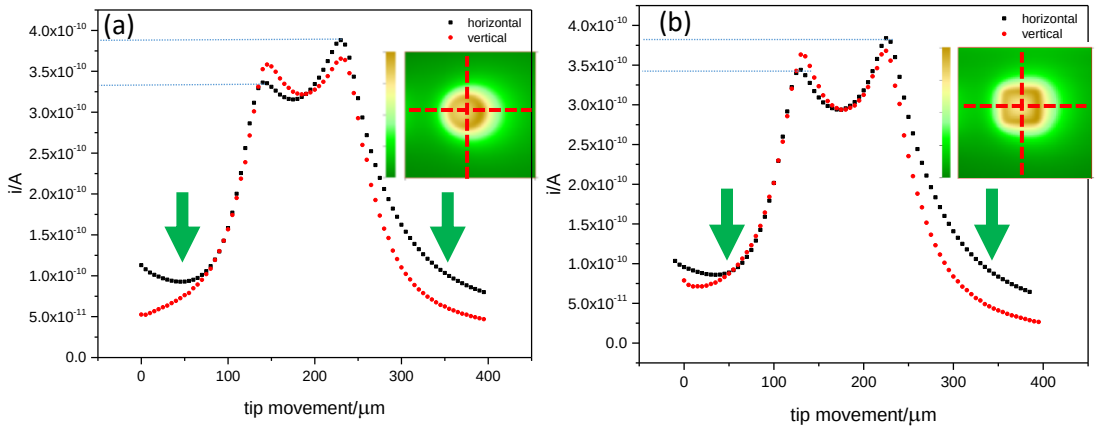

Figure 6-11. H (black squares) and V (red dots) middle line profiles across the nanoband edge (a) disc and (b) square electrodes in SG-TC mode at d = 13.2 µm with the inserts of the SECM electrode's image, containing red dashed lines presenting these line profiles. Blue dotted lines lead to the peak current values from H line profile on y-axis.

The beginning and end profiles from the disc nanoband electrode, marked with the green arrows in Figure 6-11 (a), are similar to the nanoband disc line profiles in FB mode in Figure 6-10 (a). The H line profiles are again of higher initial and final currents compared to the V ones, where both currents are comparable, suggesting that similarly to FB mode convection is more prominent in the H line profile. As in FB mode, the line profiles over the peak area are broadly overlapping, showing correspondence between H and V line profiles at these specific parts of the line profile.

Differences between the peak currents in H and V line profiles are greater in SG-TC than in FB mode, confirming that convection is more important over the electrode region in the former. The peak currents from the H line profile in Figure 6-11 (a) (blue dashed lines) show that the right-hand peak current is 0.052 nA higher than the left-hand peak. As such, convection effects result in a rather significant 13% difference in peak current values, compared to 2% difference in FB mode. The higher sensitivity of SG-TC mode to convective effects is expected, as diffusion governed mass transfer to the smaller tip in FB mode is more efficient. The peak currents in V line profile are almost identical, again reflecting the absence of convection effects which vary along the profile and giving complete symmetry in this direction. This observation again highlights the importance of considering the tip scan direction when interpreting current differences observed in SECM images.

Regarding nanoband edge square H and V middle line profile in Figure 6-11 (b), they are more comparable than the equivalent FB mode data, where the data is significantly affected by tip conditioning artefacts. In both cases, H and V current profiles start to correspond just before the first peak as a result of a marked decrease in convection effects in the collected data. The H line profile peak currents in (a) are approximately 0.33 nA and 0.38 nA for the disc; lower and higher than the left and right peaks (0.36 nA) from the V line profile, respectively. The peak currents from H line profile (0.34 nA and 0.38 nA) also differ from the V profile (0.36 nA) in the square data in (b) and there are similar differences at the end of the H and V line profiles for disc and square. This suggests similar convection effects over the square electrode area compared to the disc. Due to convection effects the H line profile is again at higher currents at both the beginning and end of the line profile (green arrows) than the V line profile in the disc and square MNEE electrode data. The effects are smaller on the left side of the line profile for the square as the difference between V and H line profiles is approximately 0.05 nA (< 2%), but this again likely to be due to two different (time dependent tip conditioning and convective) tip artefacts.

One of the main differences between disc and square data sets in Figure 6-11 regarding V line profiles is that the ending profile of the square nanoband line profile is at lower current values than the beginning profile. When evaluating the SECM image of the square electrode, little differences between all four sides of the electrode are noticeable. However, from this closer examination of this line profile, it seems that not only convection but also some time-dependent tip currents or tilting artefact could be present. However, as the peaks in this V line profile are at equivalent current values, it suggests that top to bottom tilting was not present. This means that time-dependent tip currents must have affected the early portion of this SG-TC mode image, and this affects V profiles more than H. In V line profiles, the current decrease across the profile as a result of time difference between collected data points. In the H line profile, data points were collected one after another, having minimal time difference between each point. As the V line profile was constructed from the middle data points in each H line scan, the time differences are greater (than the time taken for one H scan and the for tip to return and rest before the next scan) and the current decrease can be much more significant. These time-dependent tip currents in SG-TC mode therefore reflect a tip conditioning artefact in the V line profile data.

6.3.5 Vertical line profile dependency on the tip working distance

Convection effect has been established to be present in both FB and SG-TC modes, as indicated by its consistent occurrence in the H line profile data and its essential absence in the V direction. Thus, V middle line profiles at three tip working distances of $0.7i_T^{bulk}$, $0.8i_T^{bulk}$ and $0.9i_T^{bulk}$ (d = 9.2, 13.2 and 22.1 µm) in FB and SG-TC modes reflect disc and square nanoband edge electrode shapes with the least amount of interference from convection. These line

profiles are therefore plotted for comparison and analysis in Figure 6-13. The ends of the line profiles now represent not the sides of the image (H line profile), but the top and bottom of the image. The line profiles were each normalized to the minimum current, i_{min}, for each line profile to allow for stacked line profile comparison. From this, the beginning and end currents from all three line profiles are at approximately the same levels in both modes for both electrodes, showing minimal effects of imaging artefacts discussed in the above sections.

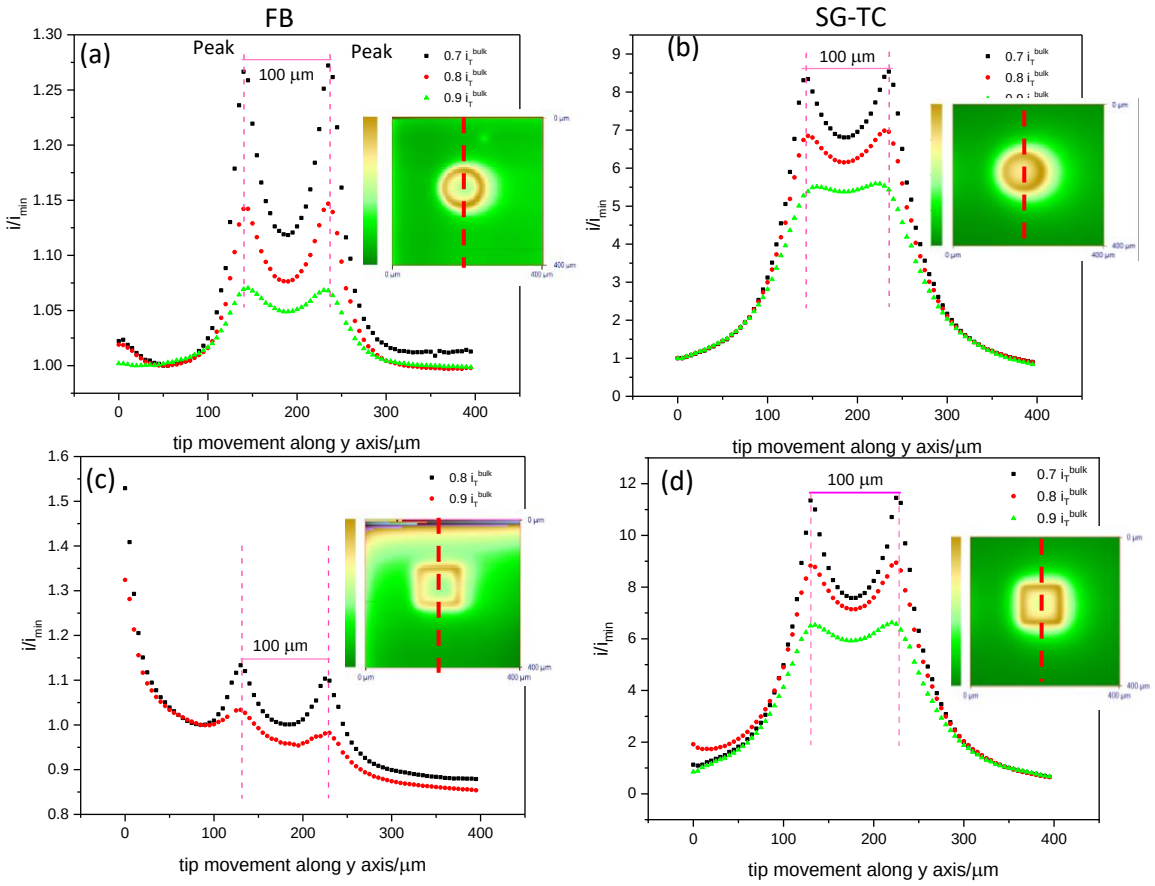

Figure 6-13. V middle line profiles at three d from the images of (a) a nanoband disc in FB and (b) SG-TC modes and (c) a nanoband square in FB and (d) SG-TC modes. Inserts in each are SECM images of the respective electrode, all imaged at d = 9.2 µm, except nanoband square electrode in (c) imaged at d = 13.2 µm due to the absence of this data. Red dashed lines on images mark the middle of the electrode, and pink dashed lines in graphs mark peak positions at d = 9.2 µm (or 13.2 um for (c)).

In all V line profiles in Figure 6-13 the peak separation is around 100 µm, as seen from the pink dashed lines indicating the band electrode positions in the figure. The currents in between the two peaks are overall higher in SG-TC than FB mode, once again confirming that diffusional broadening (hemispherical diffusion overlap from the band sides) is more pronounced in SG-TC mode. In both modes, the size of the dip between the peaks is dependent on *d*, exhibiting as expected a higher current value with increasing tip working distance, resulting in more diffusional overlap and poorer peak resolution. In all cases, the

peaks are the sharpest at the smallest *d,* and as *d* increases the image begins to resemble a micro electrode with a single hemispherical diffusion field across the entire electrode structure[5]. The two peak currents are also comparable in all line profiles, reflecting symmetry and uniform activity of the band.

Several subtle line profile differences in SG-TC mode are present due to the differences of the electrode geometry. In Figure 6-13 (d), the nanoband square has clearer and sharper peaks than the disc at the same tip working distances in (b). This is because the corners of the square are further from the centre than the equivalent band position in the circular geometry, so they contribute less to the current in the centre. In other words, due to the decreased separation between the two bands, greater diffusional overlap is present over the insulator cavity in a disc geometry.

Nanoband square in FB mode in Figure 6-13 (c) suffers from various artefacts discussed throughout this chapter. Comparison of its profile at different heights is valid but not studied in a great detail in this section also because in this early data the SECM image at 9.2 µm tip working distance was not collected. From comparison with the rest of the data it is clear that (c) is more challenging to be evaluated yet the line profiles preserve the idea that the peak separation is around 100 µm value and the peaks get more resolved at smaller tip working distances.

6.3.6 Peak separation dependency on the tip working distance

Both, H and V middle line profiles were evaluated with respect to the tip working distance variation in the above sections. In this section, the effect of *d* on the peak positions and peak current values as well as the peak separation at the three tip working distances ($0.7i_t^{bulk}$, $0.8i_t^{bulk}$ and $0.9i_t^{bulk}$ or d = 9.2, 13.2 and 22.1 µm) are evaluated in a greater detail. Data from nanoband edge disc electrode in FB and SG-TC modes are shown in Table 6-1 and Table 6-2, respectively. Peak separation in both modes have been discussed in the above sections when it contributed to other analysis, hence only additional observations are made in this section.

From Table 6-1, the relative increase of the right hand peak current (peak 2) over the left peak current (peak 1) from the H line profile in FB mode is only 1-2% at all three tip working distances. In other words, the apparent difference between the peak currents observed in the graphical line profile analysis are relatively minimal from a numerical perspective. The V line profiles suggest that the peaks are of almost identical current values, as the difference between them is smaller than 1%, which is considered within experimental error and is consistent with observations from the middle line profile analysis.

d	*X_1, peak 1/μm*	*Current/nA*	*X_2, peak 2/μm*	*Current/nA*	*Peak separation*	*Peak current ratio (peak2/peak1)*
H						
0.7i_T^{bulk}	135	0.587	235	0.601	100	1.02
0.8i_T^{bulk}	140	0.596	235	0.607	95	1.02
0.9i_T^{bulk}	145	0.605	235	0.612	90	1.01
V						
0.7i_T^{bulk}	140	0.603	235	0.606	95	1.00
0.8i_T^{bulk}	140	0.606	235	0.608	95	1.00
0.9i_T^{bulk}	145	0.610	230	0.609	85	1.00

Table 6-1. Peak position (μm), x_1 and x_2, and peak current (nA) comparison from a nanoband edge disc electrode in FB mode at three tip working distances, d, from H and V middle line profiles.

The peak separation values of H and V middle line profiles are also shown in Table 6-1. Both H and V peak separation values reflect gradual hemispherical field development with increasing tip working distance. In both cases at $0.7i_T^{bulk}$ the peak separation is 100 μm within the error of the measurement, reflecting the high dimensional fidelity of the microfabricated electrode. As the imaging step was 5 μm, making it in some cases subjective as to which pixel should be used for each peak position value, this is likely to introduce an error of up to 5 μm. The overall error of ±7 μm for the peak separation is obtained using the simple error addition rule (total error = $\sqrt{e_1^2 + e_2^2} = \sqrt{5^2 + 5^2} \approx 7$, where e_n – error in measurement of peak 1 and peak 2).

Smaller peak separation values are observed in SG-TC mode than FB mode at the same *d*, as shown in Table 6-2. This confirms that the hemispherical diffusion field developing in between the two bands is more prominent in the former mode. Peak separations from both H and V line profiles are the same for the two smallest *d* values, again being well within the measurement error. However, the peak separation in this case is identical at $0.7i_T^{bulk}$ and $0.8i_T^{bulk}$ tip working distances in both H and V line profiles. This suggests that little resolution improvement was achieved with decreasing tip working distance in this range and possibly a significantly smaller *d* should be used to capture more of the nanoband features in SG-TC mode. At $0.9i_T^{bulk}$, the closest separation indicative of the most hemispherical diffusion profile is recorded together with greater than the expected experimental error. The higher peak separation observed in the H line profile compared to the V line profile suggests the influence of convective effects.

The peak current values also vary more in SG-TC than in FB mode (last column in Table 6-2). In H line profiles the values differ by 12-16%, while in V line profiles only by 1-2%. This quantitatively confirms previous observations regarding convection effects, which is significantly present only in H line profiles. V line profiles contain such little peak current

difference that it can be considered to be due to experimental error related to peak position identification and time-dependent tip currents.

Overall, it is possible to obtain higher fidelity and lower errors from the V line profile than the H line profile data, due to the absence of convective effects. The alternative of longer increment times or smaller step sizes could be used to minimise these artefacts for H data, but both of these would mean that each imaging experiment would take significantly longer time than it was required for this data collection (approximately 30 min per image).

d	*X_1, peak 1/µm*	*Current/nA*	*X_2, peak 2/µm*	*Current/nA*	*Peak separation*	*Peak ratio (peak2/peak1)*
H						
$0.7i_T^{bulk}$	140	-0.383	230	-0.431	90	1.12
$0.8i_T^{bulk}$	140	-0.336	230	-0.388	90	1.15
$0.9i_T^{bulk}$	150	-0.277	230	-0.320	80	1.16
V						
$0.7i_T^{bulk}$	145	-0.403	235	-0.413	90	1.02
$0.8i_T^{bulk}$	145	-0.358	235	-0.364	90	1.02
$0.9i_T^{bulk}$	155	-0.298	225	-0.302	70	1.01

Table 6-2. Peak position (µm), x_1 and x_2, and peak current (nA) comparison from a nanoband edge disc electrode in SG-TC mode at three tip working distances, d, from H and V middle line profiles.

6.3.7 Hemispherical diffusion field dependency on imaged electrode size

In this chapter, the discussion has focused on the tip-substrate separation, *d*, effect on the images and their middle line profiles, which suggested that the evolution of a hemispherical diffusion field with *d* over an electrode area was more pronounced in SG-TC than FB mode. In this section, V middle line profiles (containing the least amount of artefacts) are further evaluated from both micro and nanoband edge disc and square electrodes, as shown in Figure 6-14, connecting this analysis to Chapter 5. Middle line profiles from the images collected at the greatest, *d* = 22.1 µm, and the smallest, *d* = 9.20 µm, tip working distances in SG-TC mode used in this work are compared.

From Figure 6-14, the maximum current values are significantly higher for both micro electrodes compared to the equivalent nanoband electrodes, as expected due to the greater active Pt area. This reflects greater positive feedback response over the micro electrodes, resulting in a single-peak or flat-topped response. In Figure 6-14 (a), at *d* = 22.1 µm the peaks from both geometry of microelectrode are relatively peaked and narrower than the actual diameter of the electrode (Chapter 5). Such a response suggests a clear hemispherical diffusion field profile in each case, though, when comparing the two, it is still possible to clearly separate disc and square geometry (which has a flatter top).

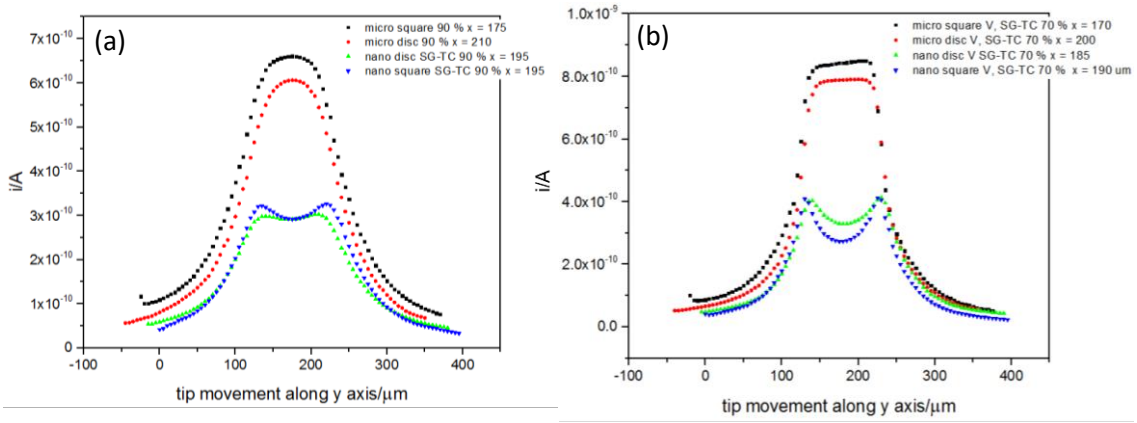

Figure 6-14. Comparison between microelectrode and nanoband edge electrode V middle line profiles at (a) d = 22.1 µm and (b) d = 9.20 µm in SG-TC mode.

MNEEs at both *d* in Figure 6-14 generated easy to sense, high signal-to-noise ratio currents, smaller in value than from micro electrodes and giving two-peak signals. Unlike line profiles from micro electrodes, the peak separations for both geometry MNEEs preserve the diameter of approximately 100 µm, as discussed in Section 6.3.6. As expected and discussed in the previous section, the line profile from a nanoband square preserves this separation more clearly than the disc at both *d* values. Nanoband disc and square peaks from line profiles at *d* = 9.2 µm in (b) suggest that the resolution of the disc peaks will be more affected by the distance due to the greater width of both peaks.

Middle line profiles from the micro electrodes at *d* = 9.2 µm in (b) are both flat-topped, and hence more similar than at *d* = 22.1 µm. However, the one from the microdisc is still characteristic for having rounder peak edges due to a more readily established hemispherical diffusion field profile for the disc geometry.

At *d* = 22.1 µm, a more rounded top indicating hemispherical diffusion can be seen for both scale electrodes, and the differences in shape between MNEE and micro disc are starting to diminish. Hemispherical diffusion field development resolution is clearly affected therefore not only by the tip working distance, but also by the electrode size and geometry. The subtle changes may not be observed when evaluating the line profiles individually, but it is possible to see them clearly in this comparison of several different line profiles.

6.4 CONCLUSIONS

High spatial resolution SECM images of single nanoband disc and square electrodes were collected in FB and SG-TC modes. Greater hemispherical diffusional overlap from the sides of the band over the middle of the disc than the square electrode was observed at all *d* as a result of the differences of the electrode geometry. Diffusion field growth with increasing *d* was recorded as predicted in both modes for both electrodes, and the currents over the insulator area in the middle of the electrode increased compared to relatively consistent and lower currents over the rest of the surrounding insulator. From both qualitative image analysis and semi-quantitative analysis of middle line profiles (extracted from these images), electrode dimensional resolution, as expected, was found to decrease with increasing tip working distance in both modes as diffusional broadening occurred. Thus, the peak separation in these middle line profiles decreased with increasing *d*, and the peaks also appeared more rounded, which reflects the hemispherical diffusion field development; again all of this was more prominent to the disc nanoband electrode than the square nanoband at the same *d*. SG-TC mode images of both electrodes were of lower spatial resolution at all tip working distances compared to FB mode, just like in Chapter 5.

Extracted H and V middle line profiles were overall largely symmetrical, except over the area where convection effects were present in the H line profiles, either due to the tip's left to right constant movement during imaging, or its right to left return to start scanning the next line. In FB mode, $FcMeOH^+$ is generated at the probe and due to the local stirring effects and availability of the additional FcMeOH from the bulk, enhanced currents are observed on the left side of the electrode region. This is unlike in SG-TC mode, where the left edge was affected only in the H scan lines that passed over the electrode area. In this case, $FcMeOH^+$ generated by the substrate is dragged from right to left upon the probe's return to the $x = 0$ position at the end of each scan line. These effects were somewhat greater in FB mode and increased with decreasing *d.* Convection effects were also observed on the right peak and in this case were greater in SG-TC mode than in FB mode and increased with increasing tip working distance in both modes. FB mode was showed to be more susceptible to time-dependent tip currents, affecting the top part of the image due to the current stabilisation over the initial H line profiles, like in Chapter 6. Such image and middle line profile analysis confirmed that significant tilting was avoided in all images. Together such image analysis has given insight into the fidelity and performance of these electrode systems and provided motivation for the further quantitation of these effects in subsequent chapters.

6.5 REFERENCES

1. Schmueser, I. *et al.* A systematic study of the influence of nanoelectrode dimensions on electrode performance and the implications for electroanalysis and sensing. *Faraday Discuss.* **164**, 295 (2013).

2. Wain, A. J. Scanning electrochemical microscopy for combinatorial screening applications: A mini-review. *Electrochem. commun.* **46**, 9–12 (2014).

3. Wiley, J. Analytical Electrochemistry : The Basic Concepts References and Links. 1996–1997 (2009).

4. Woodvine, H. L., Terry, J. G., Walton, A. J. & Mount, A. R. The development and characterisation of square microfabricated electrode systems. *Analyst* **135**, 1058–1065 (2010).

5. Terry, J. G. *et al.* Nanoscale electrode arrays produced with microscale lithographic techniques for use in biomedical sensing applications. *IET Nanobiotechnol.* **7**, 125–34 (2013).

7 QUANTITATIVE ANALYSIS OF THE LINE PROFILES FROM SECM IMAGES

7.1 INTRODUCTION

In the previous chapter, SECM images of nanoband disc and square single Pt electrodes imaged in FB and SG-TC modes were qualitatively analysed. When evaluating their V and H middle line profiles, it was confirmed that V line profiles were mostly free of significant artefacts, such as convection and time-dependent tip currents, unlike the H ones. Then, semi-quantitative analysis of these line profiles was shown to be possible, allowing evaluation of the peak currents and peak separation, as well as current ratios and convection effects on the end of the line profiles. In this chapter, full quantitative analysis is performed, fitting full experimental line profiles using two approaches: first, a Gaussian function predicting currents and then a modified Bessel function predicting concentration profiles which govern the tip currents.

7.2 QUANTITATIVE LINE PROFILE ANALYSIS USING A GAUSSIAN FUNCTION

7.2.1 Gaussian function suitability

If a line profile from an SECM image passes the Pt band electrode, it does so two times, resulting in a two-peak signal, as seen in the previous chapter from a semi-quantitative analysis of the MNEEs. Then, it is known that diffusion from a point source in spherical coordinates generates radial diffusion, which is fundamentally broadening, resulting in a Gaussian distribution (also known as a normal distribution) of diffusing species.[1,2] A Gaussian distribution was therefore used to fit nanoband edge electrode line profiles, which present two point-like sources of activity. Both experimental peaks are bell shaped, symmetrical and moderately flat on the sides just as expected from a Gaussian, which predicts that the contribution from the surrounding insulator area (the sides of these line profiles) is zero. The diffusion field should not and did not significantly extend over the insulator area at the start and end of the line profile.[3] This is directly applicable to SG-TC mode, measuring the diffusion field around the band electrode, while in FB mode the activity of the substrate affecting the diffusion field around the tip is measured. As a result, there might be some variation in such data fitting effectiveness in the latter due to a more complicated substrate and tip interaction.

The diffusion contribution in each line profile, in fact, originates not only from two individual points. Figure 7-1 (a-b) shows square and disc geometry nanoband edge electrodes, where green dots mark where the H middle line profile would be passing and show the contribution from the diffusion field emerging from the sides of the band towards the middle points. The band is continuous, meaning that there is diffusion contribution from all sides. When using the square geometry in (c), contribution from two sides towards the middle V line is equal at all times, while for the disc in (d) it is more complicated due to varying contribution from the two sides at different points along the V middle line.

In this initial quantitative analysis, it was assumed that in the middle of either V or H line profile the contribution from four sides (left, right, top and bottom) of the electrode is equal. Then, each normalized middle line profile was adjusted in the following way to minimize such additional diffusion field effects in the middle region. The largest integer current value was subtracted from normalized data points at and between the peaks, the residue value was divided by two and subtracted from the normalized current value. This way diffusion contribution only from two sides was expected to be present in this data. The following Gaussian fitting for the square geometry was known to be more applicable than for the disc geometry, which was used in this section for the preliminary analysis and it was further improved in Section 7.3. For the square, the possibility of enhanced diffusion field at the corners was not considered, which is expected not to affect the middle line profiles anyway.

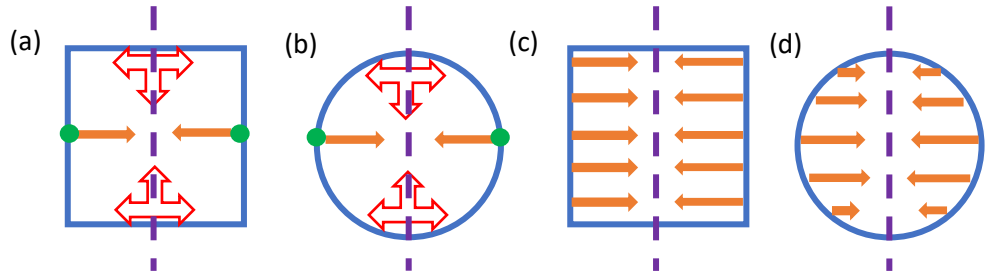

Figure 7-1. Gaussian function models diffusion from a point source (green dot in (a-b)) but in this study nanoband edge electrodes are continuous lines, forming a square or a disc. Therefore, in addition to the solid orange arrows (a-b), which present diffusion from a point, additional diffusion from the band sides (empty red arrows) contributes towards the middle of each line profile in either V or H direction. Simple data adjustment is valid for the (c) square geometry, having equal contribution from the band sides towards the middle line, since the sides of the band are equally separated at all times. For the (d) disc geometry the contribution from the sides to the middle line is less straight forward.

7.2.2 Fitting specifications

The data adjustment discussed above reduced the diffusion field impact from four to two sides, representing a line profile-like scenario. If this was an individual four-point scenario, such adjustment would be sufficient. In this case, a single line profile across the middle of the

electrode is technically a two-point scenario, and any additional diffusion field from the rest of the band was allowed in the fitting error. In some line profiles after such data adjustment, there was a gap between adjusted and not adjusted data points, especially noticeable at greater tip working distances. To avoid fitting complication, some data points at this junction were deleted to obtain as smooth as possible line profile. The resulting signal was fitted with a dual-peak Gaussian distribution, using the following equation:

$$y = y_0 + \left(\frac{A_1}{w_1\sqrt{\frac{\pi}{2}}}\right) * e^{-2\left(\frac{x_1 - x_{c,1}}{w_1}\right)^2} + \left(\frac{A_2}{w_2\sqrt{\frac{\pi}{2}}}\right) * e^{-2\left(\frac{x_2 - x_{c,2}}{w_2}\right)^2} \quad (7.1)$$

where:

y_0 = data offset (fixed to 1 in the majority of the fitting examples),

A = area under the curve,

w = peak full width at half maximum (FWHM) (manually adjusted to improve the peak fitting),

x = peak position on the x –axis in H line profile and on the y-axis in V line profile,

x_c = peak position variation for peak 1 and peak 2.

Since high symmetry line profiles were used, it was expected that $w_1 = w_2$ and $A_1 = A_2$. Any deviation from this would reflect imaging artefacts.

The peaks were selected manually, and the parameters were adjusted, setting some of them with fixed values, which are marked as italics in the tables throughout this thesis. Since the peaks in the line profiles consisted of a very small fraction of the total number of data points, the fitting process was skewed so that the points at the very peak had a tendency not to fit, and the peak values had to be manually adjusted. The aim was to fit the peaks arising from the MNEEs by initially fixing the parameter x_c for one or both of the peaks and then adjusting w to fit the peaks and their sides. For both peaks, w was found to be similar, as expected, hence it was fixed to be the same value for both peaks. The area under the curve, A, was left to vary, since it was automatically adjusted to fit w values (A and w dependency).

Overall, this set up avoided the automatic fitting being weighted towards the edges of the line profiles where the majority of the points are, allowing the most important data to be fitted. Fitting was performed on both geometries of the nanoband-edge electrodes and in both FB and SG-TC modes to give more credence to the model using such data analysis. The peak positions and currents over the area in between the peaks from the MNEEs are compared with the responses from the cumulative fit peak (generated from two individual points). Despite the necessity to adjust the settings, the fitting enabled quantitative analysis of the whole

experimental line profiles. This analysis also further emphasizes convection and time-dependent tip current artefacts, the presence of which affect the effectiveness of the fitting.

7.2.3 Determination of the fitting boundaries and parameters

Several boundary limits within the line profiles were explored to find the most effective fitting approach. Nanoband disc FB mode V and H middle line profiles from the three tip working distances of $0.7i_T^{bulk}$, $0.8i_T^{bulk}$, $0.9i_T^{bulk}$, also known as d = 9.2 µm, 13.2 µm and 22.1 µm (Section 4.5.5) were used. First, narrow limits containing just one of the peaks, which was fitted as a single Gaussian function, were set and the obtained values from independent fitting to both peaks were compared. However, this model did not allow evaluation of the artefacts, which was also the focus of this analysis, or the experimental dual-peak response, which was to be compared with the theoretical cumulative response of the diffusion field expanding from two points. The middle area between the peaks was also a key area of interest and the boundaries including both peaks were introduced.

In Figure 7-2, the limits (V red lines) captured both peaks from V in (a) and H in (b) middle line profile from the nanoband edge disc electrode. This means that data points between the peaks and on the sides (towards the beginning and ending) of the line profiles were included. Setting the limits in this way removed the majority of data points on the very sides of the peaks, so-called 'wings', forcing the fit to be weighted towards the important data points in the middle of the line profile. V line profile fitting in (a) led to a closer overlap between the experimental and modelled signals than H line profile fitting in (b), emphasizing artefacts on the right side of this line profile. Thus, the fitted line does not match the experimental data due to imaging artefacts, such as convection effects (Section 6.2.2), which are seen even more clearly against the Gaussian fitting. The function does not model any of the artefacts or tilting effects.

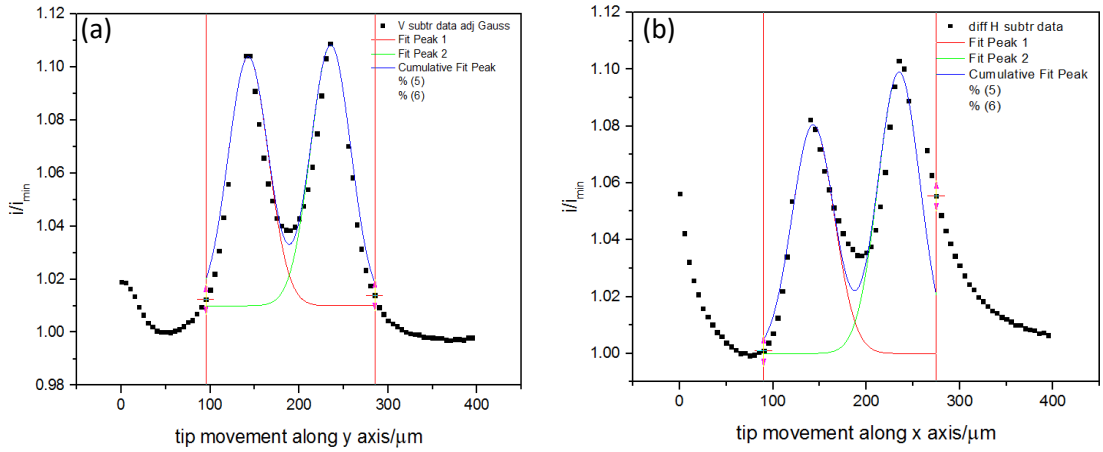

Figure 7-2. Gaussian fitting (blue line) to nanoband disc electrode (a) V and (b) H middle line profiles (black squares) in FB mode, when the fitting limits (V red lines) excluded majority of the data points on the sides.

To add some consistency to the model, the limits on both sides were expanded to $y = 1$ or as close to this value as possible. This introduced another fixed parameter, offering clearer guidance where to set the fitting boundaries on each line profile, since in the previous example it was relatively ambiguous from where data points should become excluded from the fitting. Having established fitting boundaries, the other parameters were adjusted in two ways. First, the peak positions were allowed to vary, and their width was set as the same value for both H and V line profiles, representing the expected symmetry between the two line profiles. From Table 7-1, the R^2 parameter, indicating the efficiency of the overall fit, was mostly over 0.9, suggesting that an overall good fit was obtained for both H and V middle line profiles and suggesting a good agreement between experimentally measured hemispherical diffusion field and prediction generated by the Gaussian function. As expected, the fit quality was always better for V than equivalent H line profiles, the latter suffering from more artefacts. However, the offset, $y_{0,}$ parameter was allowed to be adjusted automatically, meaning that this approach was not uniform enough, allowing for too many variations between the data sets.

	Vertical		*Horizontal*	
d = 9.2 µm	Peak 1	Peak 2	Peak 1	Peak 2
y_0	1.06 ± 0.0022	1.06 ± 0.0022	1.06 ± 0.0026	1.06 ± 0.0026
x_c	141.55 ± 0.60	237.09 ± 0.48	139.99 ± 1.03	241.72 ± 0.65
*w**	*27.06*	*27.06*	*27.06*	*27.06*
A	4.69 ± 0.17	5.29 ± 0.19	*4*	5.86 ± 0.31
R^2	0.981		0.940	
d = 13.2 µm				
y_0	*1.01*	*1.01*	*1*	*1*
x_c	142.79 ± 1.17	235.47 ± 1.08	*143*	*235*
*w**	45.05 ± 1.28	45.05 ± 1.28	*45.05*	*45.05*
A	*5.3*	*5.55*	4.55 ± 0.30	5.59 ± 0.29
R^2	0.909		0.782	
d = 22.1 µm				
y_0	1.00 ± 0.0012	1.00 ± 0.0012	*1*	*1*
Xc	142.99 ± 0.96	232.75 ± 1.00	*146*	*240*
*w**	*56.25*	*56.25*	*56.25*	*56.25*
A	2.85209 ± 0.1214	2.74 ± 0.12	1.94 ± 0.120	2.97 ± 0.13
R^2	0.961		0.826	

Table 7-1. Parameters from fitting to limited boundaries for nanoband disc in FB mode allowing parameters to vary. The w values are in green and they were kept the same for H and V line profiles at each d.

In the second fitting attempt, the best fit was achieved for H and V line profiles individually, and then the obtained parameters were compared. This allowed for a better evaluation of the artefacts and symmetry between the two lines. The y_0 parameter was also mostly set to 1, which was indeed always valid for the LHS of the normalized line profile before the electrode area. On the RHS the offset value was not necessarily precise, since convection or time-

dependent tip currents were present to a various extent on this side. However, such setting introduced more consistency in the experimental data fitting, and it was not used only when fitting the nanoband square V line profiles which experienced significant artefacts; hence the fitting was adjusted accordingly.

Table 7-2 shows the fitting parameters from this second approach, in which the peak position and width were also fitted more carefully. The w and x_c were manually adjusted until the best visual fit were achieved, as presented in the later discussion regarding Figure 7-5. From Table 7-2, w values in the H and V line profiles differed by 3 µm for the two smaller imaging distances and only by 1 µm for d = 22.1 µm. This suggests that at greater d the electrode features got more fused due to the greater hemispherical diffusion field of the substrate (diffusional overlap). Nevertheless, the differences were within the experimental error of ±5 µm which is the size of the imaging step, also responsible for relatively large spaces between data points. The peak values were chosen manually, introducing another ±2-3 µm error, resulting in a total of less than ±6 µm error.[4]

	Vertical		*Horizontal*	
d = 9.2 µm	Peak 1	Peak 2	Peak 1	Peak 2
y_0	*1*	*1*	*1*	*1*
x_c	*140*	*238*	*138*	*238*
*w**	*35*	*35*	*38*	*38*
A	8.84 ± 0.41	9.52 ± 0.44	8.29 ± 0.66	10.37 ± 0.74
R^2	0.883		0.611	
d = 13.2 µm				
y_0	*1*	*1*	*1*	*1*
x_c	*142*	*235*	*141*	*238*
*w**	*40*	*40*	*43*	*43*
A	5.31 ± 0.20	5.58± 0.20	4.53 ± 0.37	5.97± 0.36
R^2	0.928		0.691	
d = 22.1 µm				
y_0	*1*	*1*	*1*	*1*
x_c	*144*	*233*	*149*	*240*
*w**	*51*	*51*	*52*	*52*
A	2.96 ± 0.08	2.87 ± 0.08	1.88 ± 0.13	2.83 ± 0.15
R^2	0.958		0.787	

Table 7-2. Parameters from fitting to the middle line profiles from nanoband disc FB mode images at three tip working distance. Fixed parameter (italics) were used to obtain the best fitting. Data corresponds to Figure 7-5.

The obtained R^2 parameter values in Table 7-2 differ from the equivalent ones in Table 7-1. For V line profiles, R^2 decreased by 0.1, then increased by 0.02 and then was approximately the same for $0.7i_T^{bulk}$, $0.8i_T^{bulk}$ and $0.9i_T^{bulk}$, respectively. For H line profiles, in all cases the R^2

values were lower and the differences between the values in two tables are 0.3, 0.09 and 0.04 for $0.7i_T^{bulk}$, $0.8i_T^{bulk}$ and $0.9i_T^{bulk}$, respectively, suggesting significantly worse fitting at $0.7i_T^{bulk}$ than described in Table 7-1. From the visual evaluation of the experimental and modelled signal overlap the fitting quality actually improved compared to the one presented in Table 7-1, which is subjective but considered to be more important in this case than the numerical R^2 value. This is because the fitting software calculates the best fit of the majority of data points, treating them all with equal weight, but areas of interest in this analysis were not necessarily with many data points, such as the peaks, resulting in lower overall R^2 value.

Thus, decrease in the value of R^2 parameter was not of a concern and the fitting approach (Table 7-2) was used for the rest of the data fitting. The limits for fitting were clear and easy to set and the overall fitting was relatively consistent. This allows direct comparison between experimental and theoretical diffusion field responses, including the effect of overlapping diffusion fields over the middle/dip between the peaks, as well as evaluation and quantitation of the imaging artefacts in the line profiles.

7.2.4 Nanoband square FB mode middle line profile fitting

To start with, nanoband edge square electrode middle line profiles from FB mode images were fitted. As shown in Figure 7-1, this geometry was expected to be in a better agreement with Gaussian model than the disc geometry. From Figure 7-3 Gaussian fitting was effective for both H and V middle line profiles, showing close correlation between experimental and modelled signals in all graphs. V line profiles on the left are more affected by the artefacts than the H line profiles on the right, unusually but as explained throughout Chapter 6 and specifically in Section 6.3.

Even though variation of data may have caused some hesitation in earlier analysis, overall it is exciting to see it. The aim of this data collection was not simply obtaining quality images of hemispherical diffusion field evolution at several tip working distances from previously fabricated electrodes, but also to use these images for qualitative and, importantly, quantitative analysis. If all images were free from artefacts, it would be difficult to make comparisons and derive some of the conclusions regarding when and where SECM imaging artefacts occur.

Due to such significant differences between V and H line profiles, *w* values are significantly different. From Table 7-3, *w* values are 23 and 36 µm for $0.8i_T^{bulk}$ and 65 and 44 µm for $0.9i_T^{bulk}$ in V and H line profiles, respectively. The peak width in H line profile is expected to be wider than in V line profile due to convection effects, but it was not the case in this example. There was inconsistency in which direction the peaks were getting wider, and it is clear that H and V lines are not symmetrical. From qualitative image analysis in Chapter 6, it is known that the reason for the missing symmetry between H and V line profiles is the imaging artefacts and/or tilting rather than the performance of the electrode, known to be rigid and well-defined.

Understanding the reason of such artefacts occurrence allows to evaluate results with more caution and identify if this is the substrate's real feature or not. This knowledge would significantly assist analysis of the not well-defined or of changing activity substrate.

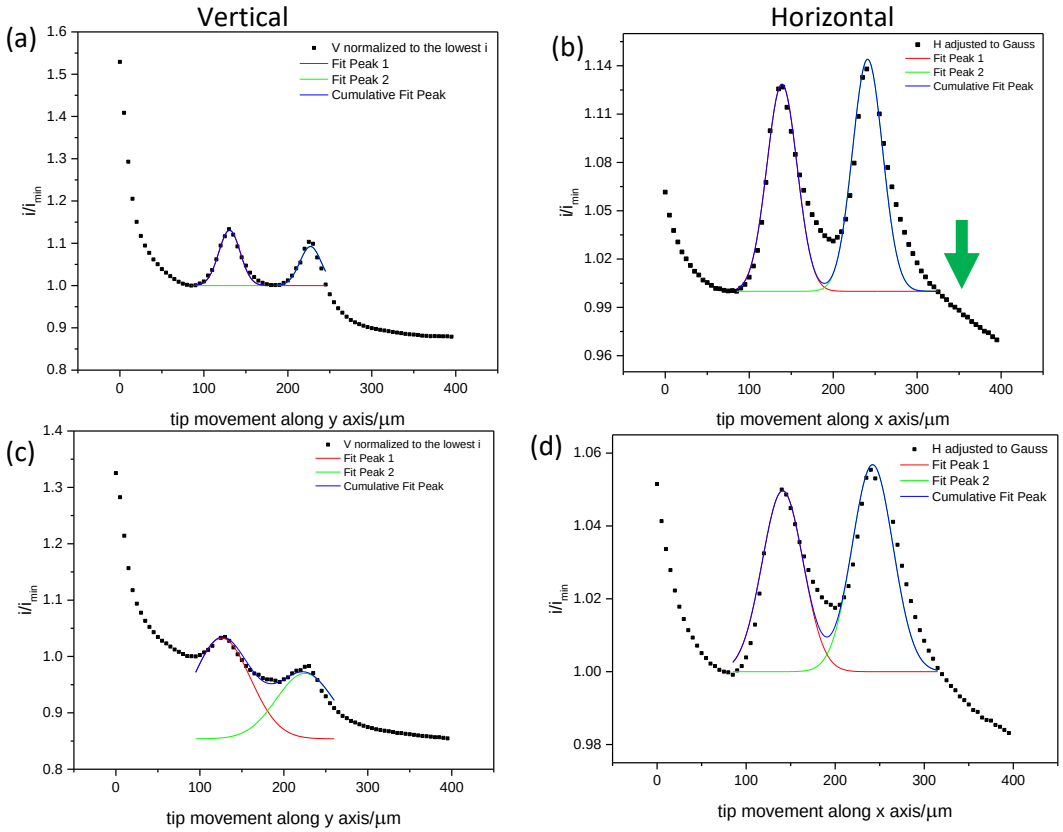

Figure 7-3. Nanoband edge square electrode V (left) and H (right) middle line profiles (black squares) and their cumulative fit peak from Gaussian function (blue line) at (a-b) d = 13.2 µm and (c-d) d = 22.1 µm in FB mode.

As a result of the artefacts in V line profiles, at d = 22.1 µm, the simplest parameter, y-offset, was not set to 1, as shown in Table 7-3, to allow for a more effective fitting. This is an exception, as for the rest of the fitting the value was set to 1, including H line profiles in this section, suggesting that the first peak (LHS) was affected by this artefact at the top of the image. Peak intensities, A_1 and A_2, are differnet to a rather significant extent (12.95 and 7.78), and symmetry in this signal is reassuringly lost.

However, this artefact seems not to have affected the R^2 parameter. It is still of greater values for V line profiles at both tip working distances compared to H line profiles, known to be affected to some extent by convection effects. Since H line profiles in Figure 7-3 (b, d) are more representative of the typical experimental data than V line profiles, such fitting effectiveness suggests that Gaussian model possibly adjusted for the slope in the signal and was still capable of fitting data to a great extent. Despite steep slope profile on the LHS of the line profile due to the imaging artefacts, the fitting confirmed that V line profiles are less

affected by convection unlike H line profiles. Both peaks and their immediate sides fit to a great extent in V line profiles.

Meanwhile, in the H direction, the right part of the line profile after the red line marking fitting boundaries is shifting downwards, marked with a green arrow in Figure 7-3 (b). As discussed in Chapter 6, it is possible that minor tilting artefact was present, and from such quantitative analysis of the whole line profile it is reassuring that the effects are minimal. The electrode area seems to be not affected or affected to a small extent, resulting in a great agreement between experimental and modelled data as well as relatively high R^2 values of 0.8. Similar peak intensity, A_1 and A_2, values reassure that the peak widths are also within a reasonable experimental and/or fitting error.

	Vertical		*Horizontal*	
d = 13.2 µm	Peak 1	Peak 2	Peak 1	Peak 2
y_0	*1*	*1*	*1*	*1*
x_c	130.50 ± 0.54	*227*	*139*	*241*
*w**	*23*	*23*	*36*	*36*
A	3.94 ± 0.13	2.80 ± 0.13	5.80 ± 0.32	6.50 ± 0.36
Reduced Chi-Sqr	8.45E-05		2.88E-04	
R^2	0.955		0.824	
d = 22.1 µm				
y_0	0.87 ± 0.012	0.87 ± 0.012	*1*	*1*
x_c	*127*	*226*	*141*	*241*
*w**	*65*	*65*	*44*	*44*
A	12.95 ± 1.16	7.78 ± 1.15	2.81 ± 0.16	3.16 ± 0.15
Reduced Chi-Sqr	1.22E-04		4.43E-05	
R^2	0.885		0.844	

Table 7-3. Summary of Gaussian fitting for square nanoband edge electrode in FB mode at d = 13.2 µm and d = 22.1 µm.

7.2.5 Nanoband square SG-TC mode middle line profile fitting

Middle line profiles from SG-TC mode nanoband square images were also fitted to check if such fitting model is suitable for both imaging modes. In this case, both H and V line profiles were as expected (Chapter 6), meaning that fitting to the middle line profiles was easier and more reassuring. To avoid repetition, only V line profile fitting results are presented in Figure 7-4.

SG-TC mode data contained less artefacts, such as convection and time-dependent tip currents, than FB mode, as discussed in Section 6.2.3, meaning that the sides of the line profiles are more comparable due to a greater symmetry. This means that fitting boundaries include the LHS from the very first data point and the RHS is very close to the final recorded

point at approximately 0.99. The *y* offset set to 1 was true and reflected a levelled signal. The image collected at 13.2 µm in Figure 7-4 (b) is the most affected by the artefact in this data set, discussed in Section 6.3.4, but it was possible to exclude this side from fitting, allowing to focus the fitting around the peak area.

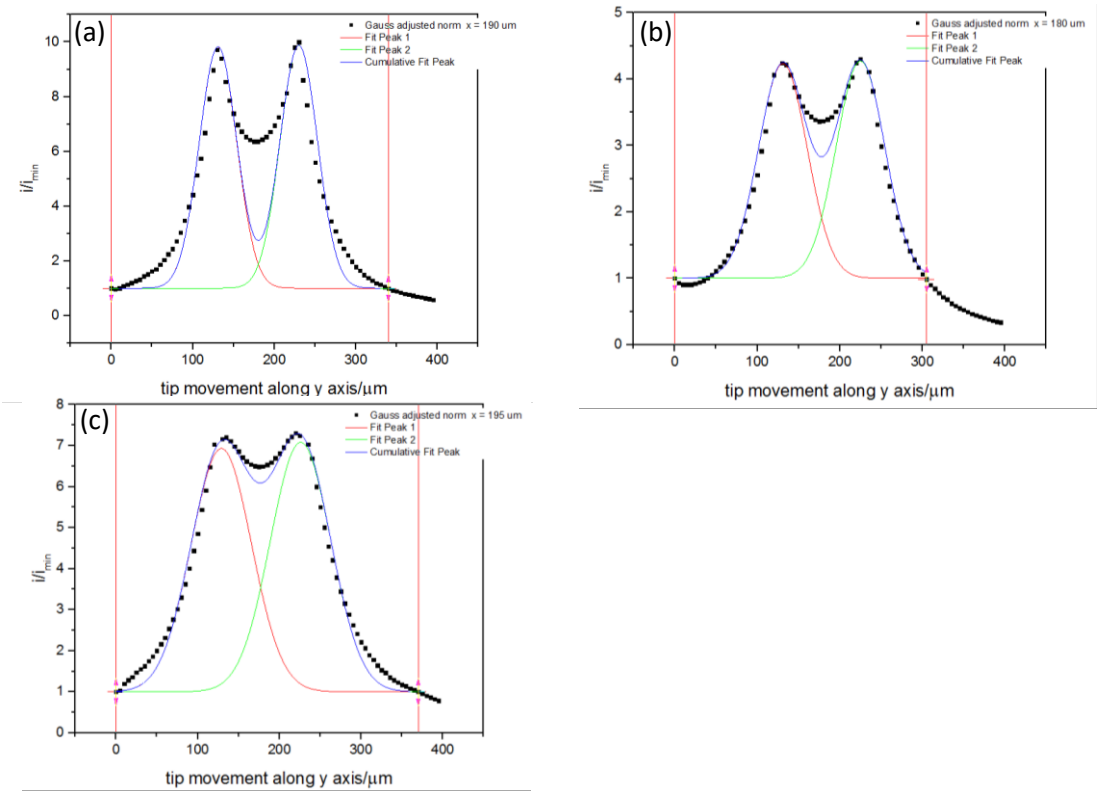

Figure 7-4. Nanoband square V middle line profiles (black squares) in SG-TC mode at increasing tip working distance (a-c) and their Gaussian fitting (blue line). V red lines capture the area where Gaussian fitting was performed.

The peaks from the graphs in Figure 7-4 look comparable, not greatly affected by the artefacts, and hence suggesting that the fitting values of *w* and *A* will be similar for both peaks. Therefore, the values of *w* were fixed to be identical for both peaks at each *d* until the best fit was obtained. From Table 7-4 the values increase with increasing *d* like in FB mode, reflecting increasing diffusional overlap in the middle of the electrode. Due to relatively significant artefacts in FB mode, direct comparison between the parameter values from the two modes is challenging. Nevertheless, the values of *w* are mostly greater in SG-TC than in FB mode at each *d*, as expected. The values of *A* from SG-TC mode line profiles are more similar than in FB mode, being well within associated error at each *d*. This confirms little amount of artefacts and symmetry between the peaks, unlike in FB mode.

Overall, Gaussian fitting is more favourable to the SG-TC than FB mode middle line profiles from the nanoband edge square electrode because of such artefacts-free line profiles with

wider peaks. This is also reflected by high R^2 parameter between 0.82 and 0.99 at the three *d* values, as shown in Table 7-4, suggesting that Gaussian function was naturally fitting majority of the data points in SG-TC mode. From evaluation of the overlap between experimental and modelled signals, square nanoband line profiles seem to be not sharp enough for their width, resulting in poorer overlap between the predicted and experimental line profiles at the dip between the peaks than in FB mode. However, the difference between the two decreases with increasing *d*. At *d* = 22.1 µm, the fitting is the most efficient, both visually and from high R^2 value of 0.986, suggesting that the Gaussian multi-peak fitting to the middle line profiles is the most successful at the greatest tip working distances and in SG-TC mode, which shows diffusion field of the substrate. As discussed in Section 7.2.1, FB mode measures the effect of the substrate on the diffusion from the tip; hence differences in the effectiveness of the fitting to the data from these imaging modes were expected. Apparently, the differences between FB and SG-TC modes become less important at greater *d*, resulting in more similar fitting results in both modes. Overall, Gaussian dual-peak fitting model can be used for both SECM modes, and in all cases R^2 parameter is better for V than for H lines. While the *w* of the peaks is different for the two ones, the data is also different, and so it is not surprising.

d	*9.2 µm*		*13.2 µm*		*22.1 µm*	
	Peak 1	Peak 2	Peak 1	Peak 2	Peak 1	Peak 2
y_0	*1*	*1*	*1*	*1*	*1*	*1*
x_c	*131*	*230*	*131*	*225*	*129*	*226*
*w**	*46*	*46*	*59*	*59*	*74*	*74*
A	508.41 ± 25.60	511.88 ± 25.60	239.02 ± 4.71	241.90 ± 4.71	549.92 ± 7.76	563.84 ± 7.76
Reduced Chi-Sqr	1.61		0.038		0.082	
R^2	0.815		0.975		0.986	

Table 7-4. Parameters from nanoband square middle V line profiles in SG-TC mode fitted to the Gaussian function at the three tip working distances.

7.2.6 Nanoband disc FB mode middle line profile fitting

Having evaluated Gaussian function fitting and its suitability for analysis of the middle line profiles from a nanoband square electrode, this section explores its application to the nanoband disc geometry. In Figure 7-5, a full data set of H and V middle line profiles at three tip working distances is shown with increasing tip working distance from top to bottom. The overall fitting appears to be successful in all line profiles and specific details are discussed below. Convection effects were found to be more prominent to FB mode, and their effect on data can be evaluated from the fitted data, while focusing on three areas: the sides of the peaks, the peaks themselves and the area between the peaks.

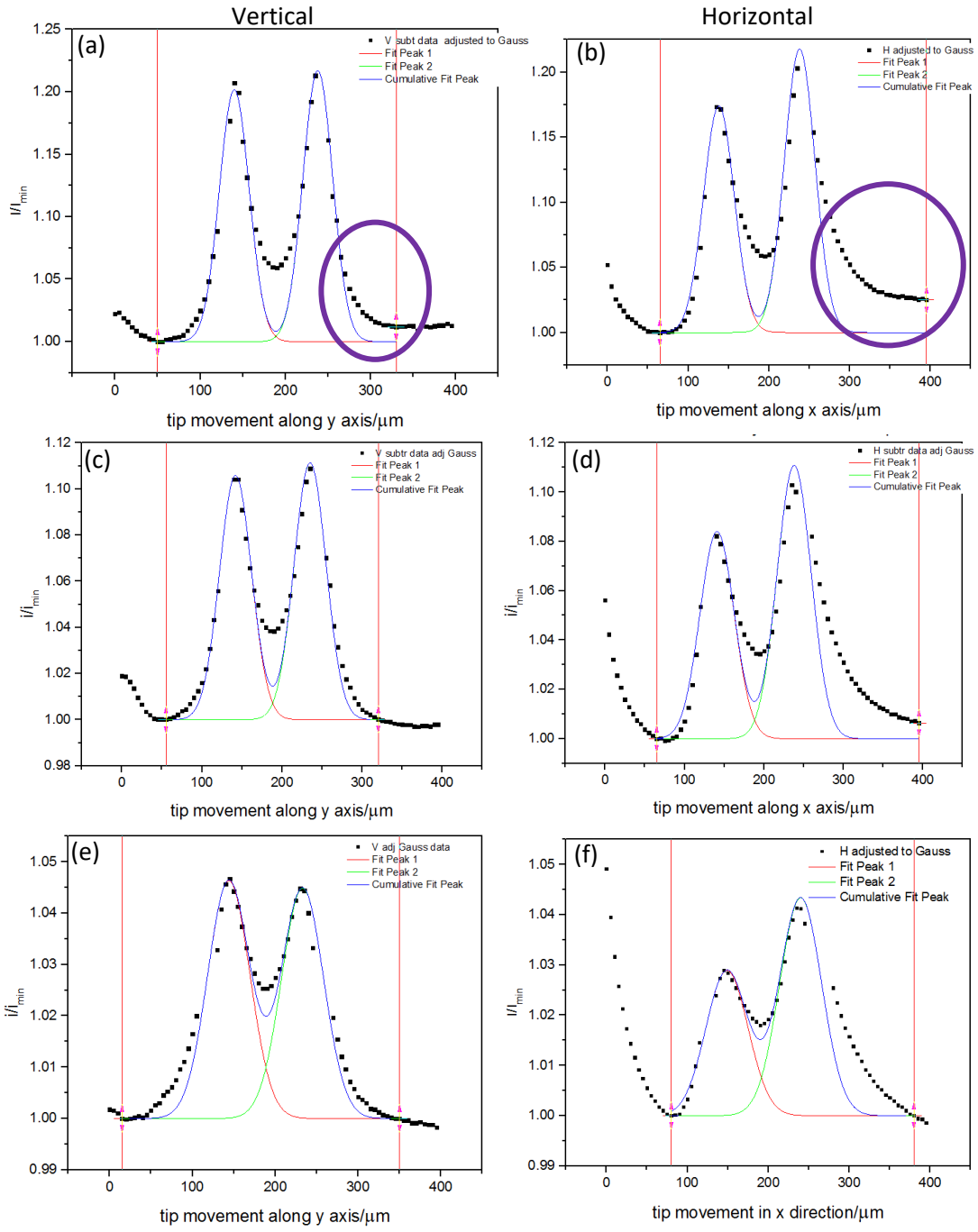

Figure 7-5. Middle line profiles from nanoband edge disc electrode in FB mode at (a-b) d = 9.2 µm, (c-d) d = 13.2 µm, and (e-f) d = 22.1 µm in V (a,c,e) and H (b,d,f) directions. Purple circles in (a-b) suggest the area where convection effects in V and H line profiles are the most significnat.

Regarding V line profiles in Figure 7-5 on the left, both peaks fit well, having comparable current values from both experimental and modelled signals. The left side of the peak mostly fits very well; however, at *d* = 22.1 µm there is some widening at the lower part of the peak of the experimental signal, possibly due to convection effects (product species displacement upon probe's return after finishing a H line profile). Since the peak width, *w*, was fixed, as

shown in Table 7-2, it is possible to evaluate whether the peaks remained symmetrical from the peak intensity, *A*, and the values are indeed similar (within fitting error). Despite this and minor mismatching on the RHS in the graph from *d* = 9.2 µm in Figure 7-5 (a), the values of *A* are within associated errors in all three V line profiles. This confirms that convection effects are minimal and can be considered as almost non-existent in these V line profiles.

Regarding the H middle line profiles on the RHS in Figure 7-5, these exhibit more imaging artefacts, especially convection, at all three tip working distances, as discussed in Chapter 6. As a result, data points are to some extent more difficult to adjust and fitting to H line profiles was clearly poorer based on visual evaluation of the overlap between experimental and modelled signals in the graphs. Peak widths are, again, fixed but the determined *A* values imply that the peaks are less symmetrical than in the V middle line profiles. The values for each *d* vary more than within their expected fitting errors, reflecting how much convection is affecting the right peak. The LHS of the line profile was excluded from the fitting boundaries, since the values are significantly higher than 1, used for the boundary's establishment throughout this work. The purple circles in Figure 7-5 (a-b) mark area on the RHS of the line profile where convection effects are the most prominent in H line profile in comparison to the V line profiles. The difference between H and V line profiles remains at all *d*.

Despite these artefacts on the extremes of the line profiles and on the RHS peak, the peak widths from both line profiles at all three *d* in Table 7-2 are similar. Values from the H line profiles are greater by 3 µm at the first two imaging distances and by 1 µm at *d* = 22.1 µm, meaning that the difference between the two is consistent and within the fitting errors. If the average of the two values was taken and the resulting value was used for both line profile fitting, the fitting results would be barely changed.

In both V and H middle line profiles, the peaks become less sharp with increasing tip working distance as a result of the larger hemispherical diffusion. This results in increasing agreement between experimental and modelled currents over the middle area between the peaks and increasing R^2 values, which are 0.883-0.958 and 0.611-0.787 for V and H lines, respectively. At all *d*, the V line profile demonstrates better fitting, evidenced by a higher R^2, than the equivalent H line profile due to the minimal effect of artefacts. However, at the greatest tip working distance (22.1 µm), experimental and modelled line profiles overlap to the greatest extent over the middle area, especially in the H line profile in Figure 7-5 (f). This suggests that at greater tip working distances the experimental hemispherical diffusion field expansion and overlap from the two band electrodes becomes more comparable with the Gaussian model. In contrast, the worst fit over the middle area between the peaks is at the smallest *d*, when the impact from the continuous band forming a circle (Figure 7-1) is sensed the most. This is an evident that the area between the peaks likely experiences current contribution not just from the two points that the tip passes in the line profile, but also from the rest of the band. For both

H and V line profiles, experimental data over the middle of the peaks was always at higher position than the modelled data, suggesting that the difference between the two is due to the hemispherical diffusion field contribution from the band sides, not accounted for by the Gaussian function model. The difference between the two signals is greater than observed for the nanoband square data, reinforcing that in the disc geometry the bands behave less like point electrodes.

7.2.7 Nanoband disc SG-TC mode middle line profile fitting

The SG-TC mode nanoband disc data was also fitted using the Gaussian dual-peak function to establish its suitability for all middle line profiles presented in Chapter 6. Unlike in the nanoband square data, SG-TC mode nanoband disc electrode H and V middle line profiles are as expected and similar to FB mode data from the square electrode. To avoid repetition, fitting to only V line profiles is shown in Figure 7-6. For completion of the analysis of the peak widths and intensities, fitting parameters are shown in Table 7-5 for both H and V middle line profiles.

From Figure 7-6, the area between the two peaks is of higher currents than in FB mode for the nanoband disc as well as SG-TC mode for nanoband square. Again, this is due to the differences between the modes (Chapter 6) and geometry of the electrodes (Section 7.2.1), such as more prominent diffusional overlap in the middle of the electrode from the sides of the band, resulting in higher tip current values in SG-TC mode. This means that the overall fit is better in SG-TC than in FB mode in all examples discussed in this chapter. The R^2 values from Table 7-5 for V line profiles (0.942-0.990) are slightly higher than for the H ones (0.918-0.964), as usual due to the absence of the convective effects in the former. However, the difference between these values is only around 2%, suggesting that data from both line profiles are equally well-predicted by the model and major artefacts were avoided, unlike in the example from Section 7.2.5. The sides of the line profiles as well as the peaks are symmetrical and in general agree to a great extent with the Gaussian signal.

Only the middle area between the peaks clearly did not fit well, with the most significant deviation at d = 9.2 µm. But the overlap between the experimental and modelled signals improves with increasing d and at d = 22.1 µm the overlap at all areas, including the middle between the peaks, was achieved to the greatest extent. This suggests that the underestimation of the diffusion from the surrounding sides of the nanoband disc to the middle points decreases with increasing d in all sets of data in this chapter. At the greatest d used in this work, experimental signal is equivalent to the modelled one (R^2 = 0.990), and this was achieved more successfully than in FB mode (R^2 = 0.958) similarly as for the nanoband square.

It is not surprising that the peak widths in SG-TC mode are also greater. In FB mode, the peak width of 35-51 µm from V line profiles indicate sharper peaks which present more distinctive

features, typical to this mode. In SG-TC mode from Table 7-5, *w* values are 59-75 and 56-72 µm for V and H line profiles, respectively. The values gradually increase with increasing tip working distance and the difference between the two is ±1-3 µm, just like in FB mode in the above section, confirming that the peaks in H and V line profiles are similar as expected.

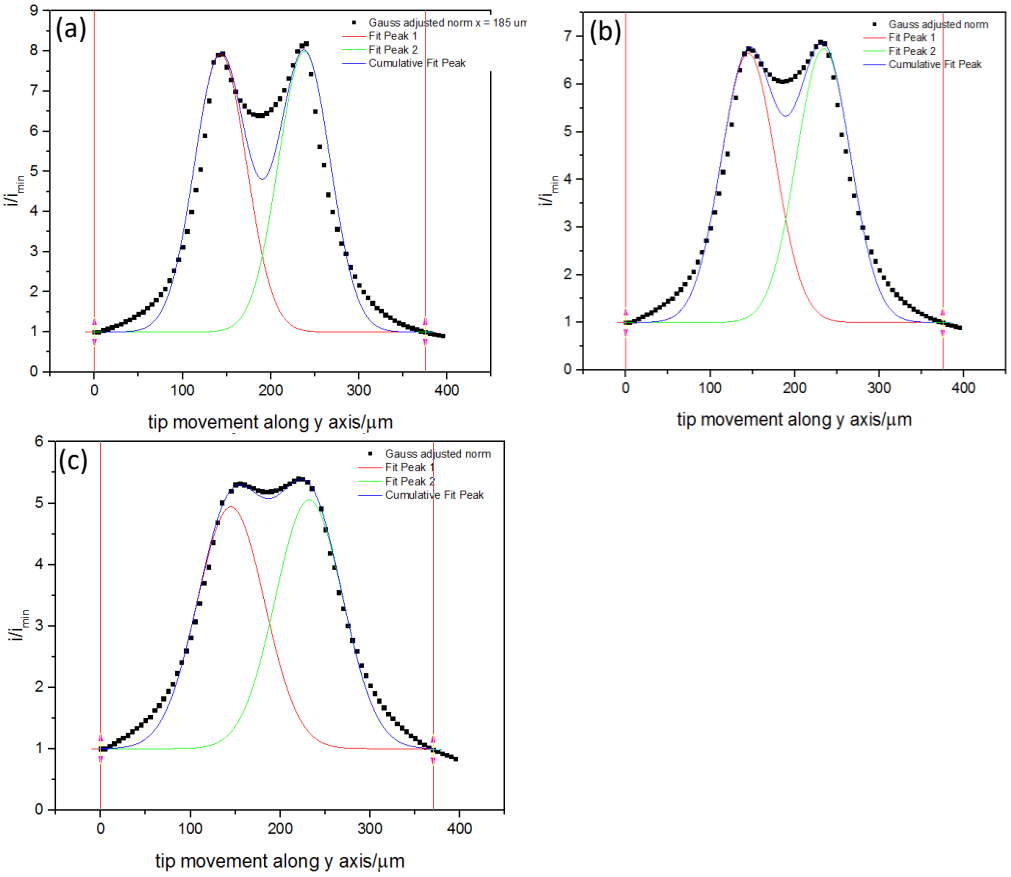

Figure 7-6. Nanoband disc V middle line profiles (back squares) in SG-TC mode and their Gaussian fitting (blue line) at (a) d = 9.2 µm, (b) d = 13.2 µm, (c) d = 22.1 µm. V red lines capture the area of Gaussian fitting.

Obtained *A* values are significantly larger in SG-TC mode than in FB mode, reflecting that the currents in Figure 7-6 are higher and so the peaks are larger. The values, again, decrease with increasing both *d* and *w* parameter, as seen from Table 7-5. The numerical values of *A* are almost twice as large in V than in H line profiles, and these values for both peaks are more similar from V line profile fitting than from H line profiles. In the latter, the peak intensities differed to a great extent representing the lack of symmetry between the two peaks. This suggests that fitting to H line profiles was not as efficient or something went wrong, as peak intensity from V and H line profiles is expected to be comparable, as seen in Figure 7-2.

Overall, the middle line profile fitting process for quantitative analysis was successful for both square and disc geometry, even though it is expected to see that the signals do not overlap over the middle area of the peaks at relatively small *d* values. Such signal difference was, as expected, slightly greater for the disc geometry.

	Vertical		*Horizontal*	
d = 9.2 µm	Peak 1	Peak 2	Peak 1	Peak 2
y_0	*1*	*1*	*1*	*1*
x_c	*143*	*238*	*140*	*233*
*w**	*59*	*59*	*56*	*56*
A	511.57 ± 14.32	516.85 ± 14.32	258.03 ± 9.45	307.36 ± 9.45
Reduced Chi-Sqr	0.39		0.18	
R^2	0.942		0.918	
d = 13.2 µm				
y_0	*1*	*1*	*1*	*1*
x_c	*145*	*234*	*142*	*234*
*w**	*64*	*64*	*63*	*63*
A	453.18 ± 8.53	460.92 ± 8.53	188.86 ± 5.53	240.37 ± 5.57
Reduced Chi-Sqr	0.13		0.050	
R^2	0.975		0.953	
d = 22.1 µm				
y_0	*1*	*1*	*1*	*1*
x_c	*145*	*232*	*147*	*236*
*w**	*75*	*75*	*72*	*72*
A	370.54 ± 4.85	380.99 ± 4.84	115.83 ± 3.65	171.05 ± 3.90
Reduced Chi-Sqr	0.030		0.015	
R^2	0.990		0.964	

Table 7-5. Comparison between V and H middle line profiles across nanoband edge disc Pt electrode in SG-TC mode at three d values.

7.2.8 Middle line profile two-peak response merging into one-peak response

When fitting nanoband square and disc data from SG-TC mode at *d* = 22.1 µm images, it was investigated what settings should be chosen to see the two-peak Gaussian signal merging into one, as if it was a line profile from a single micro electrode image. Interestingly, during the fitting of nanoband disc in SG-TC mode at *d* = 22.1 µm, the two fitted Gaussian curves were already overlapping, as shown in Figure 7-7. This reflects that hemispherical diffusion reaches a symmetrical hemisphere faster for a disc than square geometry and suggests that it is not difficult to model the scenario when the two peaks merge into one just like for a micro electrode (Chapter 5). It is more likely to observe such phenomena in SG-TC mode, where the peaks are less sharp compared to the FB mode.

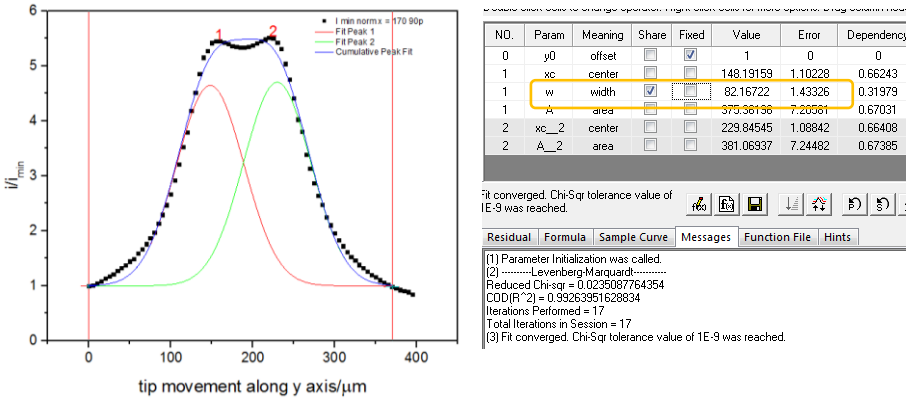

Figure 7-7. Gaussian function fitting to the nanoband edge disc electrode data in SG-TC mode in process. Orange box captures w parameter, which value suggests two-peak overlap to form a single line.

7.2.9 Evaluation of the peak position in line profiles

The experimental step size value was 5 µm, allowing some error in the peak position assignment in the original data. This is occasionally exceptionally clear, when there is space between the data points at the maximum, suggesting that the maximum peak value might actually be in between the recorded values. During the fitting process there was some control where to fix the peak in the generated line profile but then this imposes more error due to the human subjectively in choosing this value. Nevertheless, the Gaussian modelled signal enabled identification of the actual peak positions and their comparison with the experimental values in FB and SG-TC modes. Peak positions and the resulting values of the peak separation obtained from the Gaussian model and experimental V and H middle line profiles are tabulated in Table 7-6. In all cases, FB mode provides greater peak separation than SG-TC mode, as expected (FB mode is more sensitive to record the details of the substrate).

In V line profiles (upper part of Table 7-6), experimental and modelled peak positions are mostly within ±1-3 µm when comparing FB and SG-TC modes at all *d*. Therefore, the peak separations are also within similar differences. As discussed in this chapter, the peak separation decreases with increasing *d* due to the broadening of the peaks towards the centre of the band electrode. Greater differences are observed when comparing experimental V line profiles to the ones from Gaussian fitting at the largest *d* in SG-TC mode. Both experimental peaks are at significantly different values, suggesting much smaller peak separation of only 70 µm, compared to the Gaussian value of 87 µm, implying that the spatial resolution of the peaks is significantly lower in the former.

Regarding H line profiles (lower part of Table 7-6), peak 1 in the Gaussian data varies within ±1-2 µm between FB and SG-TC modes and the second peak has a greater variation of ±4-5 µm. Variation for the experimental peak positions is ±1-2 µm and ±5 µm, for peak 1 and 2, respectively. The greatest variation between experimental and Gaussian peak position is 6

µm in SG-TC mode and ±4-5 µm in FB mode, which is a smaller variation window compared to the V line profiles. Just like for the V line profiles, these discrepancies are at the largest *d* in Table 7-6.

FB	*Gaussian*			*Experimental*		
	VERTICAL					
d/µm	Peak 1	Peak 2	Peak separation	Peak 1	Peak 2	Peak separation
9.2	*140*	*238*	98	140	235	95
13.2	*142*	*235*	93	140	235	95
22.1	*144*	*233*	89	145	230	85
SG-TC						
9.2	*143*	*238*	95	145	235	90
13.2	*145*	*234*	89	145	235	90
22.1	*145*	*232*	87	155	225	70
FB	HORIZONTAL					
9.2	*138*	*238*	100	135	235	100
13.2	*141*	*238*	97	140	235	95
22.1	*149*	*240*	91	145	235	90
SG-TC						
9.2	*140*	*233*	93	140	230	90
13.2	*142*	*234*	92	140	230	90
22.1	*147*	*236*	89	150	230	80

Table 7-6. Comparison between peak positions (x_c) and peak separation values from Gaussian fitting and experimental data, where the step size was 5 µm in FB and SG-TC modes from both H and V middle line profiles. Values in red are paired as Gaussian and experimental values and they differ by a greater than the experimental error (±3 µm) value.

Overall, from such comparison of Gaussian and experimental peak positions the values were mostly within the expected ±5 µm value. The peak positions differ more than the imaging step size value in both modes only in some instances coloured in red in Table 7-6, all of which are at the greatest imaging distance. This suggests that such deviation is associated with the broadening of the peaks due to the more developed hemispherical diffusion field at greater *d*. Smaller imaging distances provide results as expected, allowing the experimental data to be used for locating a valid peak position. An error of approximately half the imaging step, which is around 3 µm in this data set, is acceptable.

7.2.10 Off-middle SG-TC mode vertical line profiles

V line profiles, which do not pass the middle of the circular or square cavity (MNEE), are referred to as off-middle line profiles, and they are compared to the middle line profiles from the same images. Again, only V off-middle line profiles that were observed to have fewer artefacts than the H line profiles are used in this section to evaluate if Gaussian function would

result in an effective fitting. In the disc geometry nanoband electrode, moving away from the central lines means that the peaks should get closer together, and they should remain at the same positions for the square geometry electrode (Figure 7-1). In both cases, the peaks should remain symmetrical.

The off-middle V line profiles from the images collected at the shortest tip working distance were derived from the image by moving by the same distance in the x-axis to the left and right of the middle line profile. These derived x-values were also used for the other *d*, as the substrate was not physically moved for each imaging experiment. Given a band electrode radius of 50 µm, the value of 25 µm was chosen to be added to and subtracted from the middle point in the H direction to find the values of V line profiles. SG-TC mode was the preferable choice, since from earlier comparison between the modes, the peaks are less sharp, resulting in a better fitting and they are less affected by convection and current fluctuating-related artefacts, which is also beneficial for a more effective data fitting.

From Figure 7-8, two off-middle V line profiles, at each side of the centre, from the nanoband edge disc and square electrodes in SG-TC mode are similar in all aspects. The symmetry between the sides of the line profile is preserved, as the beginning and ending of the line profiles overlap well and even the peaks and the area between the peaks matches to a great extent in both cases. As the *d* value was increased (from top to bottom in both sets of images), the overlap over the middle of the peaks becomes more offset. This confirms that at greater *d* the hemispherical diffusion field has indeed expanded, masking the nanoband features and hence possibly a different off-middle line profile could be used to retain more symmetry between the two line profiles. After some evaluation of the line profiles, the presented results were found to be the best. Since data from both MNEEs are similar, only one of the two electrodes and only one of the two line profiles at each *d* is used for fitting.

First, nanoband disc and square geometry is evaluated. As already seen before, the dip between the peaks is greater and more pronounced for the square geometry in Figure 7-8 (d-f). For the disc geometry, it is obvious that the peaks are coming closer together due to the more extensive diffusion field overlap, while they remain at approximately the same positions for the square geometry, as expected. Therefore, only the square electrode will be further evaluated to avoid any complications related to the disc geometry.

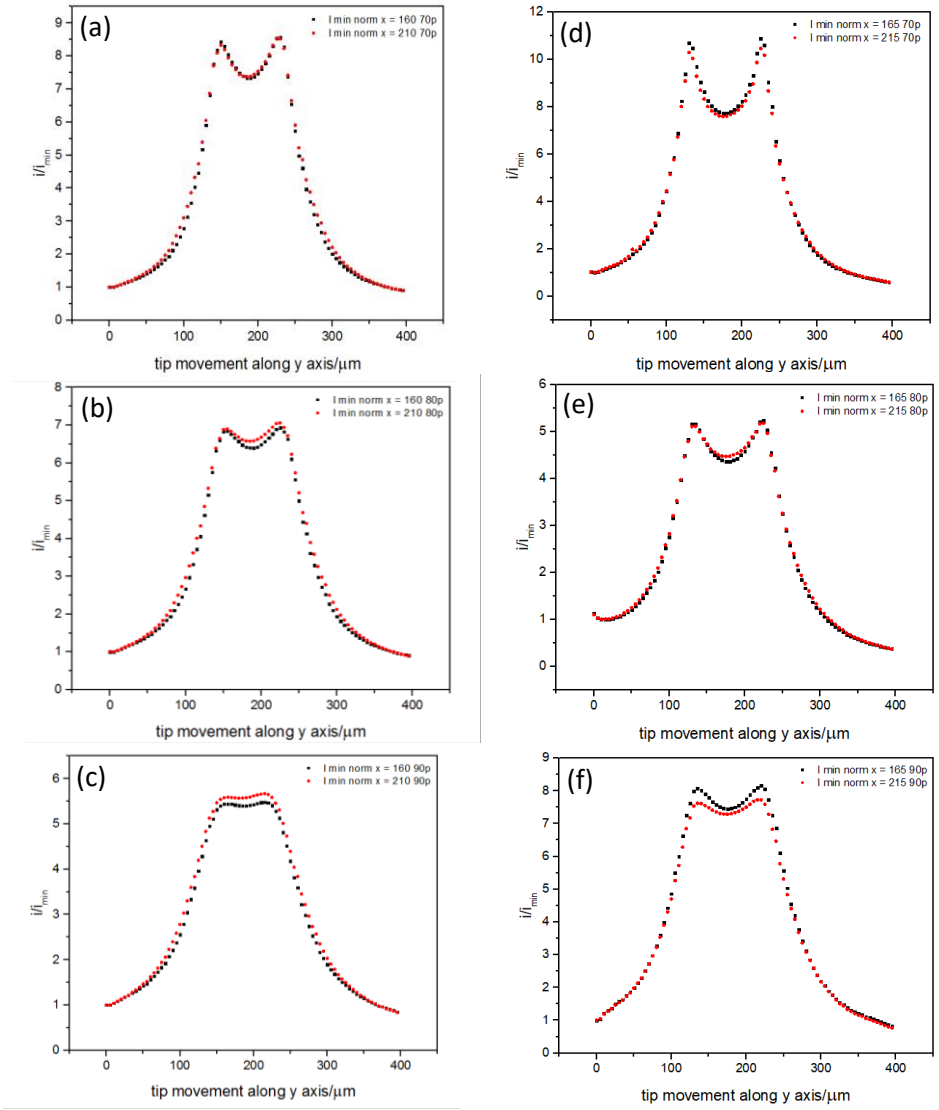

Figure 7-8. Nanoband edge disc (left) and square (right) electrode off-middle SG-TC mode V line profiles, obtained by moving to an equivalent distance to the left (black) and right (red) of the middle line at increasing tip working distances from top to bottom: (a, d) d = 9.2 µm, (b, e) d = 13.2 µm, (c, f) d = 22.1 µm.

Both off-middle line profiles at each *d* from the square electrode are compared. V line profiles at x = 165 and x = 215 at *d* = 9.2 µm in Figure 7-8 (d) are similar. The difference between the two peaks on the left is 0.192, while the peaks on the right differ by 0.166 (y-axis values) which is less than 2% in both cases, being well within the experimental error. The currents at the beginning and end of the profiles are at the same level, and so both of these observations further confirm that the experimental set-up was free of significant tilting. Due to this similarity, it is possible to use just one of these line profiles for Gaussian fitting in the following section, as they both would generate similar results. Similar observations were made for the off-middle line profiles from the image collected at *d* = 13.2 µm.

The line profiles at x = 165 and x = 215 from *d* = 22.1 µm in Figure 7-8 (f) are identical at the sides but differ in the peak activity slightly more than at shorter tip working distances. The reason is either because the LHS of the electrode was more active or because the tip generated more convection effects (product dragging) than on the RHS. The latter observation is unexpected (as product dragging would be expected to be more pronounced on the RHS of the image) but may instead be the result of product dilution due to convective stirring on the LHS at long tip working distances. In any case, the normalised current difference between the peaks is approximately 0.1, compared to a peak normalised current of around 8, corresponding to 1.25% difference, which is within an expected error.

7.2.11 Gaussian function fitting to off-middle line profiles

Gaussian fitting was successfully performed on the nanoband square off-middle line profile at x = 165 at three tip working distances to further expand the fitting applicability and evaluate how hemispherical diffusion expands in these off-middle line profiles. Fitting was performed in the same way as for the middle line profiles, except that data was not adjusted to reduce the amount of contribution from additional two sides. It was out of scope of this analysis to quantify how much contribution from each side at each point within the electrode band there actually was, and this was allowed as an error in the fitting. The *w* parameter was fixed to be the same as for the middle line profiles analysed above, *A* was allowed to vary to satisfy the fitting procedure, y_0 was fixed as 1, and the boundaries for fitting were fixed at 1 or as close to 1 as possible on both sides.

Overall the fitting was satisfactory showing good experimental and Gaussian data agreement from Figure 7-9 and Table 7-7. Hemispherical diffusion field overlap over the middle area increases with increasing *d*, resulting in a better fit, valid both from visual line profile overlap (Figure 7-9) and numerical evaluation. From Table 7-7, R^2 parameter increases from 0.78 to 0.98 with increasing tip working distance, showing the same trend as for the middle line profile fitting. For the middle line profiles from Table 7-4, the values were between 0.82-0.99. This suggests that there were some differences between adjusted middle and un-adjusted off-middle line profiles and the differences became less pronounced with increasing tip working distance.

From Figure 7-9, the lack of data adjustment around the middle of the line profile is the most noticeable at the smallest *d* in (a), where the gap between experimental and modelled data is the largest. When comparing normalized tip current values, area between the peaks from the experimental middle line profile at this *d* are at approximately 6.5 (Figure 7-4), while at the off-middle line profile they are at around 8. In both cases the peaks from the fitting curve are at approximately 3 (value at the dip of the cumulative fit peak in Figure 7-4 (a) and Figure 7-9 (a)), suggesting that data adjustment was indeed also needed for the off-middle line profiles.

As the *w* parameter was set to be within ±1 µm from the value obtained when fitting V middle line profile from the nanoband square image (Table 7-4), it confirms that the geometry is preserved when moving away from the centre of a square electrode.

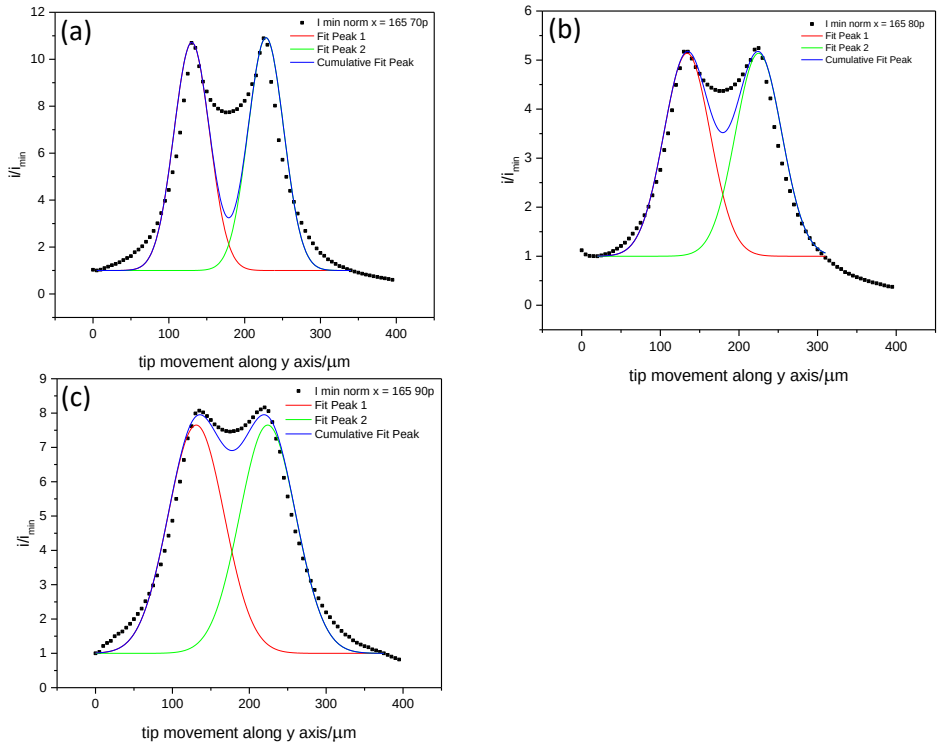

Figure 7-9. Off-middle line profiles (black squares) from nanoband edge square electrode in SG-TC mode at three tip working distances of (a) d = 9.2 µm, (b) d = 13.2 µm, (c) d = 22.1 µm and their Gaussian dual-peak function fitting (blue line).

Simple trigonometric rules or Pythagorean Theorem were used to extract at which values the peak positions at the off-middle line profiles should be present. When the band radius is the hypotenuse of 50 µm and the half of the radius is an adjacent side of 25 µm, the remaining side is easily calculated as 43.3 µm, totalling 86.6 µm for the theoretical peak-to-peak separation. From Table 7-7, the peak separation values were calculated using the difference between peak 1 and peak 2 positions (x_c), resulting in 98, 89 and 93 µm for d = 9.2, 13.2 and 22.1 µm, respectively. Hence, at the smallest and the largest d the peak separation was overestimated, whilst at intermediate d it was closest to the expected value. It appears that there is no clear trend for the peak separation with varying d, which is unlike in the middle line profile analysis.

In the case of the nanoband square geometry, the peak separation is expected to remain close to 100 µm, as with the middle line profiles. In Table 7-7, the greatest d resulted in slightly smaller peak separation of 93 µm, confirming hemispherical diffusion field expansion from the square nanoband, resulting in peaks at closer positions due to diffusional overlap from the

sides of the band. As expected, the greatest peak separation of 98 µm is at *d* = 9.2 µm. The peak separation at the intermediate *d* value is 91 µm, which is between the other two values, suggesting either an error associated to the peak position choice during the fitting process or it agrees to the greatest extent from these three values with the above calculated peak separation of 86.6 µm.

Overall, the Gaussian dual-peak fitting function is an effective quantitative analysis tool not only for the middle line profiles, but also for the off-middle line profiles in the square geometry electrode. Regarding the future fitting, data points around the peak area could be adjusted in the same way as for the middle line profiles to evaluate if fitting would be further improved.

d	*9.2 µm*		*13.2 µm*		*22.1 µm*	
	Peak 1	Peak 2	Peak 1	Peak 2	Peak 1	Peak 2
y_0	*1*	*1*	*1*	*1*	*1*	*1*
x_c	130.22 ± 1.91	228.08 ± 1.87	134	225	131	224
*w**	*47*	*47*	*59*	*59*	*73*	*73*
A	572.06 ± 32.69	584.19 ± 32.69	306.07 ± 5.30	306.07 ± 5.30	608.43 ± 6.08	608.43 ± 6.08
Reduced Chi-Sqr	2.56		0.12		0.14	
R^2	0.784		0.952		0.982	
Peak separation		98		91		93

Table 7-7. Table of Gaussian dual-peak distribution fitting parameters for the off-middle line profiles from a nanoband edge square electrode in SG-TC mode at the three tip working distances. Numbers in italic have been fixed.

7.2.12 Peak width variation with tip working distance

From Gaussian fitting to the experimental data, *w* parameter, representing FWHM, is analysed as a function of the tip working distance, *d,* to evaluate if there was a linear dependency between the two. Values of *w* presented in several sections of this chapter were gathered and linearly fitted (the least squares) to assess if the peak width was increasing linearly with increasing tip working distance. Results from V rather than H line profiles were used for this analysis, again, to avoid any possible additional imaging artefacts affecting the experimental data. FB mode nanoband square data was represented by only two data points which was not enough for this fitting, so was excluded from this analysis.

Values of *w* from V line profiles of a nanoband disc in SG-TC and FB modes and a nanoband square in SG-TC mode at the three *d* values are plotted and linearly fitted in Figure 7-10. The associated fitting data is presented in Table 7-8. All three graphs generated R^2 between 0.97 and 1, suggesting an adequate linear fit and hence dependency between the two parameters. Data points from a nanoband disc in both modes generated more of a straight line than

nanoband square data in (c). However, the offset is minor and the resulting R^2 value shows an excellent fit.

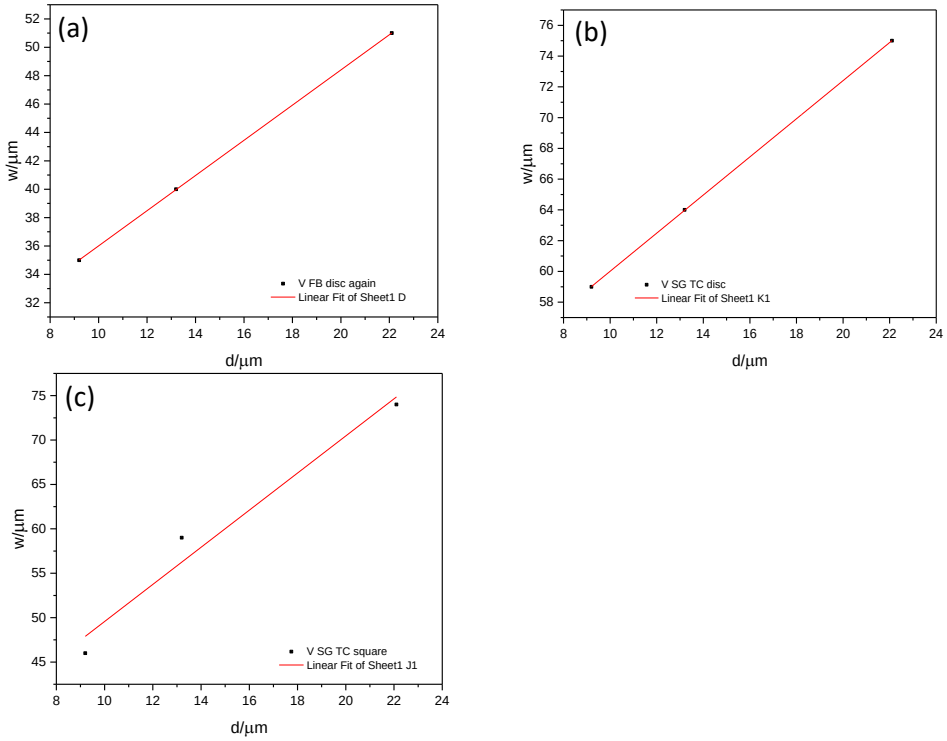

Figure 7-10. Graphs of w vs d and the linear fit (red line) to the data points (black squares) for (a) a nanoband disc electrode in FB and (b) SG-TC modes and for (c) a nanoband square electrode in SG-TC mode.

Mode	*SG-TC*	*FB*	*SG-TC*	*FB*
Nanoband	disc		square	
Intercept	47.61 ± 0.052	23.61 ± 0.052	28.67 ± 5.82	n/a
Slope	1.24 ± 0.0033	1.24 ± 0.0033	2.09 ± 0.37	
R^2	0.999	0.999	0.970	

Table 7-8. The resulting parameters of w vs d fitting for the nanoband edge disc and square electrodes in SG-TC and FB modes.

In all cases, the same procedure for fitting was performed and the width values shown in the above sections were to some extent adjusted during Gaussian fitting to allow for a better linear fitting in this case. Since the values were chosen manually, there was space for adjustment and hence errors. Nevertheless, the width values presented in these graphs did not reduce the Gaussian fitting effectiveness and these are the best *w* for each tip working distance and the electrode. The clear linear dependency with *d* agrees with the Brownian motion principles[5,6] (partition function) (Equation 2.18), in which diffusion from a point source expands with time equally in all directions, and so the width of the peak grows linearly with time (distance).

The intercept values in the three plots in Figure 7-10 vary between 23.6 µm and 47.6 µm. These values are greater for both electrodes in SG-TC than in FB mode, reflecting wider peaks due to a greater diffusional overlap in SG-TC mode and much sharper peaks in FB mode. As such, these graphs suggest that at a hypothetical tip working distance of 0 µm, which is effectively 0.5 µm due to the recess, the hemispherical diffusion field has expanded from the disc band to deliver 24 or 48 µm width peak in FB and SG-TC modes, respectively.

It could also be predicted that at 0 µm the diffusion field would collapse to 0 and 10 µm values for the modes, since 48 nm height Pt band is effectively 0 and the Pt probe has 10 µm diameter. In this case, the y-intercept should be set to these values and the effectiveness of fitting would show if it is a likely scenario or not. Also, since the tip electrode is always on and the tip current is measured in both modes, it could be expected that the value of the tip's diameter would be the expected intercept value. Despite the trends observed, the length scales explored in this section is relatively narrow, so more data and analysis are needed to fully evaluate these possible intercept scenarios. Further examples of such fitting are presented in Section 7.3.4 and in the following chapters, where a smaller substrate is imaged (Chapter 8) and a smaller probe (Chapter 9) is used for imaging. Overall, a full detailed analysis is out of scope of this thesis and these are ideas for the future work.

7.3 QUANTITATIVE LINE PROFILE ANALYSIS USING MODIFIED BESSEL FUNCTION

Diffusion from a point source is expected to be a Gaussian distribution and fitting the experimental line profiles using a Gaussian function was indeed successful, as seen in Section 7.2. While the manual adjustment of data points around the peak area is a rather tedious work, it is expected to be sufficient for the square geometry. However, it is not adequate to account for the disc geometry, where the sides of the band get closer when moving away from the middle line profile, resulting in an increasing diffusion field contribution from the sides to the middle. These more complex diffusional contributions can be accounted for when using a modified Bessel function, which is known as a solution to a Bessel equation valid for a purely imaginary number.[7] It can be used to predict the concentration profiles arising from point sources on a ring, providing a means to estimate the tip currents recorded as the middle line profiles from the disc nanoband SECM images.

7.3.1 Deriving equation for fitting

The tip limiting current (Section 2.9 and Equation (2.24)) is a function of bulk concentration, i.e. $i_L \propto c_\infty$. Hence, as suggested by Prof Philip J. Camp (School of Chemistry, UoE), the tip current measured in SECM experiments at circular nanoband substrates can be predicted by

using a modified Bessel function to determine the concentration profile associated with diffusion from point sources on a ring. A concentration function dependent on the tip position, *c(r),* Equation (7.2), was slightly adjusted using several assumptions discussed below, allowing a simplified model for the line profile fitting to be obtained, as shown in Equation (7.3).

$$c(r,z,t) = \frac{N}{(4\pi Dt)^{3/2}} I_0\left(\frac{(rR)}{2Dt}\right) \exp\left(\frac{r^2+R^2+z^2}{4Dt}\right) \quad (7.2)$$

$$c(r,z,t) = A * I_0\left(\frac{(rR)}{2Dt}\right) \exp\left(\frac{r^2+R^2+z^2}{4Dt}\right) \quad (7.3)$$

where the term before the modified Bessel function $\frac{N}{(4\pi Dt)^{3/2}}$ is a constant which can be adjusted and renamed as *A* in Equation (7.3)*;* I_0 is the modified Bessel function, *r* is the tip position in the *x*-axis, *R* is the electrode radius (50 µm in this chapter), *t* is time, *D* is diffusion coefficient, and *z* = *d* which is the tip working distance value (9.2, 13.2 or 22.1 µm in this chapter).

The tip current and bulk concentration can be related, as shown in this section. In this chapter, both the tip (*r* = 5 µm) and the substrate (50 nm band height) electrodes are relatively small (micro and nanoband edge electrode, respectively) compared to the overall substrate electrode diameter (100 µm) and to the typical diffusion length of the electroactive species. As such, they exhibit local hemispherical diffusion fields characteristic of convergent diffusion. First, $c_{ox} = 1 - c_{red}$, where 'ox' is the oxidised species and 'red' is the reduced species. In FB mode, the tip generates oxidised (product) species and senses c_{red}, while in SG-TC mode the tip senses c_{ox} at the substrate and converts the oxidised species back to its reduced form (Figure 3-9). For both modes the tip current varies, as follows:

$$i_{tip} = i_{tip,ins} + i_{FB} \quad (7.4)$$

where $i_{tip,ins}$ is the tip current above the insulator surface, as shown in Figure 7-11 (a) and i_{FB} is the additional tip current due to a positive feedback from the substrate, Figure 7-11 (b-c). In all cases, it is expected that the side diffusion (flux) of the redox species from the bulk is constant, and $i_{tip,ins}$ does not vary.

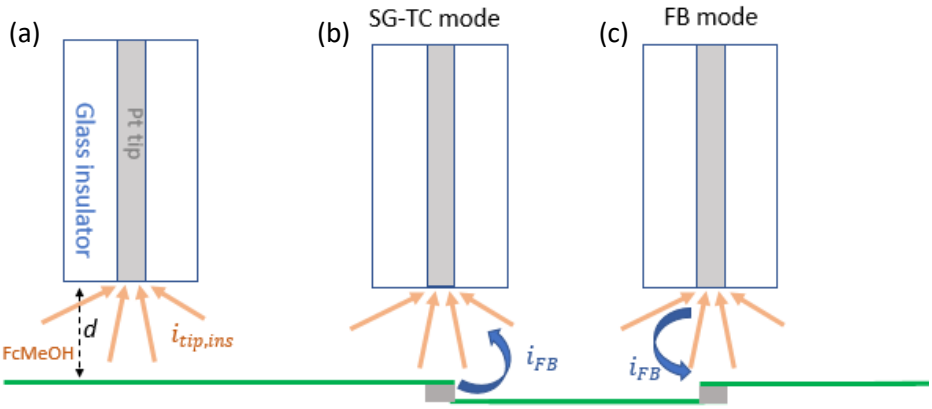

Figure 7-11. Tip current measured above (a) the insulator surface and (b-c) above the substrate, where additional feedback current, i_{FB}, (blue arrows) due to product species in SG-TC mode and reactant species in FB mode is sensed in (b) SG-TC and (c) FB modes. The value of $i_{tip,ins}$ is assumed to be constant.

Then, i_{FB} is assumed to be related to the concentration of the product species in SG-TC mode and to the reactant species in FB mode (Figure 7-11 (b-c)). In SG-TC mode, $i_{FB} \propto c_{product}$, and Equation (7.4) can be normalized to $i_{tip,ins}$:

$$\frac{i_{tip}}{i_{tip,ins}} = 1 + \frac{i_{FB}}{i_{tip,ins}} \tag{7.5}$$

The current in both modes is always measured at the tip (in this work) and the value of 1 represents the tip current over the insulator at whichever *d* value used. Then, $\frac{i_{FB}}{i_{tip,ins}}$ is an additional current due to the feedback from the underlying electrode, allowing to combine Equations (7.3) and (7.5) in Equation (7.6), which reflects the relationship between concentration and current values.

$$i = 1 + A * I_0\left(\frac{(rR)}{2Dt}\right) exp\,(\frac{r^2 + R^2 + z^2}{4Dt}) \tag{7.6}$$

A is a constant, derived by the software during fitting, allowing to adjust the scale of the line. Together with the rest of the function, it represents any additional current generated due to the presence of the underlying band, i_{FB}. Then, *r* can be changed to $(y - y_c)$ for V line profile fitting which stands for the central y-value and allows some adjustment within this value, y_c. For H line profiles it would be $(x - x_c)$. Since *D* and *t* are not defined variables in these imaging experiments, *2Dt* can be related to w^2 due to the Brownian motion (Section 2.4), such as $w = (2Dt)^{1/2}$. It is related to the expansion of the diffusion field from the electrode in all directions, and w^2 and $2w^2$ can be used, resulting in Equation (7.7).

$$i = 1 + A * I_0\left(\frac{\left((y - y_c) * R\right)}{w^2}\right) * \exp\,(-\frac{(y - y_c)^2 + R^2 + d^2}{2w^2}) \tag{7.7}$$

This expression has significantly less variables, being only the amplitude, *A*, and the width, *w*, of the peaks, compared to the Gaussian function used in the previous section. In Equation

(7.7), it is already implied that the peaks are equivalent, and the middle point between the peaks is automatically found in a precise manner during the fitting process. Also, using this function removes the need to manually alter data points as in the above section and allows to easily compare the experimental data to the predicted model. As such, 10 µm Pt probe with R_g = 10, is expected not to perturb concentration profiles evolving from the two electrodes meaning that current is proportional to concentration, $i_{tip} \propto c$.

7.3.2 Determination of the fitting boundaries

Line profile boundaries for fitting were first established for consistency throughout this analysis. This had to include consideration what limits should be used on the sides of the line profiles and whether fitting to the middle (dip) between the peaks or the peak height should be enforced. First, the boundaries were set to fit within the values of i/i_{min} being 1 or greater (≥1) to reflect current normalization and the idea that all additional current over the value of 1 is due to the presence of the substrate (Figure 7-11). Then, automatic fit was performed, without the need to adjust any of the parameters.

The overall fit was great, as seen in Figure 7-12 (a) and in Table 7-9. However, the data points at the peaks were excluded from the fitting and the sides, so called 'wings' of the line profile were not fitting great neither. Modified Bessel function was suggesting flatter side parts of the line profile, such as there was no diffusion field growth at these parts. However, in all experimental SG-TC mode data there was a gradual increase in current towards the peaks, meaning that the line profiles would never be as flat as in the model. It was examined if the fitting would improve if the boundaries for fitting were set to exclude these areas, such as suggested in Figure 7-12 (b). But the overall fit presented by R^2 value slightly decreased after such adjustment, presented in Table 7-9.

The automatic response in Figure 7-12 (a) and (b) tends to better fit data points at the middle area between the peaks than the actual peak points. This most likely is to make sure that the majority of the data points are fitted, and a couple of points that are left out do not have a significant weight to the overall fit. However, from a visual evaluation (overlap between two signals), similarly as some fitting regarding Gaussian function in Section 7.2, it appears better when including these peak points in Figure 7-12 (c). As a result, data points ≥1 were used for fitting, adjusting A parameter to fit the intensity of the peaks. As a trade-off, the middle area between the peaks fits slightly less but from the overall visual evaluation and from R^2 value such adjustment makes a difference of 0.002 in the latter parameter, allowing to confidently choose this approach of fitting. At greater than d = 9.2 µm values, the peaks are significantly less sharp and the area between the peaks is of relatively higher currents, meaning that the intensity of the peaks is not corresponding to their width. In this case, an overall better method was to fit to the middle area between the peaks, thus preserving both peaks and accepting

that intensity predicted by the model is higher than the experimental values, as presented in the following figures.

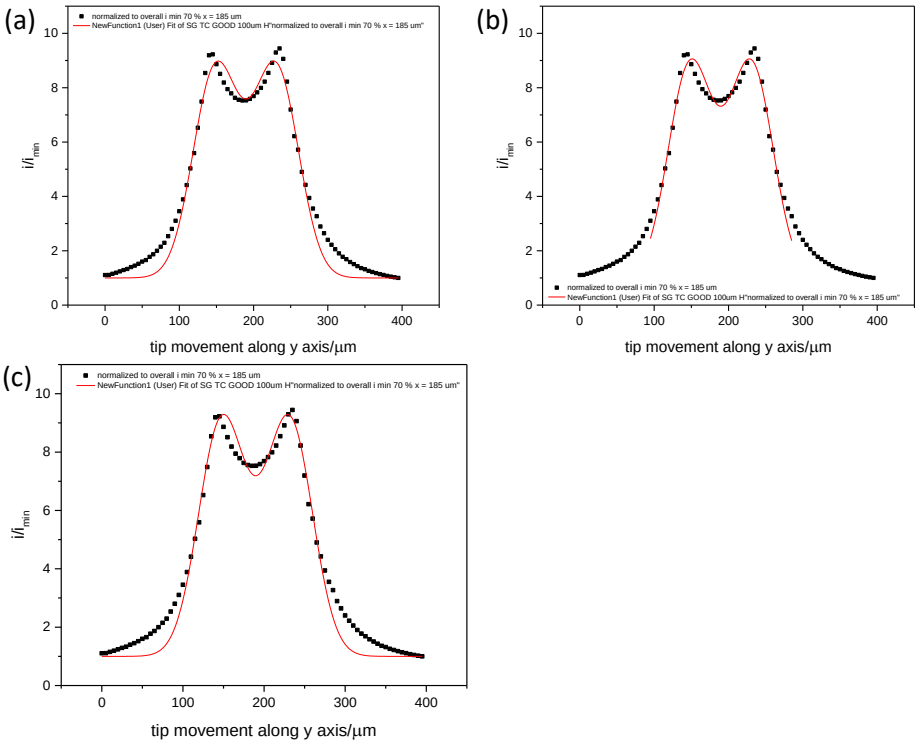

Figure 7-12. Modified Bessel function fitting to SG-TC mode V middle line profiles from a disc nanoband electrode, r = 50 µm: (a) automatic fitting within the boundaries of normalized current values being greater or equal to 1, (b) automatic fitting having manually set narrower boundaries and (c) fitting within the boundaries as in (a) but also having manually set A value, allowing to fit the peak intensity.

	(a) Automatic fit	*(b) Narrow limits*	*(c) Full limits*
A	33.04 ± 1.24	34.75 ± 1.03	*37*
w	28.30 ± 0.51	27.53 ± 0.39	26.88 ± 0.16
yc	189.69 ± 0.77	189.58 ± 0.62	189.64 ± 0.74
Reduced Chi-Sqr	0.24	0.16	0.26
R^2	0.975	0.962	0.972

Table 7-9. Fitting values, corresponding to the graphs in Figure 7-12. The best fit from R^2 value was obtained when fitting automatically in (a) but the difference was minor compared to manually adjusted A value fitting in (c). Visually the latter delivered better overlap between experimental and modelled signal.

Figure 7-12 also allowed to evaluate how the rest of the parameters got affected when variation of the fitting was performed. The centre point between the peaks, y_c, was barely changing in all three approaches from Table 7-9, being a consistent 189.6 value, which can be rounded to an integer value of 190. This reassures that the model found the dip between the peaks efficiently and there was no need for further manual adjustment. This means that only two variables were left in the fitting expression: *A* and *w*. Since they are dependent on one another

so that with increasing *A*, *w* decreases (Table 7-9 (a, c)), only one of them needs to be adjusted. When needed, the value of *A* was manually adjusted, allowing *w* to vary accordingly.

7.3.3 Modified Bessel function fitting to the experimental line profiles

Having already established that V middle line profiles contain less artefacts than the H line profiles, only the V ones from nanoband edge disc electrode images collected in FB and SG-TC modes were fitted using modified Bessel function to show the effectiveness of this fitting model. From Figure 7-13, every line profile overlaps with the modelled signal to a great extent, suggesting a great fitting from the visual evaluation. It is, of course, subjective but it has been shown to be to relevant in this data analysis and contributes to a better data understanding, since clear and relatively obvious trends are evaluated; when possible, quantitative analysis is also used.

Some differences between FB and SG-TC modes are observed, similarly as in Section 7.2. Fitting to the sides of the line profiles, marked with the boxes in Figure 7-13 (a, d), are different for the two modes. As discussed in the above section, even though in SG-TC mode the sides of the line profiles were not perfectly agreeing with the model, it was shown that it does not have a major influence on the overall fitting. Wider line profile sides, 'wings', in SG-TC mode middle line profiles in Figure 7-13 (d-f) present the net effect of the diffusion field from the substrate rather than its characteristic features. Meanwhile, the sides of the FB mode line profiles in Figure 7-13 (a-c) have a characteristic of more rounded curves towards the peaks, which corresponds to the Bessel generated response. Hence, in FB mode, there is a better overlap between two lines, resulting in a better visual fitting within the two coloured boxes.

Due to FB mode being characteristic of having more time-dependent tip current artefact than SG-TC mode, the sides of the line profiles were excluded from the fitting boundaries, as the red line in the graphs does not continue to the ends of the line profile in FB mode. However, removal of these data points simply made the line profile more symmetrical and more improved the overall fitting, reassuring that the artefacts did not affect the electrode area nor the fitting. The sides of the experimental line profile agree with the modelled response to the greatest extent at d = 13.2 µm in Figure 7-13 (b), which is the middle value of three d. The left side of the line profile at 22.1 µm in Figure 7-13 (c) is greater in the experimental line profile than in the predicted one due to the time-dependent tip currents at the start of the line profile. The right side of the experimental line profile at 9.2 µm in Figure 7-13 (a) is also of greater currents due to a possible delicate tilting or minor time-dependent tip currents, which were not sensed at greater d.

Regarding the middle area between the peaks, the fitting improves with increasing tip working distance in both modes, as in Section 7.2. The middle area between the peaks becomes more filled with the hemispherical diffusion field from the sides of the band presenting higher

currents in both modes, which are modelled well by the modified Bessel function. The fitting is exquisitely successful in SG-TC mode, as the two signals overlap to a great extent at all *d*. The extent of this signal overlapping is significantly more effective than in the Gaussian fitting, showing that modified Bessel function is more suitable and effective approach for quantitative analysis of such line profiles. FB mode is more sensitive to varying tip working distance, hence there is more variation in the effectiveness of the fit over this area. However, the sides of the line profiles fit to a great extent and the difference between the two lines over the peak area is also relatively small.

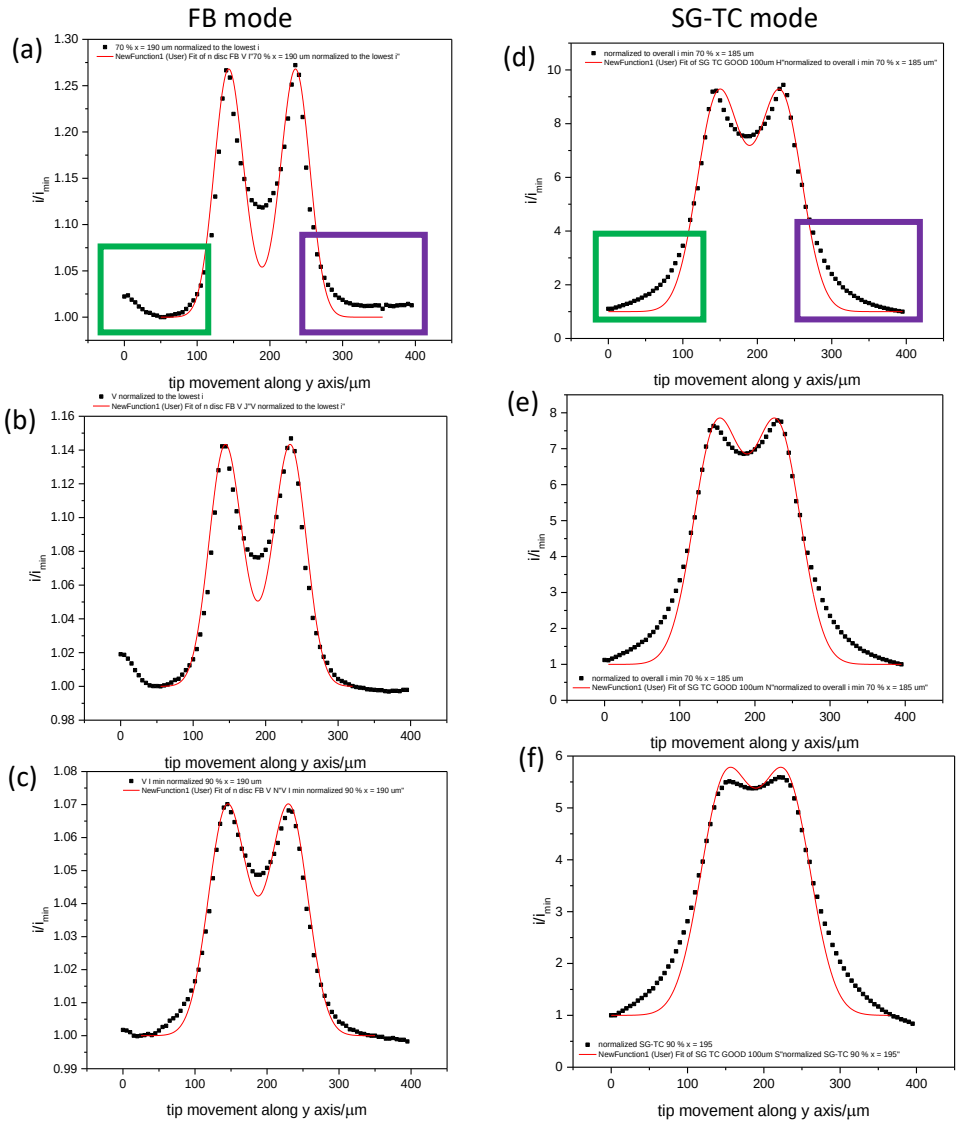

Figure 7-13. MNEE, r = 50 µm disc, V middle line profiles (black squares) fitted to the modified Bessel function (red line) at (a, d) d = 9.2 µm, (b, e) d = 13.2 µm and (c, f) d = 22.1 µm in (a-c) FB and (d-f) SG-TC modes.

The overall fit measured by R^2 is over 0.9 for all graphs in Figure 7-13, as seen from Table 7-10, reassuring great fitting of the modified Bessel function to the experimental line profiles.

The fitting is slightly better for SG-TC mode at the first two tip working distances, reflecting that poorer fit on the sides of the line profiles was compensated by an effective fitting over the middle area, resulting in an overall similar fit for both modes. At the greatest *d*, R^2 is better only by 0.0068 in FB than in SG-TC mode. The FB mode line profile in Figure 7-13 (c), the dip between the peaks is proportional to the width of the peaks, and the whole line profile shows a great compatibility with the theoretical response. In SG-TC mode in Figure 7-13 (f), the equivalent line profile is already resembling a one-peak response, which is slightly more challenging to fit. To avoid generating such one-peak response, *A* value was increased to allow for the two peaks. As a result, fitting to the intensity of the peaks suffered and the overall fit unlike in the Gaussian analysis was better to the equivalent FB mode line profile. The difference is less than 1%, still reassuring that both FB and SG-TC mode line profiles representing hemispherical diffusion profiles were closely comparable to the concentration profiles from the modified Bessel function. Data fitting was more effective with this function than with the Gaussian function in Section 7.2. The values of R^2 in SG-TC mode are consistent, while in FB mode R^2 increases with increasing *d*.

	FB			*SG-TC*		
d	9.2 µm	13.2 µm	22.1 µm	9.2 µm	13.2 µm	22.1 µm
A	1.9	0.97	0.38	37	29	22
w	19.06 ± 0.22	21.27 ± 0.16	24.68 ± 0.10	26.88 ± 0.16	28.91 ± 0.18	30.43 ± 0.19
y_c	189.30 ± 0.75	189.19 ± 0.68	187.67 ± 0.48	189.64 ± 0.74	189.62 ± 0.87	189.38 ± 1.00
Reduced Chi-Sqr	6.54E-04	1.20E-04	9.81E-06	0.26	0.21	0.12
R^2	0.913	0.953	0.986	0.972	0.968	0.961

Table 7-10. Parameters from fitting to FB and SG-TC mode disc MNEE data, r = 50 µm.

Regarding the other variables in the modified Bessel function expression in Table 7-10, some more trends are observed. The y_c value is again consistent in both modes, differencing by less than 1 µm in most of the cases, except the maximum difference of 1.5 µm between the two FB mode values. This is well within the experimental and spatial resolution errors. Values of *A* were adjusted in all cases and they decrease in both modes with increasing tip working distance value. As a result, *w* values increase and they do so more steadily than the changing *A* values, both of which are discussed in the following section. Values of *A* and *w* are related to each other, which is again clearly reflected from this data analysis.

7.3.4 Peak width and peak intensity variation with the tip working distance

Further dependency between tip working distance, *d*, and width, *w,* as well as intensity of the peak, *A*, are evaluated. The best way to do this was obtaining plots for each in Figure 7-14 in

a similar way as was done in Gaussian fitting Section 7.2.12. However, when using the modified Bessel function for fitting, derived parameters are associated with smaller errors since subjective adjustment of the parameters was avoided, reassuring that these results are overall more objective and less impacted by the manual inputs. This fitting approach also benefits from the minimum number of variables, and the overall trend and relationship between the two parameters is derived more objectively than in Section 7.2.12.

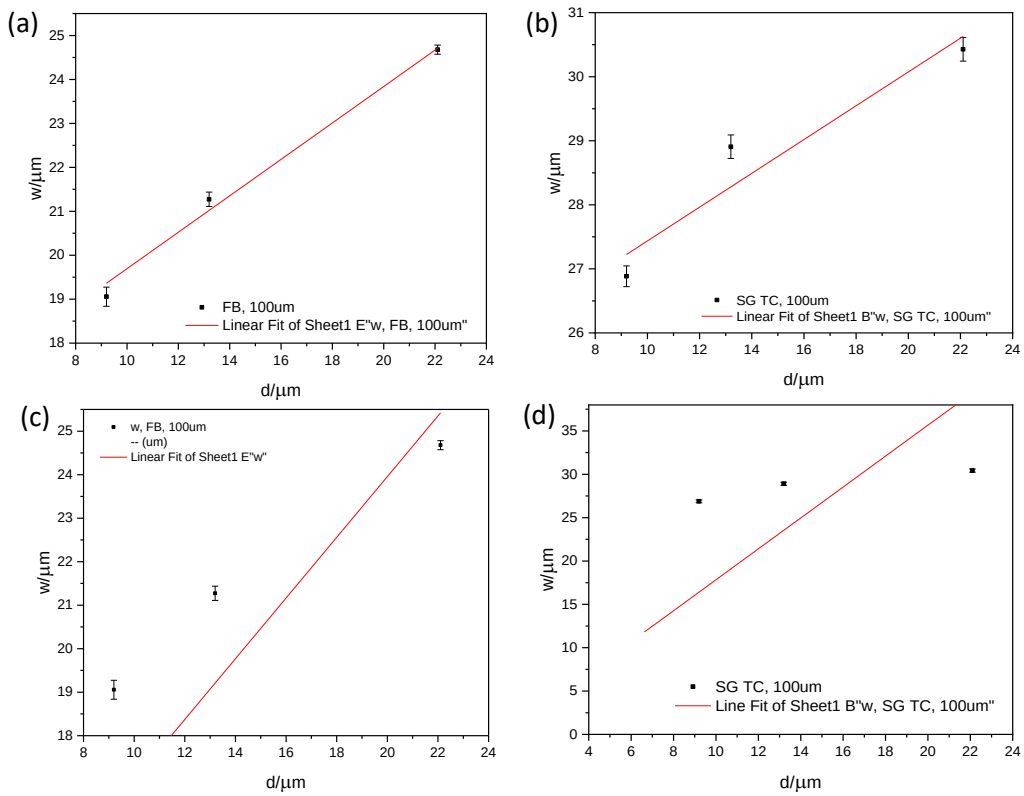

Figure 7-14. Plots of peak width, w, versus tip working distance, d, for disc nanoband edge electrode, r = 50 µm, in (a, c) FB and (b, d) SG-TC modes. Data points in (a-b) were fitted to a straight line, and in (c-d) the fitting was performed having set y-intercept to be 10 for FB mode and zero for SG-TC mode.

	100 µm, FB	*100 µm, SG TC*
Intercept	15.55 ± 0.62	24.80 ± 1.20
Slope	0.41454 ± 0.03312	0.26 ± 0.078
Residual Sum of Squares	4.46	17.35
R-Square (COD)	0.994	0.918

Table 7-11. Data points from FB and SG-TC mode straight line fitting results (Figure 7-14 (a-b)).

The plots of *w* vs *d* in Figure 7-14 (a-b) in both modes suggest that data points follow a linear trend. This agrees with the results in Section 7.2.12 and again confirms expected results due to Brownian motion. In FB mode, the straight line fit is better, resulting in R^2 = 0.994, while in SG-TC the fit results in R^2 = 0.918, as shown in Table 7-11, suggesting slightly more variation from the linear behaviour. It could be related to SG-TC mode recording hemispherical diffusion

field of the MNEE rather than the feature in FB mode. More analysis could be done to further evaluate these observations. Nevertheless, peak width was changing linearly with varying tip working distance, suggesting that further analysis also related to the Equation (7.7) could be done, allowing to evaluate if it could be further simplified by substituting *w* with *d*, and leaving with even less variables in the equation.

From Table 7-11, *y*-intercept values are 15.6 µm and 24.8 µm for FB and SG-TC modes, respectively, suggesting that at a very close proximity to the substrate the tip senses diffusion field of such width value. These values are significantly smaller than those generated from Gaussian fitting, suggesting that these two types of fitting are indeed different. Nevertheless, bigger *w* and *y*-intercept values for SG-TC than FB mode are due to the substrate generating bigger hemispherical diffusion field in the former, which senses the net effect (diffusion) of the substrate.

Since FB mode reflects behaviour and characteristics of the probe, it was considered that the width of the peaks could approach 10 µm value which is the diameter of Pt disc in the probe used for these imaging experiments when *d* approaches zero. Meanwhile, SG-TC mode reflects behaviour and characteristics of the substrate electrode which is a nanoband and so the width parameter could be expected to approach zero. Both sets of data were fitted when the y-intercept was set to 10 and 0 depending on the mode, as shown in Figure 7-14 (c-d). In both cases the fitting is less effective than in (a-b). In SG-TC mode data it seems that the values might be levelling off towards a specific value but not in a linear manner. Spatial resolution controlled by 5 µm value, 10 µm Pt tip and 100 µm disc MNEE resulted in high resolution images and great fitting to the predicted model but this last assumption might be too delicate for this set of data. Equivalent analysis is performed in Chapter 8 to data collected on 50 µm substrate and in Chapter 9 when using 1 µm Pt probe to image 50 µm MNEE. This is an assumption and work in progress and is shown for the discussion of various relationships within the data; however, it requires further work.

7.4 CONCLUSIONS

Full quantitative analysis of the MNEE line profiles was performed using the Gaussian multi-peak and the modified Bessel functions. Since the former models response from two individual points separated by a set distance, it was a more acceptable way to quantify middle line profiles from the square than disc nanoband electrodes. Data points over the middle area of the line profile were manually adjusted to remove some of the diffusion contribution from the sides of the band, and this was more effective for the square, where the sides are separated by a constant distance at all times. Due to the geometry differences, there was more unadjusted modelled contribution over the area between the peaks in the disc data at all three *d*. The width parameter was generally set the same for both peaks in all cases, confirming

symmetry and uniform activity within the band. Disc data was then fitted using specifically for the disc designed modified Bessel function, which has symmetry directly implied within the function. The fitting was easier to perform and less subjective than using the Gaussian model due to the minimal requirement to adjust the fitting parameters. The fitting was successful for data from both FB and SG-TC modes at all tip working distances.

Both fitting models do not include any of the artefacts discussed in Chapter 6, hence the differences between experimental and modelled line profiles were expected to be accounted for the imaging-related artefacts, such as convection in H line profiles and time-dependent tip currents at the beginning of the line profiles. Interestingly, higher R^2 was obtained for the tilting-affected V line profile than less affected H line profile (nanoband square electrode in FB mode), suggesting that the model adjusted for the slope in the data.

Differences between experimental and modelled signals were found over the middle area of the electrode (between the peaks) when evaluating diffusion controlled mass transfer contribution from the sides towards the middle of the electrode. For all data, the fitting effectiveness increased with increasing *d*, especially over the peak area, showing reduced effects of such contribution from the rest of the band, typically underestimated by the model. With increasing *d*, the peak separation decreased, as the peaks became broader, and their widths increased, reflecting increasing diffusional field overlap from the sides of the band, which was apparently easier to model. SG-TC mode data fitted to a greater extent than FB mode significantly in Gaussian fitting and slightly better in Bessel fitting, and this reflects that diffusion from the substrate is easier to quantify than the effect of the substrate on the tip's diffusion in FB mode. Finally, a linear correlation between the peak width, *w*, and *d* was found from both fitting approaches, reassuring that diffusion field from the electrode expanded both to the width and to the height, as suggested by Brownian motion.

7.5 REFERENCES

1. Waud, D. R. On Diffusion From a Point Source. *J. Pharmacol. Exp. Ther.* **159**, 123–128 (1967).
2. Massachusetts Institute of Technology. 3 . Diffusion of an Instantaneous Point Source. 1–7 Available at: http://web.mit.edu/1.061/www/dream/THREE/THREETHEORY.PDF.
3. Owen, S. Common Probability Distributions: The Data Scientist's Crib Sheet. *cloudera* (2015). Available at: https://blog.cloudera.com/blog/2015/12/common-probability-distributions-the-data-scientists-crib-sheet/. (Accessed: 2nd August 2018)
4. Harvard University. A Summary of Error Propagation. 1–5 (2007). Available at: http://ipl.physics.harvard.edu/wp-uploads/2013/03/PS3_Error_Propagation_sp13.pdf.
5. Kleijn, S. E. F., Lai, S. C. S., Koper, M. T. M. & Unwin, P. R. Electrochemistry of

nanoparticles. *Angew. Chemie - Int. Ed.* **53**, 3558–3586 (2014).

6. Benoit Cushman-Roisin. Chapter 2. Diffusion. *School of Engineering at Dartmouth* Available at: http://www.dartmouth.edu/~cushman/courses/engs43/Chapter2.pdf.

7. 10 Bessel functions. *The Digital Library of Mathematical Functions* Available at: https://dlmf.nist.gov/10.25.

8 SUBSTRATE AND STEP SIZE VARIATION EFFECT ON SECM IMAGES

8.1 INTRODUCTION

In the previous chapters, SECM images of 100 µm micro and nanoband disc and square electrodes opened discussion for imaging-related artefacts, such as convection effects, substrate tilting and time-dependent tip currents. These artefacts were evaluated and semi-quantified using H and V middle line profiles from the images, followed by a full quantitative analysis using analytical expressions for the line profile fitting. In this chapter, it is similarly evaluated how these imaging artefacts and image spatial resolution would change when varying the sample size and SECM scanning parameters (increment size and increment time).

Micro disc nanoband edge electrode (MNEE) of 50 µm diameter (r = 25 µm) substrate was imaged using FB and SG-TC modes. Images first presented and analysed preserve the same imaging settings and the same tip, allowing to probe the effect of changing electrode size from 50 µm to 100 µm. The step size (scanning speed) is then decreased from 5 µm to 2 µm enabling the evaluation of the step size effect on the images. Finally, effectiveness of the analytical approach using modified Bessel functions on this disc nanoband substrate is evaluated and compared to 100 µm substrate fitting results (Chapter 7), since the disc geometry has a global Bessel solution varying with the electrode radius value.

8.2 EXPERIMENTAL DETAILS

All experimental details were as in Sections 3.5.1 except for further enhancements discussed below. The MNEE (r = 25 µm) of half the electrode radius of the electrodes discussed in Chapters 6-7 (r = 50 µm) was imaged. Consequently, the edge length of the image was also reduced by half from 400 to 200 µm to preserve the ratio of the electrode size to the surrounding insulator area. This also ensured that there still is space on the sides of the electrode area to allow for the detection of any artefacts in the SECM images.

The set of previously used three tip working distances expressed as $0.7i_T^{bulk}$, $0.8i_T^{bulk}$ and $0.9i_T^{bulk}$ was not sufficient enough to capture distinguishable nanoband edge electrode in all images collected with the 10 µm probe as in Chapter 6. Hence, a smaller tip working distance of $0.6i_T^{bulk}$ was introduced to collect images in both FB and SG-TC modes used for qualitative and quantitative analysis with respect to the varied d. From Figure 4-7, where a graph of COMSOL modelled normalized tip current versus tip-substrate distance was constructed, $0.6i_T^{bulk}$, $0.7i_T^{bulk}$, $0.8i_T^{bulk}$ and $0.9i_T^{bulk}$ correspond to 6.8 µm, 9.2 µm, 13.2 µm and 22.1 µm, respectively.

8.3 QUALITATIVE ANALYSIS OF SECM IMAGES

In Figure 8-1, typical nanoband disc images at all four tip working distances in FB (left) and SG-TC (right) modes are presented. All images were collected with the same 10 µm Pt probe and 5 µm step size, used to image electrodes in Chapters 5 and 6. This means that images collected at $0.7i_T^{bulk}$, $0.8i_T^{bulk}$ and $0.9i_T^{bulk}$ are the benchmark results, providing reassurance for the observations in the earlier MNEE-related chapters. An additional $0.6i_T^{bulk}$ image contributes to a further evaluation of the tip working distance effect on the spatial image resolution.

8.3.1 Tip working distance effect on image spatial resolution

In all images in Figure 8-1, disc geometry and the effects of the decreased size of the MNEE were reassuringly captured. As seen in Chapters 5 and 6, the band shows up as the highest current band (brown colour) in contrast to the lowest current (green colour) presenting the insulator. The images at the smallest imaging distance are the sharpest (the best spatial resolution) and FB mode images are of higher electrode feature resolution than equivalent SG-TC mode images, capturing hemispherical diffusion field evolving from the substrate electrode (Section 6.2).

Such differences between the modes can be explained knowing that these experiments are not static, the two electrodes are of different sizes, and either oxidising or reducing potential is applied to both at all times. The latter has been explained in Section 6.2.1 and this contributes to the differences between the modes, prominent when the tip is brought close to the substrate. At this point, the corresponding hemispherical diffusion fields from the two electrodes differ, as shown in Figure 8-2, where the effect of the decreased electrode radius is also emphasized. In Figure 8-2 (a), a probe electrode can be considered as a more independent of the two electrodes, since it is moving in pre-set µm steps above the static substrate, and so the localised features of the surface, such as a MNEE electrode, are recorded to a greater extent in FB than in SG-TC mode.

In this chapter, the tip is a micro disc electrode of 10 µm diameter and the substrate is a MNEE which has 50 nm height Pt band spanning over 50 µm diameter. Since this radius value is half the size of the previously used 100 µm, diffusional overlap from the band sides is expected to be reached faster. This results in, not surprisingly, less spatially resolved images at the same *d* values as used in Chapter 6. A larger hemispherical diffusion field from the substrate electrode in SG-TC mode at greater *d* eventually spans over the whole 50 µm area, as illustrated in Figure 8-2 (b) and recorded in Figure 8-1 (f-h). The tip moves within a diffusion field evolving from the underlying substrate, as $FcMeOH^+$ gets generated, and with increasing tip working distance the space for the diffusion of $FcMeOH^+$ species increases, resulting in the diffusion layer growth, which eventually expands into the insulator area in the middle of the

MNEE. Also, the moving tip most likely to some extent drags $FcMeOH^+$ within the perimeter of the electrode, and this is more noticeable at larger tip working distances (Figure 8-1).

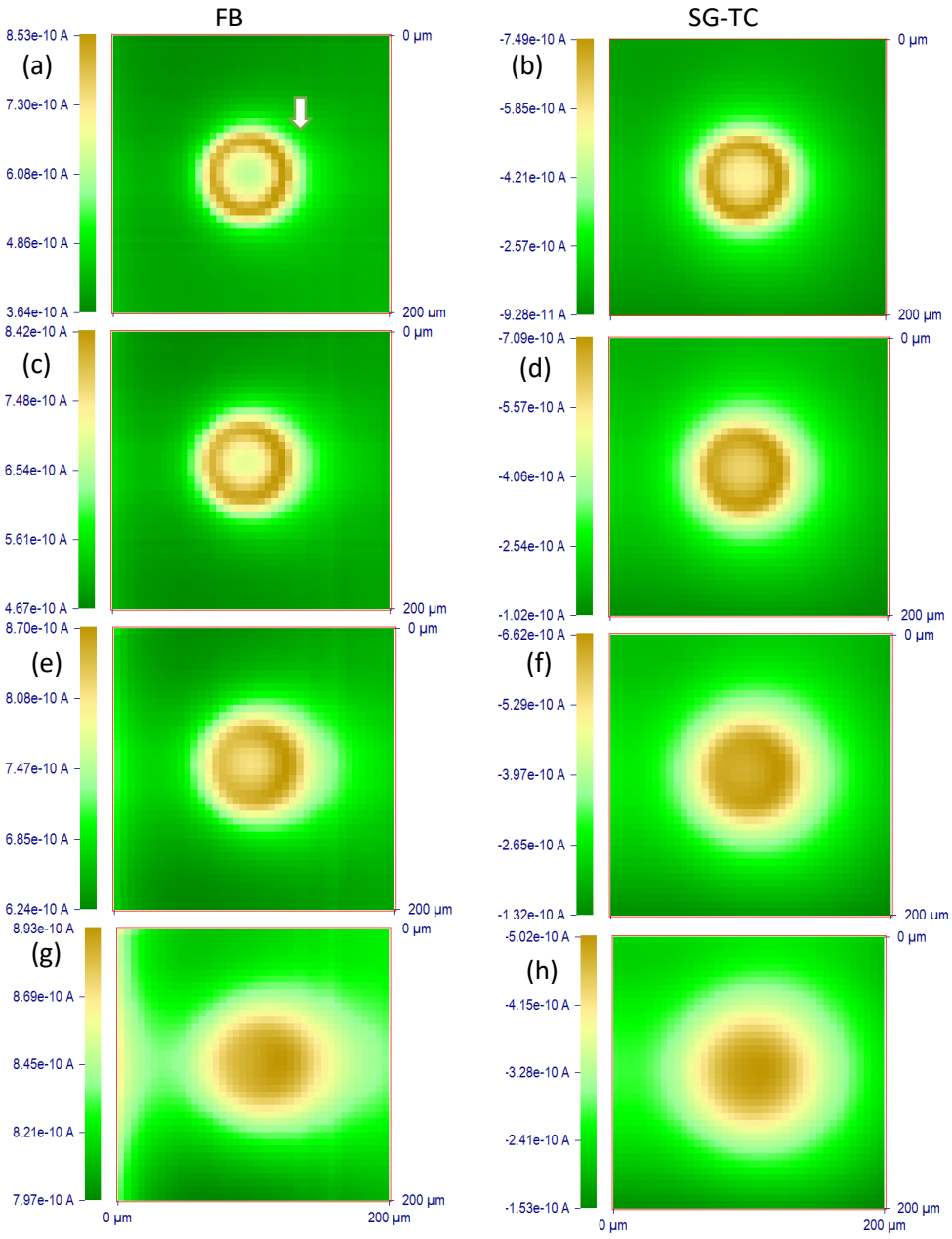

Figure 8-1. Disc (r = 25 µm) MNEE images, collected using FB mode (LHS) and SG-TC mode (RHS), a 10 µm Pt probe and a 5 µm step size at tip working distances of (a-b) $0.6i_T^{bulk}$, (c-d) $0.7i_T^{bulk}$, (e-f) $0.8i_T^{bulk}$ and (g-h) $0.9i_T^{bulk}$. White arrow in (a) marks one of three areas of focus when comparing convection artefacts between the imaging modes in text.

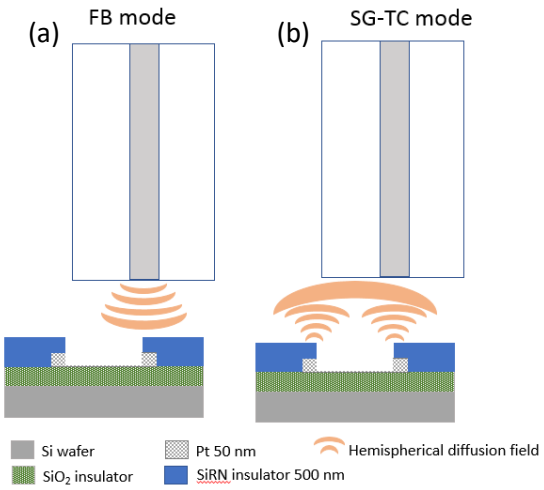

Figure 8-2. Schematic representation to show hemispherical diffusion field growth from (a) the probe electrode in FB mode and (b) from the substrate MNEE in SG-TC mode. Not to scale.

Such image comparison (together with Chapters 5-6) reassures that FB mode is more sensitive than SG-TC mode as a result of the tip electrode having a well-established denser diffusion field which evolves as the tip moves across the substrate surface and generates $FcMeOH^+$. SG-TC mode images are more fused, reflecting a struggle to capture the features of the MNEE. The substrate is static unlike the tip, which also drags some of the $FcMeOH^+$ species within the substrate's area when moving within this diffusion field (blurring effect). FB mode is better for capturing the localised features on the substrate, while SG-TC mode senses the hemispherical diffusion field of the substrate. Both imaging modes are greatly valuable and used within the research depending on the substrate of interest and what results are wanted from these images.[1]

Thus, only FB mode $0.6i_T^{bulk}$ (6.8 µm) and $0.7i_T^{bulk}$ (9.2 µm) images in Figure 8-1 clearly distinguishes that the middle of the electrode is insulator material. As expected, with increasing *d* the expanding diffusion field from the sides of the band leads to a progressive diffusional overlap in the middle of the MNEE in both modes, just like for 100 µm MNEEs in Chapter 6. SG-TC mode experiences more of such a diffusional overlap, as the centre (cavity) of the ring is becoming of a progressively higher current with increasing *d*, indicating relatively higher currents than in equivalent FB mode images.

At $0.9i_T^{bulk}$ (22.1 µm) in both modes in Figure 8-1 (g-h), the overlap is such that the images resemble micro disc electrodes, where the middle of the electrode cavity is filled with relatively high currents. This shows that decreased electrode diameter from 100 µm to 50 µm has an effect on spatial image resolution, and now smaller than 22 µm tip working distances are required for obtaining clearly resolved nanoband edge electrodes. To achieve this, the tip was brought closer to the substrate for another high spatial resolution image using *d* expressed as $0.6i_T^{bulk}$.

8.3.2 Tip working distance effect on convection

From Figure 8-1, it is ensuring that even though FB mode provides overall greater spatial resolution images than SG-TC mode, they are again more affected by convective effects just like in Chapter 6. When evaluating images on the left of Figure 8-1 from top to bottom, pale green circle representing diffusion field just outside of the electrode area and marked with a white arrow in Figure 8-1 (a) is present more on the right than the left side of the disc. The tip was scanning the substrate surface in x-axis (left to right) as in Chapter 6, and it is again no surprise to see this convection artefact. It becomes more prominent with increasing tip working distance, suggesting that the artefact is actually reduced at small tip working distances, similarly as in 100 µm MNEE images.

In the first two FB mode images in Figure 8-1 (a, c), convection effects on the right side of the electrode area are minimal, unlike in the two lower images in Figure 8-1 (e, g). At the greatest tip working distance of 22.1 µm, convective mixing has further resulted in an additional artefact at the beginning of each H line profile on the left. This side of the image in (g) is of higher currents than the rest of the insulator area, most likely due to the local stirring, induced by the rapid probe's scanning across electrode surface right to left before starting imaging the following H line profile, as explained in a more detail in Section 6.2.2. The effect is observed to the greatest extent at the line profiles passing the electrode area.

In these images, the electrode also looks more elliptical in x-axis than of a disc geometry, which was less emphasized in the previous chapters. This means that the currents are of a greater magnitude also on the right side of the insulator area compared to the ones above and below the electrode area. These additional currents are distinctive in the $0.8i_T^{bulk}$ FB mode image in Figure 8-1 (e), where higher currents on the left side of the image are still only vaguely present. The $0.9i_T^{bulk}$ image in FB mode is the most affected by the convention artefacts, which are strongly affecting both left and right of the image. The effects seem to start emerging into one big hemispherical profile resembling an ellipse.

In SG-TC mode images on the left of Figure 8-1, convection artefacts are present to a significantly smaller extent from such visual qualitative evaluation. The currents on the left side of the image are visible only in the $0.9i_T^{bulk}$ image in Figure 8-1 (h), where convection effects over the insulator area are present due to different reasons than in FB mode (Section 6.2.2). The effects are present only at the H line profiles passing the substrate electrode as $FcMeOH^+$ generated at the MNEE gets dragged towards the beginning of these line profiles, hence higher tip currents. At smaller *d*, SG-TC mode images are mostly free of apparent convection artefacts.

8.3.3 Semi-quantitative imaging artefacts analysis from the line profiles

Given that images in Figure 8-1 correspond to Figure 6-6 and 6-7, a similar approach was used to semi-quantitatively analyse line profiles in the following sections. Such analysis is more detailed than in the sections above and it allows to clarify and confirm convection effects as well as reveal any other imaging-related artefacts.

H and V middle line profiles from MNEE images in Figure 8-1 are compared in Figure 8-3. These graphs are arranged in the same way as their corresponding images: graphs on the left are from FB mode images and the ones on the right are from SG-TC mode images at increasing tip working distance from top to bottom. Not normalized (raw data) middle line profiles from each of the image are directly comparable and overlapping to a good extent. This shows symmetry in all images just like when the line profiles were normalized in Section 6.3. More specific differences between the line profiles are observed in the areas marked with purple boxes in Figure 8-3 (a), representing three zones of interest in each line profile: LHS (0-50 µm), middle (50-150 µm) and RHS (150-200 µm).

FB mode line profiles are evaluated first. As in Chapter 6, an initial line profile (box 1) in Figure 8-3 (a) suggests differences between H and V line profiles from the very beginning. The V line profile is flatter than the H one, where higher current values on the edges within this box result in a letter U-like profile. The currents on the left then gradually decrease, and at approximately x = 30 µm they are levelled with the currents from the V line profile. An efficient overlapping all the way until the final part of the line profiles (box 2) is obtained.

Currents from H and V line profiles over an insulator area on the left and right of the electrode (box 1 and 2, respectively) do not overlap in none of the FB mode graphs in Figure 8-3. These differences seem to be comparable and linked to each other: as the differences increase on both sides with increasing tip working distance, the separation between the two lines grows. The H line profiles are at higher currents at all *d* on both sides, being consistent with the visual evaluation of the images in the above section reflecting convection effects. This means that differences between H and V line profiles allow to determine how much convection is present in the H line profiles above the insulator area on both left and right of the electrode, allowing a semi-quantitative evaluation, similarly as in Chapter 6.

The $0.6i_T^{bulk}$ image and its line profiles are affected to the smallest extent by convection in this data set. This is reflected by the smallest difference between H and V line profiles on both sides, which is even more reassuring when compared to the most convection-affected H line profile in Figure 8-1 (g). Convection effects here are relatively larger than seen in Chapter 6, responsible for an oval presentation of the disc electrode (Figure 8-1). In this case, both imaged MNEE and the total imaging area are smaller than in Chapter 6, hence there is less

space for the artefacts to occur before starting to interfere with the diffusion field from the electrode surface.

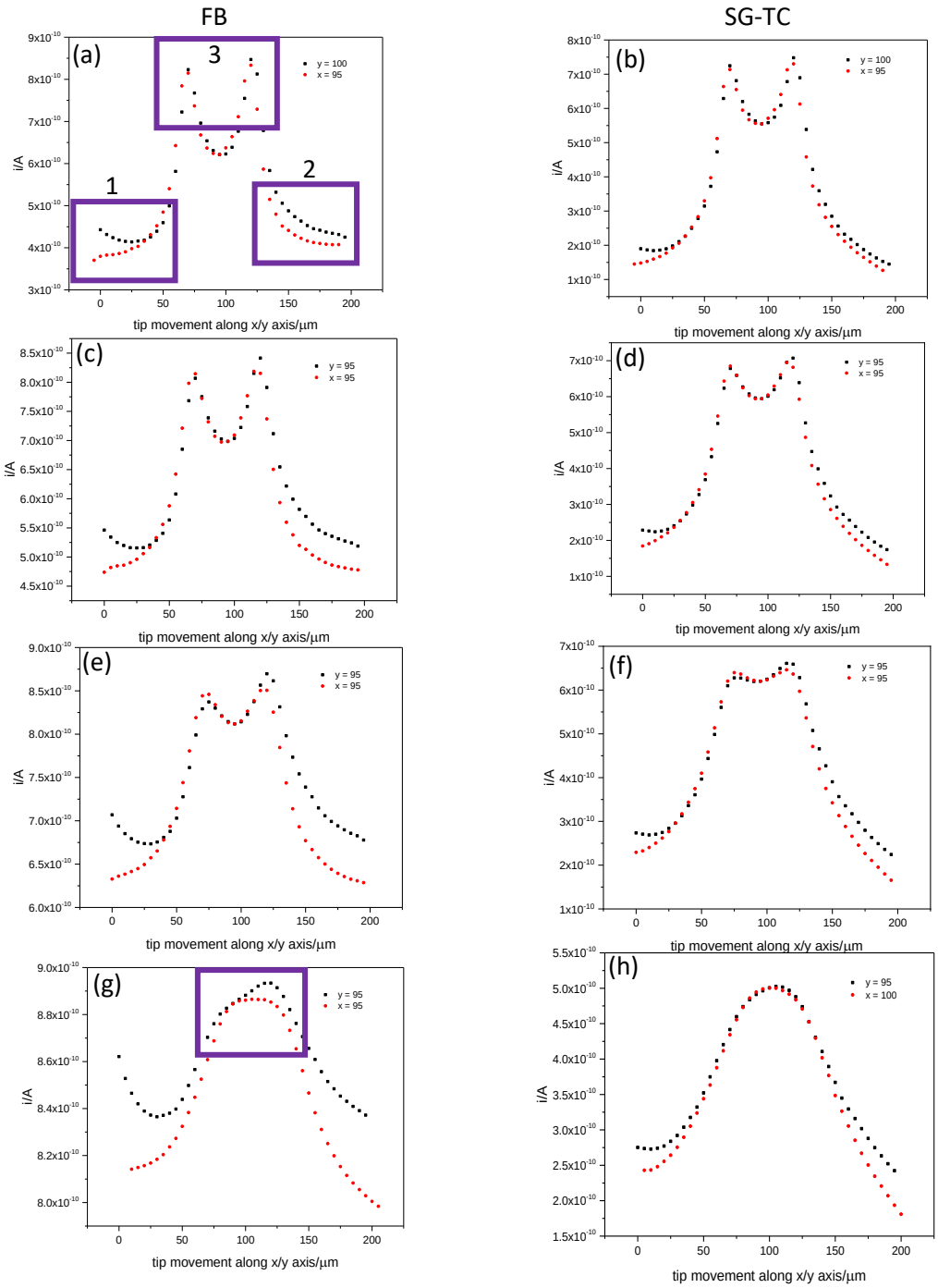

Figure 8-3. The H (black squares) and V (red circles) middle line profiles from FB (left) and SG-TC (right) mode images (Figure 8-1) collected with a 10 µm Pt probe at 5 µm step size setting. Purple boxes mark areas of interest discussed in text. Currents were not normalized, since in all graphs the line profiles (from the same image) showed a good agreement.

Regarding the peaks in box 3 in Figure 8-1 (a), they are at similar current values in both H and V line profiles at the smallest *d*. With increasing tip working distance the peaks from V line profiles remain equivalent, while the difference between the peaks in the H line profiles increases. Higher currents on the right peak reflect probe's left to right movement and match current differences on the sides of the line profile discussed above. Together these observations reassure that convection effects are responsible for current differences between H and V line profiles at all three areas, representatively marked in Figure 8-1 (a). As a result, the V line profiles are more symmetrical due to minimal convection artefacts as in 100 µm diameter MNEE analysis in Chapter 6.

More symmetry is observed both around the peak area and on the edges of the line profiles in SG-TC mode middle line profiles in Figure 8-3 (b, d, f, h) than in FB mode. First, in the area where box 1 should be, the two line profiles differ at all *d,* but this difference remains approximately constant at all tip working distances. Initial profile of the H line profiles is of a sharper U-form than in V line profiles, showing presence of some imaging artefacts; however, this U-form is also significantly shallower than in FB mode. Both observations reflect smaller and less varying with altering *d* convection effects in SG-TC mode. The line profiles are more of the mirror images from the middle-between-the-peaks perspective than they are in FB mode.

Then, the maximum peak values (box 3) in SG-TC mode are also similar, suggesting that convection effects are affecting areas in all 3 boxes to a greater extent in FB mode. In other words, H and V line profiles are differencing to a smaller extent in SG-TC mode. Interestingly, in this mode data in Section 6.3.4, convection effects over the peak area were somewhat greater than in FB mode as well as increasing with decreasing tip working distance, clearly showing that reduced substrate size has effect on convection effects in SG-TC mode.

Line profiles from the images collected at $0.9i_T^{bulk}$ in both modes resemble responses from micro electrodes. As foreseen from the qualitative analysis of the images, the peaks from these MNEE line profiles are not resolved. Instead, they merge into one peak due to expanding and overlapping hemispherical diffusion fields from the sides of the band. In Chapter 6, images and line profiles from nanoband electrodes of 100 µm dimension were all preserving the nanoband behaviour and the peaks in all of the line profiles. Here, the size of the electrode has been decreased by half and so $0.9i_T^{bulk}$ image reflects this change.

Overall, H and V line profiles differ in a similar manner as previously observed in Chapters 5 and 6. The H line profiles are more susceptible to convection and product dragging effects due to the tip's movement from left to right, while V line profiles are more symmetrical. This analysis reassures that tilting in these images was successfully prevented during the set-up, as all differences between the line profiles are explained by convection.

8.4 QUANTITATIVE ANALYSIS: MODIFIED BESSEL FUNCTION FITTING TO THE VERTICAL LINE PROFILES

Since V line profiles are less affected by artefacts, they are more suitable for further quantitative analysis, which is at the initial stage of such study. In Chapter 7, line profiles from disc nanoband images are quantitatively analysed using Gaussian and modified Bessel function fitting. Some differences between these two methods are present due to different approaches in evaluating contribution from the continuous band towards the middle line profile of interest. In Section 7.3, modified Bessel function was shown to be a better method than the dual-peak Gaussian function for fitting line profiles from disc nanoband electrode. An in-depth analysis of H and V line profile comparison was performed in Chapters 5 and 6. Therefore, only V middle line profiles from MNEE images are fitted using a well-established Bessel function method in this chapter.

8.4.1 Fitting specifications

Fitting equation and method were used as described in Section 7.3.1, except the radius of the electrode was 25 µm and an additional d value of 6.8 µm ($0.6i_T^{bulk}$) was used. The same approach as in Section 7.3.2 was applied to evaluate the boundaries and the overall fitting settings, which are: automatic fitting across the majority of data points in Figure 8-4 (a), manually adjusted peak intensity, A, within the narrower boundaries in Figure 8-4 (b) and manually adjusted A value within the full line profile in Figure 8-4 (c).

The summary results from such data comparison are presented in Table 8-1. The overall fit presented by R^2 decreases from 0.93 in (a) to 0.87 in (b) after such manual boundaries adjustment just like in Chapter 7. Also, the automatic response in (a) is to a better extent fitting data points at the middle area between the peaks, leaving the actual peak-points out, unlike in (b-c). To avoid this, for further fittings the boundaries were set selecting as many as possible data points. These include normalized current values ≥1 and the actual peak data points, just like in (c). The peaks in the line profiles get shallower as d increases and such initial fitting shows that the intensity of the peak does not correspond to its width. These insights suggest that fitting to the middle area between the peaks is the best fitting approach, which is used in the following section in Figure 8-5.

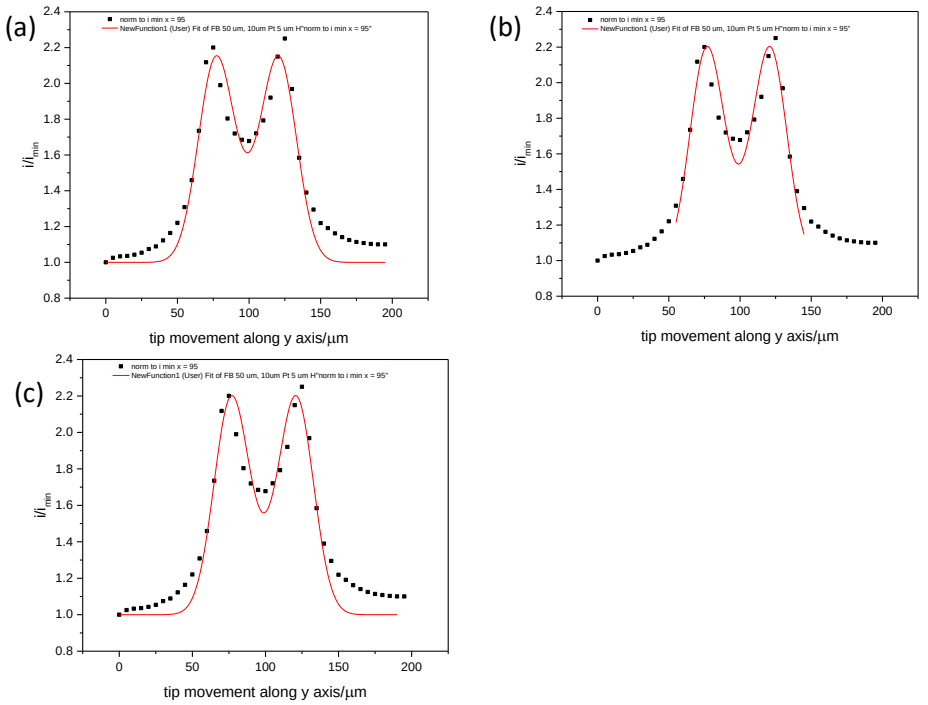

Figure 8-4. Several ways of the modified Bessel function fitting (red line) to a V middle line profile (black squares) from a MNEE, r = 25 µm: (a) automatic fitting within a full line profile, (b) fitting having manually set A value and narrower boundaries and (c) fitting within a full line profile having manually set A value for fitting the peak intensity.

	(A) AUTOMATIC FIT	*(B) NARROW LIMITS*	*(C) FULL LIMITS*
A	6.63 ± 0.49	*7.5*	*7.4*
w	11.84 ± 0.37	11.30 ± 0.14	11.40 ± 0.14
yc	98.88 ± 0.66	98.88 ± 0.62	98.87 ± 0.61
Reduced Chi-Sqr	0.011	0.012	0.012
R^2	0.93	0.87	0.93

Table 8-1. Fitting values, corresponding to the graphs in Figure 8-4.

8.4.2 Modified Bessel function fitting to vertical line profiles

In Figure 8-5, V middle line profiles from disc nanoband images are fitted to the modified Bessel function. The fit seems to be effective and overall similar to 100 µm MNEE results in Section 7.3, though there are also several differences.

Fitting to the area between the peaks within a purple box in Figure 8-5 (a) is significantly more successful than in the previous chapter. Generated modified Bessel function is at slightly lower currents only in Figure 8-5 (a), and in the rest of the graphs both lines are at similar heights. When fitting 100 µm MNEE, there was a choice whether to a greater extent fit the peaks or the area between the peaks. In this case, both fit well without the need to significantly adjust parameters, showing that modified Bessel function fitting is an effective approach for a quantitative analysis of these middle line profiles from a 50 µm MNEE.

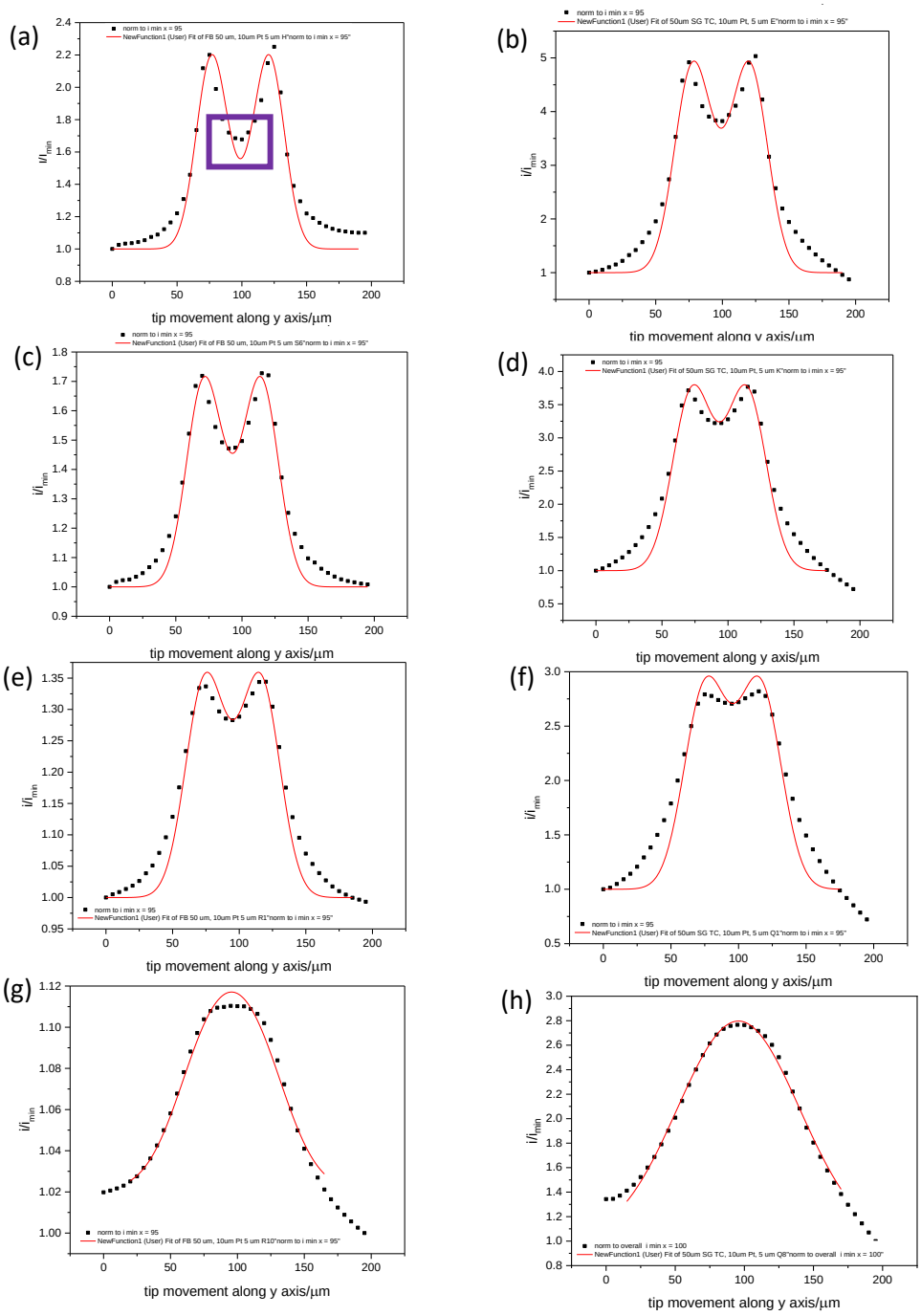

Figure 8-5. Modified Bessel function (red line) fitting to a V middle line profile (black squares) in FB (left) and SG-TC (right) mode at increasing (top to bottom) tip working distance of (a-b) 6.8 µm, (c-d) 9.2 µm, (e-f) 13.2 µm and (g-h) 22.1 µm. Purple box in (a) marks area between the peaks, where more effective fitting was achieved than in Chapter 7.

Fitting on the sides of the line profiles in Figure 8-5 (a-f) seems to be less effective than fitting over the middle area from a visual evaluation. The two lines in each graph do not overlap as efficiently as in FB mode data in Section 7.3. The sides of the line profiles are similar in both modes and they resemble SG-TC mode data from 100 µm MNEE. This is likely due to the

decreased size of the electrode and imaging area, but also, they can be considered minor and not having a significant impact on the fitting effectiveness, as seen from the fitting results in Table 8-2. The lowest R^2 value is 0.924, which is a relatively high value, as seen throughout this thesis, reflecting overall successful data fitting. The value was obtained from the SG-TC mode $0.8i_T^{bulk}$ image V line profile fitting shown in Figure 8-5 (f). The line profile experiences significant diffusional overlap from the sides of the band, resulting in such a response where the two peaks are not particularly well separated. The fitting parameters were adjusted to preserve the peaks, and this resulted in a relatively less effective overlap between the line profiles due to the absence of proportionality between the peak width and intensity. Despite this, a relatively high R^2 = 0.924 was obtained.

Similar value (R^2 = 0.929) was obtained for $0.6i_T^{bulk}$ image line profile in FB mode in Figure 8-5 (a), where the area between the peaks (purple box) does not fit as effectively as it has been seen in other examples. The fit is overall effective and if there were more data points, the corresponding R^2 value probably would be higher. Having less data points compared to the 100 µm MNEE data suggests that each point has now more weight on the overall fitting.

Overall, all R^2 values are over 0.92. For the largest tip working distance of $0.9i_T^{bulk}$ in Figure 8-5 (g, h) the maximum fitting effectiveness is reached, as the R^2 values for SG-TC and FB modes are 0.995 and 0.985, respectively. There is little difference between the two, reflecting that both line profiles are fitting to the greatest extent observed in this thesis. In both cases, the peaks have emerged into one; hence, the modified Bessel function is efficient in fitting line profiles with either two or one peak at various tip working distances, further showing its suitability and effectiveness for fitting such data.

FB	*d = 6.8 µm*	*d = 9.2 µm*	*d = 13.2 µm*	*d = 22.1 µm*
A	*7.40*	4.30 ± 0.29	*2.30*	0.24 ± 0.018
w	11.39 ± 0.14	12.57 ± 0.33	13.82 ± 0.11	24.43 ± 0.87
y_c	98.87 ± 0.61	92.85 ± 0.58	95.18 ± 0.69	95.65 ± 0.56
R^2	0.929	0.9598	0.954	0.985
SG-TC				
A	*20*	*14*	*11*	2.57 ± 0.032
w	12.93 ± 0.14	13.92 ± 0.15	14.65 ± 0.15	39.41 ± 0.42
y_c	99.10 ± 0.67	93.55 ± 0.77	95.79 ± 0.93	95.73 ± 0.33
R^2	0.947	0.943	0.924	0.995

Table 8-2. Modified Bessel function fitting to the V line profiles at four tip working distances obtained from 50 µm MNEE images. Data was collected using a 10 µm Pt probe and a 5 µm step size in FB and SG-TC modes.

The other fitting parameters from Table 8-2 are also further discussed. In majority of the cases, the peak intensity, *A*, was fixed, as discussed in Section 8.4.1 to reassure the best fitting. The value decreases with increasing *d*, which corresponds to wider peaks due to an expanding

hemispherical diffusion field from the bands in both modes. Then, the middle point (between the peaks), y_c, is within a reasonable experimental error in both imaging modes. The evaluation of the y_c values shows that in both modes at d = 6.8 µm y_c is greater than at the other tip working distances, reflecting the best resolution of the peaks and so the highest spatial resolution of the MNEE. At the other distances, the features are progressively getting masked by the diffusion fields, hence widening peaks and slightly shifted middle values. The value of A is related to the peak width, w, discussed in a greater detail in the following section.

8.4.3 Peak width variation at selected tip working distances

Plots of peak width, w, versus tip working distance, d, for a 50 µm diameter MNEE are presented in Figure 8-6. From Table 8-2, neighbouring w values at d = 6.8, 9.2 and 13.2 µm differ by approximately ±1 µm compared to approximately ±2 µm in Section 7.3.3. The differences in both cases are well within the experimental error but the former still suggests that the hemispherical diffusion field expansion from a smaller substrate is less sensitive to the three tip working distances than 100 µm MNEE. It is most likely a coincidence that both of these values and the electrode sizes differ by the factor of two.

Smaller differences between the neighbouring w values result in a more gradual w growth with increasing d for 50 µm MNEE. At the largest d (22.1 µm) the hemispherical diffusion field is captured to the greatest extent, resulting in a relatively larger value of w compared to the other two values, which is greater in SG-TC than in FB mode. Such w increase reflects one-peak rather than two-peak response. To preserve uniformity of the data points, these were excluded from the plots and linear data fitting in Figure 8-6.

The resulting R^2 values from data fitting presented in Table 8-3 are 0.99 and 0.95 for FB and SG-TC modes, respectively. Such linear fitting effectiveness reflects linear arrangement of the data points in both modes, as shown in Figure 8-6 (a-b). In a FB mode graph, data are almost perfectly linear, while in SG-TC mode minor discrepancies in the linear trend are present. These reflect that the peak width values are slightly less linearly dependent on the tip working distance than in FB mode, as observed in Section 8.3.

From equivalent 100 µm analysis (Section 7.3.4), graphs from both modes were also comparable and the fitting data is presented together with the 50 µm MNEE data in Table 8-3. Just like in 50 µm MNEE data, the R^2 values from 100 µm MNEE in both modes are greater than 0.9, and SG-TC mode results in slightly lower overall fitting values than FB mode. The fitting-associated-errors for data from both electrodes are reasonable and comparable, reassuring that the straight-line behaviour in w versus d is prominent to both electrodes. The intercept values are almost double as high as for SG-TC mode in both cases, and so the ratios of these values are also similar, being 1.39 and 1.60 for 50 and 100 µm MNEEs, respectively,

showing similar difference between the two data sets. Overall, *w* values from both 100 µm and 50 µm MNEEs are linearly arranged against tip working distance in FB and SG-TC modes.

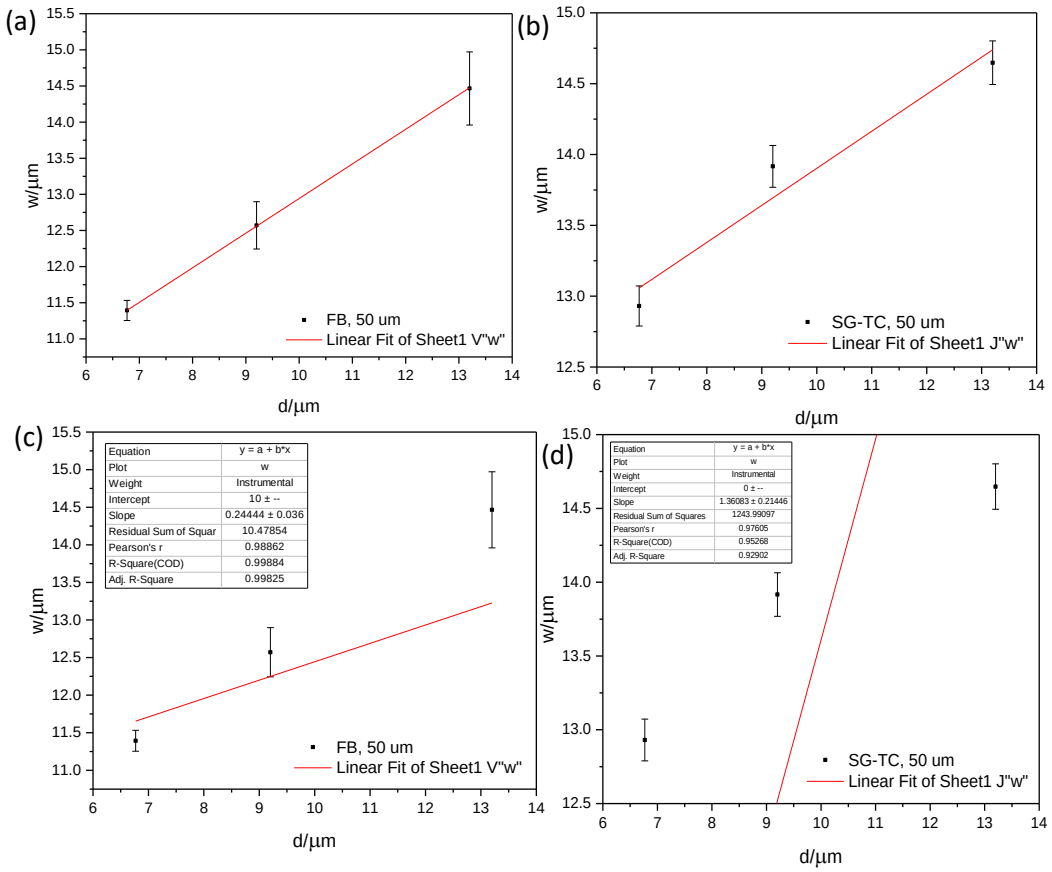

Figure 8-6. The plots of w vs d, showing errors associated with w values, derived from 50 µm MNEE (a) FB and (b) SG-TC mode V middle line profile fitting using modified Bessel function. Linear fitting (red line) was performed to data points (black dots) from both modes, leaving the y-intercept to vary in (a-b) and having set it to (c) 10 µm and (d) 0 µm.

Further, as discussed in Section 7.2.12 and Section 7.3.4, *w* vs *d* plots are fitted to a line with a set 10 µm or 0 µm intercept value, as shown in Figure 8-6 (c-d). It allows evaluation if at *d* = 0 µm, *w* value corresponds to the size of the electrode to which oxidation potential is applied, which is 10 µm and effectively 0 µm in FB and SG-TC modes, respectively. FB mode agrees with this assumption to a greater extent than SG-TC mode, as the first two data points are relatively close to the generated fitting line in Figure 8-6 (c), unlike less linear data arrangement in (d).

SG-TC mode data (intercept at 11.3 µm) suggest that the value of 10 µm might be the one to consider for both modes. The tip is a relatively larger electrode when compared to a point-source-like nanoband, and it is the tip current that is always collected. If a smaller tip or if more data points were collected at smaller tip working distances, it would be possible to further evaluate this, when knowing if the curve in Figure 8-6 would start levelling off or keep

decreasing in a more or less linear manner to a specific value. More discussion on this is presented in Chapter 9.

	50 µm, FB	*50 µm, SG-TC*	*100 µm, FB*	*100 µm, SG-TC*	*Intercept ratio, 50 µm*	*Intercept ratio, 100 µm*
Intercept	8.15 ± 0.024	11.29 ± 0.59	15.55 ± 0.62	24.80 ± 1.20	1.39	1.60
Slope	0.48 ± 0.0031	0.26 ± 0.060	0.42 ± 0.033	0.26 ± 0.078		
Residual Sum of Squares	0.00169	3.44	4.46	17.35		
R^2	0.999	0.950	0.994	0.918		

Table 8-3. Linear fitting results to w vs d plots, where 50 and 100 µm MNEEs data were used. Intercept differences between the modes for both electrodes are shown in the last columns.

8.5 IMAGING STEP SIZE EFFECT ON IMAGE SPATIAL RESOLUTION AND IMAGING ARTEFACTS

Imaging settings effect on image spatial resolution and amount of artefacts present in SECM images is evaluated using two different step size settings to collect these images. The same MNEE was imaged with a 10 µm Pt probe using a 2 µm and a 5 µm step sizes at 9.2 µm ($0.7i_T^{bulk}$) tip working distance. FB rather than SG-TC mode was used, since it has been shown that FB mode images are of a greater electrode-features resolution and more sensitive to the variation of *d*, suggesting that a broader discussion will be possible than if using SG-TC mode data.

8.5.1 Qualitative image analysis

Two FB mode images are compared in Figure 8-7. First, it is not unexpected to see that 5 µm pixels in (b) are larger than 2 µm pixels in (a), which is particularly visible when comparing electrode areas (dark brown circles). As a result, the electrode area is more pixelated in (b) than in (a). However, a smaller step size (slower scan) results in an image emphasizing probe's left-to-right movement over the insulator area, as H scan lines are more clearly visible in (a) than in (b). These H lines could be an artefact related to the stepper motor, which caused electronic or mechanical noise. As the lines are less visible towards the bottom of the image, the noise could be intermittent or position-dependent.

A smaller step size used to image the same size area as with a larger step size means that more data points were collected. Therefore, a higher spatial resolution is expected; however, the downside is that it takes longer time to complete the image, and instead of e.g. 320 s, 2000 s are required. This suggests that the measurement is likely to be more susceptible to tip-passivation effects, such as time-dependent tip currents. Thus, the insulator area over the middle of the MNEE is more resolved in a more pixelated image collected with a 5 µm rather than a 2 µm step size, suggesting that the image spatial resolution is not necessarily and

unconditionally improved if the step size is decreased. Longer quiet time (300 s) was set to correspond to a longer imaging time, both of which were significantly longer compared to imaging with 5 µm step size setting (quiet time = 60 s). Finally, the combination of a 10 µm probe and a 2 µm step size might also have led to an overlapping of some data points, resulting in such less clearly resolved insulator area.

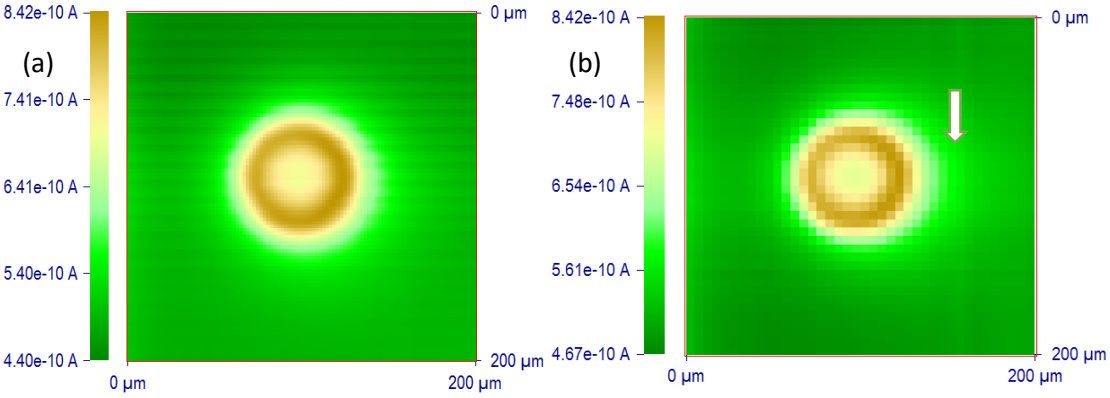

Figure 8-7. SECM FB mode images of a disc nanoband collected at $0.7i_T^{bulk}$ with a 10 µm Pt probe using (a) 2 µm step size, 300 s quiet time and (b) 5 µm step size, 60 s quiet time. White arrow marks convection effect on the RHS of the image, more visible in (b) than in (a).

From such qualitative analysis of Figure 8-7, convective effects do not seem to be particularly reduced as a result of the reduced imaging step size. It appears that the light green circle, marked with a white arrow in Figure 8-7 (b) and corresponding to the hemispherical diffusion field outside of the high current edge (brown colour) representing MNEE, is only slightly less dragged to the right in 2 µm than in 5 µm image. A 2 µm step size resulted in little improvement in the collected image resolution, nor the imaging artefacts were significantly reduced. The 10 µm Pt probe and a 5 µm step size seem to be a good combination to collect images of high-resolution electrode features within a reasonable amount of time.

8.5.2 Semi-quantitative imaging artefacts analysis using middle line profiles

In Figure 8-8, H and V middle line profiles from images in Figure 8-7 are compared to further evaluate imaging step size effect on image resolution and artefacts. The line profiles appear to show symmetry between the two in both graphs, and the 2 µm H line profile is offset only by several µm to the right from an almost perfect overlap with the 5 µm H line profile in (a). The 2 µm line profile compliments the 5 µm line profile in both H and V directions, since smaller step size generates more data points, which is clearly reflected in Figure 8-8 (a): the left peak is not clearly established in the 5 µm line profile, while it is well-defined in the 2 µm line profile. This may to some extent contribute to the differences between the peak current values, which were mostly attributed to the convection effects (Section 8.3.3).

H middle line profile from a 2 µm step line profile (black squares) is at lower current values at both initial (purple box) and final (green box) areas of the line profiles than the 5 µm step line profile in Figure 8-8 (a). This suggests that convection effects on both sides of the 2 µm line profile are actually reduced as a result of less intensive stirring by the probe due to a smaller step size, hence a slower movement of the tip. These convection differences were not particularly apparent from the qualitative analysis in the above section and are seen only from such semi-quantitative analysis.

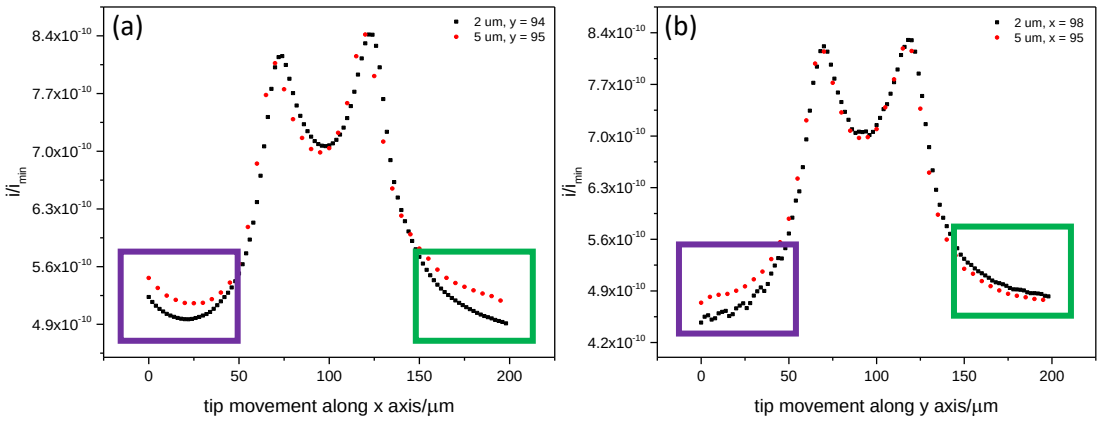

Figure 8-8. (a) H and (b) V middle line profile comparison from 2 µm (black squares) and 5 µm (red circles) step size data collected with a 10 µm Pt probe at $0.7i_T^{bulk}$ in FB mode. Coloured boxes on the graphs emphasize the beginning and the end of the line profiles.

Regarding the peaks and the area between them in Figure 8-8 (a), the first peak (at x = 96) from the 2 µm line profile is at 0.0082 nA higher current value than the 5 µm line profile. Also, towards the right side of this peak, the 2 µm data remains at slightly higher current values than the 5 µm data. This agrees with the observation from the images, where the insulator cavity was of higher currents in a smaller step size image. However, in the images the latter setting seemed to deliver less resolved MNEE, while from the line profile comparison current values differ by only approximately 1%, which is well within an experimental error. This is reassuring that the two data sets are of a similar quality and spatial resolution.

An overall overlap between the two V line profiles in Figure 8-8 (b) is more effective than in H line profiles. The final part of the line profile (green box), presenting the bottom part of the image, and the area around the peaks overlap to a great extent, reinforcing observation from all images discussed so far that V line profiles are significantly less affected by convection effects. It is expected to see little differences between these two line profiles at different scanning speeds.

The most noticeable differences are within the purple box, emphasizing that tip conditioning takes place during the initial (H) scans. This is not a convection effect and it is important to be aware of when designing the experiment and choosing how much unimportant surface

surrounding the area of interest (e.g. electrode) should be imaged, so that the artefacts would not affect important data. In both 2 µm and 5 µm V line profiles in Figure 8-8 (b), such tip conditioning does not affect the electrode area, hence efficient overlap between the two line profiles is in all but this area.

A minor difference between the two line profiles in Figure 8-8 (b) is present over an insulator area in the middle of the MNEE. This area is represented as a short flat line in the 2 µm line profile, which is different from a rounder profile in the 5 µm line profile. This suggests either better resolved insulator area or some artefacts related to the tip-conditioning when using a smaller step size. The first explanation is most likely not applicable, since it was observed from both images and H line profiles that the 2 µm step size setting did not deliver higher resolution of this insulator area. A difference like this is also not likely to be related to time-dependent tip currents because these should appear as gradual changes in current rather than highly localised abrupt changes like this. Therefore, tip-conditioning is present, which is also noticeable from the beginning profile of the line profile (purple box), since data points are somewhat disturbed and in a zig-zag alignment. While 5 µm line profile contains more convection effects, the 2 µm line profile experiences more of tip-conditioning effects.

8.5.3 Quantitative middle line profile analysis: Gaussian versus Bessel function fitting

V middle line profiles in Figure 8-8 (b) are less affected by convection effects and are used for a full quantitative line profile analysis. Since little significant difference was observed between 2 and 5 µm step size data, only 2 µm fitting graphs are shown in Figure 8-9. For a better data comparison, however, the fitting values for both data sets are tabulated in Table 8-4. Data fitting was performed using a Gaussian dual-peak and a modified Bessel function.

In Figure 8-9 (a), after an adjustment to the data points around the peak area (Section 7.2.1) in 2 µm line profile was completed, it became apparent that the difference between adjusted and not-adjusted data points is more significant than in the previous examples in Chapter 7. Several data points were deleted from both sides to allow for a better transition between the two types of data, but the line profile is still not particularly smooth, resulting in the line profile looking like it was constructed from two different-width peaks at the top and bottom of the graph. Either good fitting at the actual peak area or after the break between adjusted and not-adjusted data points had to be chosen to enable fitting.

The first option was chosen and as seen from Table 8-4, parameters from 2 µm and 5 µm V line profile fitting are different. Peaks from the 2 µm line are significantly narrower and *w* parameter value is 17 µm rather than 27 µm, which was recorded for a 5 µm step size equivalent line profile. These values were expected to be within an experimental error as a result of similar middle line profiles. Such difference reflects that additional data points in 2 µm

line profile had impact on data adjustment effectiveness and hence the fitting, which became significantly poorer. The R^2 value substantially decreased from 0.95 to 0.23, reflecting a poor overlap between the two signals in Figure 8-9 (a). Such difference in Gaussian dual-peak fitting suggests that there is more proportionality between the peak positions, sharpness and width in a 5 µm step line profile than in an equivalent 2 µm line profile. More data points from a 10 µm probe and a 2 µm step size line profile result in the response which does not agree with the diffusion field expansion from two points predicted by a Gaussian multi-peak function.

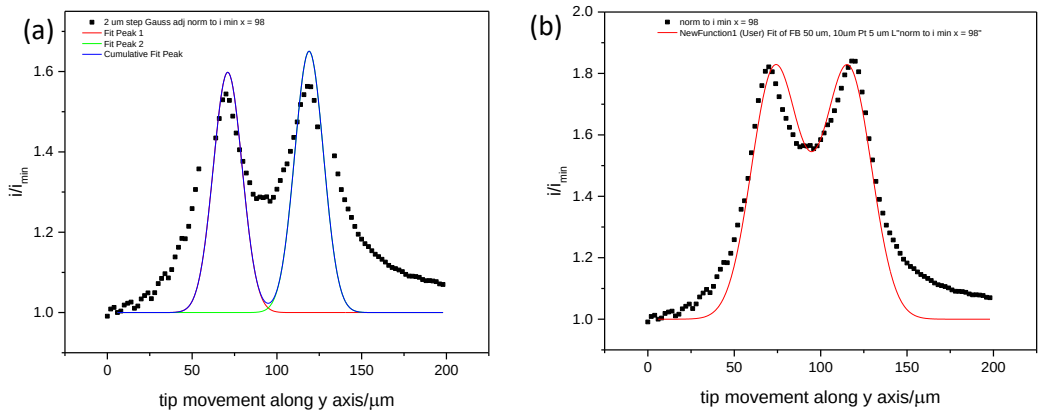

Figure 8-9. (a) Gaussian and (b) a modified Bessel function fitting to V middle line profile from disc nanoband edge FB mode image collected at $0.7i_T^{bulk}$ using a 2 µm step size. In (a), data points from the line profile around the peak area were adjusted to account for the diffusion contribution from the band (Section 7.2.1).

If data in Chapter 7 from Gaussian and Bessel fittings to 100 µm MNEE line profiles were comparable, fitting to 50 µm MNEE line profiles showed significant differences. The hemispherical diffusion field contribution from the rest of the band to the middle line profiles of a disc electrode gets more complicated and a simple data adjustment using subtraction (Section 7.2.1) is no longer effective. Data could be adjusted to a greater extent but instead a simple and effective modified Bessel function is used to quantitatively analyse such line profiles. Such fitting requires minimum manual data adjustment and results in an effective fitting for both 100 µm and 50 µm electrode diameter data, as discussed below.

Fitting using a modified Bessel function results in an effective overlap between the experimental and modelled responses, as shown in Figure 8-9 (b). Area around the peaks shows a good agreement between the two profiles, while the sides are not perfectly fitting, as observed and explained in Section 8.4. Despite this, relatively high R^2 values of 0.91 and 0.96 were achieved for V line profiles from 2 µm and 5 µm step size data, respectively, as presented in Table 8-4, indicating an effective fitting for both data sets. The values of w are 12.74 and 12.57 for 2 and 5 µm line profiles, respectively, showing difference within the experimental error, as expected, and unlike in the Gaussian fitting. This is the final comparison between the

two fitting functions, confidently suggesting that a modified Bessel function should be used for fitting any line profiles from a disc electrode SECM image. Such approach removes the need to manually adjust data points, which is not only time consuming, but also may result in disturbed line profile and higher fitting errors, as observed in Figure 8-9 (a).

Function	*Gaussian*					*Modified*	*Bessel*
Step size	2 µm		5 µm			2 µm	5 µm
	Peak 1	Peak 2	Peak 1	Peak 2			
A	12.74 ± 1.19	*13.86 ± 1.23*	*69*	*117*	*A*	*4.85*	4.30 ± 0.29
*w**	*17*	*17*	*27*	*27*	*W*	12.74 ± 0.097	12.57 ± 0.33
xc	*71*	*119*	18.48 ± 0.70	19.26 ± 0.70	y_c	94.74 ± 0.50	92.85 ± 0.58
Reduced Chi-Sqr	0.0213		0.00175		*Reduced Chi-Sqr*	0.00695	0.00281
R^2	0.228		0.949		R^2	0.912	0.960
y_0	*1*	*1*	*1*	*1*			

Table 8-4. Gaussian and modified Bessel function fitting to $0.7i_T^{bulk}$ FB mode V middle line profile from 50 µm MNEE. Data was collected with a 10 µm Pt probe together with a 2 µm or a 5 µm step size.

8.6 CONCLUSIONS

Substrate and imaging step size effects on image spatial resolution and amount of imaging artefacts were evaluated, using SECM images of a 50 µm diameter MNEE collected in FB and SG-TC modes. When using the same imaging settings as in Chapter 6, the effect of a smaller substrate was evaluated and revealed several identical trends as observed for a larger MNEE: an increase in image spatial resolution with decreasing tip working distance in both modes, higher substrate-features resolution in FB mode and more prominent convection effects to FB mode images. However, smaller substrate was not as well spatially resolved at the laregst *d*, as hemispherical diffusion field overlap from the sides of the band has expanded to a significant extent, resulting in a micro electrode-like image and middle line profiles. A smaller, tip working distance was introduced, allowing to collect another high-resolution image in both modes for an equivalent quantitative analysis to Chapter 7.

Since H middle line profiles were more affected by convection-related artefacts than V line profiles, only the latter were fitted using a modified Bessel function to show effectiveness of the model. The fitting was, again, successful, resulting in high R^2 (>0.9) values and a gradual increase of a peak width, *w*, with an increasing tip working distance, reflecting expanding hemispherical diffusion field from the substrate electrode in both FB and SG-TC modes. Values of *w* were observed to increase linearly with increasing *d*, just like for the 100 µm MNEE. Such effective fitting reassures that modified Bessel function was a suitable, relatively not

demanding and associated with little errors fitting model for both 100 µm and 50 µm MNEE data. It allows to evaluate the extent imaging artefacts have affected SECM images from the line profile analysis.

Then, SECM images were collected using identical settings except the step size was varied as 2 µm and 5 µm. The former setting allowed to collect more data points resulting in a more complete line profile and less visible pixels in the image. However, the improvement of these were minimal as well as convective effects in the H line profiles were only slightly reduced, and V line profiles from both data sets overlapped to a great extent. A larger step size allows to collect image in a less time-consuming manner, and it was shown that a combination of a 10 µm Pt probe, a 5 µm step size and 60 s quiet time were effective settings to collect good spatial resolution images with a tolerable amount of imaging artefacts. Bessel fitting to data collected with a 2 µm step size was also successful and the resulting values were within experimental error from 5 µm data. A Gaussian multi-peak function was shown not to fit smaller step size line profile, showing that this model is not as effective and falls apart as soon as either a substrate or a step size is decreased (compared to Chapter 7).

8.7 REFERENCES

1. Polcari, D., Dauphin-Ducharme, P. & Mauzeroll, J. Scanning Electrochemical Microscopy: A Comprehensive Review of Experimental Parameters from 1989 to 2015. *Chem. Rev.* **116,** 13234–13278 (2016).

9 SECM IMAGING USING A 1 µM PROBE

9.1 INTRODUCTION

SECM image spatial resolution depends on substrate electrode and probe (tip) size as well as imaging settings, which include increment (step) size and increment time. In the previous chapter, the effect of substrate and imaging step size on image resolution and the occurrence of imaging-related artefacts were shown. In this chapter, data collected on the same 50 µm MNEE but with a smaller, 1 µm diameter rather than 10 µm, Pt probe is presented. Such tip size produced significantly smaller tip working distances than extracted in Section 4.5, as derived by the established *Lefrou et al.*[1] analytical expression.

First, keeping the same step size and time settings the effect of the tip size is probed. Then, step size of 5 µm and 2 µm is varied to evaluate the step size effect on data collected with such smaller probe. Finally, increment time is varied to observe the number and degree of artefacts that result. The established modified Bessel function (Section 7.3) is then used to fit normalized tip currents from the middle line profiles of these images to evaluate if analytically generated signals are proportional to the tip currents when using both 10 µm and 1 µm Pt probes for SECM imaging in FB and SG-TC modes. Data from 1 µm probe is compared with data from the 10 µm probe throughout the text.

9.2 EXTRACTION OF TIP WORKING DISTANCES USING AN APPROXIMATE ANALYTICAL EXPRESSION

PACs measure tip working distance, d, as a percentage of the limited current observed in the bulk, i_T^{bulk}. Since the latter is different for 1 µm and 10 µm diameter probes (Equation (2.24)), d values expressed in µm are also different. The *Lefrou*[1] analysis was shown to be suitable for determining the position of the 10 µm Pt probe with R_g = 10 (Section 4.5), thus it was also used for the 1 µm Pt probe with R_g = 15 (Figure 3-10 (d)). A plot of normalized limited current observed in bulk (Equation (4.6)), I, against normalized tip working distance, L, using a = 0.5 µm, was generated, as presented in Figure 9-1. From this, 0.9, 0.8 and 0.7 of I represent L values of 5.13, 3.09 and 2.14, which correspond to the following d values: 2.57, 1.55 and 1.07 µm, in text also referred to as $0.9i_T^{bulk}$, $0.8i_T^{bulk}$, and $0.7i_T^{bulk}$, respectively.

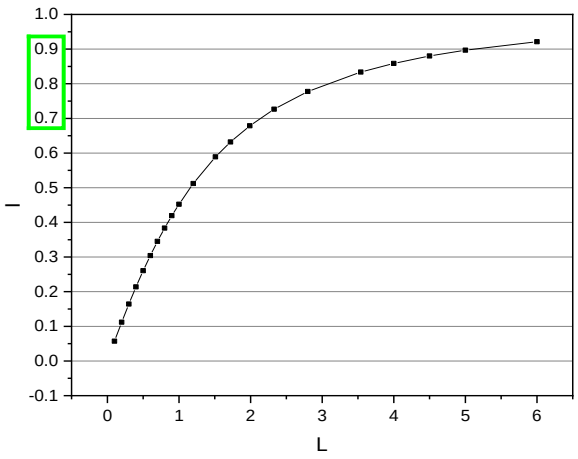

Figure 9-1. A plot of normalized current, I, versus normalized tip working distance, L, allowing to extract L values at 0.9, 0.8 and 0.7 of I, which then can be converted to 2.57, 1.55 and 1.07 µm, using the method as described in Section 4.5.1, a = 0.5 µm and Rg = 15.

9.3 IMAGES COLLECTED WITH A 5 µM STEP SIZE

Figure 9-2 contains SECM images (in FB and SG-TC modes) of the same nanoband edge disc electrode of 50 µm diameter presented in Chapter 8 but collected using a 1 µm rather than a 10 µm Pt probe. The same 5 µm step size was used to evaluate the effect of probe size on image spatial resolution and artefact occurrence. In the previous chapter, the image collected at the $0.9i_T^{bulk}$ (Figure 8-1) suggested strong diffusional overlap from the band sides. Here, a smaller tip, hence a smaller *d*, compensated for the smaller MNEE size, allowing the use of $0.7i_T^{bulk}$ instead of $0.6i_T^{bulk}$ as well as $0.8i_T^{bulk}$ and $0.9i_T^{bulk}$ tip currents to collect a set of three images.

9.3.1 Effect of probe size on image spatial resolution and imaging artefacts

Image spatial resolution in FB and SG-TC modes is evaluated from Figure 9-2. In FB mode (left side), at all *d* values, a narrow, high current band with a clear insulator area is resolved. Likewise, the smallest tip working distance of 1.07 µm generated an extremely well resolved image in SG-TC mode in Figure 9-2 (b). Unlike in the previous chapters, a clear distinction between insulator within and outside the band ring is present also at greater *d.* This clearly shows increased image spatial resolution due to this smaller tip compared to the data of both 100 and 50 µm MNEE images collected with the 10 µm tip. At such short distances of up to 2 µm, the diffusion fields emerging from the sides of the electrode separated by 50 µm have not apparently overlapped in FB, nor SG-TC mode.

Nanoband features in the image spatial resolution are dependent on *d*, just like in the other chapters. With increasing tip working distance, the hemispherical diffusion field naturally expands and the overlap from the sides of the band slowly increases. This results in the

expected decrease in a spatial resolution. Nevertheless, at least to some extent distinguishable insulator area within the band is preserved at all *d* and in all images, except for the SG-TC mode image at 2.57 µm ($0.9i_T^{bulk}$) in Figure 9-2 (f). Here, the diffusion field effects dominate the image. In SG-TC mode, consistent with Chapters 6 and 8, the band is less resolved and despite the smaller tip, there is still significant diffusional overlap from the sides of the circular band, resulting in less resolved insulator area within the cavity. All SG-TC mode images are, again, of lower resolution compared to FB mode.

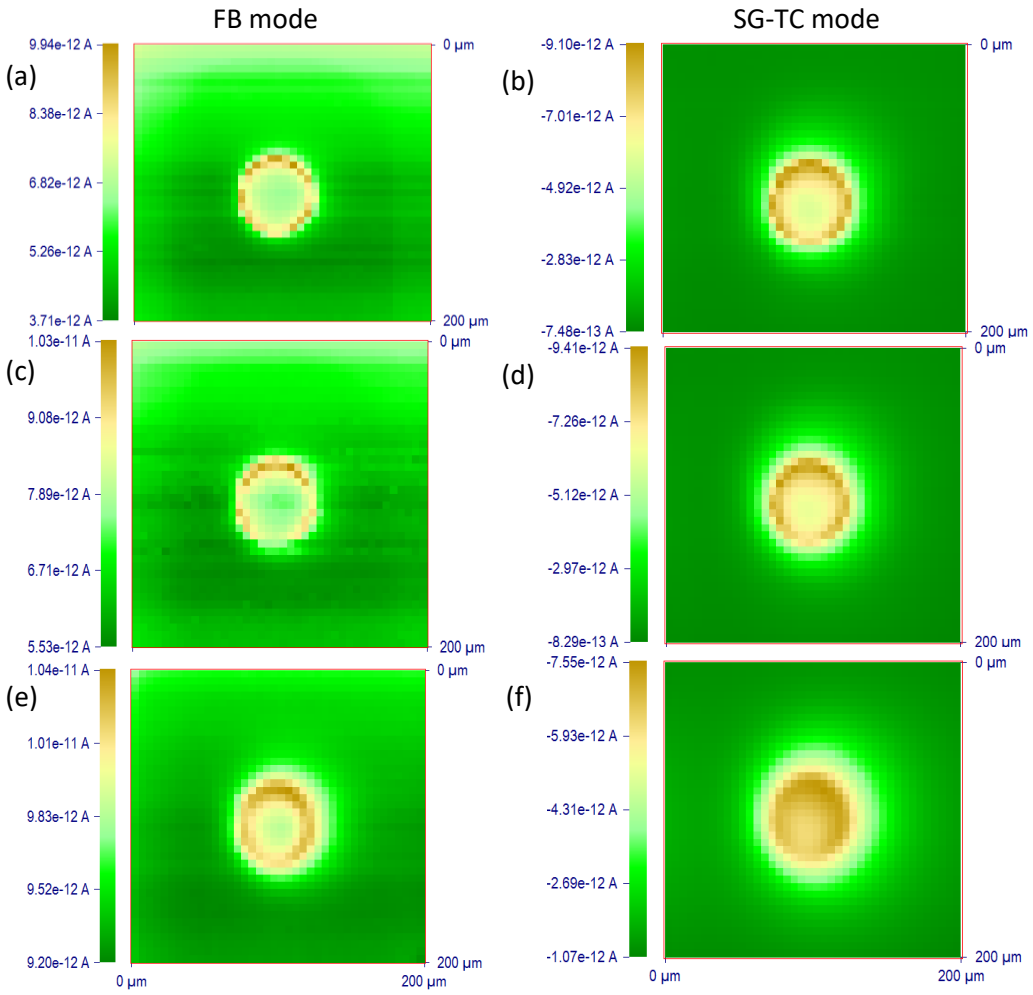

Figure 9-2. 200×200 µm SECM FB (LHS) and SG-TC (RHS) images of an MNEE (r = 25 µm), collected with a 1 µm Pt probe and a 5 µm step size setting at tip working distances of (a-b) $0.7i_T^{bulk}$, (c-d) $0.8i_T^{bulk}$ and (e-f) $0.9i_T^{bulk}$.

As reported in Chapters 6 and 8 regarding the qualitative image analysis collected with a 10 µm Pt probe, FB mode, again, not only delivers higher resolution images, but it is also observed to be more sensitive to tilting, convection and time-dependent tip current artefacts. It was also expected that data collected with the smaller tip would be more susceptible to these artefacts due to the probe being closer to the surface. From the first look in Figure 9-2, the

insulator area is indeed significantly more disturbed in FB modes images on the left, while SG-TC mode images on the right contain relatively uniform current across the surface. FB images are not only more pixelated but also more sensitive to any noise or stepper motor functioning related effects. These show up as disturbed pixels, mostly appearing in $0.7i_T^{bulk}$ and $0.8i_T^{bulk}$ images in Figure 9-2 (a, c), when the tip was very close to the substrate surface. Data collected with a larger probe was less susceptible to such effects. It is possible that the cause of these qualitative observations is due to the probe physically contacting either the surface itself or a dust particle and dragging it along. At this scale everything is more sensitive to imperfections than with the 10 µm probe.

FB mode also presents an artefact at the top part of the image, the most clearly recorded in Figure 9-2 (a).The tip currents here are higher than over the rest of the insulator area, and they decrease with increasing tip working distance. Notably, in SG-TC mode such behaviour is not observable. The reason for this might be the result of tilting or previously discussed time-dependent tip currents. From such qualitative analysis, it does not seem to affect the electrode area, yet it is present to a significantly greater extent than typical time-dependent tip currents observed in the images collected with the 10 µm probe. This could be related to a larger current density at this smaller tip, meaning that there is more chance of failing or the reason discussed below.

Below these higher currents in Figure 9-2 (a) there is a square of slightly lower currents, starting at approximately 50 µm from the top and ending at approximately 20 µm from the edges. Since the tip currents in this area are lower than over the rest of the insulator region, it suggests that the topography is slightly raised over this square region. In Section 3.2.1, electrode fabrication is described, and a Pt layer of 50 nm height was deposited below the silicon nitride top layer and etched from the underlying insulator area, resulting in a metal square under the top insulator. Therefore, it is possible that an effect of the underlying square of Pt is visible and the top layer is not completely flat. In this case, the height difference is small, hence it is only visible with a 1 µm probe at very close working distances, as it is indeed not/not as visible from any other images in Figure 9-2. Exact tip working distance variation is difficult to determine due to the probe being very sensitive at such small tip working distances, resulting in mostly minor, but still present current variation across the insulator area and this effect to some extent mixing with time-dependent tip currents and possible minor tilting front-to-back of the image. Current difference at this step is 2.6 %. These observations suggest that the substrates used are not perfect in terms of topography; although such effects are insignificant when working with larger, such as 10 µm, probes. This highlights the sensitivity of SECM when using very small probes in FB mode.

Whilst some artefact occurrence appeared to increase as a result of a smaller imaging probe, convection effects became significantly reduced if not removed altogether. In all images in

Figure 9-2, the hemispherical diffusion field is very localized and not, at least visibly, significantly disturbed by the tip's left to right H movement. Previously reported convection artefact appearance on the right side of the electrode at all times and on the left side only at greater tip working distances (as a result of the hemispherical diffusion field increase due to larger *d* and product species disturbance and relocation by the tip) is absent. This is consistent with a higher current density and a lower convection sensitivity of this small tip electrode; in other words, a smaller probe physically disturbs the solution less during movement. Some of the convection artefacts might still be present at images collected at a greater than d = 2.57 µm (the greatest *d* used in this work). Therefore, an accurate evaluation of this is limited by such qualitative, visual analysis. Quantitative middle line profile analysis in the following sections is employed to fully evaluate these observations and assist qualitative analysis in fully understanding the nature of such artefacts found within these SECM images.

9.3.2 Semi-quantitative analysis of imaging artefacts from middle line profiles

In Figure 9-3, H and V middle line profiles from SECM images in Figure 9-2 are compared to evaluate in a greater detail any artefacts observed in the above section. All line profiles are normalized in the same way as in the previous equivalent analysis (e.g. Section 6.3.1). Line profiles from FB mode images are on the left and SG-TC mode line profiles are on the right, arranged in the same way as images in Figure 9-2. From a visual evaluation, it is immediately clear that V middle line profiles are significantly more affected by the imaging artefacts than the H line profiles, which are actually of a better symmetry. This is because time-dependent tip currents affect V scans, whereas convection effects which typically affect H scans are markedly reduced.

In Figure 9-3, currents in V middle line profiles (red circles) from FB mode images are higher on the left than on the right side. The former reflects the top part of the image, which was indeed observed to have higher currents than the rest of the insulator area from the qualitative analysis of the images. However, qualitative analysis was not sufficient to immediately eliminate tilting, which can be further evaluated here. If tilting was the reason for such variation in currents, the first peak should have been of lower currents due to a smaller positive feedback, accompanying smaller negative feedback, hence higher currents over the insulator surface (Section 2.9.2). If that was the case, such behaviour would represent the tip being further away from the surface at the top. However, currents across the line profile do not follow such pattern, suggesting that another imaging artefact is present.

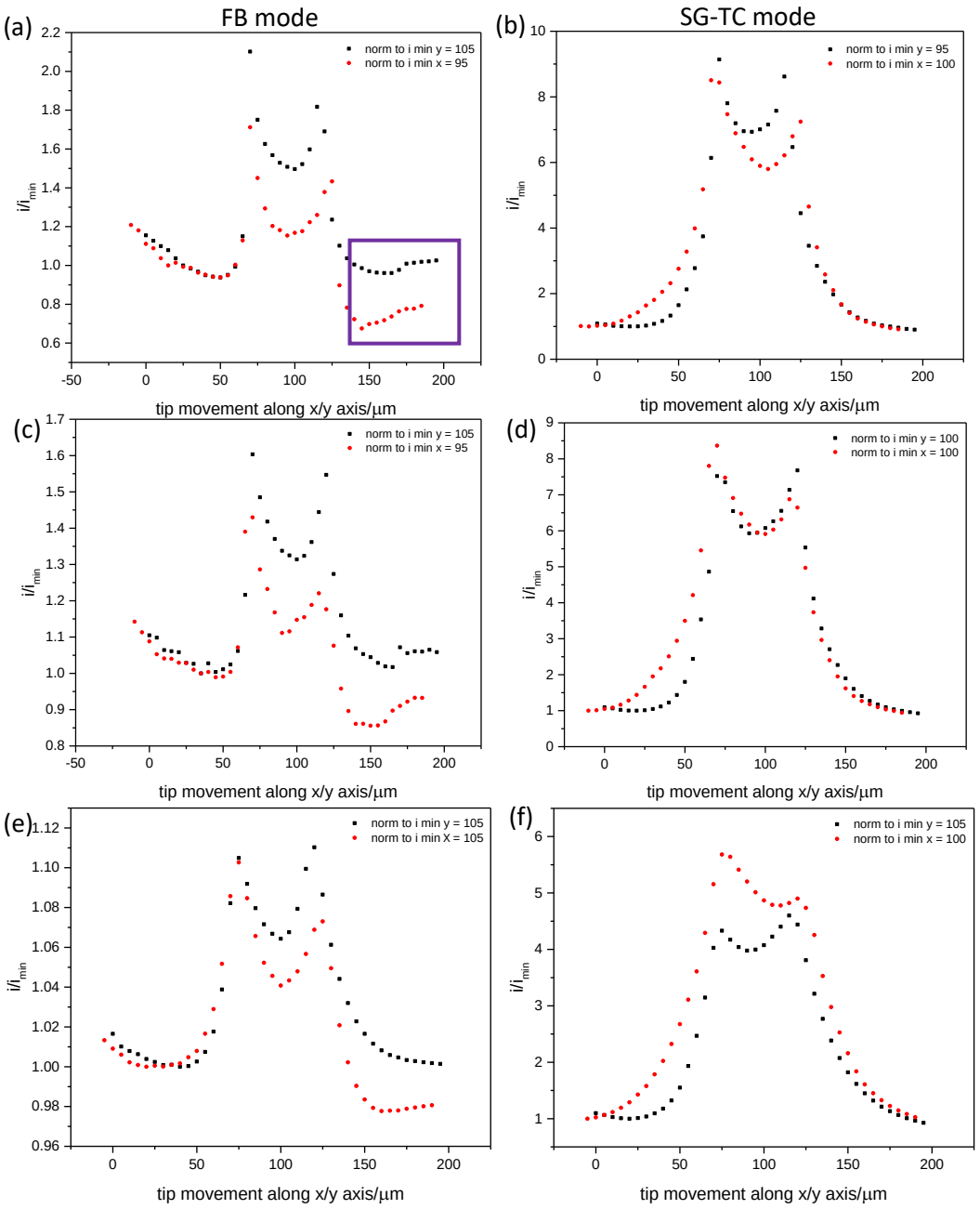

Figure 9-3. Normalized to i_{min} (before an electrode area) tip currents from H (black) and V (red) middle line profiles from FB (left) and SG-TC mode (right) SECM images (Figure 9-2) at increasing tip working distances of (a-b) $0.7i_T^{bulk}$, (c-d) $0.8i_T^{bulk}$ and (e-f) $0.9i_T^{bulk}$. Images were collected using a 1 µm Pt probe and a 5 µm step size.

Since the tip currents at the top part of the image are higher than over the rest of the insulator profile, time-dependent tip currents in combination with visible underlying Pt square seem to explain such current variation. At the very top of the line profile, V line profiles are of higher currents due to such previously observed time-dependent tip currents, but the current drop across the insulator area is more dramatic than seen in other images in this thesis, since the

effect of the raised insulator area (greater negative feedback) is sensed. The end currents from a V line profile are captured within a purple box in Figure 9-2 (a), and the currents start increasing at approximately x = 150 µm. This suggests the edge of such Pt square, hence the topography differences. Such effects are also observed in V FB mode middle line profiles at the other two *d*, but the effects decrease with increasing *d*. H middle line profiles (black squares) in Figure 9-2 also show such step (purple box in (a)), but at $0.9i_T^{bulk}$ the effect is absent, agreeing with earlier observations that FB mode is sensitive to *d* variations

SG-TC mode data in Figure 9-3 do not present these topography differences in the same manner. The middle line profiles are overall more comparable than in FB mode (especially at $0.8i_T^{bulk}$). At all *d,* the H line profiles are significantly more symmetrical than V line profiles, which are wider on the left side in a similar way as it has been observed for the convection effects on the RHS of the H line profile in the previous chapters. Also, the left peak in V line profiles is at higher currents than the right one at all *d*, which also has been associated with the convection effects in the H line profiles. Since these are V profiles, convection was not likely to be present to such a great extent in these high resolution SECM images and their middle line profiles. This is the first time such effect on the left side of the V line profile has been reported in this thesis, and it correlates with the elliptical diffusion field from top to bottom of the image observed in Figure 9-2. Since a significantly smaller, hence more sensitive, imaging probe was used, the sensitivity is expected to be greater not only to imaging settings and artefacts, but also to any technical problems. There were some technical issues during SG-TC mode experimental work regarding fine piezo controller and stepper motor movements, hence these could be the reason for such observations. It is also possible that the substrate band electrode towards the top of the image shows higher electroactivity than at the bottom, due to uneven passivation of the surface. Since SG-TC mode is known to be less sensitive to subtle surface and topography variations that FB mode, topography differences-related details are not observed in images nor middle line profiles in SG-TC mode.

When imaging artefacts were analysed in data collected with a 10 µm Pt probe, convection was more prominent in H line profiles and in FB mode (Section 8.3). In this case, the currents on both sides of the H line profile are much more comparable, suggesting smaller convection effects in data. Despite the above-mentioned other artefacts and substrate imperfections suggesting that data is not perfect (without any artefacts and current variations), it is clear that using a 10 times smaller Pt tip resulted in minimized convection artefacts, meaning that V and H middle line profiles are more similar, hence more symmetrical, especially in SG-TC mode. In Figure 9-3, V line profiles are affected to a greater extent than H, suggesting that H rather than V line profiles are suitable for a full quantitative analysis in Section 9.3.3 unlike in Chapter 8.

9.3.3 Quantitative analysis of imaging artefacts from middle line profiles

9.3.3.1 Experimental details

In this study, V middle line profiles from the images collected using a 1 µm Pt probe and a 5 µm step size contain more imaging artefacts than the H middle line profiles, since convection effects have been shown to be minimized. Middle line profiles in both directions have been used and shown to agree with the analytical expressions in the previous chapters, hence only H line profiles from this set of data are used in the following quantitative analysis. Data fitting is performed using a modified Bessel function (Equation (7.7)) established as an appropriate model for a disc electrode data.

In Figure 9-4, sides of the H middle line profiles in FB mode are more affected than in SG-TC mode. As a result, the fitting boundaries in FB mode are narrower, since the same boundaries for fitting were used as in the previous chapters and only data points ≥1 were fitted. As shown in Chapter 7, this did not have any negative impact on the fitting results, which are overall also successful in this section.

In Figure 9-3, the peaks from FB mode line profile are significantly sharper than in SG-TC mode. This means that either the width or the sharpness of the peaks was fitting to a good extent, but not both, as seen from Figure 9-4. The focus of the fitting was placed on the intensity, *A*, of the left peak.

9.3.3.2 Fitting results

From a glance at Figure 9-4, the overall fitting seems to be in better agreement with SG-TC than FB mode middle line profiles. Regarding the area between the peaks, the fit improves with increasing tip working distance in both modes, but the fitting of SG-TC mode data is more effective at all times. Currents in this central area increase significantly in the modelled line profiles with increasing *d*, resulting in a better overlap with the experimental data, finally reasonably overlapping at $0.9i_T^{bulk}$ in Figure 9-4 (f). Still, this is not as good as in the 10 µm tip data. Overall, the model is clearly starting to break down for such data collected using a 1 µm Pt probe and a 5 µm step size at all but $0.9i_T^{bulk}$ images.

From the FB mode graphs on the left in Figure 9-4, generated line profile (red) is of a flat rather than rounded profile over several areas. First, the left side was mostly excluded from the fitting boundaries but the right side of the analytical line profiles is a sharp corner-like (green box in (a)) rather than rounded, which is a common feature to the rest of the fitting examples, reflecting gradual positive feedback increase, which is apparently not that-well-modelled in this case. Also, at the smallest *d* in Figure 9-4 (a), the middle area between the peaks is of an abrupt nature, suggesting almost zero currents over the middle of this line profile area and hence a forced fitting.

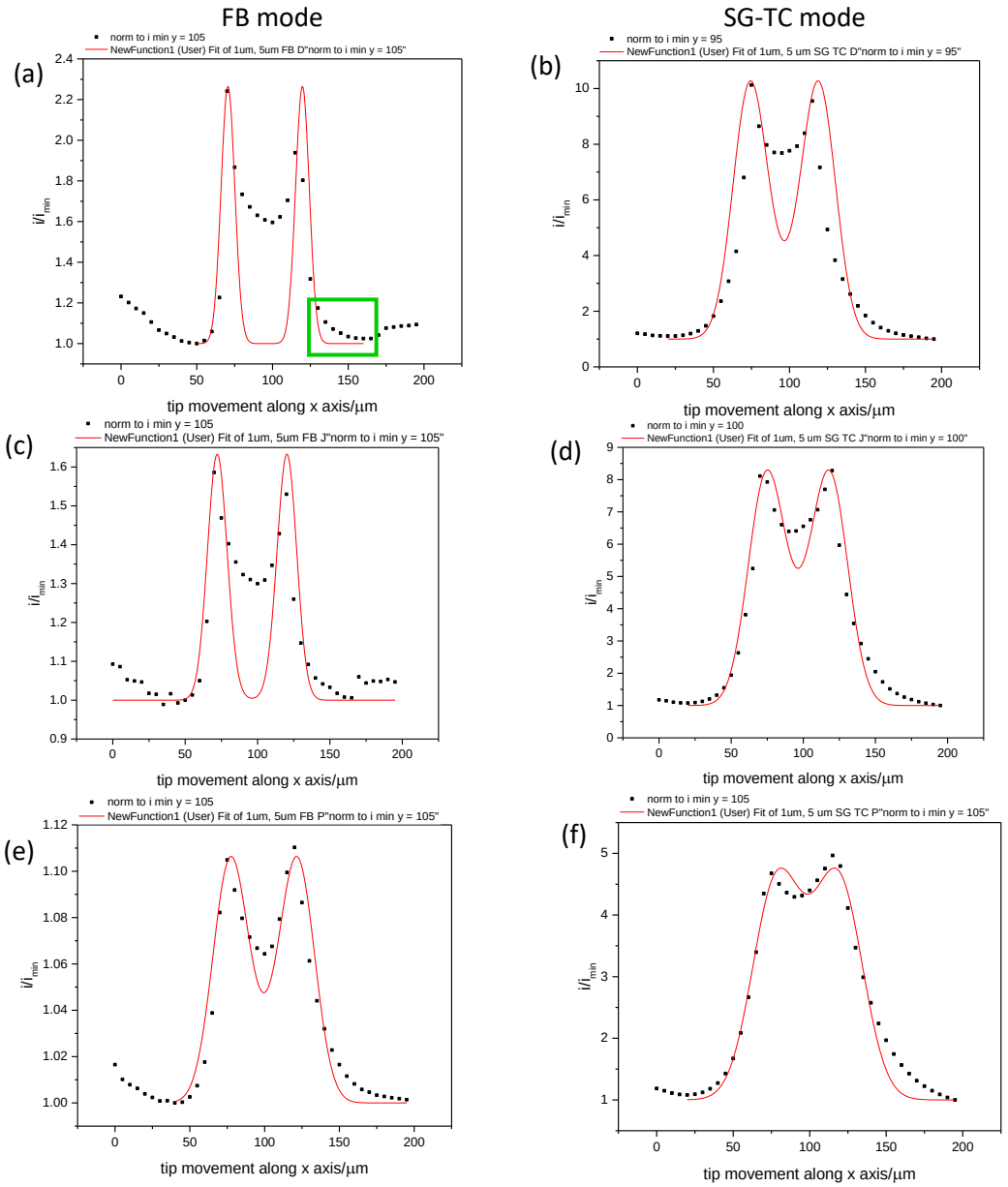

Figure 9-4. H middle line profiles (black squares) from SECM images (Figure 9-2), collected using 1 µm Pt probe and 5 µm step size, at increasing tip working distance of (a-b) $0.7i_T^{bulk}$, (c-d) $0.8i_T^{bulk}$ and (e-f) $0.9i_T^{bulk}$ from top to bottom and fitted using modified Bessel function (red line) in FB mode (left) and SG-TC mode (right). Green box in (a) emphasizes how forced fitting as a result of the breaking model looks like and captures the area where minor convection effects can be found (applicable to the other graphs).

Zero currents in the middle of the two peaks could be observed if the data points were separated by a greater distance, so that the hemispherical diffusion from each of the them would not overlap at the insulator area between them. Since this is not the case and more diffusional broadening is observed experimentally than predicted analytically, this is a further evidence that the modified Bessel function is struggling to fit 1 µm Pt tip FB mode data at as small as 1.07 µm tip working distances. This small probe must perturb the concentration profiles to such an extent that the experimental middle line profiles do not agree well with the

analytically generated signal, which is unlike when using larger *d* (as a result of a larger probe) in the previous chapters.

Regarding the sides of the line profiles, the left side in both modes and at all *d* values is fitting to a better extent than the right side. The latter is broader and hence the sides of the line profiles are not completely symmetrical, suggesting that very small amount of convection artefacts is still present. A green box in Figure 9-4 (a) captures the area where the greatest difference between the two lines is observed. This difference decreases in FB mode and is always small as well as fairly constant in SG-TC mode with an increasing tip working distance. The values are indeed minimal, being <1% in all six graphs. From the qualitative image and semi-quantitative middle line profile analysis it was implied that there are no convection effects. Only by comparing experimental and analytically derived responses can this artefact be revealed and to be present only to a small extent and mostly in FB mode on the RHS of the line profiles.

In Figure 9-4 (f), the peaks at $0.9i_T^{bulk}$ SG-TC middle line profile are slightly distorted resulting in a questionable fitting over this area. Due to a possible minor convection artefact, the right peak is elongated, affecting the visual evaluation of an overlap between experimental and modelled data. The middle of the peaks value, y_c, does not seem to be necessarily precisely identified by the model, and it was considered whether to manually set this value. However, it was decided to be consistent in the fitting approach and to use automatically generated by the expression values in all fittings, including this one.

9.3.3.3 Evaluation of fitting parameters

Fitting parameters are summarized in Table 9-1. In both modes, *A* value decreases with increasing *d,* reflecting increasing *w*, which represents wider peaks. Values of *A* vary between 18-0.57 and 51-14 for FB and SG-TC modes, respectively, and values of *w* in both modes are steadily increasing from 4.49 to 11.27 in FB mode and from 10.83 to 14.84 in SG-TC mode. The latter trend has been observed in all the previous data fitting in this thesis and confirms that the peaks become wider with increasing *d*, as a result of the expanding hemispherical diffusion field. Values of y_c are the same within a minor and reasonable experimental error, suggesting that automatic middle point between the peaks selection was effective in all cases, including above discussed $0.9i_T^{bulk}$ SG-TC mode middle line profile in Figure 9-4 (f). This offers reassurance that automatic modified Bessel function fitting is an efficient method to evaluate these line profiles, even though artefacts have an impact on the line profile visualisation, and it could appear that manual adjustment is needed.

d	***0.7i_T^{bulk}***	***0.8i_T^{bulk}***	***0.9i_T^{bulk}***
FB			
A	*18*	*6*	*0.57*
w	4.49± 0.44	6.66 ± 0.33	11.28 ± 0.17
yc	95.16 ± 1.10	96.22 ± 0.86	99.48 ± 0.65
Reduced Chi-Sqr	0.15	0.015	1.05E-04
R^2	-0.0232	0.485	0.929
SG-TC			
A	*51*	*35*	*14*
w	10.83 ± 0.31	12.20 ± 0.15	14.84 ± 0.13
yc	96.64 ± 1.12	96.36 ± 0.61	98.72 ± 0.58
Reduced Chi-Sqr	2.61	0.36	0.053
R^2	0.735	0.950	0.976

Table 9-1. Results from modified Bessel function fitting to H middle line profiles (Figure 9-4) from FB and SG-TC mode SECM images (Figure 9-2).

The values of R^2, reflecting the overall fit efficiency, from Table 9-1 are also evaluated. As expected from a visual fitting evaluation from Figure 9-4, SG-TC mode data generates a better fit than FB mode data at all *d* values, resulting in relatively high R^2 values. However, at $0.7i_T^{bulk}$ (equivalent to 1.07 µm) R^2 = 0.74 in SG-TC mode, which represents a good overall fit but is lower than for any other modified Bessel function fitting, including data collected with a 10 µm Pt probe, all of which result in $R^2 \geq 0.91$ at all *d.* In FB mode, the value is even lower, being negative (-0.023) which is the lowest from all fittings in this thesis (including Gaussian fitting). This means that the mode does not follow the trend of the experimental data and fits worse than a horizontal line.[2] Such results can be related to the fact that normalised tip currents in the middle of the MNEE on average are at 1.32 in FB mode and 6.23 in SG-TC mode. This means that there is a stronger correlation between the intensity and the width of the peak in SG-TC than FB mode, which is then also better predicted by the model. The middle area between the peaks does not fit well in $0.7i_T^{bulk}$ FB mode line profile (Section 9.3.3.2), suggesting a forced fit which results in a negative R^2 value.

With increasing *d,* the fit effectiveness increases. It is reflected by both better visual overlap between the two lines in Figure 9-4 and by significantly higher R^2 values. A value of R^2 = 0.49 was recorded for $0.8i_T^{bulk}$ (1.55 µm) middle line profile in FB mode, which shows a great improvement from -0.02, though it still implies the struggle to fit both peak-width and peak-intensity from data collected at such small tip working distance. In SG-TC mode, R^2 = 0.95, showing a greater fit, just like observed when fitting data collected with a 10 µm Pt probe. At $0.9i_T^{bulk}$ (2.57 µm), R^2 = 0.93 for both FB and SG-TC mode line profiles, showing a great improvement in data fitting when tip working distance was increased by 1 µm. Overall, the fitting gets progressively worse as *d* decreases, reflecting that the model is starting to break at approximately 1 µm tip working distances.

It is important to remember that the modified Bessel function in Equation (7.7) predicts concentration profiles, while experimental line profiles present current variation. From a steady state equation (Equation (2.20)), current and concentration are assumed to be proportional,

and this middle-line-profile-fitting approach allows to directly and successfully compare the two. For the 10 µm Pt probe data, such fitting is extremely effective for both 100 and 50 µm MNEEs, resulting in a good signal correlation and high R^2 values. When fitting 1 µm Pt probe data, the predicted concentration profiles are less comparable to the currents at such significantly smaller absolute tip working distances than used before. Instead of 9.2-22.1 µm, the values are 1.07-2.57 µm, so it may not be surprising that the concentration profiles become more perturbed, resulting in a poorer fit. The resolution of the resulting images has increased but the measurement of the concentration map is poorer. As a result of a smaller *d* and a smaller substrate electrode, the diffusion gradient is higher at and between the two electrodes. This minimizes convection but probably perturbs the concentration profiles. The model provides the correct shape, but it is not as good as fitting the 10 µm data in the previous chapter. The predicted concentration (and therefore i_{tip}), is wrong particularly over the bands as a result of the broken down model.

9.4 SECM IMAGES COLLECTED WITH A 2 µM STEP SIZE

9.4.1 Effect of a step size on image spatial resolution and imaging artefacts

The same 50 µm diameter nanoband edge disc electrode was imaged at three *d* values using a 1 µm Pt probe and a 2 µm, rather than 5 µm, step size to evaluate the step size effect on image spatial resolution and the extent of artefacts present in 1 µm Pt probe data. Increment time was decreased to 0.1 s from 0.2 s, which resulted in the images in Figure 9-5. All images seem to be of extremely high quality, having a clear insulator in the middle of the electrode band, as expected when the imaging speed is decreased as a result of the smaller step size. Resolution is to some extent comparable to 5 µm step size data set since all images contain more resolved MNEE than in 10 µm probe images.

Nevertheless, the 2 µm step size resulted in to some extent increased image spatial resolution and reduced some of the previously observed artefacts in the 5 µm data. First, images in Figure 9-5 are less pixelated that the ones in Figure 9-2 (5 µm step size) and the nanoband disc simply looks of a better quality than when imaged with such a larger step size. H lines are still visible on the insulator surface, especially in FB mode, yet as the result of the decreased imaging speed (from 25 µm s^{-1} to 20 µm s^{-1}, calculated from the ratio of increment step/increment time), they are not disrupting the band profile, unlike in the 5 µm step size images. Second, convection effects in both sets of images are minimized as a result of the reduced probe size. Quantitative analysis of the images is required to evaluate these.

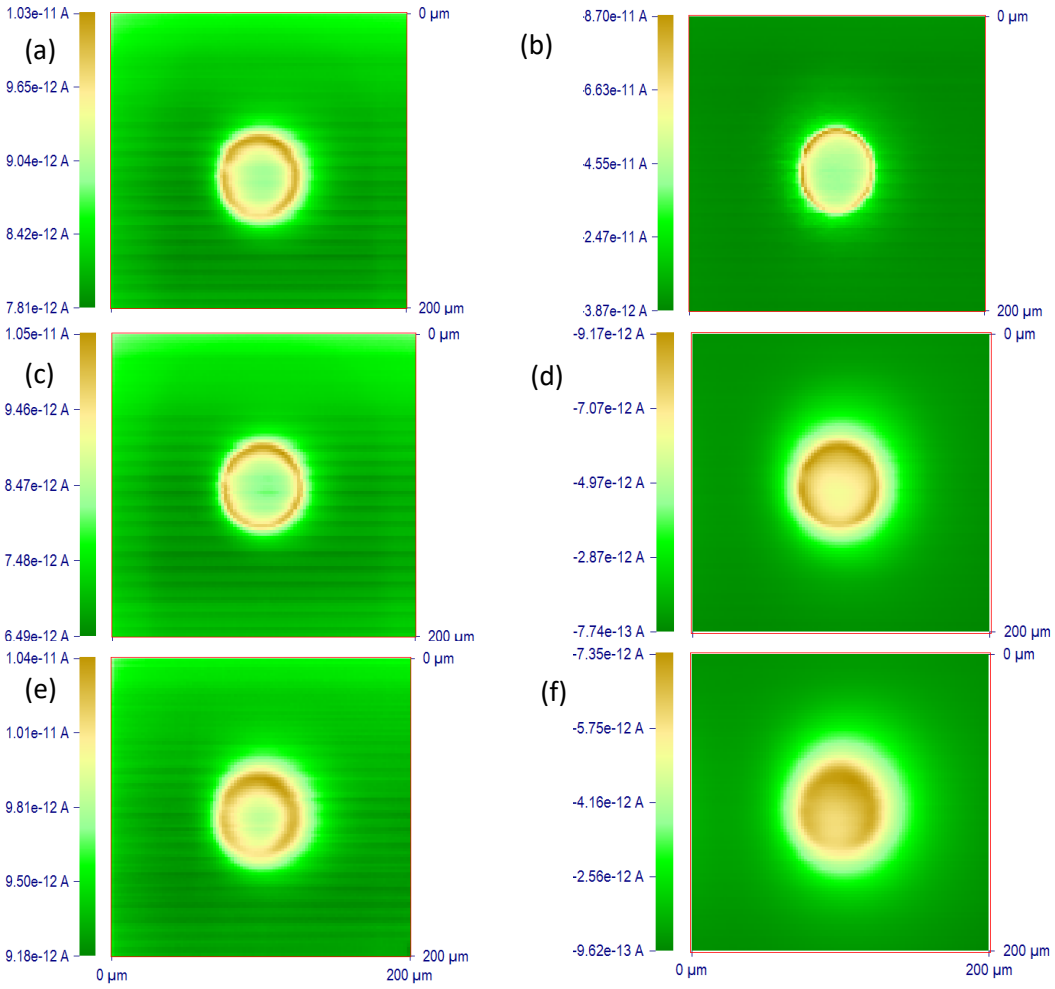

Figure 9-5. 200×200 µm SECM FB (LHS) and SG-TC (RHS) images collected with a 1 µm Pt probe, a 2 µm step size and 0.1 s increment time at increasing from top to bottom tip working distance of (a-b) $0.7i_T^{bulk}$, (c-d) $0.8i_T^{bulk}$ and (e-f) $0.9i_T^{bulk}$.

The diffusion fields broaden with increasing *d*, appearing as circles of slightly higher current (pale green) on the images in Figure 9-5. This is more significant in SG-TC mode, where at $0.9i_T^{bulk}$ the diffusional overlap from the sides of the band has expanded to the extent that the image resembles micro, rather than nanoband electrode. Since the diffusion field naturally expands with distance from the substrate electrode, it is unavoidable no matter which imaging settings are used. In FB mode, $0.9i_T^{bulk}$ image is more affected by such distance effect than the other FB mode images, yet it is still clearly preserving the insulator area in the middle of the nanoband, just like in 5 µm step size data.

It is noteworthy that the $0.7i_T^{bulk}$ SG-TC mode image is of an exceptional quality, which is comparable to the FB mode image. This has not been observed previously in this thesis, and from such qualitative evaluation, it even appears that the image is more resolved than the equivalent FB mode image. Then, $0.7i_T^{bulk}$ and $0.8i_T^{bulk}$ FB mode images are almost identical.

However, 1 µm probe is significantly smaller than previously used 10 µm probe and this means that the approach curves used to set the tip working distances ($0.7i_T^{bulk}$, $0.8i_T^{bulk}$ and $0.9i_T^{bulk}$) are significantly less reliable due to smaller tip currents. Also, the significantly smaller tip working distances, extracted as 1.07-2.57 µm (Section 9.2), are more difficult to accurately control. In case of any solid contaminant particle ("dust") sitting on the surface at the position where the approach curve was recorded, this might compromise the fidelity of the approach curve data. For a 1 µm probe, such particles would only need to be a few hundred nm large to affect the ultimate working distance. It is also possible that at the closest working distance (1.07 µm) the probe could pick up a "dust" particle from the surface, which can seriously affect the magnitude of the measured tip current (also by changing the local effective geometry of the probe apex), as mentioned in Section 9.3.1. There could be other reasons for such rather unexpected variation in resolution, but more imaging experiments are needed to elaborate this.

The raised 'square feature' over the insulator surface surrounding the electrode area briefly discussed in Section 9.3.1 is noticeable when using these imaging settings too. The effect remains subtle but now it is also present in $0.8i_T^{bulk}$ image in Figure 9-5 (b) and suggests that 50 nm height difference around the substrate area is sensed with this 1 µm probe both with 5 µm and 2 µm step size. An off-middle H line profile in Figure 9-6 is a great example of this step effect, captured within a green box. The effect is not significantly different in the two cases and, importantly, it does not affect electrode area; however, it is interesting to observe this, and it reflects that SECM FB mode is significantly more sensitive (and powerful) at such small tip working distances.

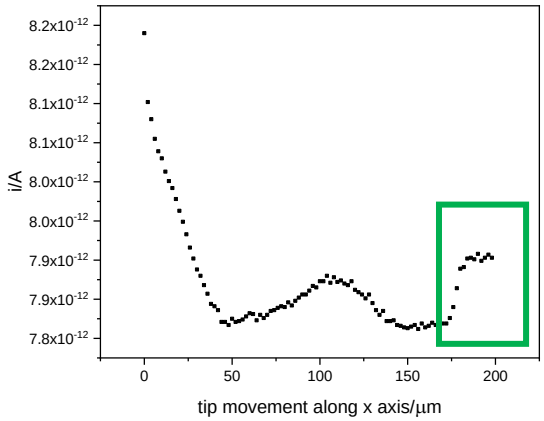

Figure 9-6. An off-centre H line profile from image in Figure 9-5 (a), emphasizing the 'step edge' within the green box.

These observations suggest that differences in data collected with a 1 Pt probe together with a 2 µm and a 5 µm imaging steps reveal more differences than in Chapter 8, when a 10 µm Pt probe data was used for a similar comparison. In Chapter 8, smaller step size simply resulted in more data points, allowing to have a more complete line profile, and in slightly

reduced convection effects as a result of imaging time variation from 320 s to 2000 s. In this case, both observations are still valid, but also the spatial resolution of disc nanoband images in Figure 9-5 has significantly increased, though the imaging time has been changed from 320 to 1000 s. Since data, again, contains little artefacts, it is reassuring that SECM is a strong imaging tool able to capture hemispherical diffusion field evolving from a 50 nm height band. This also highlights the fact that step and probe sizes should be considered together when choosing optimised settings for the imaging. The 10 µm Pt probe delivered better results with a 5 µm rather than a 2 µm step size, since the resolution was not significantly improved but it took a significantly longer time to complete one image. And the 1 µm Pt probe from a visual evaluation is more efficient with a 2 µm step size, as the images are significantly less pixelated and more clearly depicting the MNEE, suggesting that this additional time per image is more beneficial in this case.

9.4.2 Semi-quantitative analysis of middle line profiles

H and V middle line profiles from images in Figure 9-5 are compared in Figure 9-7. From the images, currents are higher at the top than over the rest of the insulator area due to time-dependent tip currents and underlying Pt square, just like in Section 9.3. Then, convection artefacts have been shown to be significantly reduced when using 1 µm Pt probe, resulting in V line profiles being less symmetrical than H line profiles in Figure 9-7. Therefore, the results of the comparison between the line profiles are expected to be similar as in Section 9.3.2.

In all of the previous semi-quantitative analysis, the minimum current value before the electrode area in H line profile was used to emphasize any convection effects on the right side of the line profile when comparing H and V middle line profiles. Since V line profiles in this section are, again, expected to be more affected than H ones due to even more reduced convection, it was instead decided to emphasize the time-dependent tip current effects on the left side of the V line profile. This was done by normalizing middle line profiles to an overall the smallest current value, i_{min}, which was found to be after the electrode area. The shape of the line profiles does not change with such slightly different normalization process, and as a result, in Figure 9-7, the line profiles contain the same within experimental error currents on the right side of the graphs and different currents due to time-dependent tip currents in the early V lines (and underlying Pt square) on the left side of the graphs.

Observations from the qualitative image analysis in the above section are further confirmed using Figure 9-7. First, FB mode middle line profiles have characteristic sharp peaks, reflecting excellent resolution of the band features at all *d*. When evaluating currents over the peaks and between them, they decrease with decreasing tip working distance as usual. When comparing the graphs visually without looking at the current values, they all seem to be similar, reassuring high resolution of all FB mode images.

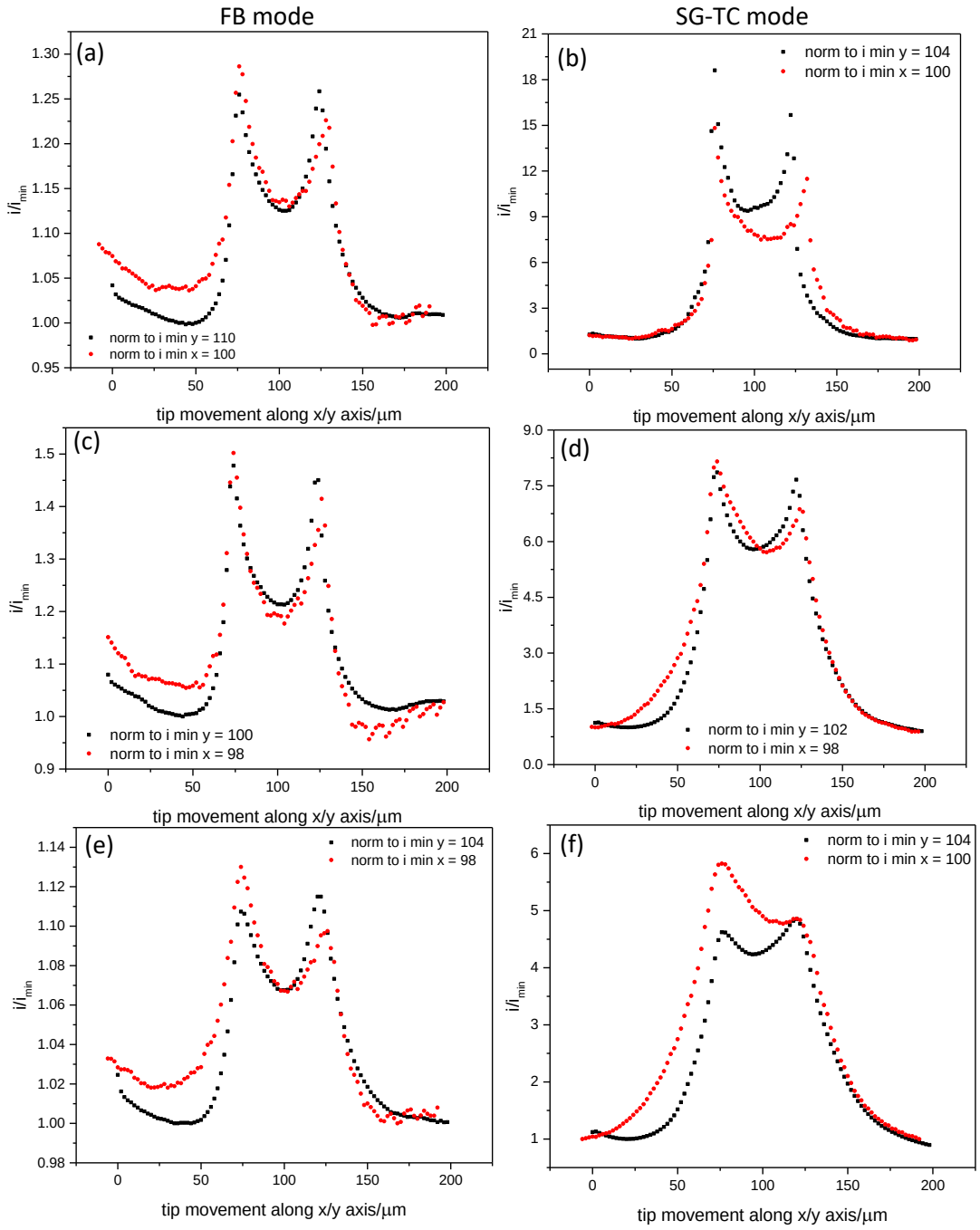

Figure 9-7. H (black squares) and V (red circles) middle line profile comparison from SECM images (Figure 9-5) collected with 1µm Pt probe and 2 µm step size at (a-b) $0.7i_T^{bulk}$, (c-d) $0.8i_T^{bulk}$ and (e-f) $0.9i_T^{bulk}$ tip working distances in FB (left) and SG-TC (right) modes.

Then, SG-TC mode middle line profiles in Figure 9-7 reflect increasing hemispherical diffusion overlap over the middle of the electrode from the sides of the band to a greater extent than in FB mode. The peaks become significantly less sharp with increasing *d*, consistent with the images in Figure 9-5. However, from the image in Figure 9-5 (f), although the nanoband image resembles a micro electrode, the middle line profiles in Figure 9-7 (f) contain two peaks rather than one, confirming that nanoband features are still preserved.

Imaging artefacts are also further evaluated by contrasting FB mode H (black) and V (red) middle line profiles in Figure 9-7. The latter are more affected than the H line profiles, as the beginning of the line profile (the top part of the image) is at higher currents than in the equivalent H line profile. This reflects time-dependent tip currents also seen at 5 µm step size images in this chapter and in data collected with the 10 µm Pt probe, where these were observed to settle until the electrode area. This together with some effect of the underlying metal square, result in the left peak being of higher currents than the right peak. FB mode V line profiles are also rather disturbed on the right side and over the dip between the peaks, which is not visible from the corresponding images in Figure 9-5. This shows that FB mode is clearly more sensitive to any noise, topography variation and time-dependent tip currents, which affect all insulator areas in the images.

Regarding SG-TC mode graphs on the right side in Figure 9-7, differences between H and V line profiles at $0.8i_T^{bulk}$ and $0.9i_T^{bulk}$ show that not only in FB, but also in SG-TC mode some of the artefacts are present. H and V middle line profiles overlap on the right side to a greater extent than in FB mode, confirming the latter mode is more susceptible to imaging artefacts (and minor topography differences). With increasing tip working distance, the currents increase on the left side of the V line profiles compared to the right side. The difference between the two line profiles in each graph is, again, smaller than in FB mode, suggesting that SG-TC mode records significantly less amounts of any remaining convection (in H line profiles) and other imaging artefacts. However, such current increase in V line profiles at greater than 1.5 µm tip working distances might not be due to time-dependent tip currents but instead due to the imaging-related issues (stepper motor), resulting in elliptical presentation of the electrode in exactly vertical direction (Section 9.4.1). The effect was the most significant in $0.9i_T^{bulk}$ image, which is reflected in its V middle line profile. As a consequence of this, the recorded currents might not be precise. A combination of a smaller probe and a smaller step size than used in the previous chapters suggests that collected data in both modes is more sensitive to any imaging artefacts and difficulties during the experimental procedure.

The H middle line profiles are relatively artefact-free, as expected, in both modes. In FB mode, the left side contains some current stabilisation artefact, most likely due to a rapid probe's returning from right to left to start imaging a new H line profile, but this does not affect the electrode area. At $0.7i_T^{bulk}$, both peaks are at equivalent currents, at $0.8i_T^{bulk}$ the left peak is of higher currents and at $0.9i_T^{bulk}$ the right peak is at slightly higher currents. However, these differences are minor, being in sub-pA, confirming that the peaks at all *d* are at equivalent currents within an experimental error, and convection has even less effect on this data than in Section 9.3. In SG-TC mode, the initial currents on the left side of the line profiles are of significantly lower currents than in FB mode, resulting in a relatively flat, artefacts-free sides of the line profiles. In both modes, H line profiles are symmetrical, and from all of the

observations in this Section 9.4 it is implied that they are more suitable for quantitative analysis using analytical expression in the following section.

Finally, $0.7i_T^{bulk}$ FB mode H middle line profiles from 5 and 2 µm step size images are directly compared in Figure 9-8. The current amplitude differs, making it more challenging to stack the two line profiles one over another even when normalized. Nevertheless, the latter setting, as in the previous chapter, delivers a greater number of data points, hence a more complete line profile and more clearly recorded peaks. Such comparison also emphasizes that convection is indeed further decreased, since the sides of the line profiles (affected by the convection in the previous examples) are flatter when using a 2 µm setting (and slower imaging speed).

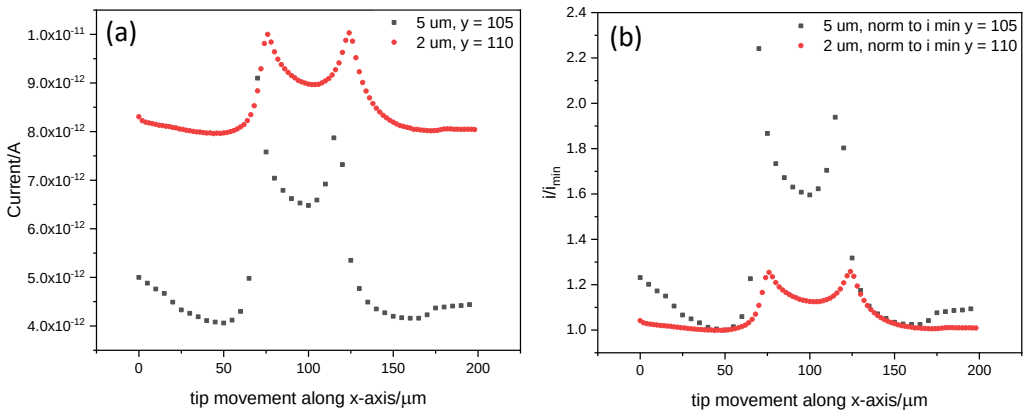

Figure 9-8. H middle line profiles from SECM FB mode $0.7i_T^{bulk}$ images collected using 1 µm Pt probe and 5 µm (black squares) and 2 µm (red circles) step size. Currents are (a) raw and (b) normalized to i_{min} located before an electrode area in each line profile.

9.4.3 Quantitative middle line profile analysis using a modified Bessel function

The H middle line profiles from 50 µm MNEE images collected with a 1 µm Pt probe and a 2 µm step size are fitted using established modified Bessel function, as in Section 9.3.3. All line profiles were now normalized to the overall smallest current value, which was consistently at the beginning of the line profile in FB mode and at the end of the line profile in SG-TC mode. Experimental data fitting allows to evaluate if modelled concentration profile is proportional to the experimental currents from such sharp resolution images presented as line profiles as well as to effectively quantify imaging artefacts.

The sides of the experimental line profiles in Figure 9-9 are quantitatively evaluated regarding convection effects to confirm if the effects are negligible as appeared in qualitative and semi-quantitative analysis. In both modes, the right side of the line profile, marked with a green arrow in (a), is characteristic of being to some extent off-set from the modified Bessel function response. The points of interest in FB mode are at x = 135; 140; 155 and in SG-TC mode at x = 150; 155; 166 for $0.7i_T^{bulk}$, $0.8i_T^{bulk}$, $0.9i_T^{bulk}$, respectively. The greatest measured difference

across both modes is below 5 pA, which is very small and suggests that convection effects at all *d* are overall consistent and negligible.

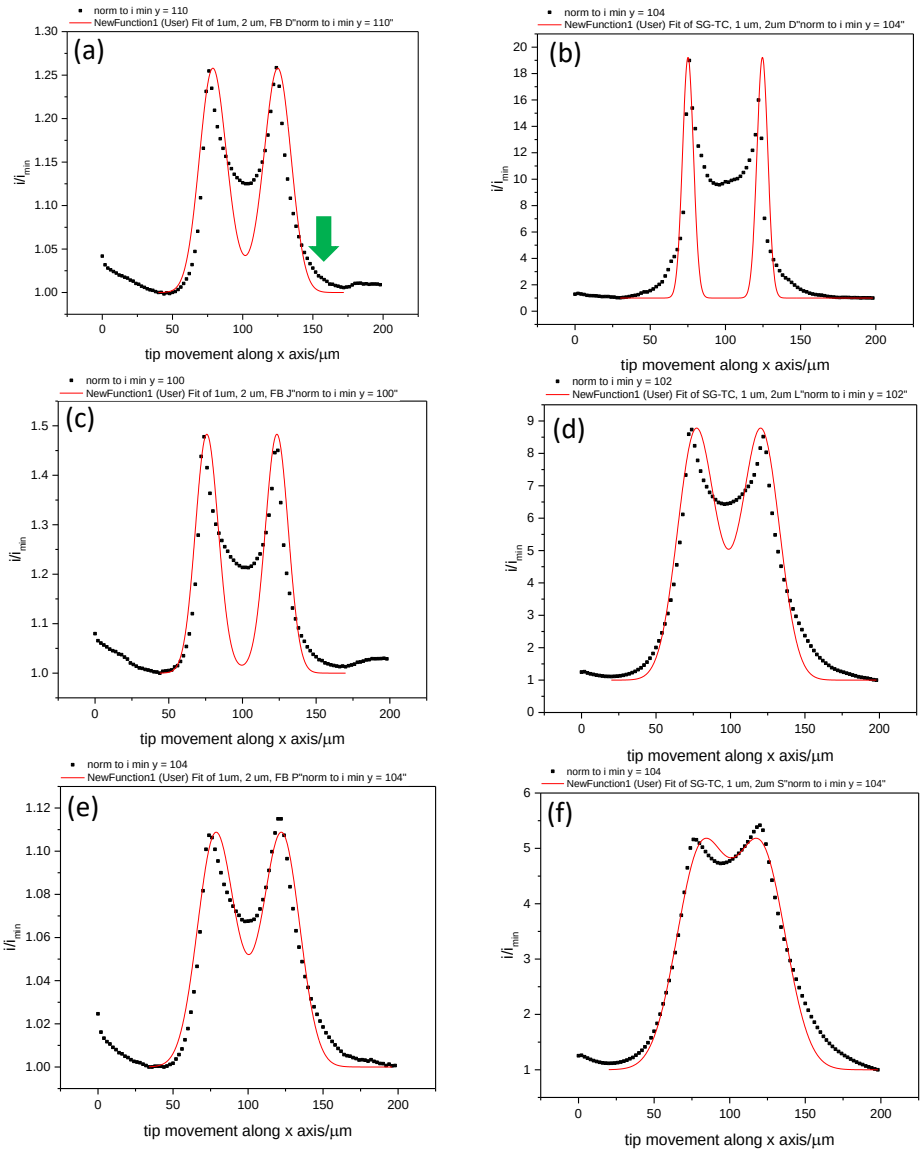

Figure 9-9. Modified Bessel function fitting (red line) to H middle line profiles (black squares) from SECM images (Figure 9-5), collected with a 1 µm Pt probe and a 2 µm step size over 200×200 µm area at (a-b) $0.7i_T^{bulk}$, (c-d) $0.8i_T^{bulk}$ and (e-f) $0.9i_T^{bulk}$ tip working distances in FB (left) and SG-TC (right) modes. Green arrow in (a) marks the area where convection effects are evaluated.

From both Figure 9-9 and Table 9-2, it is again clear that fitting to the data collected using a smaller, 1 µm instead of 10 µm, probe becomes more difficult just like in Section 9.3. Therefore, the peaks in Figure 9-9 graphs are very sharp, and it was a trade-off whether to focus the fit on the peak height or the peak width. It is particularly characteristic in SG-TC mode $0.7i_T^{bulk}$ graph in Figure 9-9 (b), where A = 330, which is a higher value than it has been usually observed in this thesis. Peak intensity and width in 1 µm Pt probe and 2 µm step size data at $0.7i_T^{bulk}$ are not well balanced, suggesting that the concentration profile function was struggling

to fit such sharp peaks. It is clear that the model starts to break at as small as 1-2 µm tip working distances. In FB mode, A = 1.7, which is a rather low value, and at $0.8i_T^{bulk}$, A = 4, which for the first time in this thesis disturbs the trend of a regularly decreasing A with increasing d due to the reasons discussed in the above sections.

d	***0.7i_T^{bulk}***	***0.8i_T^{bulk}***	***0.9i_T^{bulk}***
FB			
A	*1.7*	*4*	*0.57*
w	9.21 ± 0.16	7.54 ± 0.21	11.49 ± 0.088
yc	101.85 ± 0.50	99.59 ± 0.56	100.46 ± 0.35
Reduced Chi-Sqr	0.0014	0.0082	7.50E-05
R^2	0.788	0.592	0.952
SG-TC			
A	*330*	*39*	*15*
w	3.60 ± 0.21	11.76 ± 0.096	15.21 ± 0.079
yc	99.84 ± 0.53	98.76 ± 0.38	101.012 ± 0.34
Reduced Chi-Sqr	22.87	0.44	0.054
R^2	0.0289	0.938	0.980

Table 9-2. Modified Bessel function fitting results to H middle line profiles (Figure 9-8) from SECM images collected with a 1 µm Pt probe and a 2 µm step size.

Another previously observed and, in this case, disturbed trend is a more effective fitting to SG-TC than FB mode data. From Figure 9-9, SG-TC mode $0.7i_T^{bulk}$ graph is characteristic of sharper peaks, informing about more resolved electrode features, than equivalent FB mode graph. Therefore, SG-TC mode middle line profile fitting resulted in a much lower R^2 of 0.029 compared to 0.79 in FB mode, as shown in Table 9-2. With increasing tip working distance, R^2 values increase as usual, suggesting a better overlap between experimental and modelled data.

In SG-TC mode, at $0.8i_T^{bulk}$ the value sharply increases to 0.94 and to 0.98 at $0.9i_T^{bulk}$, because of a more effective overlap between experimental and modelled signals at the area between the peaks in Figure 9-9 (c, e). Such effective fit was typical to the data collected with a larger step size and/or probe. In FB mode, the increase is more gradual, R^2 being 0.59 and 0.95 for the two d, which could be related to the remaining relatively large gap between experimental and modelled data points representing additional diffusion field over the middle of the electrode which was not as effectively modelled as in the other examples.

Comparison of experimental data with the modified Bessel function estimation suggests that 1 µm Pt probe and 2 µm step size settings disturb local concentration profile at both $0.7i_T^{bulk}$ and $0.8i_T^{bulk}$ in FB mode and only at $0.7i_T^{bulk}$ in SG-TC mode. This suggests that smaller probe delivers sharper signal (more characteristic of the MNEE details rather than the hemispherical diffusion field) and the concentration profile gets significantly more perturbed, resulting in not as effective fitting. For comparison, when using a 10 µm probe, the signal was predictable, and it fitted modified Bessel function to a significantly greater extent in all examples. When comparing this 2 µm data with the 5 µm step size data in Section 9.3.3, the results are

equivalent within an experimental error, except at the smallest *d*, when SG-TC mode delivers closely comparable to FB mode signal. Overall, these observations reassure that at smaller than 2 µm *d* the fitting to 1 µm Pt probe data using modified Bessel function becomes less effective than seen in the other chapters of this thesis.

9.5 INCREMENT TIME EFFECT ON SECM IMAGING

Variation of substrate and probe sizes as well as imaging step size effect on imaging spatial resolution and artefacts, such as convection and time-dependent tip currents, have been evaluated in the above sections of this chapter. Since scanning speed (µm s^{-1}) is a step size over an increment time, by varying the former in Section 9.3 and Section 9.4 scanning speed effect evaluation on these SECM images was presented. In this section, scanning speed effect on SECM imaging is evaluated by varying time increment per pixel (increment time). The same 50 µm diameter nanoband disc electrode as in the above sections of this chapter was used for this increment time effect on image spatial resolution and imaging artefacts evaluation in FB and SG-TC modes.

To have some benchmark results before analysing smaller and more sensitive 1 µm probe results, increment time effect on images collected with a larger 10 µm Pt probe is evaluated first. In Figure 9-10, all images were collected at $0.7i_T^{bulk}$ and using time increment of 0.1 s in (a-b) and 0.05 s in (c-d). The electrode area in all examples is presented as a brown colour and the surrounding insulator area as a green colour, as in most of the images shown in this thesis. Since longer time per pixel means slower scanning, it consequently results in higher resolution images. In this case, the speed difference was minimal; therefore, the improvement in resolution is minor when comparing the two sets of images collected at 0.1 s and 0.05 s increment time settings. FB mode images on the left in Figure 9-10 are of relatively higher spatial resolution than images on the right collected in SG-TC mode, as expected and seen throughout this thesis.

Then, convection artefacts increase with decreasing time per pixel also as expected. This is reflected in the hemispherical diffusion field immediately surrounding the electrode area distortion towards the scanning direction (left to right). It is more prominent to the FB mode image collected at 0.05 s in Figure 9-10 (c) than at 0.1 s setting in (a), also being the reason for slightly lower currents at the middle of the electrode in the latter, reflecting slightly better insulator area resolution. This convection effect is also the reason for higher currents on the left side on the electrode surrounding insulator area. The probe is stirring solution to a greater extent than at longer increment time, resulting in higher currents at the beginning of each H line profile and agreeing with the previous analysis (Section 6.3).

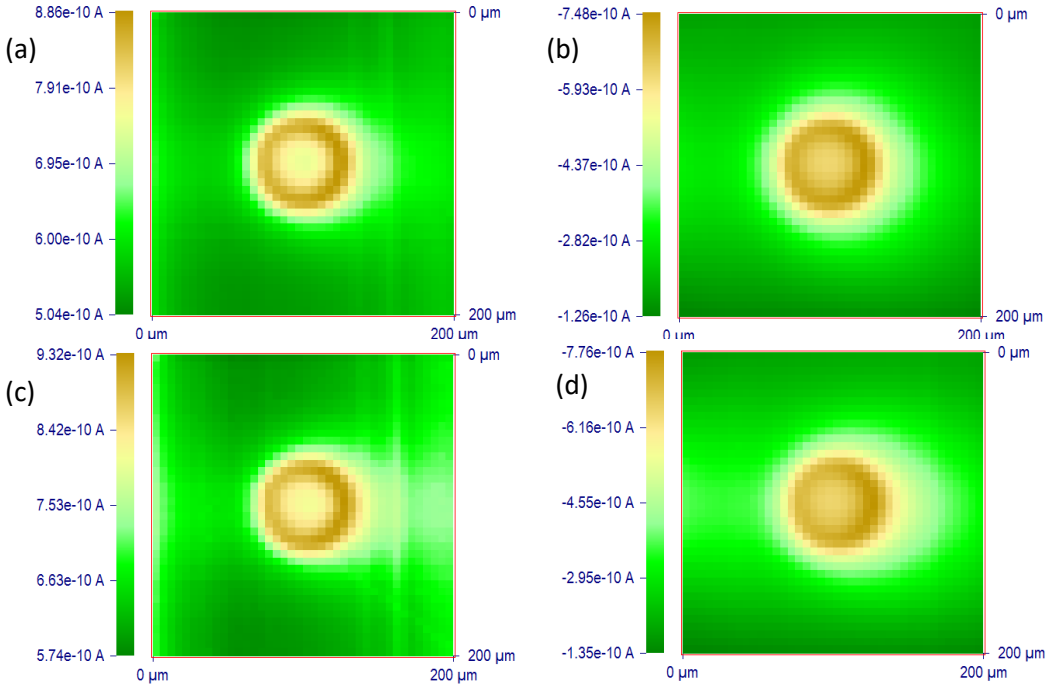

Figure 9-10. Images showing an effect of increment time variation on FB (left) and SG-TC (right) mode images: (a-b) 0.1 s and (c-d) 0.05 s per pixel. Images were collected using a 10 µm Pt probe and a 5 µm step size over 200×200 µm area.

In SG-TC mode, increment time effects on image spatial resolution and imaging artefacts are smaller than in FB mode. Tip currents over an insulator cavity within the electrode are similar at both speeds. The right side of the image in Figure 9-10 (d) shows some signs of greater convection effects (product species being displaced towards the right-side during the scanning process) at 0.05 s than at 0.1 s. Some of the product species are also displaced across the electrode area towards the beginning of the H line profiles upon probe's return to the left side. This results in higher currents on the edge of the insulator area, just like in Section 6.3.4. Overall, convection effects are slightly more prominent in FB (a, c) than SG-TC (b, d) mode, correlating well with the previous observations from the 10 µm Pt probe data.

Different increment time settings were then evaluated in the images collected with a 1 µm Pt probe at $0.8i_T^{bulk}$ in FB mode, as presented in Figure 9-11. Only FB mode was used to avoid repetition and in this chapter it has been shown that smaller probe delivers high resolution images at this tip working distance and this mode is more susceptible to variation of imaging settings. As observed earlier within this chapter, using a smaller (1 µm) probe leads to significantly minimized convection effects and a greater spatial resolution. As a result, both images collected at 0.1 s in (a) and 0.05 s in (b) clearly distinguishes the electrode and insulator areas and there is little difference between the two. Apparently, the difference between images collected at 0.1 and 0.05 s increment time when using a 1 µm probe are less significant than when using a 10 µm Pt probe.

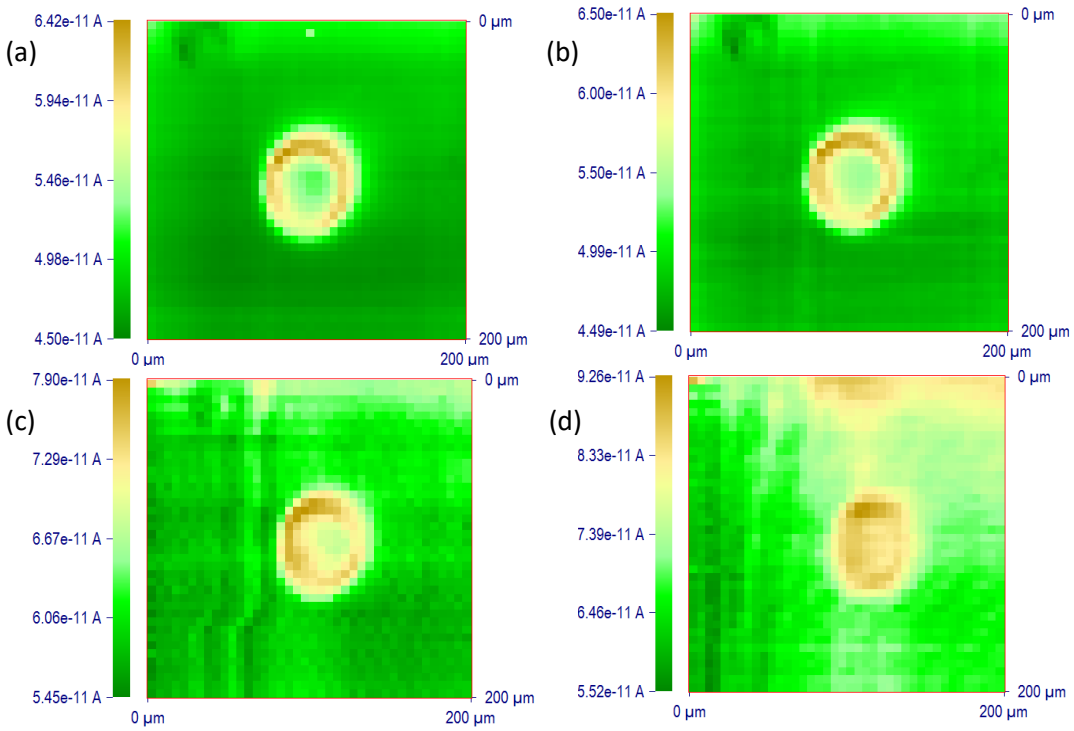

Figure 9-11. SECM images of disc nanoband, r = 25 µm, collected using a 1 µm Pt probe, 5 µm step size and 60 s quiet time over 200×200 µm area at $0.8i_T^{bulk}$ in FB mode and different increment time values of: (a) 0.1 s, (b) 0.05 s, (c) 0.02 s and (d) 0.01 s.

A smaller tip electrode is expected to establish a steady state quicker than a larger electrode, and it was investigated if even faster scanning (smaller increment time) would allow collection of satisfactory resolution images. First, shorter increment times, such as 0.02 and 0.01 s in Figure 9-11 (c-d), again, did not have much impact on the convection effects. The 1 µm probe can be confidently used without the need to worry about this artefact, usually encountered in the images collected with the 10 µm probe. However, the image spatial resolution is affected to a greater extent than observed before. Both images result in distorted disc nanoband electrode image, which is rather elliptical than circular, the insulating region in the centre of the nanoband electrode is less well resolved, and the overall image quality is poorer. It suggests that the rapid probe movement results in the tip electrode not establishing a true steady-state diffusion profile with the substrate electrode, and the fast step motor movement becomes less reliable. There is also an increased amount of pixels that stand out from the image and some patches of higher currents at the top part of the images, suggesting that smaller than 0.05 s increment time results in additional imaging-related artefacts. These were not observed in any of the other images of this electrode presented in this chapter.

Overall, a 5 µm step size and not lower than 0.1 s increment time should be used for imaging substrates such as 50 µm MNEE. Images in this thesis were mostly collected using 0.2 s with 5 µm and 0.1 s with 2 µm settings combination. This results in 25 µm s^{-1} and 20 µm s^{-1} scanning

speed values and suggests that these settings are effective combinations for high resolution images with minimal artefacts, collected within a reasonable amount of time (320 s and 1000 s, respectively). Greater than these scanning speeds increase convection effects (for 10 µm probe) and result in not accurate SECM images of the substrate current map.

9.6 DEPENDENCE OF PEAK WIDTH (*W*) ON TIP WORKING DISTANCE (*D*)

9.6.1 *W* vs *d* graphs from data collected using 1 µm Pt probe

The plots of *w* vs *d* were constructed in Figure 9-12 to evaluate peak width dependency on the tip working distance. In this section, a 1 µm Pt probe and 5 µm and 2 µm step sizes were used for a 50 µm diameter MNEE SECM imaging. The values of *w* together with their associated errors were extracted from modified Bessel function fitting to the H middle line profiles from SECM images collected at *d* = 1.07 µm; 1.55 µm and 2.57 µm and discussed in the above sections of this chapter.

First, results from fitting to FB mode data points collected using a 5 µm step size are shown in Figure 9-12 (a). Values of *w* follow a linear trend, reflected by a high R^2 value of 1 associated with a linear fit, as shown in Table 9-3. The resulting *y*-intercept value is -0.35, and when it was fixed to 1, the fitting remained effective, as R^2 = 0.999. This suggests that a briefly presented assumption (in Section 7.3.4) that the peak width would fall to a specific value (in this case the diameter of the probe) at a close to zero *d* value is possibly valid in FB mode.

Equivalent analysis was performed using *w* values from SG-TC mode data in Figure 9-12 (b). The linear fitting is also effective, resulting in high R^2 value of 0.999, suggesting that the peak width in both modes is linearly related to the tip working distance. The resulting *y*-intercept value is 8.17, and when having it fixed to 0, reflecting Pt height in the nanoband (50 nm), the visual presentation of the generated line is significantly steeper than the one made up from the data points in the graph, even though the resulting R^2 value is still high (0.967) (not shown).

Then, *w* vs *d* plots from the 1 µm Pt probe and 2 µm step size in FB and SG-TC modes are presented in Figure 9-12 (c-d). When comparing data points arrangement, it is immediately noticeable that earlier discussed resolution related observations are reflected in a poorer linear fitting. In FB mode in Figure 9-12 (c), $0.7i_T^{bulk}$ and $0.8i_T^{bulk}$ *w* value arrangement is distorted and not linear. Despite this, the R^2 value is still relatively high, being 0.858. Similar value of R^2 = 0.882 is generated for SG-TC mode fitting, where *w* from $0.7i_T^{bulk}$ middle line profile fitting was unusually low, reflecting exceptional, yet unusual image resolution in this mode. The values of *y*-intercept are different to 5 µm step size values (Table 9-3); however, since the linear relationship between data points is much poorer than in the above discussed data set, it is not surprising. When *y*-intercept values were fixed to 1 and 0 for FB and SG-TC modes,

respectively, high R^2 values of 0.975 and 0.985 were obtained, but, again, these results should be considered carefully.

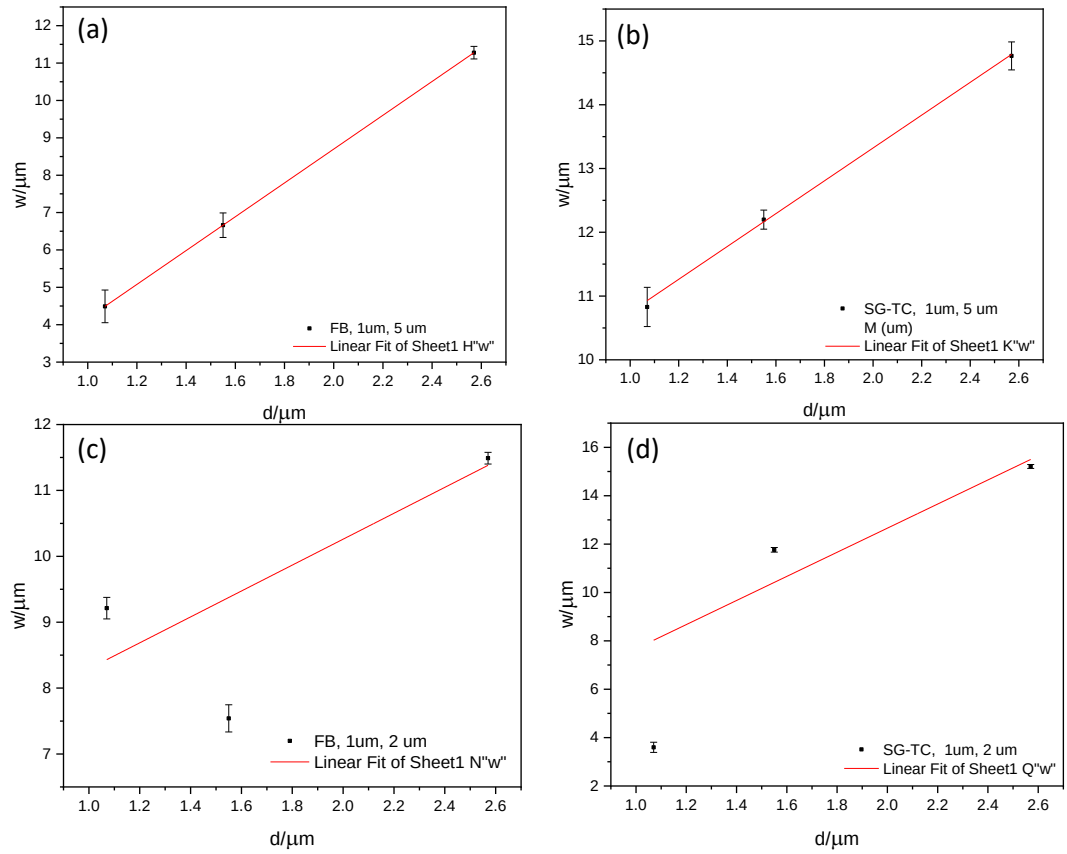

Figure 9-12. Plots of w vs d, including errors (vertical bars) associated with w values (black circles) and linear fitting (red line) to these values. The values of w were obtained from modified Bessel function fitting to H middle line profiles from SECM images of 50 µm MNEE collected using a 1 µm Pt probe and a 5 µm step size in (a) FB and (b) SG-TC mode and using a 1 µm Pt probe and a 2 µm step size in (c) FB and (d) SG-TC mode.

Imaging settings	*5 µm step size*		*2 µm step size*	
Imaging mode	FB	SG-TC	FB	SG-TC
Intercept	-0.35 ± 6.81E-6	8.17 ± 0.17	6.33 ± 2.63	2.69 ± 5.72
Slope	4.52 ± 2.97E-6	2.57 ± 0.091	1.97 ± 1.18	4.98 ± 2.66
R^2	1	0.999	0.858	0.882

Table 9-3. Results from linear fitting of w vs d plots (Figure 9-12).

Further evaluation and more experimental data, including another assessment of SECM images collected using a 1 µm Pt probe and a 2 µm step size, are needed to confidently determine what *y*-intercept value in each mode should be expected. In this data set, the sizes of the two electrodes are very similar (1 and <1 µm), making it less clear if intercept at 1 or 0 should be expected. This means that the intercept value falls to either the tip diameter in both modes or to the electrode diameter, which is different for FB and SG-TC modes, since different electrodes generate $FcMeOH^+$. Since the current is always measured at the tip and its size possibly determines the width of the measured diffusion field in both modes, it could be expected that the former assumption is more probable.

9.6.2 Comparison between peak widths observed when using 1 µm and 10 µm probes

In the previous section, we analysed the relationship between the peak width (spatial resolution) and the tip working distance for a 1 µm probe. In order to assess the effect of probe size on this relationship, in this section we compare this data with peak widths measured using a 10 µm probe presented earlier in this thesis. The plots of *w* vs *d* in Figure 9-13 were composed using the values of *w* from different line profiles fitted using modified Bessel function and discussed throughout this thesis. This includes FB and SG-TC mode data of 100 µm disc nanoband imaged with a 10 µm Pt probe and a 5 µm step size in (a), 50 µm nanoband disc images using a 10 µm Pt probe and a 5 µm step size in (b) and 50 µm nanoband disc images using a 1 µm Pt probe and a 5 µm step size in (c). Data from all three data sets as well as from 1 µm Pt probe and 2 µm step size was separated into FB and SG-TC modes in (d-e), using normalized distance, *L*, for the x-axis, enabling such data comparison.

Peak width values from 100 µm MNEE data in Figure 9-13 (a) are higher in SG-TC than in FB mode. This reflects resolution differences between the modes, emphasizing that FB mode is more detail-specific, hence measured diffusion field is narrower. Overall, an arrangement of data points is resembling two parallel lines, which are linear as presented by high R^2 values (>0.9) in both cases, as shown in Table 9-4. When substrate size is decreased to 50 µm MNEE in Figure 9-13 (b), *w* values from both modes are more similar to each other at each *d* than in (a). Only at the largest *d* there is a relatively significant gap between the two. This suggests little difference between these data sets in (b), and hence similar image spatial resolution in both modes. Smaller linear *w* vs *d* dependency in SG-TC mode than in FB mode is reflected by a lower R^2 value of 0.6 compared to 0.93, respectively.

Data from a smaller 1 µm probe used to image the same 50 µm electrode keeping the same step size in (c) results in, again, close to parallel relationship between the two data sets. This is accompanied by high, almost equal to 1, R^2 values, as presented in the above section. The overall arrangement of data points from FB and SG-TC modes is similar to the arrangement in (a). Both data sets were collected using a 5 µm step size (and the same 0.2 s increment time, hence at the same imaging speed), suggesting that smaller MNEE should be imaged with a smaller probe to generate more effective and not somewhat limited by the probe size

results. As seen from Figure 9-13 (b), 10 µm probe was struggling to reflect FB and SG-TC mode differences, as *w* values are mostly similar at selected *d* values.

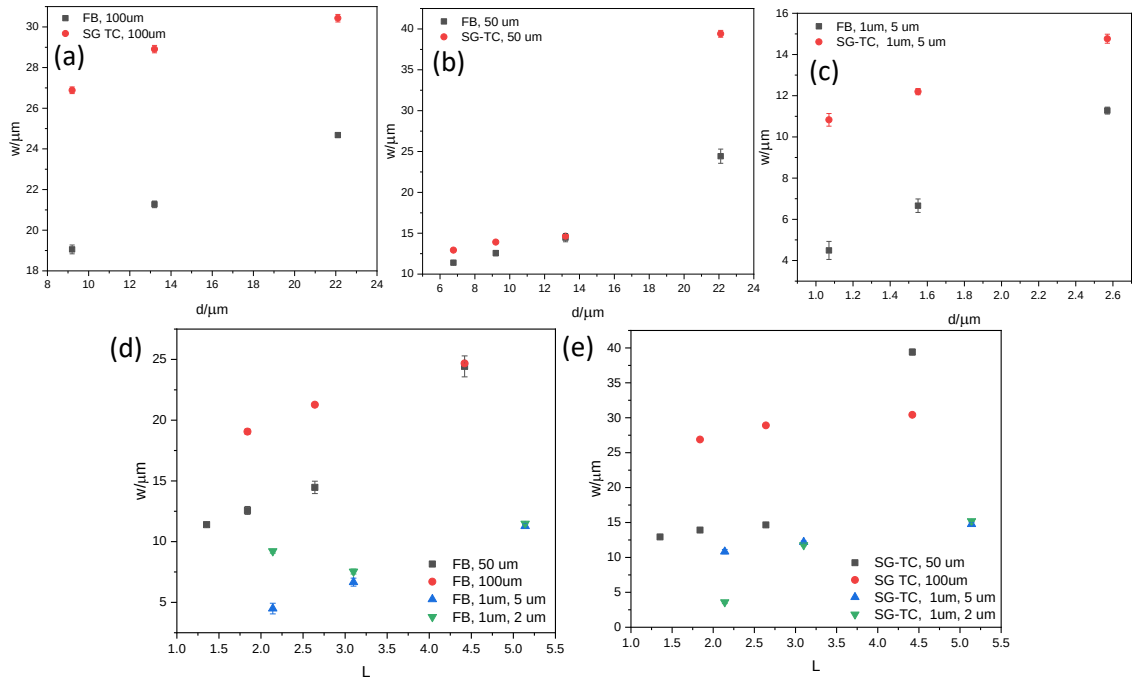

Figure 9-13. Comparison of w vs d graphs containing data from several data sets. The values of w were gathered from middle line profile fitting from the following SECM images: (a) 100 µm and (b) 50 µm disc nanoband imaged with a 10 µm Pt probe and a 5 µm step size in FB and SG-TC modes, (c) 50 µm nanoband disc images using a 1 µm Pt probe and a 5 µm step size in FB and SG-TC modes, (d) FB and (e) SG-TC mode data from (a-c) together with 50 µm nanoband disc images collected using a 1 µm Pt probe and a 2 µm step size, using L for x-axis.

	100 µm, SG TC	*100 µm, FB*	*50 µm, FB*	*50 µm, SG TC*
Intercept	24.80 ± 1.20	15.55 ± 0.62	6.43 ± 1.11	3.76 ± 6.69
Slope	0.27 ± 0.079	0.42 ± 0.033	0.72 ± 0.14	1.10 ± 0.63
Residual Sum of Squares	17.35	4.46	16.67361	1424.77
R^2	0.918	0.994	0.934	0.604

Table 9-4. Linear fitting of w vs d results collected from 100 µm and 50 µm MNEEs data sets in FB and SG-TC modes, using 10 µm Pt probe and 5 µm step size.

Then, *w* values from all three sets of data collected using a 5 µm step size and data points from 1 µm Pt probe and 2 µm step size settings for 50 µm MNEE imaging are plotted on the normalized *d* axis in Figure 9-13 (d-e). Such comparison is interesting since this data fitting was performed separately, one data set at a time and with minimal parameter adjustments. In FB mode in (d), at *d* = 22.1 µm 50 µm (black) and 100 µm (red) MNEE data points from 5 µm step size overlap, reflecting that the same width diffusion field emerging from the band electrode was recorded independent of the different separation between the two bands. There are some differences between *w* values from these data sets at the other *d*, though one would expect the values to be the same or wider from 50 µm MNEE data due to a greater diffusional overlap in the middle of the electrode. Instead, this may suggest that due to more intense convection effects (left to right along x-axis) hemispherical diffusion fields from each band resulted in a greater overlap than when imaging over a smaller diameter disc. There is even

more variation of *w* values in SG-TC mode. Since identical imaging settings were used in both cases, more experimental work is required to better understand this phenomenon.

Values of *w* from the smaller probe (blue and green triangles) are smaller due to smaller tip working distances, suggesting a substantial resolution increase compared to the other two data sets, as observed from the qualitative analysis. In both FB and SG-TC modes it is clear that there is little difference between data sets from 5 µm and 2 µm imaging steps. This suggests that resolution from both imaging settings is similarly high and the same width diffusion fields from the bands were recorded; however, from qualitative analysis it has been shown that 2 µm step size reduced some of the artefacts, which is not reflected in this analysis. This emphasizes that both qualitative and quantitate evaluation of images and middle line profiles are important. Together with comparison with other data sets, it becomes possible to derive some trends and observations which would benefit imaging other substrates.

9.7 CONCLUSION

The effect of substrate and probe size, imaging step size and increment time on image spatial resolution as well as imaging artefacts were evaluated. Smaller, 1 µm rather than 10 µm, Pt probe resulted in smaller tip working distances, allowing to get closer to the substrate surface. This resulted in expected higher spatial resolution 50 µm MNEE SECM images in FB and SG-TC modes compared to the 10 µm Pt probe data. However, working with a smaller probe has its challenges, especially in FB mode: in order to see positive/negative feedback, the tip has to be brought much closer to the sample (in absolute terms), resulting in the current being more sensitive to any sample tilt. Also, there is an increased likelihood of the tip catching the surface or debris on the surface as it scans. On the advantageous side, working with such a small probe is more sensitive to differences in electrochemical activity at the surface, which might justify current variations in these SECM images. The use of a smaller probe also resulted in reduced convection effects, allowing now to use either H or V line profile for semi- and full quantitative analysis using modified Bessel function. H line profiles were used to compare experimental currents to modelled concentration profiles.

Images collected using the 2 µm step size and the 1 µm Pt probe were of the best resolution from all images presented in this thesis and from a qualitative analysis seemed to have reduced quantity of imaging artefacts. Despite this increased spatial resolution, modified Bessel function struggled to fit a number of H middle line profiles, as the peaks in the line profiles were sharper than observed in the previous chapters. We attribute this to a more highly perturbed local concentration profiles at the short (1-2 µm) tip working distances. Also, working with such a small probe means significantly smaller tip bulk currents, so PAC experiments are less reliable and more sensitive to the presence of any “dust” or similar particles on the

substrate surface than when using 10 µm Pt probe. With increasing *d,* the fitting improved, but remained lower in FB mode, as observed in the previous chapters.

Increment time effect on the image spatial resolution and imaging artefacts was evaluated when using both probes for imaging the same substrate. When $t \leq 0.1$ s, as expected, some variation in spatial resolution and more pronounced convection effects were observed with the larger probe, and FB mode was again more sensitive to these changes. The images collected with the 1 µm probe were not susceptible to any convection artefacts at none of the selected values. Interestingly, at $t < 0.02$ s the electrode appeared elliptical and distorted, and some additional artefacts evolved at the top of the images.

The values of *w* from modified Bessel function fitting to all imaging settings combinations presented in this thesis were plotted against *d*. This reassured that substrate, probe and imaging step sizes affect image spatial resolution, which can also be presented as the peak sharpness (width). Correlation between substrate and probe sizes was observed, and when the two were proportional, parallel lines generated from *w* values from both modes were obtained. Data from 1 µm probe and 5 µm step size resulted in linearly arranged data points, while equivalent 2 µm step size data was arranged in a less linear manner, reflecting variation in image resolution. From such analysis, spatial resolution was somewhat similar of all 1 µm probe images and the 5 µm step size was an overall efficient setting, providing great resolution images obtained within a shorter amount of time than when using a 2 µm setting.

9.8 REFERENCES

1. Lefrou, C. & Cornut, R. Analytical expressions for quantitative scanning electrochemical microscopy (SECM). *ChemPhysChem* **11**, 547–556 (2010).
2. What Is R Squared And Negative R Squared. *Fairly Nerdy* (2017). Available at: http://www.fairlynerdy.com/what-is-r-squared/.

10 CONCLUSIONS AND FUTURE WORK

SECM spatial resolution has been widely discussed and addressed in terms of using probes of various sizes in micro and nano scale. However, typically encountered imaging artefacts have been mostly accepted or ignored together with the fact that SECM does not have a well-established benchmark system unlike other imaging techniques. This thesis is focused on both of these overlooked sides of SECM. In-house micro fabricated Pt single and array micro electrodes as well as MNEEs were used as substrates for SECM imaging. The overall conclusions of this thesis are around the two main observations:

1. The in-house fabricated devices were shown to provide a useful benchmark substrate for SECM tips and SECM measurement systems;
2. SECM tips themselves reveal a number of interesting qualitative and quantitative information about the performance of individual and array electrodes.

Each is discussed in a greater detail as follows.

10.1 SUBSTRATES FOR SECM VALIDATION AND BENCHMARKING

Photolithographic techniques used for the electrode fabrication ensured that the devices are robust, reproducible, well-defined and (due to their small size) able to reach steady state currents within seconds (Chapter 3). As a result of such qualities, these substrates were shown to be effective for validating the performance of SECM imaging probes and measurement systems. Knowledge of the substrate's expected electrochemical behaviour and its well-defined geometry allows both evaluation of the probe's response and its comparison to the expected response in the SECM images.

Electrodes were of a disc or a square geometry of a known radius or an edge length, respectively, and as expected only the electrode area was found to show positive feedback (as expected for a conductor). The surrounding insulator area was shown by SECM to be without significant pinholes and to be uniform, confirming the initial control optical images and CV experiments which determined the experimental steady state current of each of the electrodes (Chapter 3). These defined and reproducible SECM images of several samples were established as a set of reference images. Therefore, discrepancies over this area could then be immediately attributed to an experimental artefact, the performance of the tip or measurement system, all of which needed to be addressed.

For example, during comparison studies using 2 µm and 5 µm step sizes when imaging a 50 µm diameter MNEE with a 10 µm Pt probe (Chapter 8) and a 1 µm Pt probe (Chapter 9), the pixels were more visible in the 5 µm setting images than in the 2 µm ones, as expected, but the smaller step size images contained horizontal lines across the insulator area when using

both probes. Since the surface is known to be uniform by a combination of methods, this immediately suggested that such an effect is prone to the probe's behaviour or an artefact. In considering its nature, when using a larger probe, such as the 10 µm diameter, these H lines could be an artefact related to the stepper motor as a result of electronic or mechanical noise. As the lines were less visible towards the bottom of the image, the noise could be intermittent or position-dependent. When using the smaller, 1 µm diameter, probe, the origin could be the same or different. An alternative explanation is related to the increased sensitivity of the tip, as the tip working distances were significantly reduced from 6.8-22.1 µm to 1.07-2.57 µm. (The values of *d* were extracted from COMSOL modelled responses over an insulator surface at several *d*, which were fitted using an approximate analytical expression, as described in Chapter 4, and extracted using the same expression described in Chapter 9, respectively). In the smaller *d* case, any dust contamination on the surface or tip could result in not only less precise *d* setting during the PAC experiment, but if this dust or any other contamination gets trapped between the tip and the substrate, this could result in such horizontal effects being due to the dragging of a dust particle by the tip. Smaller probes allow imaging of smaller substrates and hence NPs have been shown to be not a limit for the SECM if an adequate probe system is chosen (Introduction). However, this system at such small *d* values and with tips of smaller dimensions are more sensitive and more prone to such imperfections during the measurements.

Another clear example of tip/SECM system evaluation is that during the imaging with a 1 µm probe there were some definite technical issues related to the motor movements. The resulting images contained elongated electrodes in y-axis (Chapter 9), producing an ellipse instead of previously observed and expected circular geometry. This immediately suggested that the movement of the probe was affected, since our electrodes are of this known geometry. After the stepper motors were changed, the results improved. This confirmed that experiments performed previously by another group member were likely affected by a similar system malfunction; however, this user's substrate was not as well defined as the electrodes developed in this thesis, and this issue was not immediately apparent.

During the SECM imaging using a 10 µm Pt probe, tip conditioning effects, also referred to as time-dependent tip currents, were also observed, but mostly affecting only the measurements performed in FB mode (Chapters 5-6). This was apparent as higher currents over the insulator area at the top of the image (where imaging was started) than over the rest of the insulator, and in most of the examples these currents gradually stabilised before the electrode area was imaged. However, it has been shown how the SECM image looks when the tip current has not fully settled before the electrode area, resulting in higher currents not only over the insulator area, but also over the top part of the electrode area compared to the rest of the image (Figure 6-5 (a)). These substrates allowed the observation of this tip-related effect (a typical SECM imaging artefact), which likely shows that the tip electrode can become passivated either due

to chemical contaminants in the solution or physical contaminants (e.g. dust particles) picked up from the substrate surface by the tip. These effects were also observed from a semi-quantitative analysis of these high spatial resolution SECM images when using middle line profiles extracted from the images in the H and V directions.

Overall, these SECM images allowed the system and tip performance to be assessed. Performing images of such a well characterised substrate is a good way to ensure that none of these possible issues are a problem prior to imaging an unknown substrate.

10.2 GATHERED INFORMATION ABOUT THE SUBSTRATE ELECTRODES

The substrate electrodes developed and imaged have also revealed important information about their behaviour. First, the tip allowed the evaluation of whether the substrate was tilted and if the electrochemical activity of the substrate was uniform across both conductor and insulator surfaces. Tilting is expected to be minimized or removed during the set up; however, it is a manual task and occasionally some effects remain present, which can be noticed only throughout the experimental work. An example of the sample tilt was shown in Figure 5-1 (d), where the electrode was found to be slightly tilted diagonally. The effects became less significant with increasing *d*, as the percentage effect of the current variation decreased.

Also, details on the electrode surrounding insulator surface were observed. In the image of one of the MNEEs, the insulator area showed up as higher currents over a well-defined area; however, the currents were not as high as over a pure conductor (Figure 6-4 (a)). This could be due to the insulator layer thinning over the insulator surface or it could be a pinhole defect exposing the (clean) conductor. A small hole would lead to rapid radial diffusion from the hole and an apparently increased tip current compared to a larger insulator area.

Finally, when using the 1 µm tip for imaging the 50 µm MNEE at 1-2 µm tip working distances, an enhanced current detected difference in negative feedback due to topography difference in FB mode images. This was observed due to the square of Pt metal (50 nm height) around the electrode area, which was clearly presented as a ‘step’ in the H line profiles (Figure 9-6). This showed that the area outside this square is lower, hence a less negative feedback.

SECM images and the tip sensitivity allowed evaluation of the image spatial resolution and diffusion fields from various electrodes. FB mode images were more sensitive to tip working distance variation than SG-TC mode images. The electrode features (image spatial resolution) decreased faster in FB mode than in SG-TC mode with increasing *d*, showing that the hemispherical diffusion field overlap from the sides of the band was reached at a smaller distance from the electrode in the former mode (Chapter 6 and 8). Hemispherical diffusion has been predicted (Introduction) as being characteristic of both disc and square geometry at sufficient times (larger *d* values), and these SECM images in FB and SG-TC modes for both

single and array electrodes provide visual confirmation of this literature prediction. For example, microsquare electrodes of 30 µm edge length were imaged as discs due to hemispherical diffusion fields at selected imaging settings (Chapter 5). These images would also reveal different electrode cleanliness (activity), which is useful for the identification of the heterogeneity of the electrodes.

SECM images of the two array designs also allowed evaluation of the onset of individual diffusion field overlap from the neighbouring electrodes as a function of *d*. This was seen to be different for the chosen square arranged array compared to the hexagonally arranged array. The arrays were of similar specifications, and the latter preserved localized diffusion fields of the individual electrodes which did not appear to overlap during the experiments. The square electrode array also readily showed convection effects, resulting in H lines of higher currents when passing the electrode area compared to lower current H lines where the electrode was absent. Further work to establish differences might be useful.

In addition, consideration of the SECM imaging process has revealed insight into tip-related imaging artefacts. Typically, experimental protocols are designed so that it is considered that only a natural convection remains. However, in SECM imaging forced convection caused by the tip movement can affect substrate images. For example, from the microelectrode substrate data, SG-TC mode was seen to be more susceptible to convection (Chapter 5), whilst in FB mode, these effects were smaller. Convection effects were observed not only on the right side of the image due to the left to right tip imaging motion, but also on the left, as a result of forced convection arising from the tip returning from right to left to start scanning another H scan line, with either $FcMeOH^+$ being displaced from right to left by the tip in SG-TC mode or additional FcMeOH transport from the bulk to the tip upon the probe's return in FB mode. The increase of the tip current on the right side of the micro electrode image and current increase on the left side of the image in SG-TC mode are both therefore related to convection, and it is interesting that the microsquare electrode was more susceptible to convection than microdisc electrode at the same *d* due to the differences in diffusional transport (Chapter 5).

From nanoband edge electrode images, unlike the microelectrode images, it is interesting that FB mode showed more convective effects than SG-TC mode (Chapter 6-9). FB mode effectively probes the convective effect on tip diffusion, while SG-TC mode probes convective effect on substrate diffusion. Since micro electrodes have Pt metal on the whole electrode area compared to a thin band in MNEEs, the tip was smaller than the substrate and convection effects in FB mode over such large electrode area were negligible. But when the amount of metal in the substrate electrode is decreased, the probe is larger than the substrate. The response of the latter is smaller and hence any variations become more significant in relative terms, which is relevant to FB mode which is known to be more sensitive than SG-TC mode. In other words, nanoband diffusion is enhanced over the microelectrode; hence the forced

convective effect is decreased in SG-TC mode such that the effect is more clearly seen in FB mode.

H and V middle line profile comparison (semi-quantitative analysis) allowed quantitation of tip-induced convection. V line profiles were more symmetrical than the H ones, confirming the absence of variations in convection and that only diffusion accounted for the variation within V line profiles. For example, currents to the right of the microdisc electrode in H line profile were of the order of 5% higher than the equivalent V line profile (FB mode, d = 13.2 µm (Figure 5-5)), due to the presence of convective effects.

Finally, quantitative analysis of the full line profile was performed through experimental middle line profile fitting using a multi-peak Gaussian function and a modified Bessel function. The former was appropriate and found to be suitable for square electrode data, while the latter was the preferred approach for disc geometry electrode data fitting (Chapter 7). This demonstrates that convection and diffusion effects can be separated and analysed in quantitative analysis, and differences between experimental and modelled responses were accounted for the imaging artefacts. When using the 10 µm probe, such a comparatively simple quantitative analysis was very efficient for both disc and square electrodes. However, experimental data from the 1 µm probe (Chapter 9) did not agree with the modified Bessel function to such a good extent as the 10 µm data from both 100 µm and 50 µm MNEE images. The concentration profiles became more perturbed by such a small probe, where the tip current densities were enhanced. It would be interesting to perform such imaging and quantitative analysis of the data collected with more different size probes, allowing evaluation whether the 10 µm probe size is the optimum size to enable such simple analysis.

10.3 SUMMARY AND FUTURE WORK

Substrates used in this thesis were microfabricated Pt micro electrodes and MNEEs of high fidelity, controlled design, shape and dimension. They are robust and thus can be used multiple times, which makes them suitable not only for qualitative but also for quantitative analysis, enabling structured identification, evaluation and quantitation of the typical imaging artefacts. Analysis of these SECM images showed that these electrodes can be used as a promising benchmark system for a typical SECM imaging, which is still lacking a well-established standard allowing to easily separate expected effects from the substrate and from the imaging artefacts or a failure of the set-up. It is believed that these electrodes are already good calibration sources.

Nevertheless, there are several things that could be done in the future to add further credibility to the results and/or improve them. For example, a cleaning procedure was shown to be effective, but the cleaning protocol could be improved to make it more structured and defined for anyone to use. Then, there were some technical issues with the stepper motor when using

a 1 µm probe. Several FB and SG-TC mode images were still elongated in y-direction (Section 9.3), suggesting that the technical issue may not have been solved in this case. Another set of MNEE images with could be collected to further evaluate smaller probe effect on SECM images. Finally, and most importantly, determination of the optimum probe size for imaging could be revealed through more imaging experiments with different probes, as briefly discussed in the previous section. These data would also allow establishing when the simple analysis method can and cannot be used and establishing the fundamental *d* sensitivity in FB and SG-TC modes. These steps seem to be crucial in determining how a quantitative calibration method will work. Then, COMSOL modelling could also be extended into 3D imaging of concentration profiles (for comparison with the experimental data) and even used to model convection effects observed in SECM images.

More work could also be performed on the arrays to show that they are as good for SECM benchmarking system as single electrodes. It needs to be evaluated what size electrodes should be used, hence how much available insulator area surrounding the electrodes would be required to ensure that imaging artefacts, such as tilting, convection and time-dependent tip currents, are separated from the substrate's response. Then, middle line profiles could be also analysed and fitted using a modified Bessel function if the electrodes are of a disc geometry. This would ultimately reveal if imaging artefacts are more or less apparent when imaging an array instead of a single electrode, and if the model works for more than one electrode at a time.

Also, such SECM imaging allows evaluation of whether hemispherical diffusion layers do or do not overlap from the neighbouring electrodes at selected *d* values, which could potentially assist in designing arrays. This is also relevant if either edge or middle electrode in the array behaviour is preferred for sensing purposes; SECM images of such substrates allows evaluation of the two electrode types. Such analysis would also allow evaluation whether the edge electrodes in an array behave differently to the middle electrodes, and how many rows or columns in from the edge are required before the electrodes behave as middle electrodes. This knowledge is important when designing, studying and using smaller arrays (when more of the electrodes are not in the middle).

This study also brings one closer to the analysis and characterisation of the individual electrodes in an array for quality control purposes. Such a method would take a significant amount of time to test each of the electrodes in an array of thousands of units; unless analysis of combinations of the array electrodes would be possible at large *d*. Then, the electrodes that result in lower current would be focused in to see which and how many electrodes cause this effect. Hence this is an initial study to show that SECM can be used to characterise and evaluate individual array elements, rather than simple one array unit, which is standard in some of the experiments, such as CV.

Electrodes which produce less current than the others as a result of being less active due to either fabrication-related defects or being slightly dirtier can be identified in the array, and such approach could be applied to a broader application of the detection of defects. For example, the results could be further analysed to find the real reasons for inconsistency of the electrodes' activity, and so the SECM technique could be used in the industrial fabrication applications, where defects really matter and their presence significantly affects the performance and price of the product. SECM provides electrochemical information about the substrate which combined with the optical information can be used for not only visual array evaluation but also for the evaluation of the array activity and performance. A combination of such information for various surfaces will be useful, especially if the surface or the species causing the loss of activity are optically transparent and cannot be optically evaluated.